

Public gather comme Date 1. At		ON PAGE		Form Approved OMB No. 0704-0188
		1 hour per response, including the time for reviewing instructions, searching existing data sources, collection of information. Send comments regarding this burden estimate or any other aspect of this collection of information, including suggestions for reducing burden, to the Washington Headquarters Services, Directorate for Information Operations and Reports, 1215 Jefferson Avenue and Budget, Paperwork Reduction Project 0704-0188, Washington, DC 20503.		
12-10-92		3. REPORT TYPE AND DATES COVERED		Final 1/1/92 - 12/31/92
4. TITLE AND SUBTITLE		5. FUNDING NUMBERS		
Quantum Effect Physics, Electronics and Applications		N00014-92-J-1325		
6. AUTHOR(S)		4145408-01		
Prof. Henry Smith				
7. PERFORMING ORGANIZATION NAME(S) AND ADDRESS(ES)		8. PERFORMING ORGANIZATION REPORT NUMBER		
Research Laboratory of Electronics Massachusetts Institute of Technology 77 Massachusetts Avenue Cambridge, MA 02139				
9. SPONSORING/MONITORING AGENCY NAME(S) AND ADDRESS(ES)		10. SPONSORING/MONITORING AGENCY REPORT NUMBER		
Office of Naval Research 800 North Quincy Street Arlington, VA 22217-5000				
11. SUPPLEMENTARY NOTES The view, opinions and/or findings contained in this report are those of the author(s) and should not be construed as an official Department of the Army position, policy, or decision, unless so designated by other documentation.				
12a. DISTRIBUTION/AVAILABILITY STATEMENT		12b. DISTRIBUTION CODE		
Approved for public release; distribution unlimited.				
13. ABSTRACT (Maximum 200 words)  Work by Prof. Smith and his collaborators is summarized here				
				
14. SUBJECT TERMS		15. NUMBER OF PAGES		
16. PRICE CODE				
17. SECURITY CLASSIFICATION OF REPORT		18. SECURITY CLASSIFICATION OF THIS PAGE		19. SECURITY CLASSIFICATION OF ABSTRACT
UNCLASSIFIED		UNCLASSIFIED		UNCLASSIFIED
20. LIMITATION OF ABSTRACT		UL		

NSN 7540-01-280-5500

Standard Form 298 (Rev 2-89)  
Prescribed by ANSI Std Z39-18  
298-102



**RESEARCH LABORATORY of ELECTRONICS**  
MASSACHUSETTS INSTITUTE OF TECHNOLOGY  
CAMBRIDGE, MASSACHUSETTS 02139-4307

December 15, 1992

Dr. Larry R. Cooper  
Scientific Officer  
Code 1114SS  
Office of Naval Research  
800 North Quincy Street  
Arlington, VA 22217-5000

In accordance with the terms of the Office of Naval Research Grant No. N00014-92-J-1325, I am sending you the following material:

Type of Material: Final Report (Proceedings)

Title: International Workshop on Quantum-Effect Physics, Electronics, and Applications

Submitted by: Professor Henry Smith

Period Covered: January 1, 1992 - December 31, 1992

Number of Copies: One

Distribution: Navy Distribution List (2)

Mary S. Greene  
Publications Office  
RLE 36-412

cc: Prof. Smith  
D. Duffy  
A.F. Favoloro, E19-702  
File

OSP 11616

**Quantum Effect Physics,  
Electronics and Applications**



*Quantum Effect Physics, Electronics and Applications* contains contributions presented at an international workshop, held in Luxor, Egypt from 6-10 January 1992. The workshop was attended by 90 researchers from all over the world and contained 14 sessions comprising a total of 60 presentations.

Following the recent, rapid developments in this subject, and thanks to the international experts in the field who attended the workshop, this book comprises the most up-to-date summary of quantum phenomena and transport mechanisms in semiconductor devices. It will thus be of great value to physicists, electronic and electrical engineers, and nanotechnologists.

Aspects covered:

- Competing Concepts and Technologies with Quantum Effects
- Theoretical Calculations and Models of Bandstructure, Transport, Fluctuations, and Noise in Confined Geometries
- Nanofabrication
- Transport Experiments
- Optical Properties and Spectroscopy Results in Vertical Superlattices, Wires and Dots, and Arrays of Dots and Anti-dots
- Resonant Tunnelling and Coulomb Blockade
- Applications Based on Quantum Phenomena

# **Quantum Effect Physics, Electronics and Applications**

**Proceedings of the International Workshop on  
Quantum Effect Physics, Electronics and Applications**

**Edited by K Ismail, T Ikoma  
and H I Smith**

92-32561

270pb

**92 12 22 139**

**Institute of Physics Conference Series Number 127  
Institute of Physics Publishing, Bristol and Philadelphia**

Copyright © 1992 by IOP Publishing Ltd and individual contributors. All rights reserved. No part of this publication may be reproduced, stored in a retrieval system or transmitted in any form or by any means, electronic, mechanical, photocopying, recording or otherwise, without the written permission of the publisher, except as stated below. Single photocopies of single articles may be made for private study or research. Illustrations and short extracts from the text of individual contributions may be copied provided that the source is acknowledged, the permission of the authors is obtained and IOP Publishing Ltd is notified. Multiple copying is permitted only under the terms of the agreement between the Committee of Vice-Chancellors and Principals and the Copyright Licensing Agency. Authorization to photocopy items for internal or personal use, or the internal and personal use of specific clients, is granted by IOP Publishing Ltd to libraries and other users registered with the Copyright Clearance Center (CCC) Transactional Reporting Service, provided that the base fee of \$4.50 per copy is paid directly to CCC, 27 Congress Street, Salem, MA 01970, USA. 0305-2346/92 \$4.50+.00

CODEN IPHSAC 127 1-264 (1992)

*British Library Cataloguing in Publication Data*

A catalogue record for this book is available from the British Library

ISBN 0-7503-0225-9

*Library of Congress Cataloging-in-Publication Data are available*

<b>Accession For</b>	
NTIS GRA&I <input checked="" type="checkbox"/>	
DTIC TAB <input type="checkbox"/>	
Unannounced <input type="checkbox"/>	
<b>Justification</b>	
<b>By</b> _____	
<b>Distribution/</b>	
<b>Availability Codes</b>	
<b>Dist</b>	<b>Avail and/or Special</b>
A-1	

DTIC QUALITY INSPECTED 5

Published by IOP Publishing Ltd, a company wholly owned by the Institute of Physics, London Techno House, Redcliffe Way, Bristol BS1 6NX, England  
US Editorial Office: IOP Publishing Inc., The Public Ledger Buildings, Suite 1035, Independence Square, Philadelphia, PA 19106, USA

Printed in the UK by Galliard (Printers) Ltd, Great Yarmouth, Norfolk

## Preface

This book contains contributions presented at the International Workshop on Quantum Effect Physics, Electronics and Applications. The workshop was held in Luxor, Egypt, from January 6 to 10, 1992.

The workshop was attended by 90 researchers from all over the world, who are experts in the subject of the workshop. The number of sessions organized was 14, comprising a total of 60 presentations, divided into 16 invited talks, 31 regular talks, and 13 short talks. The topics covered during the workshop addressed subjects such as theoretical calculations and modelling of quantum confined structures, nanofabrication of confined geometries, transport experiments and optical properties of quantum wires and dots, resonant tunnelling and Coulomb blockade, and applications based on quantum phenomena.

In view of the rapid evolution of this subject during the past few years, and thanks to the large number of experts in this field who attended the workshop, this book comprises the most up-to-date results. It is divided into seven chapters. The first comprises three talks which were given in the plenary session. Although not directly related to quantum phenomena, the three talks covered topics that can be regarded as competing concepts and technologies with quantum effects in terms of their potential for the future.

The second chapter covers theoretical calculations and models of bandstructure, transport, fluctuations, and noise in confined geometries. By confinement we mean two-dimensional, one-dimensional, and zero-dimensional structures. In every chapter the talks are organized in this way. The third chapter deals with nanofabrication, its challenges, and its prospects.

In the fourth chapter, experimental transport results are presented. This covers ballistic transport, electron motion in the presence of a modulating potential, and transport in quantum wires and point contacts.

The fifth chapter deals with optical properties and spectroscopy results in vertical superlattices, wires and dots, and arrays of dots and anti-dots. The materials discussed were not limited in this case to GaAs and its related compounds, but also covered Si/SiGe heterostructures.

The sixth chapter covers one of the most promising aspects of quantum transport, which is resonant tunnelling and Coulomb blockade. The seventh chapter moves to applications based on quantum phenomena covering the device level, the circuit level and the system level.

In addition to the discussions held during the technical sessions, this workshop has offered the unique opportunity to its attendees to discuss many interesting issues on an informal basis, surrounded by an atmosphere with a mixture of the very old and the very new.

The success of the workshop is a result of the effort of many individuals. We are indebted to Professor F Ismail, Dean of the Faculty of Engineering, Cairo University, and Professor A Bilal, Head of the Electronics and Communications

Department for their support and encouragement. We are very grateful to the following for the local organization: O ElSayed, S Habib, A Shalash, S Salah, M Arafa, K Awadi, H Radwan, M Metwally and O Baghdadi.

The workshop was sponsored and financially supported by Cairo University, the Ministry of Foreign Cooperation, the Japanese Foundation for Promotion of Material Science and Technology, Defence Advanced Research Projects Agency (DARPA), and the following corporations: Giza Engineering Systems, Fujitsu, Hitachi, Matsushita, Mitsubishi, NEC, BTT, Sanyo, Sony, and Toshiba.

**K Ismail**  
**T Ikoma**  
**H I Smith**

**Organizing and Programme Committee**

**K Ismail**, Chairman, Cairo University  
**T Ikoma**, Co-Chair, University of Tokyo  
**H I Smith**, Co-Chair, Massachusetts Institute of Technology  
**L Esaki**, International Business Machines  
**J P Kotthaus**, University of Munich  
**S Namba**, Osaka University  
**H Sakaki**, Tokyo University  
**H van Houten**, Philips

## Contents

### v Preface

### Chapter 1: Competing Concepts and Technologies

1-6 Silicon ULSI: future and limitations from a materials viewpoint  
*S Asai*

7-12 Neural networks and learning  
*Y S Abu-Mostafa*

13-18 Thoughts on the impact of biology on the design of electronic devices and systems  
*C D W Wilkinson*

### Chapter 2: Theoretical Calculations and Models

19-24 Kinetic conductance and the characteristic carrier traversal times of small conductors  
*M Büttiker and H Thomas*

25-28 Spatial distribution of quantum mechanical currents and charge in a model semiconductor nanostructure  
*K-F Berggren, C Beshev and Z-L Ji*

29-32 Quantum noises in mesoscopic conductors: origins and suppression  
*A Shimizu, M Ueda and H Sakaki*

33-36 Dynamics of electron-wave packets in nanostructures  
*A Endoh, S Sasa, H Arimoto and S Muto*

37-40 Quantum Hall effect: edge-state conduction and critical localization of bulk states  
*T Ando*

41-44 Analysis of Hall resistance anomalies with wave mechanics  
*K Kawamura, H Sawano and T Ueta*

45-50 Scattering and quantum localization of electrons in a waveguide by static and time-varying potentials  
*P F Bagwell, A Kumar and R Lake*

51-54 Plasmon-phonon coupling and depolarization effects in quantum well wires  
*L Wendler and R Haupt*

55-58 Magnetophonon resonances in quantum wires  
*N Mori, H Momose and C Hamaguchi*

59–64 The influence of the Coulomb interaction on the electronic spectrum of quantum dots  
*W Häusler and B Kramer*

65–68 Spin scattering effect in metallic quantum dots  
*S-I Kobayashi, H Goto and S Katsumoto*

69–72 Green's function in magnetic fields  
*T Ueta*

### **Chapter 3: Nanofabrication**

73–78 Nanofabrication: challenges and opportunities  
*D P Kern*

79–84 Neutral atom nanolithography  
*K K Berggren, M Prentiss, G Timp and R E Behringer*

85–94 Focused ion beam processing of mesoscopic quantum structures  
*P M Petroff, Z Xu, Y J Li, M Miller and M Wassermeier*

95–98 Fabrication and spectroscopic studies of InP/GaInAs/InP and GaAs/GaInAs/GaAs quantum-well wire structures  
*L Samuelson, K Georgsson, A Gustafsson, I Maximov, L Montelius, S Nilsson, M-E Pistol, W Seifert and A Semu*

99–102 Observation of quantum confinement in strain-induced quantum wires/dots  
*I-H Tan, T Yasuda, R Mirin, D Lishan, E Hu, J Bowers and J Merz*

103–106 Lateral barrier modulation—a new technique for the definition of high quality quantum wires and dots for optical investigations  
*Ch Gréus, A Orth, J Straka, K Pieger and A Forchel*

107–110 Ultra-fine AlGaAs/GaAs quantum-well wire fabrication combining electron beam lithography and wet chemical etching  
*Y Shiraki, S Fukatsu, R Ito, E Ishikawa, K Onabe, K Momma and N Ogasawara*

111–114 Side gating for  $\delta$ -doped quantum wires  
*T J Thornton, Y Feng, J J Harris and D Williams*

115–118 Control of surface and interface Fermi level pinning for compound semiconductor nanometer scale structures  
*H Hasegawa, J Fujikura, M Akazawa and H Tomozawa*

119–122 Nanometer x-ray mask created using precise crystal growth  
*K Furuya, Y Miyamoto and D Yamazaki*

123–126 Si super-heteroepitaxy and its application to new structure FETs  
*M Miyao and K Nakagawa*

**Chapter 4: Transport Experiments**

127-132 Ballistic transport and low-frequency noise in high mobility two-dimensional electron systems  
*S Tarucha, T Saku, Y Hirayama, J R Phillips, K Tsubaki and Y Horikoshi*

133-136 Non-linear electron focusing in 2DEG systems with an applied DC current  
*K Nakazato, R I Hornsey, T J Thornton, J R A Cleaver and H Ahmed*

137-140 Electron transport in the transition regime between 2D and 0D behaviour  
*O Berthold, J Smoliner, V Roßkopf, E. Gornik, G Böhm and G Weimann*

141-144 Superlattice effects on the weak localization of a grating gate Si-MOSFET  
*J R Gao, C de Graaf, J Caro, S Radelaar and K Heyers*

145-148 Magnetoresistance in GaAs-AlGaAs heterostructures under two-dimensional lateral potential modulation  
*F Nihey and K Nakamura*

149-152 Magnetic breakdown in a two-dimensional electron gas subjected to a periodic potential  
*P H Beton, M W Dellow, P C Main, L Eaves and E S Alves*

153-156 Ballistic conductance steps and electron focusing in long samples  
*S Washburn, K Ismail and K Y Lee*

157-162 Electron scattering in AlGaAs/GaAs hetero-quantum wires  
*T Ikoma, T Odagiri and K Hirakawa*

163-166 Boundary scattering in quantum wires fabricated using ion implanted gates  
*R J Blaikie, K Nakazato, T J Thornton, J R A Cleaver and H Ahmed*

167-170 Fluctuations effects in the low temperature magnetoresistance of micron scale semiconductor junctions  
*J P Bird, Y Ochiai, T Onishi, T Kitatani, M Kawabe, K Ishibashi, Y Aoyagi and S Namba*

171-174 Experiments on mechanically controllable break junctions of niobium and platinum  
*C J Muller, J M van Ruitenbeek and L J de Jongh*

175-178 High temperature operation of ballistic constrictions  
*G L Snider, M S Miller, M J Rooks and E L Hu*

179-182 Conductance oscillations in a quantum point contact of high-mobility hole gas  
*M Noguchi, K Hirakawa and T Ikoma*

**Chapter 5: Optical Properties**

183-188 Spectroscopy of quantum-dot atoms and antidot arrays  
*D Heitmann, B Meurer, K Kern, P Grambow, K Ploog and Y H Zhang*

189-194 Opto-electronics with n-i-p-i doping superlattices  
*G H Döhler*

195–198 Resonant electron capture in AlGaAs/GaAs quantum well structures  
*A Fujiwara, S Fukatsu, Y Shiraki and R Ito*

199–203 Optical properties of in-situ grown GaAs quantum wires by MOCVD selective growth  
*Y Arakawa, Y Nagamune, S Tsukamoto and M Nishioka*

205–208 Optical properties of AlGaAs serpentine superlattice quantum wires  
*H Weman, M S Miller, C E Pryor, P M Petroff, H Kroemer and J L Merz*

209–212 Novel linear and nonlinear optical properties of Si–Ge microstructures  
*M Jaros, K B Wong and R J Turton*

**Chapter 6: Resonant Tunnelling and Coulomb Blockade**

213–218 Momentum conservation in 1D–2D tunnelling processes  
*J Smoliner, W Demmerle, E Gornik, G Böhm and G Weimann*

219–224 Gated resonant tunnelling diodes  
*P H Beton, M W Dellow, P C Main, L Eaves, T J Foster, C J G M Langerak, M Henini, A F Jezierski, S P Beaumont and C D W Wilkinson*

225–228 Tunnelling spectroscopy of a leaky electron waveguide  
*J A del Alamo and C C Eugster*

229–234 Single electron pump and turnstile in semiconductor nanostructures  
*L P Kouwenhoven, A T Johnson, N C van der Vaart and K J P M Harmans*

235–238 Coulomb blockade in the few-electron limit  
*C J B Ford, M Field, P J Simpson, M Pepper, D Popovic, D Kern, J E F Frost, D A Ritchie and G A C Jones*

**Chapter 7: Applications**

239–243 Circuit-level applications of quantum effect device (RHET)  
*A Shibatomi and N Yokoyama*

245–248 Buried-quantum well resonant tunnelling transistor in the  $\text{Al}_x\text{Ga}_{1-x}/\text{In}_x\text{Ga}_{1-x}\text{As}$  material systems  
*D Lippens, P Mounaix, H Leroux, O Vanbésien, V Sadaune and E Barbier*

249–252 Voltage tuned interference in an AB ring  
*S Katsumoto, N Sano and S Kobayashi*

253–256 Technical developments towards quantum-effect microwave electronics  
*H L Hartnagel*

257–260 Optically driven quantum networks: an approach to programmable matter?  
*G Mahler and H Körner*

261–262 Author Index

263–264 Keyword Index

## Silicon ULSI: future and limitations from a materials viewpoint

Shojiro Asai

Advanced Research Laboratory, Hitachi, Ltd.  
Hatoyama, Saitama 350-03, JAPAN

### Abstract

Problem areas in materials for future ULSIs(Ultra-Large-Scale Integrated circuits) are identified and possible solutions are discussed. Many new materials have already been used in addition to the usual silicon, its oxide and aluminum to make state-of-the-art LSIs which contain up to forty million transistors and feature line-widths around 0.8  $\mu\text{m}$ . Why the materials have to be reviewed to further exploit the ultimate potential of integrated circuits and what are the most likely candidates? Will we rely solely on silicon till the predicted physical limit around 0.1  $\mu\text{m}$  is reached? Those are the issues we would like to address here.

### 1. Introduction

The silicon LSI has been the work-horse of modern-day convenience. It has underlain all the wonder of electronics, reduced the price of its convenience and set the rate of its progress. Its complexity has increased tremendously over the past years. From the materials viewpoint, the integrated circuit started out as simple bipolar or p-MOS transistor structures where materials involved were just silicon, its oxide, and aluminum. Today, it has become far more complicated, because of the density, performance, and reliability requirements. We have the poly, or poly-crystalline silicon, silicon nitride, Al-Si alloys, refractory contact barriers, phosphosilicate glass for passivation, just to name a few. Materials specifications have also become more demanding, because of yield and reliability requirements. Silicon crystals itself has been constantly improved in terms of control over its oxygen content, for example.

The evolution described above has been driven by the the need to meet ever-increasing demand for denser, faster, more functional LSIs. To be able to foresee what will happen next, we have to look closely into the limitations of what we are using at present. In a perspective along the direction toward which the outside demand pushes future LSIs, we will try to identify problem areas with basic materials implications. There is no doubt that, during its evolution up to the ultimate density, where a minimum feature size around 0.1  $\mu\text{m}$ , or even below, will be used, we will be introducing more new materials and more new specifications for all kinds of ULSI materials.

The scrutiny that is going on is comprehensive, covering all kinds of materials involved. Silicon, the good old stuff, is no exception. Its position as the dominant starting material for the LSI is hard to challenge. However, a review is now in order to see if we can keep building the transistor in the LSI as we have always been and if it can remain all-silicon as it has always been. The limitation of currently-used ion implantation as a device-building technology is being discussed, on the one hand. Molecular-beam epitaxy and atomic layer doping, as powerful alternatives, are rapidly coming to maturity, on the other. These new technologies may totally change the way the device is structured in ULSIs.

The position of  $\text{SiO}_2$  as the dominant dielectric material may never change, but it will have to be augmented by various other dielectrics. Metals have been in a constant review, also. The properties of the substitutes have to be characterized for their conductivity and long-term reliability. A careful observation of what is being discovered tells us that minimal-size imperfections are showing up in silicon, metallic, and dielectric materials and that their sizes are approaching atomic dimensions. Boldly stated, control in atomic dimensions is being required in all semiconductor materials.

## 2. Problem Areas in Future ULSIs

### 2.1 Silicon Limits

How small one can make a silicon transistor as a component of LSIs has been discussed over and over. Hoeneisen and Mead made a prediction in the early 1970's that the minimum-size silicon MOSFET would have a source-to-drain distance of about 0.2  $\mu\text{m}$ . Their calculation was based on a rather crude device design, assuming, for example, a uniformly doped substrate and a junction depth fixed at half the channel length. More advanced transistor engineering these days has demonstrated workable devices down to 0.1  $\mu\text{m}$ . In any case, factors that limit transistor miniaturization are p-n junction breakdown at the drain, and tunneling current through the gate oxide. The problem of avalanche breakdown will be dealt with first, and the issue of gate dielectrics will be addressed later in the next section.

The properties of the material determine the performance of the device that is made out of it. In fact, the product of speed and breakdown voltage of a device is proportional to the product of carrier velocity and the highest electric field the semiconductor material can sustain. We can do a lot of engineering on these material properties in the active semiconductor with the advent of heteroepitaxy. It will be feasible to start from a silicon substrate, grow a layer of high-carrier-mobility semiconductor such as Ge or SiGe for the channel, while using another hetero-junction at the source and drain which would deter the carriers from avalanching. The band-gap engineering, as it is called, will be extensively used to overcome the silicon limits of the future ULSI devices.

All the silicon limits are not intrinsic. Practical limits are also set by the spatial scattering of dopant atoms in silicon which is inevitable with ion implantation. It causes a certain variation in the threshold voltages and junction breakdown characteristics which becomes a severe problem in designing a circuit with a large number of transistors. The quality of silicon crystal is also in question. The density of defects which generate an excessive generation-recombination current is one of the toughest issues in yield control for the DRAM(Dynamic Random Access Memory). The leakage current has been related to, but has not been quite nailed down to, the behavior of point defects such as oxygen impurity in the grown silicon and heavy-metal impurities that segregate at such defects. It is critically important to continue finding out about the behavior of point imperfections and improving on as-grown crystal quality.

### 2.2 Dielectric Limits

The most important role of dielectrics in ULSIs is in the gate insulators in either an MOS transistor or a capacitor. The need for a high-dielectric-constant material is more stringent in MOS capacitors, where a certain amount of signal charge has to be stored in a minimized area. A figure of merit here is the maximum dielectric density, or the product of the dielectric constant and the breakdown electric field, which can vary by more than a factor of two over various dielectric materials and combinations thereof. The most useful dielectric of all,  $\text{SiO}_2$ , has the robustness that cannot be matched by any others, but it does not top others in terms of dielectric density.  $\text{Si}_3\text{N}_4$  and its derivatives, with effective dielectric constants up to about 80 % higher than  $\text{SiO}_2$ , have actually been used for this purpose. A material which is highlighted more recently is  $\text{Ta}_2\text{O}_5$ . It has long been successfully used for discrete capacitors, but has been too leaky for use in LSIs. Sputtering or CVD(Chemical Vapor Deposition) of a  $\text{Ta}_2\text{O}_5$  film on top of a thin  $\text{SiO}_2$  film and a series of succeeding annealing process, however, have proved to be quite feasible. This will be the technology for the 256Mb DRAM and beyond.

Ferroelectric films such as PZT(Pb Zirconate Titanate) is also being considered for DRAMs because of their extremely high(in excess of 1000) dielectric constants. CVD as well as sputtering of these materials are being extensively studied for use in Gigabit DRAMs. It is still premature to judge if they are feasible, but a rapid progress is expected. Ferroelectricity itself may be used in future non-volatile memories and field-programmable logic LSIs.

The need for high-dielectric-constant materials comes also from the push toward the physical transistor limits. Direct tunneling across the gate SiO<sub>2</sub> sets one of the fundamental device limits at the thickness of about 3 nm regardless of the dielectric material. The situation is alleviated by using a dielectric with higher dielectric constant, and thus with a larger thickness to the same field effect. There have been attempts to use various dielectrics including Si<sub>3</sub>N<sub>4</sub>, SiON, and composite layers of these with SiO<sub>2</sub> as the gate insulator material. The maximum dielectric density is again the figure-of-merit. The only reason why none of these exotic gate insulators have been in practical use so far is because SiO<sub>2</sub> is still good enough for currently engineered transistor sizes, where the insulator thickness is between 10 nm and 15nm.

### 2.3 Metallic Limits

As transistors are scaled down, so are the wire's width, its spacing, and contact hole size. A smaller contact hole means an increased current density, which causes accelerated interface reaction between the Si and Al alloy at the contact. The interface reaction takes two forms. Spikes of Al are formed in the substrate Si, which penetrate through the diffused layer and result in leaky junctions. The silicon melts into the aluminum to make the contact too resistive and eventually open-circuited. Traditionally, the interface reaction between Si and Al has been suppressed by the use of Al-Si alloy. But with the aggravated reactions in small contacts, it has become necessary to use a barrier metal which hardly reacts with neither Si or Al. The materials used for this purpose include WSi<sub>2</sub>, TiW, and TiN. Processing techniques for these materials have evolved from crude sputtering to more sophisticated CVD processes. Their electrical properties and reliabilities have also been studied.

Aluminum or its alloy as a wiring material has also been questioned over the years. This is because electro-migration and stress-induced migration develop cracks more easily in Al wires than in other metals with higher melting points. Various substitutes for aluminum alloys have been studied. Of critical importance are the conductivity, melting point(a measure of migration resistance), workability during both deposition and etching, and corrosion resistance. Refractory-Al-refractory sandwiches, tungsten, and copper have been studied.

Four levels of metals are currently used for fastest bipolar logic LSIs. MOS LSIs, on the other hand, have had two metal layers in addition to the gate level, which can be used as part of wires. Multiplicity in metal levels calls for self-planarizing deposition of various materials involved. As the number of logic gates is increased on a chip, increased also is the number of interconnects, which in turn means an increased silicon surface area for them. There are thus increased need for multiple levels of metals to accommodate the increased number of wires, which also means increased number of via holes. Via-hole filling with selective CVD, use of easy-flow glasses for planarizing inter-level insulation, and other various techniques are being applied. Simultaneous wiring metal deposition and via-hole filling using tungsten CVD have also been proposed. Insulators with low dielectric constants are looked for isolating between metal levels.

More sophisticated interconnection will be required in the future, because the signal delay on a chip will become a major issue in fast logic and memory devices. On-chip long-distance wiring will be laid down on a special layer with broader lines. The use of multi-leveled, "printed-circuit silicon board" may be used to accommodate multiple, flip-bonded chips. Even a combination of on-chip and off-chip optical interconnects with microlasers and micro-receivers may be used in the future. The epitaxial growth of light-emitting semiconductors on silicon will then be required.

### 3. Emerging Technologies

### 3.1 Atom-Level Materials Parameter Control in the Vertical Dimension

In compound semiconductors, crystal growth, rather than ion implantation and oxidation, has been the dominant way of forming the basic device structures. Initially, crystal growth was chosen as a last resort because the process of ion implantation and high-temperature annealing does not work quite adequately with compound semiconductors. Sophisticated low-temperature epitaxial growth techniques, especially, MBE(Molecular-Beam Epitaxy) and MOCVD(Metal-Organic CVD), have been worked out to enable very complicated device structures, including those for lasers and HEMTs. Structures that are called heterojunctions, where semiconductor lattices with different atomic compositions epitaxially meet with each other, are quite extensively used in those devices.

The HEMT is a device using a layer of narrow-gap, high-mobility semiconductor for the channel and another wide-band-gap semiconductor on top as the gate insulator. The top layer is doped with impurities which supply the channel with the carriers. A similar structure has been built with a Si substrate, with a layer of SiGe and Ge for the channel. With Ge or SiGe, a considerable increase in speed of the device has been obtained. A number of attempts have been reported to build a hetero-epitaxial bipolar transistor for higher cutoff frequencies. It should also be possible to increase the avalanche breakdown voltage of a p-n junction by introducing a heterojunction. It may even be possible to do it without deteriorating its forward characteristics which is important to maintain the transistor gain, since, in general, the minority carrier in the channel or the base and the carrier which dominates the band-to-band excitation of electron-hole pairs in the depletion region do not coincide. This kind of engineering has been quite customary in optical devices made of compound semiconductors, but has never been adopted for silicon-based LSIs. It will have to be very seriously considered as an alternative in future LSI technologies.

The variation in MOSFET threshold voltages and breakdown characteristics, by narrowing the logic window, can be a serious factor slowing down circuits. This problem can be diminished by ALD(Atomic-Layer Doping), which can minimize the device characteristics variation due to impurity distribution. Introduction of discontinuity in atomic scale, which has been monopolized by compound semiconductors so far, will thus greatly expand the physical limits of silicon-based LSIs. There will be a variety of device applications once atomic-scale control becomes possible in the lateral dimension as well as in the vertical dimensions.

The potential application of MBE is not limited within the semiconductor material. A successful growth of a metal silicide on silicon has been reported. Heterostructures of this kind may be very useful as a contact barrier or a contact plug. Crystallization of Ta<sub>2</sub>O<sub>5</sub> on top of SiO<sub>2</sub> has proven to be useful in making the composite dielectrics more robust for capacitance application. It has been reported that atomic-level smoothness of the initial silicon surface does result in good oxide-silicon interface. It is also reported that the interface smoothness between the SiO<sub>2</sub> and the poly can be crucial in forming a viable tunnel barrier for non-volatile memories. Atomic ordering, such as that realized by MBE, at the interface in the insulator-to-insulator or silicon-to-insulator heterojunctions is likely to be good for device characteristics.

A serious question here is if such technologies as Hetero-MBE and ALD can be economically feasible even in future generations of ULSIs. It remains to be challenged if we can come up with further innovations which make these emerging technologies a must to get around, or at least alleviate, the silicon limits with justifiable increases in cost. It is interesting to note that a thin crystalline layer of a material, despite its own intrinsic atom spacing, can conform to the substrate in atomic ordering. Strained hetero-epitaxy, as it is called, has so far been reported only in limited combinations of materials. However, it is actually opening up a whole new area of materials engineering in thin-film systems, which can encompass all kinds of heterojunctions between semiconductors, metals, and insulators.

### 3.2 Materials Characterization Down to Atomic Dimensions

It has been, and will continue to be, important to characterize the silicon and associated semiconductor materials. The sizes of the defects, or deep-level centers, in crystal silicon causing the marginal leakage current in the DRAM or CCD(Charge-Coupled Device) are approaching those of atoms. SEM(Scanning Electron Microscope), TEM(Transmission Electron Microscope), STM(Scanning Tunneling Microscope) and other new means of instrumentation are going to be indispensable for advancing the ULSI technology. What is badly needed now is a technique with an atomic resolution and a spectroscopic capability of identifying atoms under examination for their elements in realistic, three-dimensional, device structures.

There are indications that single-crystal metal wires outlast polycrystalline metal wires. Crystallization is a key process also in making Ta<sub>2</sub>O<sub>5</sub> more reliable as a capacitor dielectric. A smoother silicon surface results in a better Si-SiO<sub>2</sub> interface. On the other hand, amorphous SiO<sub>2</sub> has performed wonderfully as the gate insulator, and other non-crystalline wiring and insulating materials as well. These results indicate that atomic ordering in a material is an important factor which determines its electrical property and reliability whether it is made of a metal, semiconductor, or an insulator. It will be very important to establish materials science and technology which cover generalized heterostructures and point defects.

### 3.3 Active Atomic Control in Horizontal Dimensions

Surprisingly powerful techniques are emerging in laying bricks for electronic devices, and they may take over the roles played now by lithography and etching, which are essential processes in LSI fabrication in determining basic structures consists of lithography and etching. Placement and removal of individual atoms on a substrate in atomic precision have recently been demonstrated by the use of STM(Scanning Tunneling Microscope)s. These reports are striking, because they have demonstrated the possibility of structuring atomic composition of a matter in any wanted dimensions: the horizontal dimensions as well as the vertical dimension in ULSI structures. It may not be a dream to manipulate and arrange single atoms to make a semiconductor device.

Obviously, the biggest problem in applying atomic manipulation in fabricating a structure as complex as a ULSI is the throughput. Placing atom by atom using an STM, as it looks at present, will be too slow. Technologies such as atomic layer epitaxy and atomic layer doping, which have relatively high processing speed, will be introduced more easily. The lateral dimension is harder. New concepts involving some kind of parallelism and/or self-organization in arranging atoms will have to be introduced. "Atomics," or characterization and manipulation of matters in atomic dimensions, is the ultimate means of microfabrication and has a tremendous future.

### 4. Conclusions

To explore and exploit the potential of the ULSI is a great challenge. It will continue till the ultimate minimum feature size for silicon LSIs around 0.1  $\mu\text{m}$  is reached, where a Gb memory and a BIPS(Billion Instructions Per Second) processor will be realized. It calls for very extensive and intensive work in materials science and technology.

A close look at the limitations in the currently used technologies and the potentials of emerging new technologies gives us a forecast of future directions. Silicon will continue to be "the semiconductor" for ULSI as far as the ion implantation limitations and physical transistor limits are still afar. As these limits are approached, however, the basic transistor structure will have to be reviewed. Technologies such as MBE and ALD, with all the variety of new device physics and structures which heterojunctions offer, will have a great impact. Carrier velocity and junction breakdown will be engineered using semiconductor heterojunctions.

New dielectric and metallic materials will also be introduced. Dielectric density and reliability are the major concern for dielectrics. Conductivity and migration resistance are major issues in metallic materials. "Heterostructures" will not be confined

## 6        *Quantum Effect Physics, Electronics and Applications*

within the semiconductor. Various forms of insulator-to-insulator and insulator-to-conductor heterojunctions will be used.

Characterization of materials will be increasingly important. Metrology and analysis will have to be developed so as to enable materials characterization down to atomic dimensions. Manipulation of matters in atomic dimensions, will then be utilized in the area of fabrication or processing. We will start using techniques such as MBE, MOCVD, and ALD to define device structures in the vertical dimension. STM and particle beams will then be used in defining the horizontal dimensions as well. Some kind of structure self-organization and parallel processing may be introduced to enhance the speed.

Underlying all these technologies will be the progress in understanding atom-level material physics and interface reactions. Artificial materials, which can be realized only through the use of atom-level fabrication may make a great deal of contributions to future ULSIs.

The frontier of future ULSIs will be opened through the doors of new materials research, which has always provided pleasant surprises.

## **Neural networks and learning**

Yaser S. Abu-Mostafa

California Institute of Technology, Pasadena, California, USA 91125

**ABSTRACT:** The resurgence of interest in neural networks and learning over the last decade has had a profound impact on research work in computational devices and systems. Optical computers and analog VLSI owe their renewed vitality to the need to implement large-scale neural networks efficiently. It is the purpose of this paper to provide the basic background on neural networks and learning.

### **1. NEURAL NETWORKS**

Neural network models offer an interesting alternative to performing certain computations. They have been particularly considered for unstructured computations [3] such as pattern recognition and artificial intelligence problems, and approximations to large optimization problems.

There are two popular models of neural networks, the feedback model [9] and the feedforward model [15]. The feedback model is what triggered the current wave of interest in neural networks. The architecture of feedback networks can be described as an undirected graph. The nodes are called neurons, and the edges are called synapses.

What characterizes a neural architecture in general, whether it is feedback or feedforward, is that the number of neurons is huge, and that each neuron performs a very simple task. In most models, neurons perform threshold logic only. Another common characteristic of many neural networks is that the number of synapses per neuron is large. Usually a neuron is connected to a good fraction of all other neurons.

In the feedforward model, the neurons are arranged into layers. There are only directed synapses between each layer and the next. Thus the connection is loop-free. The inputs are applied to the first layer, and the outputs

are collected from the last layer. A feedforward network is a special case of combinational circuits, with the additional feature that the intermediate variables in the network can assume non-binary values.

The neuron in both models performs the same function. The output  $y$  is determined by the inputs  $x_1 \dots x_N$  according to a threshold rule. In the case of binary variables, the neuron simulates a function from  $\{-1,+1\}^N$  to  $\{-1,+1\}$  (we follow the neural network notation taking the binary convention to be +1s or -1s instead of 1s or 0s). The output depends on the input through a set of real numbers called the weights  $w_1 \dots w_N$ , a weight for every input variable. If the sum  $\sum_{i=1}^N w_i x_i$  exceeds an internal threshold  $t$ ,  $y$  is set to +1; if it is less than  $t$ ,  $y$  is set to -1.

The set of functions that can be implemented using a single neuron is well understood. It is the set of threshold functions, or linearly separable functions. If we consider the hypercube  $\{-1,+1\}^N$ , any dichotomy that can be represented by a hyperplane that separates the points can be simulated by a single neuron. Non-binary neurons are also commonplace in neural network models. In this case, the threshold function produces an output that varies continuously between -1 and +1 as the signal  $\sum_{i=1}^N w_i x_i - t$  varies from large negative to large positive.

The operation of the feedforward model is that of a combinational circuit, where the inputs propagate and interact in one direction to produce the output. The computation time is the time required for the signals to propagate and for the output to settle. The operation of the feedback model is closer to that of a sequential computer, where the system is initialized to a state and evolves in time to a final state. This simulates a computation, where the initial state is the input and the final state is the output.

The question of stability is crucial for feedback networks in order to guarantee a meaningful operation. The question does not arise in feedforward networks because they are loop-free. It is important to predict how a feedback network evolves in time when the neurons are initialized to a certain state vector of bits. This evolution is

analyzed with the help of an energy function that can be defined in terms of the states of the neurons and the (fixed) weights and thresholds. Under certain conditions, the energy decreases monotonically as the network moves from one state to the next. In these cases, stability and convergence can be addressed by analyzing the descent of the scalar energy function instead of the transition of the state vector. This parity of state vector transition and energy function descent is the key to understanding how to perform actual computations using feedback networks.

The neurons and the synapses can be considered the hardware of a neural network, while the weights and thresholds can be considered the software. To program a neural network, we choose a set of weights that makes the normal operation of the network simulate the computation we have in mind. If the choice of the weights and thresholds in terms of the desired computation could be automated, it would constitute a learning mechanism. For example, we could start with a set of training samples from the function we want to implement, and the learning mechanism would then choose the proper weights and thresholds that make the network simulate the function. This method would eliminate the need to design a new network each time we have a function to implement.

Most of the interest in neural networks arose from their use to perform useful computations. Roughly speaking, these computations fall into two categories, natural problems and optimization problems. Natural problems such as pattern recognition are typically implemented on a feedforward network. The characterization of which functions can be implemented on feedforward networks is discussed in [13]. Optimization problems are typically implemented on a feedback network. One famous example is the Traveling Salesman Problem (TSP) in which a salesman is supposed to tour a number of cities (visiting each exactly once, then returning to where he started) and desires to minimize the total distance of the tour. The intercity distances are given as the input, and the desired output is a shortest (or near-shortest) tour.

In order to implement a solution to the TSP or any other optimization problem on a feedback network, the energy function is used as a medium

[10]. As we discussed above, the operation of the feedback network implies a descent on the energy surface. By designing the network so that the minimum of the energy function coincides with a minimum-length tour, the network becomes a computer that searches for the minimum tour. For small-size instances of the problem, there are reports of efficient neural-network solutions to the TSP and other optimization problems. The solutions are vulnerable to the major problem of descent methods, namely local minima.

## 2. LEARNING

While learning in general stands by itself as a research discipline, learning in feedforward networks has been given special attention. Problems for which learning has the most potential to offer a solution are the natural variety, such as pattern recognition. For these problems, the representation of the data is crucial to the complexity of the problem. A picture can be represented just as a matrix of pixels, or it can be represented using a higher level set of primitives that are better suited for recognizing the contents of the picture. In a feedforward network, there are several internal representations of the data at each level of pixels. This gradual transformation from raw data to higher levels of representation is very interesting, especially if the representations arise spontaneously via the learning mechanism.

To define learning from examples in a formal way, we start by describing a simple setup. We have an *environment* such as the set of visual images, and we call the set  $X$ . In this environment we have a *concept* defined as a function  $f : X \rightarrow \{0,1\}$ , such as the presence or absence of a tree in the image. The goal of learning is to produce a *hypothesis*, also defined as a function  $g : X \rightarrow \{0,1\}$ , that approximates the concept  $f$ , such as a pattern recognition system that recognizes trees. To do this, we are given a number of examples  $(x_1, f(x_1)), \dots, (x_N, f(x_N))$  from the concept, such as images with trees and images without trees.

In generating the examples, we assume that there is an unknown probability distribution  $P$  on the environment  $X$ . We pick each example independently according to this probability distribution. The statements in the theory hold true for any probability distribution  $P$ ,

which sounds very strong indeed. The catch is that the same  $P$  that generated the example is the one that is used to test the system, which is a plausible assumption. Thus we learn the tree concept by being exposed to 'typical' images.

The hypothesis  $g$  that we produce approximates  $f$  in the sense that  $g$  would rarely be significantly different from  $f$ . This definition allows for two tolerance parameters  $\epsilon$  and  $\delta$ . With probability  $\geq 1 - \delta$ ,  $g$  will differ from  $f$  at most  $\epsilon$  of the time. The  $\delta$  parameter protects against the small, but nonzero, chance that the examples happen to be very atypical.

A learning algorithm is one that takes the examples and produces the hypothesis. The performance is measured by the number of examples needed to produce a good hypothesis as well as the running time of the algorithm. The running time of the learning algorithm is a key concern. As the number of examples increases, the running time generally increases. However, this dependency is a minor one. Even with few examples, an algorithm may need an excessive amount of time to manipulate the examples into a hypothesis. The independence of this complexity issue from the information issue is apparent. Without a sufficient number of examples, no algorithm slow or fast can produce a good hypothesis. Yet a sufficient number of examples is of little use if the computational task of digesting the examples into a hypothesis proves intractable.

#### REFERENCES

- [1] Y. S. Abu-Mostafa and J. St. Jacques, "Information capacity of the Hopfield model," *IEEE Trans. Inform. Theory*, vol. IT-31, pp. 461, 464, 1985.
- [2] Y. S. Abu-Mostafa, "Neural Networks for computing?" in *Neural Networks for Computing*, J. S. Denker (ed.), New York, AIP Conf. Proc., vol. 141, pp. 1-6, 1986.
- [3] Y. S. Abu-Mostafa and D. Psaltis, "Optical Neural Computers," *Scientific American*, vol. 256, no. 3, pp. 88-95, 1987.
- [4] E. B. Baum, "On the capabilities of multilayer perceptrons," *Journal of Complexity*, Academic Press, vol. 4, pp. 193-215, 1988.
- [5] E. B. Baum and D. Haussler, "What size network gives valid generalization," *Neural Computation*, MIT Press, vol. 1, pp. 151-160, 1989.

## 12      *Quantum Effect Physics, Electronics and Applications*

[6] A. Blumer, A. Ehrenfeucht, D. Haussler, and M. Warmuth, "Classifying learnable geometric concepts with the Vapnik-Chervonenkis dimension," *Proc. ACM Symp. on Theory of Computing*, vol. 18, pp. 273-282, 1986.

[7] J. Bruck and J. Goodman, "On the power of neural networks for solving hard problems," in *Neural Information Processing Systems*, D. Z. Anderson (ed.), New York: AIP, pp. 137-143, 1988.

[8] T. M. Cover, "Geometrical and statistical properties of systems of linear inequalities with applications in pattern recognition," *IEEE Trans. Electronic Components*, pp. 326-334, June 1965.

[9] J. J. Hopfield, "Neural networks and physical systems with emergent collective computational abilities," *Proc. Natl. Acad. Sci. USA*, vol. 79, pp. 2554-2558, 1982.

[10] J. J. Hopfield, "Collective computation, content-addressable memory, and optimization problems," in *Complexity in Information Theory*, Y. S. Abu-Mostafa (ed.), Springer-Verlag, pp. 99-114, 1988.

[11] J. S. Judd, "On the complexity of loading shallow neural networks," *Journal of Complexity*, Academic Press, vol. 4, pp. 177-192, 1988.

[12] J. Komlos and R. Paturi, "Convergence results in an associative memory model," *Neural Networks*, vol. 1, no. 3, pp. 239-250, 1988.

[13] R. P. Lippman, "An introduction to computing with neural nets," *IEEE ASSP Magazine*, 1987.

[14] R. J. McEliece, E. C. Posner, E. R. Rodemich, and S. S. Venkatesh, "The capacity of the Hopfield associative memory," *IEEE Trans. Inform. Theory*, vol. 33, pp. 461-482, 1987.

[15] D. E. Rumelhart, G. E. Hinton, and R. J. Williams, "Learning internal representations by error propagation," in *Parallel Distributed Processing*, vol. 1, Cambridge, MA: MIT Press, 1986.

[16] L. G. Valiant, "A theory of the learnable," *Communications of the ACM*, vol. 27, pp. 1134-1142, 1984.

[17] V. N. Vapnik and A. Chervonenkis, "On the uniform convergence of relative frequencies of events to their probabilities," *Theory of Probability and Its Applications*, vol. 16, pp. 264-280, 1971.

## **Thoughts on the impact of biology on the design of electronic devices and systems**

C.D.W.Wilkinson

Department of Electronics and Electrical Engineering,  
The University, Glasgow, Scotland

### **Introduction**

Historically, it has customary to describe the working of the brain by analogy with the most advanced information handling system devised by man. Thus the brain was compared to the working of an automatic telephone switchboard, and to the workings of the early strictly serial computers.

On the other hand, the brain itself carries electrical signals using a vast number of neurons, which can be connected in ways totally unlike that of a computer. The detailed coding of the signals is only understood partially in the outer input devices - eye and ear - and not in the central nervous system. The complete wiring diagram of a simple worm is known from the work of White, Southgate, Thomson and Brenner (1986) - this monumental task involved the correlation of many thousands of electron micrographs; but even in this very simple case it is true to say that the total logic of the system is not wholly understood. Understanding of Higher cognitive functions has not been achieved - in particular Memory is a mystery.

But regarded as a system the brain is immensely attractive, as a model to emulate. It is multitasking, has extremely powerful pattern recognition capabilities, works well with noisy signals and performs fuzzy logic, has some capacity for self repair, and is very compact and consumes little power.

One application of biological ideas has already had a significant impact in computing science - the concept of the neural network ( see for example Hertz, Krogh and Palmer(1990)). This paper is concerned with two topics which may shed light on this interface between electronics and neural science; attempts to make interconnected patterns of living nerve cells and study their electrical behaviour over time, and recent studies of the role of pheromone in insect colonies in allowing collective decision making without local interaction.

### **Interconnected Networks of Neurons**

In order to organise a network of nerve cells, it is necessary to have a source of suitable cells which are viable and form synapses in culture, to make a suitable guiding structure and have a means of

listening to the electrical signals between the neurons over long time, and to try to analyse the resulting mass of data.

The choice of cell type involves a host of cell biological questions. Cells can be grown from a cell line ( an essentially immortal strain which can be grown in large quantities as required of baker's yeast ) and can be cultured from animal tissue. Unfortunately a useful nerve cell line does not seem to exist, so primary cells are used. The invertebrates are, in general, blessed with larger neurons than the vertebrates. Much work has been done with invertebrate nerve cells and so the role in life and behaviour pattern of certain nerve cells in the body of invertebrate can be firmly identified. Such identified cells form a sensible starting point for investigation. However the goal must be to progress towards the study of nerve cells from the central nervous system in vertebrates.

There are a number of guidance cues which influence cells which can be used to make a pattern of nerve cells. The adhesion and guidance of cells is affected by chemical clues - the presence of proteins in particular - and by topographic cues. Patterns of adhesive molecules which caused the formation of cellular networks have been demonstrated by Kleinfeld et al and by Britland et al, both using photolithographic processes. The topographic approach has been investigated by Clark et al(1987,1990,1991). The reaction of cells to steps etched into poly(methylmethacrylate) using photolithographic masking and dry etching in oxygen, was investigated as a function of step height and cell type ( Clark et al,1987). It was found that the degree of inhibition of a cell in crossing a step, either up or down, was probabilistic, but that the degree of inhibition increases with step height. A 10 $\mu$ m high step is sufficient to deter all by 10% of baby hamster kidney Cells. Cells that do not cross the step may align to it.

The response of cells to a step depends on their type. It was found that the probability of crossing for baby hamster kidney cells, chick heart fibroblasts and chick cerebral hemisphere cells ( neural cells ) was both the same, but leucocytes or white blood cells - as befits their role in the body - were much less inhibited by this step.

The effect of a grooved substrate (Clark et al(1990)) is to cause alignment of the cells to the grooves and in some cases the shape of the cells changes, becoming elongated in the direction of the grooves. The degree of reaction can be measured by measuring the angle between the cells and the grooves a few hours after deposition of the cells. Again the reaction is probabilistic; for example the probability of a baby hamster kidney cell being within 10° of the direction of the grooves for 2 $\mu$ m wide grooves with 2 $\mu$ m spaces etched 2 $\mu$ m deep into poly(methylmethacrylate) is over 80%. The degree of alignment increases sharply with etch depth, grating pitch is a less important parameter. These grooves were of a width commensurate with the cell width - and the interesting question of the reaction of cells to very fine grooves so that there are many grooves under each cell, was examined by Clark et

al(1991). It was found that the reaction of baby hamster kidney cells was marked even to grooves only  $0.2\mu\text{m}$  deep. However isolated chick embryo nerve cells were not aligned by these very fine grooves.

A cell's reaction to topographic features is dependent on the extent to which the feature alters the probability of a cell making a successful protrusion and contact in a given direction. This ability to make protrusions is a function of the cyto-skeleton - the framework of microfiliaments, microtubules and intermediate filaments which are present inside the membrane.

Granted that a guiding structure can be made, the next step is to provide probing of the neuronal signals. The conventional approach of neurophysiology is to use micro-electrodes, fine capillary tubes filled with saline. These provide an excellent signal to noise ratio but have disadvantages for the long term observation of neural networks. It is difficult to handle more than say three at the same time, and as the process is inevitably traumatic to the neuron, observation over extended times is not feasible.

Surface micro-electrodes overcome these problems, albeit at the expense of signal to noise ratio. Edell(1986) has used arrays of microelectrodes to observe signals in cat, and Thomas et al (1982) used them in culture. In our experiments, Connolly et al (1989) the electrode is a  $60\text{nm}$  thick layer of gold, insulated by a  $1\mu\text{m}$  thick layer of plasma deposited silicon nitride. The silicon nitride is opened by reactive ion etching in a  $\text{C}_2\text{F}_6$  discharge to reveal a  $8\mu\text{m}$  by  $8\mu\text{m}$  area of electrode. An array of 32 electrodes is opened at the same time, each electrode contact is bonded to a wire and then to a external 32-way edge connector. A ring is cemented over the patterned area, so that saline and growth medium can be supplied to the cells over the electrodes. The electrodes are normally platinised to reducing their resistance. Such electrodes gave signals of amplitude between  $100$  and  $400\mu\text{V}$  with a noise level of  $10\mu\text{V}$  for beating cardiac cells from chick embryos. This signal to noise ratio can be increased by using a deep groove, as was shown by Lind et al(1991) using finite element analysis to model an microelectrode.

Thus exercise grounds for nerve cells, complete with guiding structures and extra-cellular electrodes for long term recording can be made. The central nervous system of the pond snail *Lymnaea stagnalis* has been studied extensively using classical neurophysiological techniques, and so neurons can be identified and their involvement in rhythmic behaviour patterns such as feeding and locomotion are known. Identified dopaminergic neurons of this animal were cultured and formed active electronic connections, reproducing *in vitro* the behaviour seen *in vivo*. This was observed using extra-cellular electrodes and the behaviour persisted for a week.

The leech gives an useful experimental vehicle as neurons can be removed from it with long processes still attached. Such neurons have

been stimulated by injection of a current pulse using an extra-cellular electrode, and the resulting action potential detected at two further extra-cellular electrodes.

So both detection and stimulation can be done using extra-cellular electrodes. Building up to networks containing three to five nerve cells seems entirely possible, and it is at this level of complexity that one can hope to observe phenomena that can ultimately be applied to electronic design.

### Behaviour of Social Insects

Looking at the electrical signals in a network of nerve cells is a direct approach to learning about the control of information by nature; an alternative and fascinating method is to study how colonies of insects make collective decisions.

There are many insects which are *social*, that is live together in large colonies which show remarkable organisation in their foraging and nest-building activities. The understanding of this behaviour presents a challenge. Recently there have been a series of papers by a group of workers in Belgium (Deneuborg, Goss, Pasteels and others) and the UK (Franks and others) who had described both theoretically and experimentally the behaviour of army ants, and emphasised the role that the positive feedback provided by pheromone deposition and detection can provide in establishing complex foraging patterns.

Army ants live in very large colonies and forage for food in very large numbers. Franks (1982) describes a swarm raiding party of *Eciton burchelli* containing 200,000 ants raiding in a dense phalanx 15m wide and covering an area of 1000m<sup>2</sup> in a day. The raid system consists of a dense carpet of ants 1m wide at the leading edge of the swarm, and a system of trails. These trails, along which the ants run to the swarm front and return carrying prey, contain loops, small and frequent near the swarm front, larger and less common further back, which coalesce into a single trail leading back to the nest. This complex structure changes with time but its basic features are always preserved. The ants in this huge raid party are virtually blind; the complex structure of the raid appears to be generated by the blind leading the blind (Franks 1991).

The ants follow a trail of pheromone laid down by previous ants on their way to and from the front, and in their turn lay down more pheromone. Deneuborg (1990) showed that the characteristic patterns of army ant raids could be self-organising, that is generated by the interactions between many identical foragers, each obeying a simple set of rules for trail-laying and trail following. The assumptions of the model were

- 1) The ants lay pheromone trails both on the way out to the raid front and on the return journey.

2) Where the trail divides, an individual ant's choice of left or right depends on the relative strength of pheromone  $P$  on each branch as

$$\text{Probability of choosing left } q_{\text{left}} = 1 - q_{\text{right}} = \frac{(5 + P_1^2)}{(5 + P_1^2) + (5 + P_r^2)}$$

where  $P_r$  and  $P_1$  are the amounts of pheromone to the right and left.

3) The velocity of the ants increases sigmoidally as a function of the strength of the pheromone just ahead of the ant.

$$\text{Probability of moving per step} = \frac{1}{2} + \frac{1}{2} \cdot \tanh\left(\frac{P_1 + P_r}{P_{1/2}} - 1\right)$$

where  $P_{1/2}$  is a constant level of pheromone.

4) The number of ants leaving the colony is relatively constant.

Monte-Carlo simulations based on these assumptions produced patterns which show all the features of the ant trails in the tropics. Interestingly, changing the density of the prey in the model changed the pattern. if each point has a probability of 1/2 of containing one item of food, the trail pattern that emerged was similar to that of *E. burchelli* having one swarm front and a decreasing density of trail loops away from the swarm front, leading to one main trail to the nest. Now *E. burchelli* eats solitary arthropods which are rather common but small packets of prey (Franks et al 1991). On the other hand with a simulation with sparsely distributed packets of dense prey, a foraging pattern emerged, consisting of many swarm fronts again with interconnecting paths leading back to the nest. This is characteristic of the trails of *E. radix*, an ant which is a specialist predator of other social ants.

Thus the model has explained the complex patterns that emerge. The optimisation of the pattern, with one branch where it is advantageous and the necessary spreading to form an attacking phalanx seems to be inherent in the self-organisation mediated by the mechanism of pheromone trail laying. The model suggests that the different trail patterns of ants of different species (*E. radix* and *E. burchelli*) may be due to the different densities of prey on which they normally feed, and not to any genetic origin. In experiments by Franks et al(1991) on placing food packets in front of the swarm front of *E.burchelli* it proved possible to break up the swarm into separate swarm fronts. In Frank et al (1991) it was also shown experimentally that the velocity of the ants does depend on the amount of pheromone ahead of the ant. It may have struck the reader that given these pheromone laying and following attributes, ants once going in a circle, will go on and on until exhausted.

So a track of saturated pheromone can be established by putting many ants into a circular mill formed by concentric rings of cardboard,

removing the first ants, introducing a few fresh ones, and measuring the decrease in velocity as the phenomone decays with time.

Deneubourg and Gross (1989) give a general account of these autocatalytic interactions in social animals. They conclude that 'It is our belief that any species adopting allelomimetic (following your neighbour) behaviour will unwittingly and automatically dote itself with a capacity for collective decision making and pattern formation and general structuring that far exceeds that of its isolated individuals'.

### Acknowledgements

The help and assistance of my colleagues in Glasgow, Dr.Lorna Breckenbridge, Dr.Peter Clark, Dr. Patricia Connolly, Prof.Adam Curtis ,Dr.A.T.Julian Dow, Mr.Richard Wilson and Dr.Robert Lind must be gratefully acknowledged. The expert technical assistance of Mr. Bill Monaghan, Mrs. Lois Hobbs and Mr. Robert Harkness in the photolithographic definition and manufacture of structures and of Ms. Mary Robertson and Mr.Mike McGrath in the culture and growth of cells, was extremely important in the progress of this work. Financial assistance from the British Petroleum Venture Research Unit, the Welcome Trust and SERC is gratefully acknowledged.

### References

Britland S,Perez-Arnaud E,Clark P,McGinn B and Connolly P 1991 submitted to Biotechnology Progress

Clark P,Connolly P,Curtis, A S G,Dow J A T and Wilkinson C D W1987 Research Development Biology 99 439-448

Clark P,Connolly P,Curtis, A S G,Dow J A T and Wilkinson C D W1990 Development 108,

Clark P,Connolly P,Curtis, A S G,Dow J A T and Wilkinson C D W1991 J. of Cell Science 99 73-77

Deneubourg N L, Aron S,Goss S and Pasteels J M (1990) J. Insect Behaviour 3,159-68

Franks N R 1982 in Leigh E G,Rand A S and Windsor D W The Ecology of a Tropical Forest (Washington DC:Smithsonian Institute Press) pp 389-95

Franks N R,Gomez N,Goss A and Deneubourg J L 1991 J. of Insect Behaviour 4 583-607

Hertz J,Krogh A and Palmer R G 1990 Introduction to the Theory of Neural Computation (Redwood City: Addison Wesley)

Lind R,Connolly P,Wilkinson C D W and Thomson R (1991) Sensors and Actuators 3 23-30

Kleinfeld D,Kahler K H and Hockberger P E 1988 J. Neuroscience 8 4098-4120

White J G,Southgate E,Thomson E N and Brenner S 1986 Phil. Trans B 314 1-340

## Kinetic conductance and the characteristic carrier traversal times of small conductors

M. Büttiker

IBM T. J. Watson Research Center, Yorktown Heights, NY 10598, USA

H. Thomas

University of Basel, Klingelbergstr. 82, CH-4056 Basel, Switzerland

**ABSTRACT:** The current response to oscillating external electric fields induced along the probes of a phase coherent conductor is calculated. For non-interacting carriers we find an expression of the equilibrium ac-conductance in terms of the scattering matrix of the conductor. Our derivation invokes the Kramers-Kronig relations for the scattering matrices. The low-frequency departure of the conductance away from the dc-conductance is Drude like but with the role of the scattering time played by weighted averages of the time taken by carriers for traversal, reflection or dwelling in the conductor.

### 1. INTRODUCTION

Transport equations which relate the total current at a contact via transmission probabilities to the chemical potentials at the contacts have been a very successful tool for the analysis of many conductance phenomena especially in small conductors<sup>1</sup>. Recently this approach was extended to include fluctuations of the currents away from their steady state average. Expressions were derived<sup>2-5</sup> which relate the low frequency spectral density of the mean square current fluctuation at a given contact and the correlations of currents at differing contacts to the scattering matrix of the conductor. The frequency dependence of the fluctuation spectra was addressed in Ref. 6. Below we discuss to what extent a dynamic, frequency-dependent conductance can be related to the scattering matrix of the conductor. We analyze a configuration in which carriers are subject to oscillating external fields in the contacts leading to the conductor. We consider a perturbation,

$$H' = \sum_a I_a \Phi_a \quad (1)$$

where  $I_a$  is the total carrier current in lead  $a$  and  $\Phi_a$  is a flux which does not penetrate the sample (see Fig. 1). Clearly, as long as the flux  $\Phi_a$  is time independent it has no effect on the carrier kinetics. However, if the flux is time-dependent it induces a voltage  $V_a = d\Phi_a/dt$ . In particular, an oscillatory flux  $\Phi_a(t) = \delta\Phi_a(\omega) \exp(-i\omega t)$  induces a voltage  $\delta V_a(\omega) = -i\omega \delta\Phi_a(\omega)$ . We are interested in the conductance (admittance)  $g_{\alpha\beta}(\omega) = \delta I_\alpha(\omega)/\delta V_\beta(\omega)$  which relates the current response in probe  $\alpha$  to the voltage induced in contact  $\beta$ .

Eq. (1) is a perturbation on a Hamiltonian which describes electron propagation in a confining potential and possibly an impurity potential. Probes leading away from the conductor widen into

asymptotically perfect regions in which carrier motion in a longitudinal direction and in the transverse directions are separable. Reservoir  $\alpha$  supports  $M_\alpha$  quantum channels. The reflection of waves incident from reservoir  $\alpha$  is determined by a scattering matrix  $s_{\alpha\alpha}$  of dimension  $M_\alpha^2$  and transmission into probe  $\beta \neq \alpha$  is determined by a scattering matrix  $s_{\beta\alpha}$  of dimensions  $M_\beta \times M_\alpha$ . In the steady state the current in probe  $\alpha$  is related to the chemical potentials

$$I_\alpha = \sum_\beta g_{\alpha\beta} V_\beta \quad (2)$$

via conductances<sup>1</sup>

$$g_{\alpha\beta} = \frac{e^2}{h} \int dE (-df/dE) \text{Tr}[1_\alpha \delta_{\alpha\beta} - s^\dagger_{\beta\alpha}(E) s_{\beta\alpha}(E)]. \quad (3)$$

Two features of Eqs. (2) and (3) have attracted considerable attention from a community interested in formal linear response theory. First, Eq. (2) gives a relation between the total currents at the contacts and the chemical potentials of the reservoirs. It is not immediately evident from a linear response point of view that the net current is independent of the perturbing electric field inside the conductor. Second, the conductances given by Eq. (3) exhibit the microreversibility symmetry  $g_{\alpha\beta}(B) = g_{\beta\alpha}(-B)$ . In some discussions the conductances are calculated by evaluating the dissipated power<sup>7,8</sup>. Such discussions necessarily lead to a symmetrized conductance  $(1/2)(g_{\alpha\beta}(B) + g_{\beta\alpha}(B))$  and not to Eq. (3). A formulation of linear response was needed which went beyond the standard discussions<sup>9,10</sup>. Here we are interested in the frequency dependent deviations from Eqs. (2) if the applied voltages are time dependent. The discussion given below does not attempt to provide a full answer: The perturbation, Eq. (1), represents only the "surface" portion of the energy  $H' = \int dx^3 j(r,t) A(r,t)$ , which generally provides the starting point for a more complete linear response analysis. It is only in the  $\omega = 0$  limit that it is sufficient to consider the perturbation given by Eq. (1). Clearly, for  $\omega \neq 0$  the response depends on the particular spatial dependence of the perturbing electric field. In a loop connected to a lead which is in turn connected to an electron reservoir, an oscillating flux inducing a radial field in the loop also causes an oscillating current in the lead<sup>11</sup>. In contrast to the very often invoked spatially uniform electric field perturbation which is presumably active only in the bulk of the sample<sup>12</sup>, Eq. (1), emphasizes electric fields which accelerate carriers in the contacts. Further, we treat non-interacting carriers: The inclusion of interactions in many cases is crucial to obtain a sensible answer. Fluctuation spectra without coupling and with coupling to the Maxwell fields for current instabilities in bulk semiconductors are compared in Ref. 13. Current instabilities share with conductors for which the Coulomb blockade is relevant<sup>14</sup> a sensitivity to the impedance of the external circuit<sup>13,15</sup>. The frequency response and the generation of higher harmonics in small conductors has been investigated by Webb et al.<sup>16</sup> and de Vegvar et al.<sup>16</sup> and is reviewed in Ref. 17 by Washburn and others.

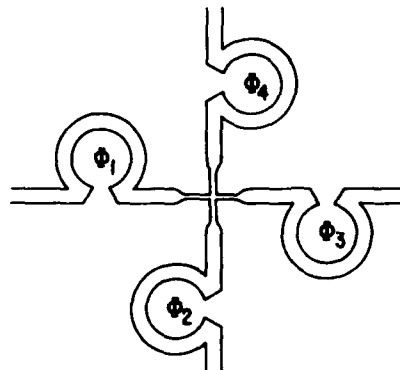


Fig. 1. Schematic view of sample and fluxes used to induce electric fields.

## 2. AC-CONDUCTANCE

The average current in probe  $\alpha$  in response to an oscillating flux near probe  $\beta$  is determined by a generalized susceptibility<sup>18</sup>,  $\langle \delta I_\alpha(\omega) \rangle = \sum_\beta K_{\alpha\beta}(\omega) \delta \Phi_\beta(\omega)$  given by

$$K_{\alpha\beta}(\tau) = \frac{i}{\hbar} \langle [I_\alpha(\tau), I_\beta(0)] \rangle \Theta(\tau). \quad (4)$$

Here  $[ ]$  denotes the commutator.  $\Theta$  is the step function. The brackets  $\langle \rangle$  describe a quantum and statistical average over an equilibrium ensemble. The conductance is

$$g_{\alpha\beta}(\omega) = \frac{1}{\hbar\omega} \int_0^\infty d\tau \exp(i(\omega + i0^+)\tau) \langle [I_\alpha(\tau), I_\beta(0)] \rangle. \quad (5)$$

Our method of evaluating this average closely follows recent work<sup>2,6</sup> on current fluctuation spectra: The correlation of the current fluctuations at contact  $\alpha$  and contact  $\beta$  is determined by  $\langle [I_\alpha(\tau), I_\beta(0)]_+ \rangle$  where  $[ ]_+$  denotes the anti-commutator. In this work the current matrix elements  $I_{\beta\gamma mn}(\alpha)$  calculated in probe  $\alpha$  for a scattering wave incident in probe  $\beta$  in the transverse state  $m$  and a scattering wave incident in probe  $\gamma$  in the transverse state  $n$  are expressed in terms of scattering matrices of the conductor. It was found that the current matrix elements  $A_{\beta\gamma mn}(\alpha) \equiv (v_{\beta m})^{-1/2} (v_{\gamma n})^{-1/2} I_{\beta\gamma mn}(\alpha)$  normalized by the channel velocities  $v_m$  and  $v_n$  are given by<sup>2,6</sup>

$$A_{\beta\gamma}(\alpha, E, E + \hbar\omega) = \delta_{\alpha\beta} \delta_{\alpha\gamma} I_\alpha - s^\dagger_{\alpha\beta}(E) s_{\alpha\gamma}(E + \hbar\omega). \quad (6)$$

Eq. (6) is exact only in the zero-frequency limit. For  $\omega \neq 0$ , short wave length oscillations of the order of the Fermi wavelength and extremely long wavelength oscillations of the order of the Fermi velocity divided by the modulation frequency are neglected. Using Eq. (6) and proceeding as in Refs. 2,6 or 10, we find for the conductance

$$g_{\alpha\beta}(\omega) = \frac{e^2}{(2\pi)^2 \hbar} \int dE \int dE' \text{Tr} [1_\alpha \delta_{\alpha\beta} - s^\dagger_{\beta\alpha}(E') s_{\beta\alpha}(E) - s^\dagger_{\alpha\beta}(E') s_{\alpha\beta}(E)] \quad (7)$$

$$\frac{f(E) - f(E')}{\hbar\omega} \frac{1}{i(\hbar\omega + E - E' + i0^+)}.$$

Eq. (7) is still a formal expression. A key difficulty which arises in all these calculations is the energy integration in Eq. (7). Baranger and Stone<sup>9</sup>, in a veritable tour de force, perform this integration on the level of Green's functions. Shepard<sup>10</sup> provided a clue by appealing directly to the analytical properties of the current matrix elements. We have found an especially simple and direct way to perform this integration by making use of the causality requirement of the scattering matrix expressed by the Kramers-Kronig-relations,

$$\int_{-\infty}^{+\infty} \frac{s(E')}{E_1 - E' \pm i0^+} dE' = \begin{cases} -2\pi i s(E_1) \\ 0 \end{cases}. \quad (8)$$

$$\int_{-\infty}^{+\infty} \frac{s^\dagger(E')}{E_1 - E' \pm i0^+} dE' = \begin{cases} 0 \\ 2\pi i s^\dagger(E_1) \end{cases}. \quad (9)$$

These relations may be derived from the more common ones for the retarded Green's function by observing that the latter is related by the Lipman-Schwinger equation to the T matrix which is in turn simply related to the S matrix<sup>19</sup>. Using Eqs. (8) and (9) we find, with a little algebra,

$$g_{\alpha\beta}(\omega) = \frac{e^2}{h} \int dE \text{Tr}[I_\alpha \delta_{\alpha\beta} - s_{\alpha\beta}^\dagger(E) s_{\alpha\beta}(E + \hbar\omega)] \frac{f(E) - f(E + \hbar\omega)}{\hbar\omega}. \quad (10)$$

Eqs. (10) are the key results of this paper. In the zero frequency limit Eqs. (10) agree with Eqs. (2). Eqs. (10) exhibit the micro-reversibility symmetry  $g_{\alpha\beta}(\omega, -B) = g_{\beta\alpha}(\omega, B)$  and obey the reality condition  $g_{\alpha\beta}(\omega) = g_{\beta\alpha}^*(-\omega)$ . The real (dissipative) part of the frequency dependent conductance is

$$g'_{\alpha\beta}(\omega) = \frac{1}{2} [g_{\alpha\beta}(\omega) + g_{\beta\alpha}^*(-\omega)] = \quad (11)$$

$$\frac{1}{h} \int dE \text{Tr}[I_\alpha \delta_{\alpha\beta} - \frac{1}{2} [s_{\alpha\beta}^\dagger(E) s_{\alpha\beta}(E + \hbar\omega) + s_{\beta\alpha}^\dagger(E) s_{\beta\alpha}(E + \hbar\omega)]] \frac{f(E) - f(E + \hbar\omega)}{\hbar\omega}.$$

The real part of the conductance is via the fluctuation dissipation theorem related to the equilibrium current fluctuations

$$\int_{-\infty}^{\infty} d\tau \exp(i\omega\tau) \frac{1}{2} < [I_\alpha(\tau), I_\beta(0)]_+ > = 2\epsilon(\omega, kT) g'_{\alpha\beta}(\omega). \quad (12)$$

In Eq. (12) the energy of a harmonic quantum oscillator is denoted by  $\epsilon(\omega, kT)$ . The non-dissipative part (out of phase) response of the conductance is given by

$$g''_{\alpha\beta}(\omega) = \frac{1}{2} [g_{\alpha\beta}(\omega) - g_{\beta\alpha}^*(-\omega)] = \quad (13)$$

$$i \frac{e^2}{h} \int dE \text{Tr}[\frac{1}{2} [s_{\alpha\beta}^\dagger(E) s_{\alpha\beta}(E + \hbar\omega) - s_{\beta\alpha}^\dagger(E) s_{\beta\alpha}(E + \hbar\omega)]] \frac{f(E) - f(E + \hbar\omega)}{\hbar\omega}.$$

Eq. (11) can also be obtained from the frequency dependent-current fluctuation spectrum calculated in Ref. 6, by using Eq. (12) as a definition of the real part of the ac-conductance. Kramers-Kronig-relations connect the real and imaginary part of the conductance.

### 3. LOW FREQUENCY CONDUCTANCE

Below we briefly investigate the low-frequency behavior of the conductance and link it to the characteristic times for carrier traversal, reflection and dwell times<sup>20-24</sup>. In the limit of very small frequencies Eq. (10) gives the following corrections to the steady state conductances:

$$g_{\alpha\beta}(\omega) = g_{\alpha\beta}(0) - \frac{e^2}{2\pi} \omega \int dE \text{Tr}[s_{\alpha\beta}^\dagger(E) \frac{\partial s_{\alpha\beta}(E)}{\partial E}] \left( -\frac{df}{dE} \right). \quad (14)$$

The right-most term in Eq. (14) has the dimension of conductance times a frequency times a time scale. Typically, the duration of a scattering event is linked only to the imaginary part of the logarithmic derivative of the scattering amplitude, i. e.  $\text{Im}[d(\log s_{\alpha\beta mn})/dE]$ . In Ref. 20 it was pointed out that the real part of this derivative also has physical meaning. We introduce,  $\tau'_{\alpha\beta mn} = \hbar \text{Re}[d(\log s_{\alpha\beta mn})/dE]$  and introduce  $\tau''_{\alpha\beta mn} = \hbar \text{Im}[d(\log s_{\alpha\beta mn})/dE]$ . The time scales which count are averages<sup>24</sup> over all quantum channels in a given probe. The probability that a carrier is in channel  $m$  in probe  $\alpha$  is  $|s_{\alpha\beta mn}|^2$ . Thus the carriers which are characterized by  $\tau'_{\alpha\beta mn}$  give a contribution  $|s_{\alpha\beta mn}|^2 \tau'_{\alpha\beta mn}$  to the channel averaged "time" scale  $\tau'_{\alpha\beta}$ . Summing over all channels gives<sup>24</sup>

$$\tau'_{\alpha\beta} = \frac{\hbar}{2} \text{Tr}[s_{\alpha\beta}^\dagger(E) \frac{\partial s_{\alpha\beta}(E)}{\partial E} + \frac{\partial s_{\alpha\beta}^\dagger(E)}{\partial E} s_{\alpha\beta}(E)] / \text{Tr}[s_{\alpha\beta}^\dagger(E) s_{\alpha\beta}(E)]. \quad (15)$$

and similarly,

$$\tau''_{\alpha\beta} = \frac{\hbar}{2i} \text{Tr}[s^\dagger_{\alpha\beta} \frac{\partial s_{\alpha\beta}(E)}{\partial E} - \frac{\partial s^\dagger_{\alpha\beta}(E)}{\partial E} s_{\alpha\beta}] / \text{Tr}[s^\dagger_{\alpha\beta} s_{\alpha\beta}(E)]. \quad (16)$$

If the voltages applied to all the terminals are in synchronism and of equal magnitude,  $\delta V_\alpha = \delta V$  independent of  $\alpha$ , the resulting conductance is purely real. Thus the weighted average of  $\tau'$  vanishes  $\Sigma_\beta \text{Tr}[s^\dagger_{\alpha\beta} s_{\alpha\beta}] \tau'_{\alpha\beta} = 0$ . Due to the oscillating voltages, additional charge is brought into the conductor or flows out of the conductor and the imaginary part of the conductance is determined by the dwell time

$$\tau_{d,\alpha} = \frac{1}{M_\alpha} \sum_\beta \text{Tr}[s^\dagger_{\alpha\beta} s_{\alpha\beta}] \tau''_{\alpha\beta} = \frac{1}{M_\alpha} \frac{\hbar}{2i} \sum_\beta \text{Tr}[s^\dagger_{\alpha\beta} \frac{\partial s_{\alpha\beta}(E)}{\partial E} - \frac{\partial s^\dagger_{\alpha\beta}(E)}{\partial E} s_{\alpha\beta}]. \quad (17)$$

Eqs. (15-17) are valid in the zero temperature limit. In the presence of an elevated temperature we average both the nominator and denominator over the Fermi function. Now the conductance is simply

$$g_{\alpha\beta}(\omega) = g_{\alpha\beta}(0) - (g_{\alpha\beta}(0) - g_{c,\alpha} \delta_{\alpha\beta}) \omega (\tau'_{\alpha\beta} + i\tau''_{\alpha\beta}), \quad (18)$$

where  $g_{c,\alpha} = (e^2/h)M_\alpha$ .  $\tau'$  and  $\tau''$  can be separately determined if the phase of the current response relative to the oscillating voltage can be measured. Alternatively, we can use  $|g_{\alpha\beta}(\omega) - g_{\alpha\beta}(0)| / g_{\alpha\beta}(0) = 1$  as a criterion for a critical frequency  $\omega_c$  marking a significant departure from the steady state behavior<sup>20</sup>. This critical frequency leads to traversal and reflection times given by

$$\tau_{\alpha\beta} = 1/\omega_c = \sqrt{(\tau'_{\alpha\beta})^2 + (\tau''_{\alpha\beta})^2}. \quad (19)$$

A combination of two time scales of this form was advocated in Ref. 21 to give a measure of characteristic tunneling times. In contrast to  $\tau_{\alpha\beta}$  determined by Eq. (19),  $\tau'_{\alpha\beta}$  and  $\tau''_{\alpha\beta}$  are not necessarily positive. If all voltages oscillate in synchronism and are of equal magnitude, the current in probe  $\alpha$  is determined by

$$\sum_\beta g_{\alpha\beta}(\omega) = -i\omega \tau_{d,\alpha} g_{c,\alpha} = -i\omega \tau_{d,\alpha} (e^2/h) M_\alpha, \quad (20)$$

and hence the dwell time is a measure of the current in probe  $\alpha$ .

#### 4. DISCUSSION

To understand these results better let us compare Eq. (18) with the results obtained from a Drude discussion. Consider current flow perpendicular through a disk of crosssection A and thickness d. The particle current is  $\mathbf{j} = \sigma(\omega)\mathbf{E}$  and the displacement current is  $\mathbf{j}_D = -i\omega\epsilon\mathbf{E}$ . With the help of the Drude formula  $\sigma(\omega) = \sigma_0/(1 - i\omega\tau) \approx \sigma_0(1 + i\omega\tau)$  we obtain to linear order in  $\omega$  an admittance  $\mathbf{Y} = \mathbf{G}(1 + i\omega\tau) - i\omega\mathbf{C}$  with  $\mathbf{G} = \sigma_0 A/d$  and  $\mathbf{C} = \epsilon A/d$ . In contrast to the momentum relaxation time  $\tau$  in the Drude expression, Eq. (18) contains two "time" scales. A complex time scale appears because the ac-conductance is sensitive to the energy variation of both the amplitude and the phase of the scattering matrix elements. The capacitive term in the admittance is negligible compared to the relaxation term as long as the relaxation time  $\tau$  (or  $\tau''_{\alpha\beta}$ ) exceeds the RC time (or  $\tau''_{\alpha\beta} > C_{\alpha\beta}/g_{\alpha\beta}$ ). Since both  $\tau''$  and the capacitance are for metallic conductors proportional to the density of states, this inequality is generally obeyed unless<sup>15</sup>  $g_{\alpha\beta} < (e^2/h)$ .

## REFERENCES

1. M. Büttiker, *Phys. Rev. Lett.* **57**, 1761 (1986); *IBM J. Res. Develop.* **32**, 317 (1988); For a historical review see R. Landauer, in *Analogies in Optics and Micro Electronics* edited by W. van Haeringen and D. Lenstra, (Kluwer Academic Publishers, Dordrecht, 1990). p. 243.
2. M. Büttiker, *Phys. Rev. Lett.* **65**, 2901 (1990).
3. M. Büttiker, *Physica* **B175**, 199 (1991).
4. C. W. J. Beenakker and H. van Houten, *Phys. Rev. B* **43**, 12066 (1991).
5. T. Martin and R. Landauer, *Phys. Rev. B*, (in press).
6. M. Büttiker, *Phys. Rev. B*, Feb. (1992).
7. D. S. Fisher and P. A. Lee, *Phys. Rev. B* **23**, 6851 (1981).
8. A. D. Stone and A. Szafer, *IBM J. Res. Develop.* **32**, 385 (1988); O. Viehweger, *Z. Phys.* **B77**, 135 (1989).
9. H. U. Baranger and A. D. Stone, *Phys. Rev. B* **40**, 8169 (1989).
10. K. Shepard, *Phys. Rev. B* **43**, 11623 (1991).
11. M. Büttiker, *Phys. Rev. B* **32**, 1846 (1985).
12. A critique of high frequency linear response using spatially uniform fields is given by R. Landauer, in *Nanostructure Physics and Fabrication*, edited by M. A. Reed and W. P. Kirk, (Academic Press, Boston, 1989). p. 3.
13. M. Büttiker and H. Thomas, *Z. Phys.* **B33**, 275 (1979); *Z. Phys.* **B34**, 301 (1979).
14. T. A. Fulton and G. J. Dolan, *Phys. Rev. Lett.* **59**, 109 (1987); T. A. Fulton, P. L. Gammel, and L. N. Dunkelberger, *Phys. Rev. Lett.* **67**, 3148 (1991).
15. M. H. Devoret, et al., *Phys. Rev. Lett.* **64**, 1824 (1990); Yu. V. Nazarov, *Sov. Phys. JETP* **68**, 561 (1989).
16. R. A. Webb, S. Washburn, and C. P. Umbach, *Phys. Rev. B* **37**, 8544 (1988); P. DeVegvar, et al., *Phys. Rev. B* **40**, 3491 (1988).
17. See the articles by S. Washburn; B. Kramer and J. Masek; V. I. Falko and Y. Fu in "Quantum Coherence in Mesoscopic Systems", B. Kramer, ed., NATO ASI, Vol. 245 (Plenum Press, New York, 1991).
18. L. D. Landau and E. M. Lifshitz, "Statistical Physics", Part 1, (Pergamon Press, Oxford, 1980).
19. A. Messiah, "Quantum Mechanics", North Holland Publishing Company, Amsterdam (1958).
20. M. Büttiker and R. Landauer, *Phys. Rev. Lett.* **49**, 1739 (1982).
21. M. Büttiker, *Phys. Rev. B* **27**, 6178 (1983).
22. C. R. Leavens and G. C. Ares, *Solid State Commun.* **62**, 1101 (1987); M. Büttiker and R. Landauer, *IBM J. Res. Dev.* **30**, 451 (1986).
23. H. A. Fertig, *Phys. Rev. Lett.* **65**, 2321 (1990).
24. M. Büttiker, in "Electronic Properties of Multilayers and low Dimensional Semiconductors", edited by J. M. Chamberlain, L. Eaves, and J. C. Portal, (Plenum, New York, 1990). p. 297-315.

## **Spatial distribution of quantum mechanical currents and charge in a model semiconductor nanostructure**

K-F Berggren a,b), C Beshev b) and Zhen-Li Ji a)

(a) Dept of Physics and Measurement Technology, (b) National Supercomputer Centre - NSC  
Linköping University, S-581 83 Linköping, Sweden

**ABSTRACT:** The distribution of electron densities and velocities is computed for ballistic transport in a model crossbar structure. As the energy is increased one observes a transition from laminar to vortex flow. The vortices form a volatile and complicated flow pattern as shown by a few selected examples.

### **1. INTRODUCTION**

We consider the quasi-two-dimensional electron gas (2DEG) residing at the interface in e.g. a modulation doped GaAs/AlGaAs heterojunction. This electron gas may be confined laterally into a quasi-one-dimensional channel by e.g. the action of a split gate over the AlGaAs. When a negative voltage is applied to the split gate, electrons are depleted from the 2DEG under the gate and a quasi-one-dimensional (Q1D) channel is defined (Thornton et al. 1986, Berggren et al. 1986). More generally, a gate patterned according to some predefined design may be used to shape the electron gas into nanopatterns such as grids, rings, dots etc. Because of the smallness of such structures quantum mechanical effects are strongly manifested at low temperatures. In narrow channels electrons propagate in one-dimensional (1D) subbands, of which only a few may be occupied. In high-mobility samples like GaAs/AlGaAs the mean free path exceeds several microns at low temperatures. In short channels or electron wave guides, connecting e.g. two 2DEG regions acting as source and drain, one therefore encounters ballistic transport and quantization of the conductance. Then each conducting spin-degenerate 1D subband contributes  $2e^2/h$  to the differential conductance (Wharam et al. 1988, van Wees et al. 1988). Here will study theoretically the somewhat related case of two short channels forming a cross. The reason for selecting this particular case is the existence of discrete modes trapped at the intersection of two perpendicular, infinite channels (Schuldt, Ravenhall, and Wyld 1989, Berggren and Ji 1991, Avishai et al. 1991). When the channels are made finite and open-ended, as in our case, the trapped modes turn into broadened resonances.

### **2. DEFINITION OF THE MODEL NANOSTRUCTURE**

Our model semiconductor structure consists of two short intersecting, perpendicular channels, one of which connects to two 2DEG reservoirs acting as source and drain as for the above case of a single short channel. Alternatively we may view the system as a quantum box with leads to the 2DEG regions. Here we prefer, however, to refer to our structure as two intersecting channels since we will discuss in some detail the case when the size of the cross is larger than the average spatial extension of the trapped modes mentioned above. Our model device is shown in Fig.1. For simplicity we assume that the electrons move in perfectly flat regions limited by infinite, hard walls. The sharp corners are another simplifying assumption. In a real case the potential would be softer and corners would be rounded. Refinements of this

kind imply considerable computational complications but not necessarily a qualitatively different physics.

When a weak potential difference is applied between source and drain an electric current will flow in the crossbar region. The dimensions of this region is smaller than the 2D mean free path and in this sense the transport through the channel region is ballistic. We also assume that charging and other interaction effects may be neglected. We therefore solve the one-electron Schrödinger equation exactly in the different regions indicated in Fig. 1 and ensure continuity of amplitudes and derivatives at the different boundaries. In Fig 1 one would thus have for the section with label 1

$$\Psi_1(x, y) =$$

$$\sum_n (B_n^1 e^{i q_n x} + C_n^1 e^{-i q_n x}) \sin\left(\frac{n\pi}{w}(y + w/2)\right) \quad (1)$$

and similarly for the remaining sections of the cross. The sinusoidal function describes transverse standing waves with energies  $E_n = \hbar^2(n\pi/w)^2/2m^*$  with  $n=1,2,\dots$ . The exponential functions describe motion along the channel.

The energy of the electron is therefore  $E = E_n + \hbar^2 q_n^2 / 2m^*$ . If the energy of the incoming electron is less than the subband threshold  $E_n$  the quantity  $q_n$  will be imaginary, i.e. there will be exponentially damped and growing solutions. Typically such solutions appear when tunneling via bound states takes place. Incident electrons with wave vector  $\mathbf{k}=(\kappa, \kappa)$  and energy  $E = \hbar^2 k^2 / 2m^*$  are represented by

$$\Psi_i(x, y) = e^{i k x + i k y} + \int_{-\infty}^{\infty} dk' A_L(k') e^{-i k' x + i k' y} \quad (2)$$

where the last term accounts for back scattering. A similar form holds for the transmitted wave function. For details see e.g. Berggren and Ji (1991).

### 3. CONDUCTANCE

Using the one-electron wave functions indicated above we have evaluated the conductance assuming that the electron transport is ballistic (Berggren and Ji 1991). Furthermore we have assumed zero temperature and that the potential drop between source and drain is small. Hence only electrons at the Fermi energy contribute to the conductance. When the energy of the incoming electrons is varied (or alternatively the widths of the channels) the conductance varies strongly compared to the case of a single channel referred to above. There is an intricate pattern of resonances or tunneling associated with the bound states already mentioned and 'anti-resonances' due to interference effects. Because of the finite length of the channels there are also resonances associated with standing waves in the crossbar structure. The conductance at zero temperature and weak field

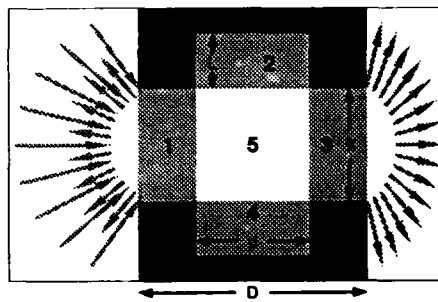


Fig. 1. Computational model a symmetric quantum cross nano-structure with dimensions  $D=200$  nm,  $d=100$  nm,  $w=100$  nm and  $L=0.95$  nm. Incident electrons from the left may be backscattered or transmitted to the right hand side as indicated by the arrows.

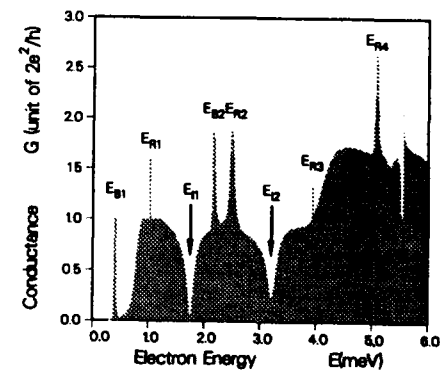


Fig. 2. The conductance  $G$  (in units of  $2e^2/h$ ) at different energies  $E$  (in meV) of the carriers for the model quantum structure of Figure 1 with  $L=50$  nm.

for the case  $L=50\text{nm}$  is shown in Fig 2. Bound state resonances are denoted by  $E_{B1}$  and  $E_{B2}$ . Resonances that derive from the finite dimensions are denoted  $E_{R1}, \dots, E_{R4}$ . Due to interference effects the conductance vanishes at  $E_{I1}$  and  $E_{I2}$ .

Fig.3 shows the conductance for different extensions of the symmetric perpendicular bar. As  $L$  increases one finds that  $E_{B2}$  and  $E_{R2}$  change position. The reason is that  $E_{R1}, \dots, E_{R4}$  are sensitive to  $L$  while  $E_{B1}$  and  $E_{B2}$  remain more stable. We have not resolved all peaks in Fig.3 numerically because they are very narrow and therefore require more extensive computing.

#### 4. ELECTRON DISTRIBUTIONS

The series of graphs in Fig.4 shows some typical electron densities associated with the current flow, i.e. contributions to the density derive only from incident states at the Fermi energy. The first case shows the tunneling via the lowest bound state characterising an infinite cross. Clearly the wave-function is well localized to the interior region of the crossbar structure. The second case shows the electron density for an energy just slightly larger than  $E_{I1}$  at which the channels are switched off due to interference effects. The electrons accumulate essentially to the left part of the structure because interference is partly blocking the channel. At  $E_{I2}$  the channel is completely blocked but electrons still penetrate the channel to the left as above. The picture to the left in the bottom row shows the electron cloud as the resonances  $E_{B2}$  and  $E_{R2}$  overlap. Hence its overall features can be understood in terms of a hybridization of the two states.

#### 5. SPATIAL DISTRIBUTION OF VELOCITIES

The corresponding quantum-mechanical current distributions show that the flow of carriers is laminar at low energies. As the energy is increased to the extent that interference becomes important vortices appear in the current as shown by the second case in Fig.4. Although the origin of the vortices is purely quantum mechanical, one is thus dealing with a situation that makes one think of the *transition from laminar to vortex flow* in classical media. On further increase of the energy the vortices will form an increasingly complex and volatile pattern that even brings phenomena like turbulence and chaos to mind. Minutest changes in energy or dimensions may cause e.g. strong clockwise rotational flow to flip instantaneously into counter clockwise motion and vice versa. The process reminds of spin flips. Obviously visualization and computer animation become useful tools for displaying and analyzing complex physical events of this kind. Hence the computed spatial distributions of current and charge as a function of energy have been analyzed and documented in the form of a video.

Avishai Y, Bessis D, Giraud B G and Mantica G 1991 Phys. Rev. B 44 8028  
 Berggren K-F, Thornton T J, Newson D J and Pepper M 1986 Phys. Rev. Lett. 57 1769  
 Berggren K-F and Ji Zhen-Li 1991 Phys. Rev. B 43 4760 and references quoted.  
 Schult R L, Ravenhall D G and Wyld H W 1989 Phys. Rev. B 39 5476  
 Thornton T J, Pepper M, Ahmed H, Andrews D and Davies G J 1986 Phys. Rev. Lett. 56 1198  
 van Wees B J, van Houten H, Beenaker C W J, Williamson J G, Kouwenhoven L P, van der Marel D and Foxon C T 1988 Phys. Rev. Lett. 60 848  
 Wharam D A, Thornton T J, Newbury R, Pepper M, Ahmed H, Frost J E F, Hasko D G, Peacock D C, Ritchie D A and Jones G A C 1988 J. Phys. C: Solid State Phys. 21 L209

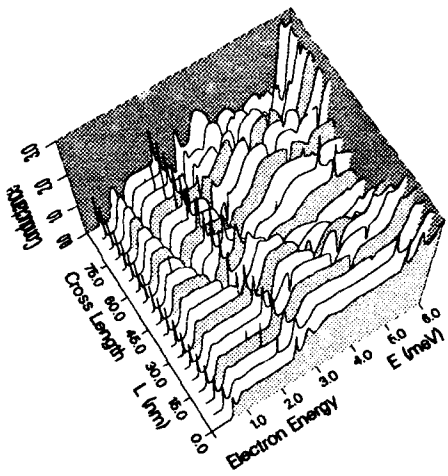


Fig. 3. Conductance  $G$  ( in units of  $2e^2/h$  ) as a function of Fermi energy  $E$  ( in meV ) and extension  $L$  of the stubs ( in nm ).

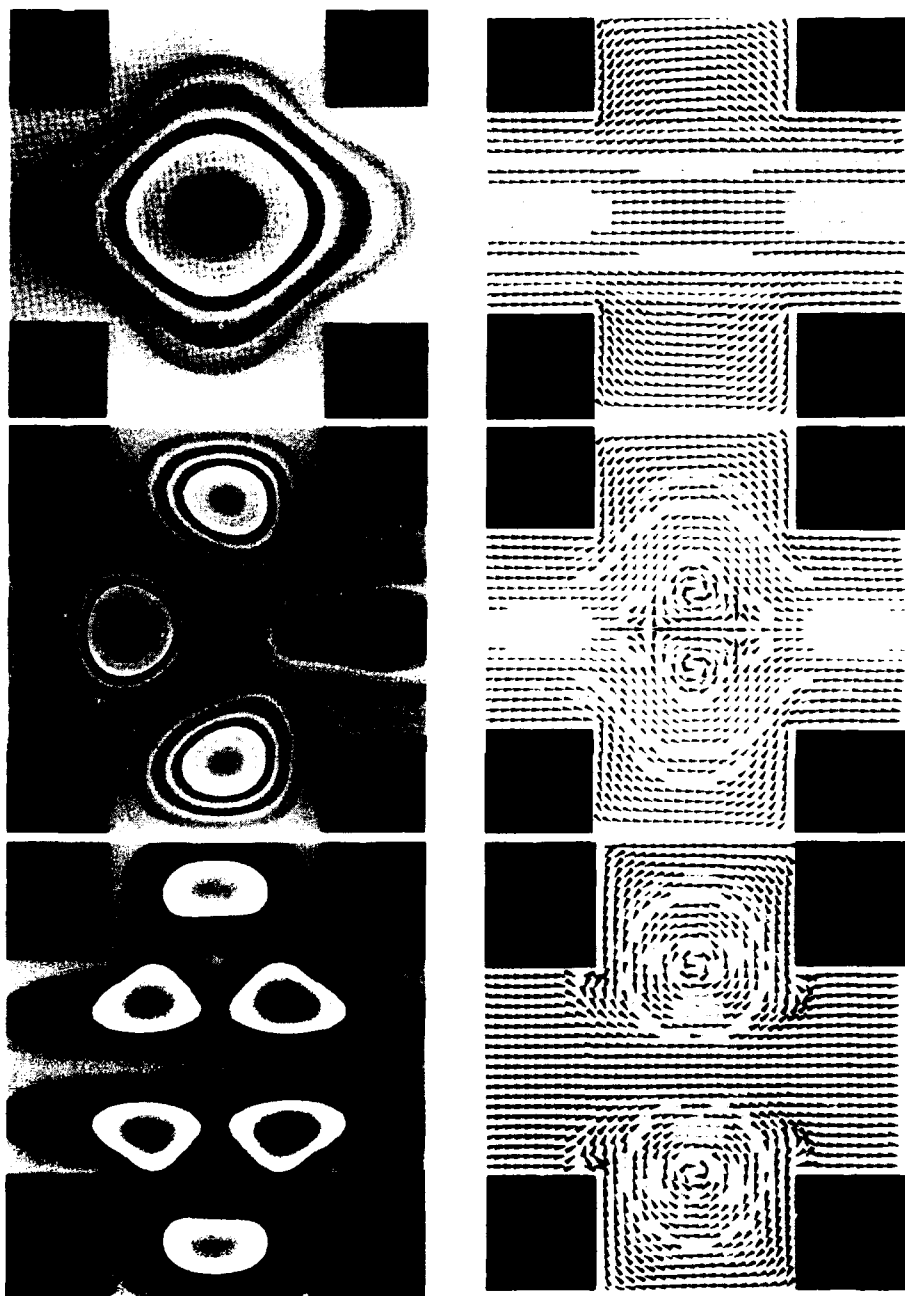


Fig. 4. Distribution of charge (left column) and velocities (right column). Upper case shows laminar flow at the lowest bound state resonance at  $E_{B1}$ . The middle row displays vortices that appear when the energy is close to  $E_{I1}$ . In the case displayed the energy is somewhat higher than  $E_{I1}$ . The two upper rows refer to  $L=50$  nm. The bottom row shows the formation of strong vortices as  $E_{B2}$  and  $E_{R2}$  hybridize when  $L=63$  nm. A small reduction of  $L$  by as little as 1 nm induces a rapid change. Clockwise rotational motion swiftly becomes counter clockwise and vice versa while the charge distributions remains practically unchanged.

## Quantum noises in mesoscopic conductors: origins and suppression

Akira Shimizu,<sup>a)</sup> Masahito Ueda,<sup>b)</sup> and Hiroyuki Sakaki<sup>a,c)</sup>

<sup>a)</sup>Quantum Wave Project, ERATO, JRDC, 4-3-24-302 Komaba, Tokyo 153, Japan

<sup>b)</sup>NTT Basic Research Laboratories, Musashino-shi, Tokyo 180, Japan

<sup>c)</sup>IIS and RCAST, University of Tokyo, Japan

It is pointed out that the excess noise of mesoscopic conductors found by Lesovik is the usual granularity noise, which is a general noise of quantum mechanics. It is also shown that *neither* the dephasing *nor* the electron-electron inelastic scattering is sufficient to suppress the excess noise. The excess noise is suppressed and the noise characteristics becomes those of macroscopic conductors only when the transit time of an electron across the conductor exceeds the energy relaxation time due to the electron-phonon scatterings.

### INTRODUCTION AND SUMMARY

Electric currents in single-mode mesoscopic conductors exhibit *neither* the universal conductance fluctuation (UCF) *nor* the chaotic fluctuation when external fields and impurity configuration are fixed. However, when each measurement of the current  $J$  is performed *in a finite detection time*  $\tau_{det}$ , other noises of more fundamental origins would be found, which vanish in the limit of  $\tau_{det} \rightarrow \infty$ . That is, measured values of  $J$  (which is the average over the time  $\tau_{det}$ ) fluctuate from measurement to measurement. In other words, the current-current power spectrum is nonzero. The origins of this fluctuation may be (a) emission noise, (b) granularity noise, (c) Johnson-Nyquist noise, (d) imperfect coherence of electrons, (e) possible noises in an external input, (f) 1/f noise, and (g) coupled noises of these noises. When the temperature  $\Theta$  and the source-drain voltage  $V_{SD}$  are low enough, then noise (d) would be small. It is not clear whether noise (f) is present in perfectly-fabricated conductors. Noise (c) is finite even at  $\Theta = 0$ , but is smaller than (b) when  $J$  is not too small. By neglecting noises (d), (f) and (c), we previously reported the fundamental limits of quantum interference devices (Shimizu and Sakaki 1991).

On the other hand, Lesovik (1989) and Büttiker (1990) derived a formula for the excess noise ( $\equiv$  noise at  $J \neq 0$  minus noise at  $J = 0$ ). This noise is similar to the classical shot noise (CSN) in the sense that it is proportional to  $J$ , and may be called "quantum shot noise" (QSN) if one wishes to stress this similarity. However, an important difference is that QSN is smaller than CSN in magnitude. We here focus on this QSN, and point out two things. Firstly, QSN is equivalent to noise (b), the granularity noise (GN). Since GN is a very fundamental noise in quantum mechanics, it is *not* specific to mesoscopic systems or fermion systems. Secondly, we answer the following question: "Macroscopic conductors exhibit *neither* QSN *nor* CSN. What makes such a big difference between mesoscopic and macroscopic conductors?" It is shown that simple dephasing processes (caused, e.g., by magnetic impurities) *cannot* suppress QSN: Both the Landauer formula (for the average current) and the Lesovik formula (for the excess noise) remain valid if the definition of the transmittance is slightly modified. It is further pointed out that even the electron-electron inelastic scatterings is *not* sufficient to suppress the excess noise, either. It is concluded that the only mechanism which suppresses the excess noise is the energy transfer from the electron system to other systems, which is usually caused by the electron-phonon scatterings.

### GRANULARITY NOISE

The wave-particle duality, the most characteristic feature of quantum mechanics (QM), manifests itself in interference experiments: Any particle can interfere like a classical wave, whereas it will appear as a localized particle even after the interference has taken place. When we focus on the wave nature, the particle nature gives rise to a quantum noise in the observed interference pattern. This is the granularity noise. For example, suppose that a particle has entered into a scattering region, where the particle is elastically scattered, and there are two possible destinations  $D_+$  and  $D_-$ . In the case of two-terminal conductors, for example,  $D_+$  and  $D_-$  correspond to the drain reservoir (to which forward-scattered wave comes) and the source reservoir (to which backward-scattered wave returns), respectively. Let us consider how accurately an experimenter can measure the wave intensities  $T_{\pm}$  at  $D_{\pm}$ . If the wave were classical, the signals  $n_{\pm}$  from detectors placed at  $D_{\pm}$  would equal to  $T_{\pm}$ . However, the particle nature violates the classical relationship  $n_{\pm} = T_{\pm}$ . This is because (i)  $n_{\pm}$  can only take either 0 or 1 whereas  $T_{\pm}$  (which become probabilities in QM) can take an arbitrary value between 0 and 1, and also because (ii) it can happen (as long as  $T_+ \neq 0$ ) that  $n_+ = 1, n_- = 0$  even when  $T_+ < T_-$ . Hence  $n_{\pm} \neq T_{\pm}$  in general, and each observed value of  $n_{\pm}$  fluctuates randomly about the expectation value  $\langle n_{\pm} \rangle$  ( $= T_{\pm}$  in this case). This is the granularity noise for the case of two destinations. Because of this noise, the experimenter cannot estimate  $T_{\pm}$  from a single measurement. To estimate  $T_{\pm}$ , QM requires him to repeat the same measurement many times, and then the average value of  $n_{\pm}$  will approach  $T_{\pm}$ . Let  $N$  be the number of the repetition, or, equivalently, the number of the particles passing through the scatterer. Then the total particle counts at  $D_{\pm}$ ,  $N_{\pm} \equiv \sum n_{\pm}$ , obey the simple binomial distribution;

$$P_N(N_+) = \binom{N}{N_+} T_+^{N_+} T_-^{N_-}, \quad N_+ + N_- = N, \quad T_+ + T_- = 1. \quad (1)$$

Hence, the average

$$\langle N_{\pm} \rangle = NT_{\pm}, \quad (2)$$

and the fluctuation

$$\langle \delta N_{\pm}^2 \rangle = NT_+T_-. \quad (3)$$

Equations (2) and (3) are equivalent to the Landauer formula and the Lesovik (1989) formula, respectively. Note that in the above derivation we have assumed nothing about the nature of the particle. Hence, GN is quite widely encountered in quantum systems, including both fermions and bosons (see, e.g., Loudon 1983). That is, GN or QSN is *not* specific to electrons in mesoscopic conductors. Note also that the important assumption leading to GN is that each particle determines its destination independently of other particles. That is, GN is characteristic of such *uncorrelated* particles. This uncorrelated property should be distinguished from the regularity of the flow of electrons emitted from the reservoirs. Such regularity is related with noise (a), the emission noise (EMN), which will be briefly discussed in the next section.

### HOW TO OBSERVE GRANULARITY NOISE IN SEMICONDUCTORS

Pioneering experimental results on the excess noise have been reported recently (Li et al. 1990). However, one should be careful in comparing them with theory. For example, in general there exists EMN in addition to GN and other possible noises

(Shimizu and Sakaki 1991). Note that EMN would vanish if the state of the form  $(\prod_{k \sim k_F} c_k^\dagger) |0\rangle$  were emitted from the source reservoir. This is because such a state is an (approximate) eigenstate of the current operator, and thus exhibits no current fluctuations. However, the statistical properties of the emitted particles in general depend on the whole circuit (Shimizu and Sakaki 1991) including the nature of the reservoirs. The experimental work by Li *et al.* (1990) employed a two-terminal structure to measure the excess noise. Unfortunately, it is impossible to separate GN from EMN in two-terminal conductors, and, what is worse, EMN depends on GN because the external circuit controls the total current which includes both GN and EMN. A good way to circumvent this difficulty is to use a Mach-Zehnder-type interferometer or a beam splitter, in which GN and EMN can be measured separately (Shimizu and Sakaki 1991). Such an interferometer may be fabricated by appropriately gating the two-dimensional electron gas.

### FROM MESOSCOPIC TO MACROSCOPIC CONDUCTORS

Let us consider a two-terminal conductor of length  $L$ , and write  $T_+$  and  $T_-$  of Eqs.(1)-(3) as  $T$  (transmittance) and  $R$  (reflectance), respectively. We focus on GN only, ignoring EMN and the other noises for simplicity. When  $L$  is increased  $T$  will be decreased, and Eq.(3) approaches CSN,  $NT$ . However, it is known that the excess noise of macroscopic conductors is much lower than CSN or GN. For example, Tapster *et al.* (1987) utilized this fact to generate a regulated photon flow from a light-emitting diode. As conjectured by Beenakker and van Houten (1991), this suppression of GN should of course be caused by some inelastic scatterings. However, the following important points were unknown yet:

- (i) What type(s) of the “inelastic scatterings” is relevant? Is the dephasing sufficient for the suppression?
- (ii) How GN behaves as a function of  $L$ ?

There are many time scales in the problem: the transit time  $\tau_{tr}$  of an electron passing through the conductor, the lifetime  $\tau_{life}$  of an exact one-body eigenstate, the dephasing time  $\tau_\phi$  for an electron to change its phase by  $2\pi$ , the electron-electron energy relaxation time  $\tau_{ee}^{er}$  for an excited electron to relax onto the Fermi surface by exciting other electrons, the electron-phonon energy relaxation time  $\tau_{ep}^{er}$  for an excited electron to relax onto the Fermi surface by exciting phonons, and so on. Note that even in the simple case of interacting electrons in random potentials  $\tau_{life}$ ,  $\tau_\phi$  and  $\tau_{ee}^{er}$  are different from each other in general (see, e.g., Al'tshuler and Lee 1988). Note also that  $\tau_{ee}^{er}$  and  $\tau_{ep}^{er}$  are in general longer than the simple electron-electron and electron-phonon collision times  $\tau_{ee}$  and  $\tau_{ep}$ , respectively.

As for question (ii), we have found the universal functional forms in the “elastic dephasing” regime (see below)  $\tau_\phi < \tau_{tr} < \tau_{ee}$ ,  $\tau_{ep}$ , and in the “classical regime”. In the latter regime, for example, the excess noise is inversely proportional to  $L$ . That is, once  $L$  is increased to the classical regime the excess noise starts to decrease monotonically, leading to the absence of the excess noise in macroscopic conductors. However, this does not answer our question fully, because we must clarify what makes conductors “classical”. That is, we must also clarify point (i), which will be considered below.

Our task is to find what is the relevant time scale(s). In the case of UCF, for example, the relevant time scale is  $\tau_\phi$ : With increasing  $\tau_{tr}$  the magnitude of UCF starts to decrease when  $\tau_{tr}$  exceeds  $\tau_\phi$  (Al'tshuler and Lee 1988). By contrast, we can show that the dephasing is irrelevant to the suppression of GN. To show this fact, let us

consider the *elastic* dephasing regime where  $\tau_\phi < \tau_{tr} < \tau_{ee}, \tau_{ep}$ , which may be realized in samples with magnetic impurities. To avoid complicated things (such as Kondo effect, strong sensitivity of the scattering matrix to the spin configurations, and so on) which are not interesting to us here, we assume that the density of the magnetic impurities is high and their coupling to the conduction electrons is weak and ferromagnetic. In such a case, we can define the "spin-unconscious" transmittance, which is the sum of the probabilities for an up- or down-spin electron to pass through the conductor with the spin conserved and that with the spin inverted. With this extended definition of the transmittance, it can be shown that *both* the Landauer formula and the Lesovik formula remain valid. This also shows that  $\tau_{life}$  is also irrelevant because  $\tau_{life} = \tau_\phi$  in this simple example.

We can further show that  $\tau_{ee}^{er}$  is *not* sufficient to suppress the excess noise, either. This may be understood by considering the regime where  $\tau_{ee}^{er} < \tau_{tr} < \tau_{ep}^{er}$ . Let us start with the system without electron-electron interaction. Under a finite  $V_{SD}$ , the electron distribution function near the fermi surface is broadened by a width of order  $eV_{SD}$ . This leads to the excess noise. Now we turn on the electron-electron interaction. It will renormalize the conductance by, e.g., renormalizing the scattering amplitudes. To make the discussion transparent, let us modify the elastic scattering potential in such a way that the value of the conductance becomes the same as that without the electron-electron interaction. The electron-electron collision will change the energies of individual electrons, and the electron distribution approaches something like the shifted Fermi distribution of some temperature  $\Theta_e$ . If  $\Theta_e$  were equal to the lattice temperature  $\Theta$ , which is assumed to be zero for simplicity, then the excess noise would vanish because the zero-temperature distribution exhibits no noise (except for a small zero-point fluctuation (Shimizu and Sakaki 1991)). However,  $\Theta_e \sim eV_{SD}/k_B > \Theta$  because the *total* energy of the whole electron system is conserved when  $\tau_{tr} < \tau_{ep}^{er}$ . This broadening of the distribution leads to the noise proportional to  $J$ . That is, an excess noise still exists. Note that  $\Theta_e > \Theta$  is not due to the Joule heating which occurs in the reservoirs in this case.

It is found that only when  $\tau_{tr}$  exceeds  $\tau_{ep}^{er}$  the excess noise becomes very small and the noise property becomes that of macroscopic conductors. In this case, the electrons transfer a part of their energy to the phonon system, resulting in  $\Theta_e = \Theta$ . When the thermal contact of the sample with its holder is good enough,  $\Theta$  is kept constant if  $V_{SD}$  is not too large. Hence, the electron system obeys the shifted Fermi distribution of temperature  $\Theta_e = \Theta = 0$  which is independent of  $J$ . The excess noise is absent in such a case. We anticipate that our conclusions will be confirmed by careful measurements of the excess noise.

#### REFERENCES

- Al'tshuler B L and Lee P A 1988, *Phys. Today* 41 36.
- Beenakker C W J and van Houten H 1991, *Phys. Rev. B* 43 12066.
- Büttiker M 1990, *Phys. Rev. Lett.* 65 2901.
- Lesovik G B 1989, *JETP Lett.* 49 592.
- Li Y P et al. 1990, *Appl Phys. Lett.* 57 774.
- Loudon R 1983, *The Quantum Theory of Light* 2nd ed. (Oxford).
- Shimizu A and Sakaki H 1991, *Phys. Rev. B* 44 13136.
- Tapster P R et al. 1987, *Europhys. Lett.* 4 293.

## Dynamics of electron-wave packets in nanostructures

Akira Endoh, Shigehiko Sasa, Hiroshi Arimoto and Shunichi Muto

Fujitsu Laboratories Ltd.  
10-1 Morinosato-Wakamiya, Atsugi 243-01, Japan

**ABSTRACT:** We performed time-evolved numerical simulation of a two-dimensional electron wave packet by the finite difference method to study the dynamics of electron waves. In single slits, there is a time delay in the diffracted subpeaks. The Fourier transformation of the wave packet shows that the time delay is caused by a k-space peak separation process occurring inside the slit.

### 1. Introduction

The wave nature of electrons observed in nanostructures is expected to give new insights into device operation. A number of static physical properties of electron waves in nanostructures have been investigated both theoretically and experimentally. In addition to static properties, knowledge of dynamics is indispensable for proposing and designing new devices. In our previous work (1991), we studied electron wave static properties using the finite difference method to solve the time-dependent Schrödinger equation of a two-dimensional electron wave packet (EWP). In this work, we analyzed EWP dynamics.

### 2. Numerical Simulation

In our numerical simulations, we calculated the wave function  $\psi$  using a difference equation of the time-dependent Schrödinger equation,

$$\begin{aligned} \psi(x, y, t + \Delta t) = & \psi(x, y, t - \Delta t) \\ & + (i\hbar/m^*) [\Delta t/(\Delta r)^2] \\ & [\psi(x + \Delta r, y, t) + \psi(x - \Delta r, y, t) + \psi(x, y + \Delta r, t) + \psi(x, y - \Delta r, t) - 4\psi(x, y, t)] \\ & - (i/2\Delta t/\hbar) V(x, y) \psi(x, y, t), \end{aligned} \quad (1)$$

where  $\hbar$  is the Planck constant divided by  $2\pi$ ,  $m^*$  the electron effective mass,  $i$  the imaginary unit,  $\Delta t$  the time step,  $\Delta r$  the grid step, and  $V$  the potential energy.

As an initial wave function, a two-dimensional Gaussian wave packet,

$$\psi(x, y, t=0) = (\alpha/\pi)^{1/2} \exp[i(k_x x + k_y y) - \alpha(x^2 + y^2)/2], \quad (2)$$

was used, where  $\alpha$  is a parameter determining distribution width, and  $k_x$  ( $k_y$ ) the wave number for the  $x$  axis ( $y$  axis) calculated from the incident energy of the EWP. In our present simulations, the initial wave numbers  $k_x$  and  $k_y$  were made equal. Namely, an initial EWP is propagated at  $45^\circ$  from  $x$  and  $y$  axes (from the lower left corner to the slit center in Fig. 1(a)). The electron effective mass  $m^*$  was assumed to be  $0.068 m_e$  ( $m_e$ : electron rest mass), in consideration of GaAs. The slit in the potential barrier was set to be rectangular and the potential barrier energy was set at 0.25 eV. The total simulation area was a  $600 \times 600 \text{ nm}^2$ . The time step  $\Delta t$  was 0.2 fs and the grid step  $\Delta r$  2 nm.

### 3. Results and Discussion

Figure 1 shows the traces of peak positions of the EWP transmitted through a single slit (a) and a double slit (b). Cahay *et al.* (1989) performed a similar simulation to ours and, for an EWP through a single slit, confirmed the formation of subpeaks due to electron diffraction. We (1991) also confirmed electron diffraction peaks for a single slit, and in addition, confirmed formation of peaks due to electron interference for a double slit for the first time. Moreover, we (1991) found that the starting point of electron diffraction is the center of the slit entrance side and that of electron interference is the center between the two slit exits side. When an EWP passes through a single slit, subpeaks due to diffraction appear in the transmitted EWP. We (1991) have already shown that the lateral wave number of these peaks is quantized as allowed by the wave number in the potential slit. At the simulation time steps of Fig. 1(a), the subpeaks do not lie on concentric circles. This means that, for a single slit, there is a time delay in the diffracted subpeaks. The delay time increases as the diffraction angle (or quantization number) increases. The subpeak delay time for a  $14^\circ$  diffraction angle ( $n = 1$ ) is 5 fs, for  $31^\circ$  ( $n = 2$ ) is 17 fs, and for  $59^\circ$  ( $n = 3$ ) is 61 fs. In Fig. 1(b), each peak at the same time step lies

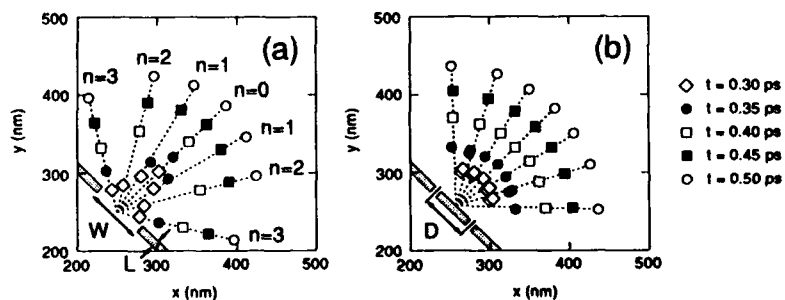


Fig. 1 Traces of peak positions of the EWP transmitted through a slit.

(a) Single slit ( $W = 70 \text{ nm}$ ,  $L = 10 \text{ nm}$ ), (b) Double slit ( $W = 10 \text{ nm}$ ,  $D = 60 \text{ nm}$ ,  $L = 10 \text{ nm}$ ).

on concentric circles. The simulation was sufficiently long to conclude that there is no time delay for a double slit.

The state of the EWP inside the slit provides useful information for interpreting the mechanism of a time delay. Since it is difficult to understand the state of the EWP in the real space (*r*-space), we performed the Fourier transformation of the EWP from *r*-space to the wave number space (*k*-space). The EWP in *k*-space,  $F(k_x, k_y, t)$ , is calculated by the equation,

$$F(k_x, k_y, t) = (1/2\pi) \iint \psi(x, y, t) \exp[-i(k_x x + k_y y)] dx dy. \quad (3)$$

We selected the EWPs at  $t = 0.25$  and  $0.40$  ps for both single and double slits to perform the Fourier transformation, since the probability density of the EWP inside the slit exhibits its maximum at  $t = 0.25$  ps and the EWP is almost transmitted at  $t = 0.40$  ps.

Figure 2 shows the time-evolved EWP in *k*-space for a single slit when it is inside the slit and transmitted. The initial ( $t = 0$ ) EWP in *k*-space is localized at  $k_x = k_y = 3 \times 10^8 \text{ m}^{-1}$ . When the EWP is inside the slit, the Gaussian wave packet in *k*-space exhibits a random circular distribution and small quantized subpeaks in lower numbers for certain wave numbers. These subpeaks grow taller with time. Since electron diffraction starts from the center of the slit entrance, as shown in Fig. 1(a), the peak formation indicates that electron diffraction is in progress inside the slit. While the EWP is inside the slit, its lateral wave number is confined by the quantized wave number. Therefore, the kinetic energy in the propagating direction decreases with an increase in potential energy due to lateral quantization. The wave

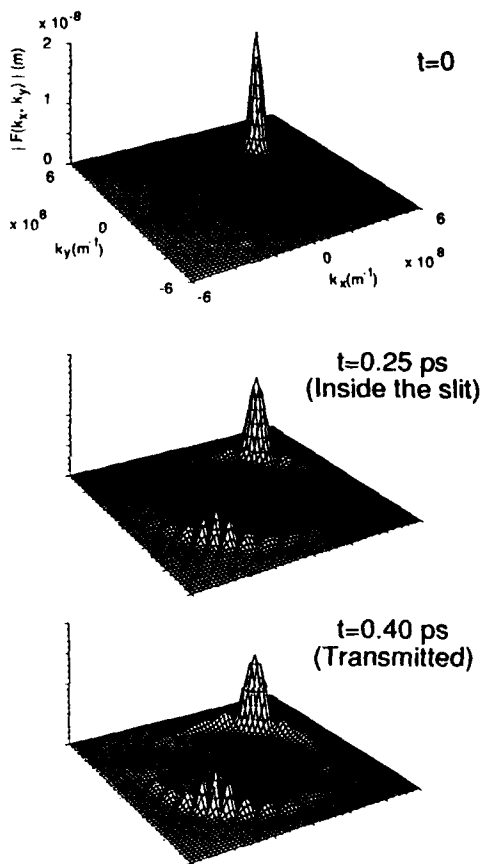


Fig. 2 Bird's eye views of the time-evolved EWP in the wave number space (*k*-space) through a single slit. The slit is 70 nm wide and the potential barrier 50 nm thick.

number in the propagating direction decreases with an increase in quantization number. This results in a time delay in diffracted subpeaks.

Figure 3 shows the time-evolved EWP in k-space for a double slit. Since electron interference starts from the center between the two slit exits, as shown in Fig. 1(b), while the EWP is inside the slit, k-space peak separation does not cause a delay in the interference peaks. At  $t = 0.25$  ps, interference peaks are already under formation, although the EWP is still inside the slit. This means that the EWP knows of the occurrence of electron interference before confluence of the separated waves. Also at  $t = 0.25$  ps, a circle of the same energy is not formed yet. Deviation from the circle would indicate a transient breakdown of the energy conservation law.

#### 4. Conclusion

To study electron wave dynamics, we performed time-evolved numerical simulation of a two-dimensional EWP by solving the time-dependent Schrödinger equation. There is a time delay in the diffracted subpeaks through a single slit, while there is no time delay in the interference peaks through a double slit. This phenomenon can be interpreted by the difference in r-space starting points and its relevance to k-space peak separation inside the slit.

#### Acknowledgements

We thank Drs. M. Ozeki and O. Ohtsuki for their encouragement in this work.

#### References

Cahay M, Kreskovsky J P and Grubin H L 1989 *Solid-State Electronics* **32** 1185  
 Endoh A, Sasa S, Arimoto H, Muto S and Fujii T 1991 *Extended Abstracts of the 1991 International Conference on Solid State Devices and Materials* pp 365-7

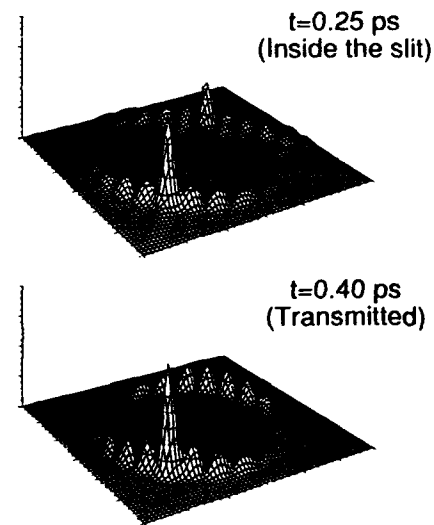


Fig. 3 Bird's eye views of the time-evolved EWP in the wave number space (k-space) through a double slit. The 10 nm wide slits are spaced 60 nm apart and the potential barrier 50 nm thick.

## **Quantum Hall effect: edge-state conduction and critical localization of bulk states**

**T. Ando**

*Institute for Solid State Physics, University of Tokyo  
7-22-1 Roppongi, Minato-ku, Tokyo 106, Japan*

Transmission probability of edge states is calculated in the quantum Hall regime and its energy and size dependence is shown to be determined by localization of bulk Landau states.

### **1. INTRODUCTION**

A key ingredient of the quantum Hall effect is the localization of Landau states in the presence of random potential fluctuations. It has been shown in various different ways that the Hall conductivity is quantized into integer multiples of  $-e^2/h$  when states around the Fermi level are all localized (Ando 1985, Prange and Girvin 1987, Aoki 1987). In quantum wires the Hall effect is usually understood in terms of the transmission probability of edge channels (Büttiker 1986). The relation between these two pictures remains still unclear.

In the picture based on bulk Landau states, the width of the Hall steps, i.e., the region where the Hall conductivity changes from a quantized value to another, is determined by delocalized states existing in the vicinity of the center of each Landau level (Wei et al 1988, Wakabayashi et al 1989). In the edge current picture, on the other hand, the Hall-step width should be determined by the backscattering through mixing with broadened bulk Landau states (see, for example, Ohtsuki and Ono 1989, Ono et al 1989). In this paper, the backscattering probability of edge states is calculated numerically. It will be shown that the dependence of the Hall-step width on the wire width is determined by the energy dependence of the localization length of bulk Landau states.

### **2. METHOD**

We consider a two-dimensional (2D) system on a square lattice (site number  $M$  in the  $y$  direction) and introduce effects of scattering through randomness of site energy distributed uniformly with a width corresponding to broadening  $\Gamma$  of the Landau level. A magnetic field  $H$  is included in the form of a Peierls' phase factor in the nearest-neighbor transfer integral. For sufficiently large  $M$  the lattice system corresponds to a continuum system with width  $W = (M+1)a$  where  $a$  is the lattice constant.

At  $x = \pm L/2$ , the system is connected to an infinitely long ideal wire which eventually connected to a reservoir. In order to calculate transmission probability for the whole energy range of the broadened 2D Landau levels, we shall lower the bottom energy

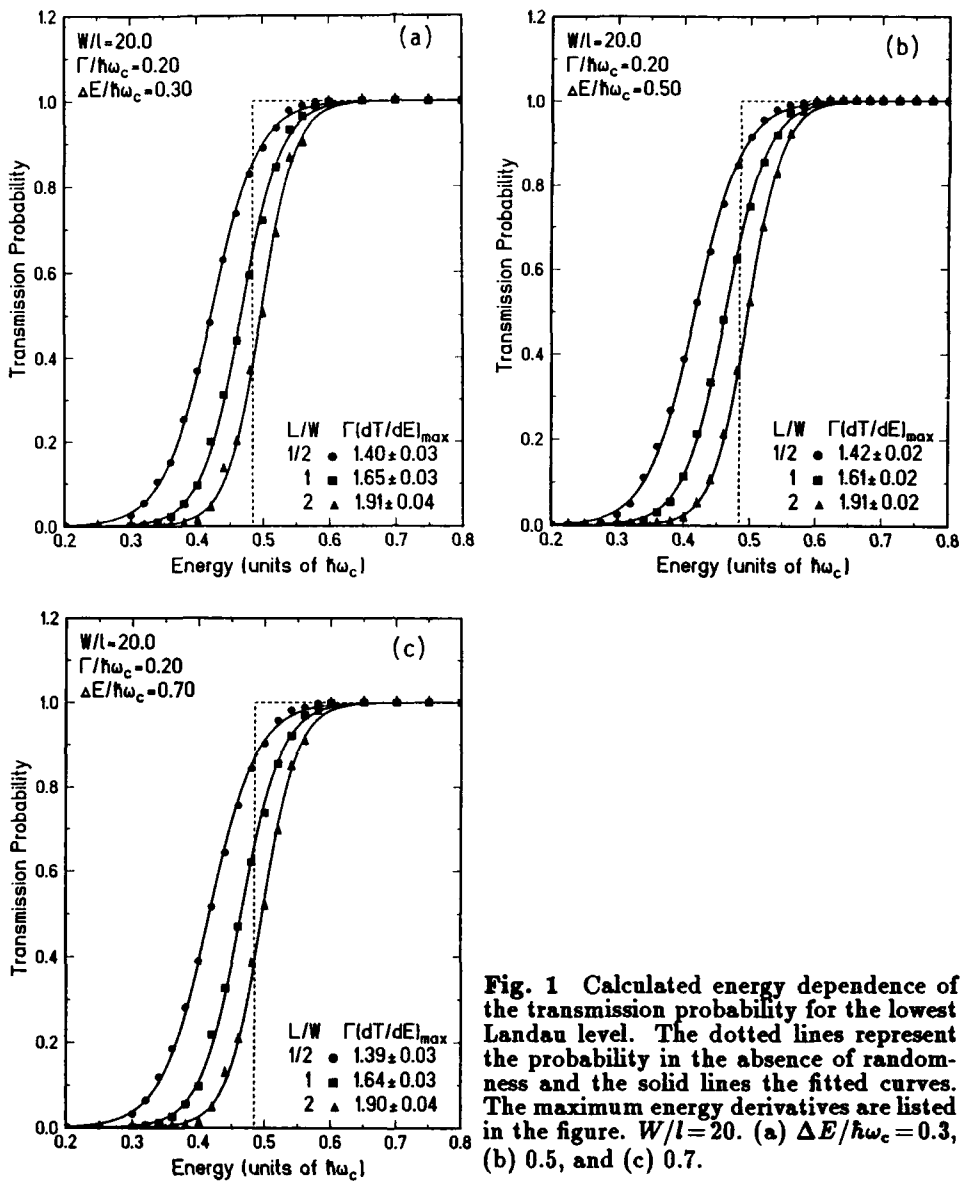


Fig. 1 Calculated energy dependence of the transmission probability for the lowest Landau level. The dotted lines represent the probability in the absence of randomness and the solid lines the fitted curves. The maximum energy derivatives are listed in the figure.  $W/l=20$ . (a)  $\Delta E/\hbar\omega_c=0.3$ , (b) 0.5, and (c) 0.7.

in the ideal wires by  $\Delta E$  ( $\Gamma < \Delta E < \hbar\omega_c - \Gamma$  with  $\omega_c = eH/mc$ ). The transmission probability is calculated using the Green function technique already described (Ando 1991).

Numerical calculations are performed for rectangular systems  $L/W = 1/2, 1$ , and  $2$ . The system size is  $W/l = 5, 10, 15, 20, 25, 30, 35, 40, 50$  with  $l$  the magnetic length defined by  $l^2 = c\hbar/eH$ , and the corresponding site number is  $M+1 = 8, 16, 24, 40, 56, 80, 100, 128, 200$ . The transmission probability for a given energy is calculated by averaging over those of typically  $10^4$  different samples.

### 3. RESULTS

Figure 1 gives some examples of calculated energy dependence of the transmission probability  $T$  for the lowest Landau level. The broadening of the Landau level is  $\Gamma/\hbar\omega_c=0.2$  and the system size is  $W/l=20$ . The results show clearly that a change in the choice of shift  $\Delta E$  causes negligible effects.

In order to deduce effective energy width over which the transmission probability increases from zero to unity, we fit the results to the function  $T(E)=1/\{\exp[\beta(E-E_{th})]+1\}$ . The parameter  $\beta$  or  $\Gamma(dT/dE)_{\max}$  represents the inverse of the effective energy width and  $E_{th}$  the effective threshold energy. The fitted results are shown by solid lines in Fig. 1. The resulting  $\Gamma(dT/dE)_{\max}$ 's are listed in each figure.

Figure 2 gives the steepness parameter as a function of the width in logarithmic scales. It is clear that the results can be fitted to a straight line except those for smallest  $W/l=5$ , showing that  $\Gamma(dT/dE)_{\max} \propto W^{1/s}$ . The exponent is almost independent of the form of the system and obtained as  $s=2.2 \pm 0.1$ .

The threshold energy becomes larger with increasing  $L$  for a given  $W$  but the threshold for systems with different  $L/W$ 's becomes closer with increasing system size. Figure 2 contains also the difference in the threshold energy  $\Delta E_{th}^{(2)}=E_{th}^{L/W=2}-E_{th}^{L/W=1}$  and  $\Delta E_{th}^{(1/2)}=E_{th}^{L/W=1}-E_{th}^{L/W=1/2}$ . Although statistical errors are much larger,  $\Delta E_{th}$  is also fitted to a power law dependence,  $\Delta E_{th} \propto W^{-1/s'}$ . The resulting  $s'=1.9 \pm 0.2$  agrees with  $s$  within statistical errors.

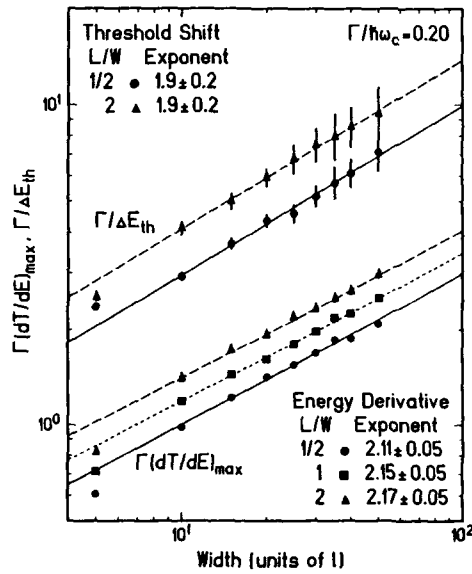


Fig. 2 Log-log plot of the maximum energy derivative of the transmission probability as a function of the system width. The straight lines represent  $\Gamma(dT/dE)_{\max} \propto W^{1/s}$  with exponent  $s$  listed at the bottom-right corner of the figure. The dots denoted as  $\Gamma/\Delta E_{th}$  represent the threshold energy difference between  $L/W=1$  and  $1/2$ , and the squares the difference between  $L/W=2$  and  $1$ . The exponents  $s'$  defined by  $\Delta E_{th} \propto W^{-1/s'}$  are listed at the top-left corner.

Numerical Thouless-number study of localization for Landau levels has shown that states are all localized except those lying in the vicinity of the center in two dimension (Ando 1983). The critical exponent  $s$ , defined by  $\alpha \propto |E|^s$  with  $\alpha$  the inverse localization length and the energy origin at the center, was obtained as  $s \sim 2$  for the lowest Landau level. This result was confirmed later by finite-size scaling calculations (Aoki

and Ando 1985). More recent finite-size scaling calculations within a random-matrix model gave the exponent  $s \approx 2.34$  (Huckestein and Kramer 1990).

Let  $E_- (< 0)$  the energy below the Landau level where the transmission becomes appreciable and  $E_+ (> 0)$  the energy above which the backscattering becomes negligible. For sufficiently large systems where localization length  $\alpha^{-1}$  is only the relevant length scale, these energies are determined by the condition  $h_{\pm}[\alpha(E_{\pm})L, \alpha(E_{\pm})W] = 1$  with  $h_{\pm}$  a certain function. This leads to  $E_{\pm}/\Gamma = \pm C_{\pm}(W/l)^{-1/s}$  for  $\alpha(E) \propto |E|^s$  with  $C_{\pm}$  an appropriate constant depending only on the ratio  $L/W$ . Therefore, the width of the energy region over which the transmission probability varies from zero to unity is given by  $E_+ - E_- \propto W^{-1/s}$ , i.e.,  $\Gamma(dT/dE)_{\max} \propto (E_+ - E_-)^{-1} \propto W^{1/s}$ . The same is applicable to the threshold shift and  $\Delta E_{\text{th}} \propto W^{-1/s}$ . This means that the exponent  $s$  and  $s'$  obtained above are both equal to that for the inverse localization length of bulk 2D Landau states.

The critical exponent obtained in the present study is  $\sim 2.2$ . This is consistent with that of almost all the existing theory either numerical or analytic because actual errors are likely to be larger than  $\sim \pm 0.1$  estimated statistically. Quite recently, Koch et al. (1991) investigated the system-size dependence of the width of the transition region between quantized Hall plateaus and deduced a critical exponent ( $s \sim 2.3$ ) for the localization length of bulk Landau states.

### Acknowledgments

This work is supported in part by the Industry-University Joint Research Program "Mesoscopic Electronics" and by the Grants-in-Aid for Scientific Research on Priority Areas "Electron Wave Interference Effects in Mesoscopic Structures" and "Computational Physics as a New Frontier in Condensed Matter Research" from the Ministry of Education, Science and Culture, Japan.

### References

- Ando 1983 *J. Phys. Soc. Jpn.* 52 1893; 53 3101; 53 3126
- Ando T 1985 *Prog. Theor. Phys. Suppl.* 84 69
- Ando T 1989 *Phys. Rev. B* 40 9965
- Ando T 1991 *Phys. Rev. B* 44 8017
- Aoki H and Ando T 1985 *Phys. Rev. Lett.* 54 2238; *J. Phys. Soc. Jpn.* 54 2238
- Aoki H 1987 *Rept. Prog. Phys.* 50 655
- Büttiker M 1986 *Phys. Rev. Lett.* 57 1761
- Huckestein B and Kramer B 1990 *Phys. Rev. Lett.* 64 1437
- Koch S, Haug R J, von Klitzing K and Ploog K 1991 *Phys. Rev. Lett.* 67 883
- Ohtsuki T and Ono Y 1989 *J. Phys. Soc. Jpn.* 58 1705
- Ono Y, Ohtsuki T and Kramer B 1989 *J. Phys. Soc. Jpn.* 58 956
- Prange R E and Girvin S M 1987 *The Quantum Hall Effect* (Springer, New York, 1987)
- Wakabayashi J, Yamane M and Kawaji S 1989 *J. Phys. Soc. Jpn.* 58 1903
- Wei H P, Tsui D C, Paalanen M A and Pruisken A M M 1983 *Phys. Rev. Lett.* 51 1294

## Analysis of Hall resistance anomalies with wave mechanics

Kiyoshi Kawamura, Hiroyuki Sawano and Tsuyoshi Ueta

Department of Physics, Faculty of Science and Technology, Keio University,  
3-14-1 Hiyoshi, Kohoku-ku, Yokohama 223, Japan

**Abstract.** The Kirchhoff-Helmholtz formula in the tight-binding approximation is applied to analyze the anomalous Hall resistance exhibited by mesoscopic systems. The picture in the billiard model is accurate when lower modes of electrons are injected while higher modes of electrons do not behave as imagined by that model.

### 1. Introduction

The Hall resistance anomalies (Beenecker and van Houten 1991, Roukes *et al* 1987) exhibited by devices fabricated on interfaces of GaAs/AlGaAs have been successfully analyzed in terms of the billiard model, that is, in classical picture of electrons (Beenakker and van Houten 1989, Ford *et al* 1989).

The Kirchhoff-Helmholtz integral formula is useful to solve a differential equation of an elliptic type. A similar formula in the tight binding approximation will be described in section 2 as well as appropriate boundary conditions to study the Hall resistance. Some features of electron waves within the devices of the Hall resistance experiments will be described in section 3.

### 2. Kirchhoff-Helmholtz Formula in the Tight-binding Approximation

We consider an electron system whose wave function obeys the tight binding equation for a square lattice

$$E\psi(\mathbf{n}) = \sum_i T_{\mathbf{n},\mathbf{n}+\mathbf{a}_i} \psi(\mathbf{n} + \mathbf{a}_i) \quad (1)$$

where  $\mathbf{n}$  label the lattice sites and  $\mathbf{a}_i$ , displacements to the nearest neighbors. The hopping parameter, which is  $T$  in the absence of a magnetic field, is modified by it as follows (Peierls 1933);

$$T_{\mathbf{n},\mathbf{n}+\mathbf{a}_i} = T \exp(2\pi i \mathbf{A} \cdot \mathbf{a}_i) \quad (2)$$

The solution to the equation (1) is computed by using the following formula;

$$\psi(\mathbf{n}) = \sum_{i=1}^4 \sum_{\substack{\mathbf{n}' \in \Omega \\ (\mathbf{n}' + \mathbf{a}_i) \notin \Omega}} [G(\mathbf{n}, \mathbf{n}') T_{\mathbf{n}, \mathbf{n}' + \mathbf{a}_i} \psi(\mathbf{n}' + \mathbf{a}_i) - G(\mathbf{n}, \mathbf{n}' + \mathbf{a}_i) T_{\mathbf{n}' + \mathbf{a}_i, \mathbf{n}'} \psi(\mathbf{n}')]. \quad (3)$$

if the site labeled by  $\mathbf{n}$  is involved within the region  $\Omega$ . This is the Kirchhoff-Helmholtz formula in the tight binding approximation (Kawamura 1978) and  $G(\mathbf{n}, \mathbf{n}')$  represents the Green function for which we have employed the semiclassical expression although an rigorous expression has been obtained by one of the present authors (Ueta 1992).

When  $\mathbf{n}'$  label those sites which are adjacent to walls,  $\psi(\mathbf{n}' + \mathbf{a}_i)$  on the right-hand side should vanish. Within each wave guide, a wave function is a linear combination of  $\exp(\pm ik_x x) \sin(m\pi y/N)$  in which the  $x$ -axis is defined by the central line of the wave guide and  $m$  are integers up to  $N$  which represents the width of the wave guide in the unit of the lattice constant. When a site labeled by  $\mathbf{n}'$  is located at the orifice of the wave guide,  $\psi(\mathbf{n}')$  and  $\psi(\mathbf{n}' + \mathbf{a}_i)$  are represented by these linear combinations. When we pick up from equations in (3) those in which  $\mathbf{n}$  belong to the same set as the set of  $\mathbf{n}'$  on the right-hand side, they form coupled linear equations which determine the remaining unknowns. By solving these equations we obtain the transmission coefficient from a certain wave guide to remaining waveguides and then, by using the Landauer-Büttiker formula, the Hall resistance is computed for various devices represented in figures presented below.

### 3. Electron Waves within Devices for Hall Effect Measurements

The diffraction is a characteristic phenomenon exhibited by waves and it cannot be ignored when we discuss wave propagation in mesoscopic systems in the ballistic regime. Since the details of the electron diffraction has been published (Kawamura *et al* 1992), the description about it will be omitted except that electrons injected from a wave guide is separated in two beams. The separation takes place because electrons within a wave guide take zigzag paths and, consequently, the wave vector of each beam is one of two alternating values of momentum (divided by  $\hbar$ ) of the zigzag motion.

We have computed wave functions within three types of devices of cross geometry assuming that an incident electron wave belongs to a certain transverse mode. In Figure 1, the contours of electron intensity are plotted for the incident wave belonging to the fundamental transverse mode. Electrons are injected from the wave guide on the left-hand side. A magnetic field is applied to these devices so that a classical electron path bends to the left. It is shown in Figure 1a that, in accordance with the picture in the billiard model, electrons cannot round the sharp corner in a weak magnetic field. Values of the Hall resistance in this case is smaller than the classical values (quenching of the Hall resistance). In the 'rounded' cross (Figure 1b), electrons are reflected by a wall on the upper-right hand corner and enter into the wave guide attached to the bottom and the Hall resistance in this case is negative valued. When a small island is put at the center of the rounded cross (Figure 1c), electrons which are scattered by this island enter into the upper wave guide and they contribute to the enhancement of the Hall resistance. In this way, the theory of the Hall resistance anomalies in the billiard model (Ford *et al* 1989) is verified by the wave mechanics when the incident electron wave belongs to lower modes.

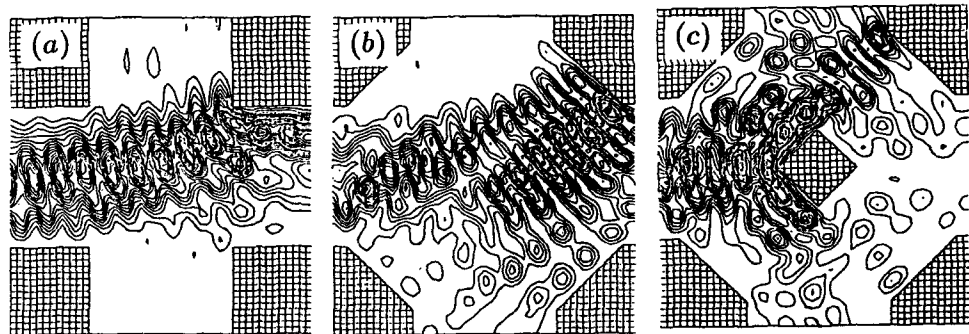


**Figure 1.** Contours of  $|\psi(n)|^2$  when the fundamental mode of waves are injected from the wave guide on the left-hand side. The width of the wave guide is twenty two in the unit of the lattice constant and the magnetic flux enclosed by a unit cell is  $1 \times 10^{-3}$  in the unit of  $\phi_0 = (h/e)$ .

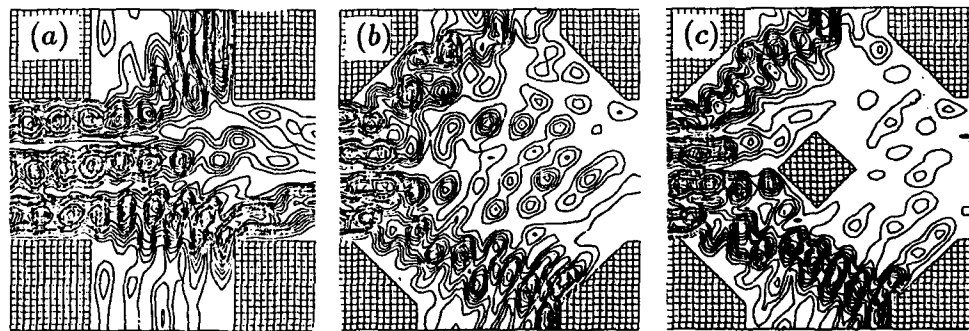


**Figure 2.** Contours of  $|\psi(n)|^2$  when higher modes of waves are injected. The size of the electron channel and the strength of the magnetic field is as same as those in Figure 1.

When, however, electrons belonging to higher modes are injected, the picture in the billiard model is not valid. Since the injected electrons have large transverse component of momentum, an appreciable part of them enter into the wave guides at the top and the bottom even in the absence of a magnetic field. Then, electrons can enter into the upper wave guide in the presence of a weak magnetic field (Figure 2a) not because their path is bent by the Lorentz force but because their initial velocity at the orifice is directed to that wave guide. The electron path which is initially directed toward the lower wave guide bend slightly upward and the intensity of electrons going to the upper wave guide exceeds that going to the lower wave guide. As consequence, those electrons belonging to the higher modes contribute to positive Hall resistance. From the same reason, electrons can enter into the upper wave guide in the 'rounded' cross not being reflected by the wall (Figure 2b). In this case, the Hall resistance is positive valued in contrast to the prediction of the naive billiard theory. Since the injected electrons are separated, their intensity near the center of the cross is so weak that the island at the center of the cross plays no essential role [Compare Figures 2b and c].

From studies of the transmission coefficients among those wave guides, we have verified the above-described dependence of the Hall resistance on transverse mode of incident wave. Discussion on the Hall resistance anomalies based on the wave mechanics will be published elsewhere.

#### Acknowledgments

The present work is supported partially by a Grant-in-Aid for Scientific Research on Priority Area, "Electron Wave Interference Effects in Mesoscopic Structures" from the Ministry of Education, Science and Culture.

#### References

Baranger H and Stone A D 1989 *Phys. Rev. B* **40** 8169-8193  
Beenakker C W J and van Houten H 1991 *Solid State Physics* vol 44 (San Diego: Academic Press Inc.) pp 1-228  
Beenakker C W J and van Houten H 1989 *Phys. Rev. Lett.* **63** 1857-1860  
Ford C J B, Washburn S, Büttiker M, Knoedler C M and Hong JM 1989 *Phys. Rev. Lett.* **62** 2724-2727  
Kawamura K 1978 *Z. Phys.* **B30** 1-11  
Kawamura K, Ueta T and Sawano H 1992 *Japan. J. Appl. Phys.* (in press)  
Peierls R E 1933 *Z. Phys.* **80** 763-791  
Roukes M L, Sherer A, Allen S J Jr., Graighead H G, Ruthen R M, Beeke E D and Harbison J P 1987 *Phys. Rev. Lett.* **59** 3011-3014  
Ueta T 1992 *Proc. Int. Sympo. on Science and Technology of Mesoscopic Structures, Nara Nov. 6-8, 1991* (Tokyo: Springer Verlag) to be published

## Scattering and quantum localization of electrons in a waveguide by static and time-varying potentials

Philip F. Bagwell, Arvind Kumar<sup>†</sup>, and Roger Lake

School of Electrical Engineering, Purdue University, West Lafayette, IN 47907 USA

<sup>†</sup> Massachusetts Institute of Technology, Cambridge, MA 02139 USA

**ABSTRACT:** We compare the transmission through static defects in an electron waveguide with the scattering from a one-dimensional potential barrier which oscillates in time. The multiple spatial 'subband' conduction channels in the waveguide, and multiple energy 'sideband' channels for the oscillator, produce transmission resonances near the 'bound' and 'quasi-bound' states in these potentials. Additional novel transmission behavior in a highly disordered waveguide arises from the interplay of electron localization with the confinement subbands.

### 1. INTRODUCTION

Transmission through a potential in which a limited number of quantum scattering channels are open, extensively studied in atomic and nuclear physics, has recently become of interest for electron transport in mesoscopic semiconductors. The Büttiker-Landauer formula gives the electrical conductance  $G$  for such a multiple-channel semiconductor as

$$G(E) = 2 \frac{e^2}{h} \sum_{ij} T_{ij}(E) = 2 \frac{e^2}{h} T(E) \quad , \quad (1)$$

where the transmitted current  $J_i^{\text{trans}}(E)$  in channel  $i$  is related to the incoming current  $J_j^{\text{inc}}(E)$  in channel  $j$  through the transmission coefficient  $T_{ij}(E)$  by

$$J_i^{\text{trans}}(E) = T_{ij}(E) J_j^{\text{inc}}(E) \quad . \quad (2)$$

$G(E)$  as a function of Fermi energy  $E$  can display interesting resonances near 'bound' and 'quasi-bound' states in the scattering potential, similar to the well-known transmission resonances in double barrier resonant tunneling structures.

The 'bound state' and 'quasi-bound state' energies are defined as the poles of any transmission coefficient  $T_{ij}(E)$ , i.e. the complex energies  $E = E_R + iE_I$  which satisfy  $0 = 1/T_{ij}(E)$ . One can easily appreciate this definition (Oppenheim 1983), since  $T_{ij}(E) \rightarrow \infty$  implies a response even if the input tends to zero. At the poles of  $T_{ij}(E)$ , the wavefunction grows (or decays, if  $E_I < 0$ ) exponentially in time as

$$\Psi(x, y, t) = \psi(x, y) e^{-iEt/\hbar} = \psi(x, y) e^{-iE_R t/\hbar} e^{E_I t/\hbar} \quad . \quad (3)$$

If  $E_I = 0$  the state is 'bound', while a pole of  $T_{ij}(E)$  at  $E_I \neq 0$  is a 'quasi-bound state'.

## 2. SINGLE IMPURITY IN A WAVEGUIDE

Consider a two-dimensional quantum wire confined in the  $y$ -direction and free along the  $x$ -direction. We choose the impurity potential to be  $V(x, y) = \gamma\delta(y - y_i)\delta(x)$ . The Büttiker-Landauer conductance through this potential (Chu 1989, Bagwell 1990a 1990b) is shown in Fig. 1(a). Conductance through the 'acceptor' impurity ( $\gamma > 0$ ) is only slightly different from the quantized ballistic conductance steps, as the step edges have been rounded by scattering. In contrast, conductance through the 'donor' impurity ( $\gamma < 0$ ) displays distinct resonances before the opening of each confinement subband.

The physical origin of this difference in transmitted fluxes through donor versus acceptor impurities can be understood by inspection of Fig. 1(b). In a bulk semiconductor the donor impurity produces a 'donor level' (bound state) below the conduction band minimum of the semiconductor. When confinement subbands are formed in this doped semiconductor, 'quasi-donor levels' (quasi-bound states) are also formed just below the new quasi-one-dimensional subbands, producing the transmission resonances shown in Fig. 1(a). The dashed lines in Fig. 1(b) indicate the dispersion relation for the closed scattering channels, also called evanescent or cutoff channels.

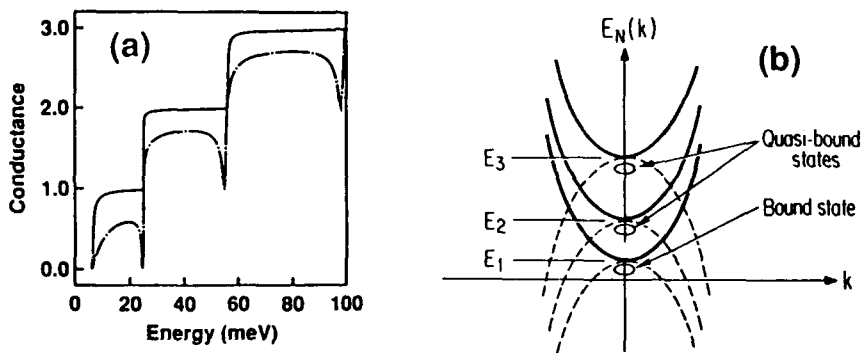


Fig. 1. (a) Conductance through an acceptor impurity (solid) and a donor impurity (dashed) in an electron waveguide (Bagwell 1990a). (b) Energy band structure for the waveguide showing the position of donor and quasi-donor levels (Kumar 1991a).

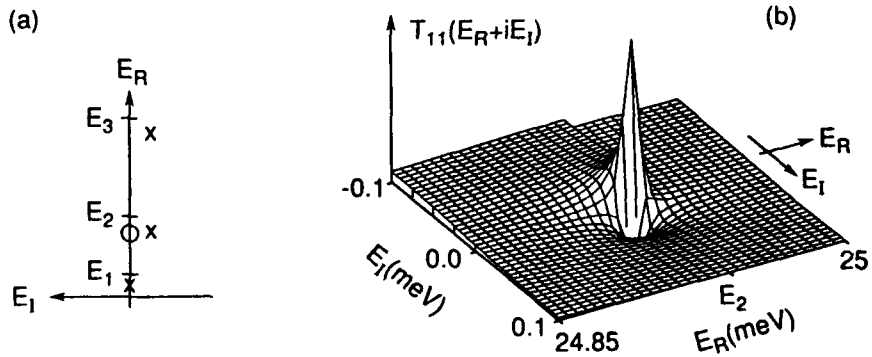


Fig. 2. Transmission coefficient  $T_{11}(E)$  as a function of complex energy showing (a) the pole positions (X's) and (b) details of the pole and zero near  $E = E_2$ .

The poles of  $T_{11}$  for the donor impurity are plotted in Fig. 2(a). The single 'donor level' pole ( $E_R < E_1$  and  $E_I = 0$ ) does not decay with time, while the 'quasi-donor level' poles, associated with the higher lying confinement subbands ( $E_1 < E_R$  and  $E_I < 0$ ), decay at a rate  $|E_I|/\hbar$ . The temporal decay of these 'quasi-donor levels' occurs because the levels are degenerate in energy with and coupled to propagating waveguide channels, so that particles can leak out through the open ends of the waveguide. And in contrast to resonant tunneling, where the transmission coefficient is maximum near the pole of  $T(E)$ , the transmission coefficient through an attractive impurity in waveguide passes through a minimum near the 'quasi-donor level' pole (Fig. 2(b)).

The transmission coefficients and their complex energy poles can be calculated analytically for a simple two-subband model of a waveguide (Bagwell 1990b). The exact current transmission amplitude  $t_{11}$  in this model, where  $T_{ij} = t_{ij}t_{ij}^*$ , is

$$t_{11} = \frac{1 + (mV_{22}/\hbar^2\kappa_2)}{1 + (mV_{22}/\hbar^2\kappa_2) + i(mV_{11}/\hbar^2k_1)} \quad (4)$$

Here  $m$  is the electron effective mass,  $E_1$  and  $E_2$  the first and second confinement subband energies, the wavevector  $k_1$  is determined from  $E - E_1 = \hbar^2 k_1^2/2m$  and the evanescent wavevector  $\kappa_2$  is found from  $E_2 - E = \hbar^2 \kappa_2^2/2m$ . The coupling constants are  $V_{22} = \gamma|\chi_2(y_i)|^2$  and  $V_{11} = \gamma|\chi_1(y_i)|^2$ , where  $\chi_1(y_i)$  and  $\chi_2(y_i)$  are the normal mode wavefunctions evaluated at the lateral impurity position  $y_i$ .

Expanding the square roots in  $\kappa_2$  and  $k_1$ , which is valid if the real part of the pole ( $E_R$ ) is not too near a subband edge and the imaginary part of the pole ( $E_I$ ) is not too large, one finds the 'donor level' pole ( $0 = 1/t_{11}$ ) at a purely real energy

$$E_R \simeq E_1 - \frac{mV_{11}^2}{2\hbar^2} \quad , \quad E_I = 0 \quad , \quad (5)$$

and the 'quasi-donor level' pole ( $0 = 1/t_{11}$ ) at the complex energy

$$E_R \simeq E_2 - \frac{mV_{22}^2}{2\hbar^2} \equiv E_2 - E_B \quad , \quad E_I \simeq -\frac{mV_{12}^2}{2\hbar^2} \left[ \frac{4E_B}{E_2 - E_1} \right]^{1/2} \quad , \quad (6)$$

where  $V_{12}^2 = V_{11}V_{22}$ . The imaginary part ( $E_I$ ) of the 'quasi-donor level' pole is proportional to the coupling strength  $V_{12}^2$  between the lowest two subbands as expected. We have noted similar transmission resonance phenomena for two attractive impurities in a waveguide (Kumar 1991a), where the quasi-donor levels form 'molecular' bound states rather than 'atomic' ones.

### 3. STRONG ELECTRON LOCALIZATION IN A WAVEGUIDE

As more impurities are added to the waveguide, the electronic wavefunctions are believed to become localized by quantum diffusion to a region of size  $\xi$  along the  $x$ -direction. For a wire having a fixed impurity density, one can probe this length  $\xi$  by studying the variation of conductance  $G(E, L)$  versus wire length  $L$ , also called the 'scaling' behavior of  $G(L)$ . It is difficult to extract information about  $\xi$  from a single wire, since the conductance fluctuates rapidly with energy or length. To eliminate these fluctuations, we average the conductance over many different random arrangements of the disorder to

obtain the 'ensemble averaged' conductance  $\langle G \rangle$ . This  $\langle G \rangle$  corresponds physically to measuring the conductance of an array of many independent narrow wires in parallel. The mean conductance  $\langle G(L) \rangle$  for different Fermi energies near  $E_2$  and  $E_3$  is shown in Fig. 3, where the point scattering potential is identical to Kumar (1991b). It is believed that  $\langle G \rangle$  should follow the exponential scaling law  $\langle G \rangle = G_0 \exp(-L/\xi)$ , and we find  $\langle G \rangle$  indeed decreases roughly exponentially with length  $L$ . However, the scaling behavior of  $\langle G(L) \rangle$  in a multi-subband wire depends strongly on the type of impurities present. In Fig. 3(a), where all the impurities are acceptors, there is an abrupt decrease in the localization length  $\xi$  as the Fermi energy moves into a new subband. This abrupt variation of  $\xi$  with Fermi energy is not observed in Fig. 3(b) where half the impurities are donors. Fig. 3 also appears to be in conflict with the estimate of Thouless (1977), who argued that  $\xi = N\ell$  in a wire with  $N$  occupied subbands and mean free path  $\ell$ . Indeed, the localization length  $\xi$  does not appear to be a strong function of the number of propagating channels, as evidenced by the small change in slope as the Fermi energy moves from the second subband ( $0.9E_2$ ) into the third subband ( $0.9E_3$ ).

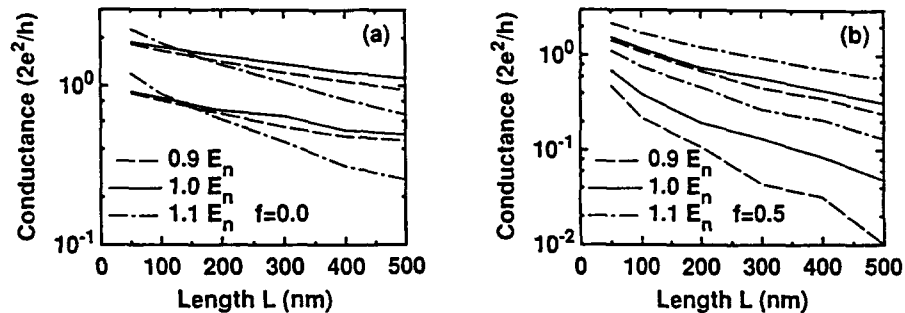


Fig. 3.  $\log \langle G \rangle$  versus wire length  $L$  for a parallel array of 500 disordered quantum wires when the impurities are (a) all acceptors ( $f=0.0$ ) and (b) half donors ( $f=0.5$ ).

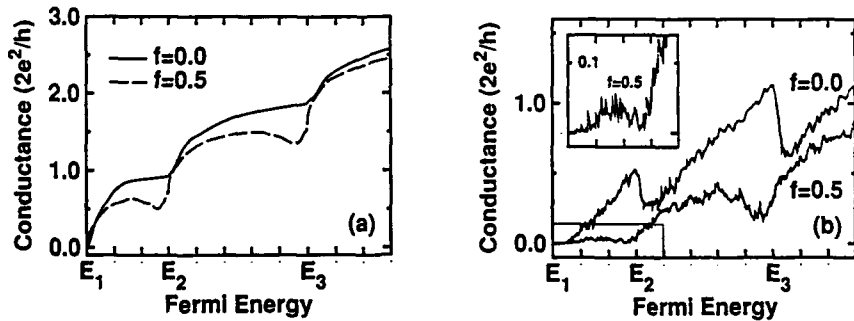


Fig. 4. Conductance through a parallel array of 100 (a) short quantum wires and (b) long quantum wires (Kumar 1991b). A fraction  $f$  of all impurities are donors.

The abrupt variation of localization length near a subband crossing in Fig. 3 (a) produces an unusual structure in the conductance versus Fermi energy shown in Fig. 4(b): A sharp drop in the conductance occurs just after a subband crossing in long quantum wires when mainly acceptor impurities are present. The conductance of an array of short quantum wires having much less disorder, shown in Fig. 4(a), is qualitatively similar to

the conductance through a single impurity from Fig. 1(a). Fig. 3 proves that there is no unique 'ensemble averaged conductance' of a disordered quantum wire. The ensemble averaged conductance versus Fermi energy depends strongly on the type and amount of disorder present in the wire. These results are very different from the conductance of a single moded wire, where  $\langle G(L) \rangle$  does not depend on the impurity type.

#### 4. TRANSMISSION THROUGH AN OSCILLATING POTENTIAL

Transmission through oscillating potentials can simulate electrical conduction in the presence of phonons, light, or applied AC voltages. An electron at energy  $E$  incident on a potential oscillating at frequency  $\omega$  produces transmitted and reflected 'sidebands' at energies  $E_n = E + n\hbar\omega$ , where  $n = 0, \pm 1, \pm 2$ , etc. To explore the physics of such an oscillator, we consider (Bagwell 1992) the electron transmission through a one-dimensional potential having both a static and oscillating part,  $V(x, t) = (V_s + V_d \cos(\omega t))\delta(x)$ . We compute the total electron transmission  $T(E) = \sum_n T_{n0}(E)$ , summed over all propagating sideband channels  $n$ . (Channel '0', at  $E = E_0$ , is the only incoming channel.)

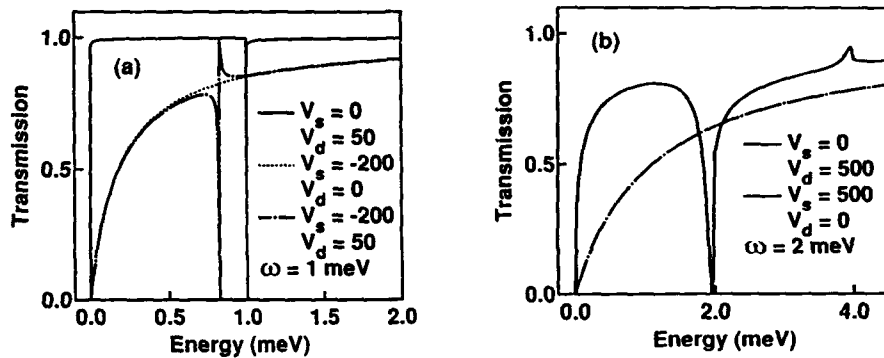


Fig. 5. Transmission through (a) a weak oscillator (both with and without a static attractive potential) and (b) through a stronger oscillating barrier (Bagwell 1992).

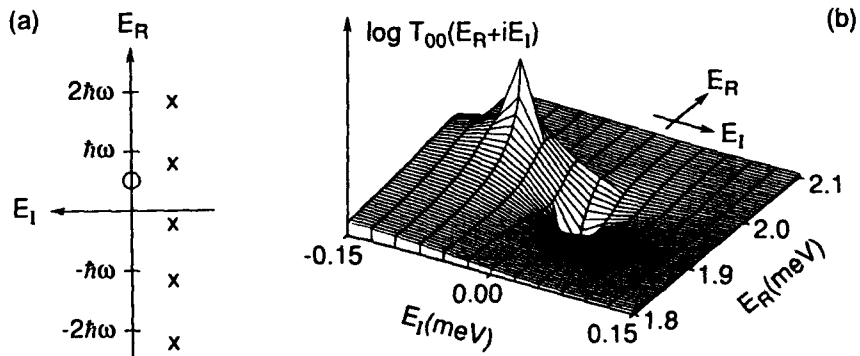


Fig. 6.  $T_{00}(E)$  through the stronger oscillator showing (a) pole positions and (b) detail near the  $E = \hbar\omega$  channel opening for  $V_d = 500$  and  $V_s = 0$ , corresponding to Fig. 5(b).

Fig. 5(a) describes  $T(E)$  through a weak oscillator. A sharp drop in transmission is observed when the first emitted sideband channel opens at  $E = \hbar\omega$ , but not when higher sideband channels open. If a static attractive potential well is combined with

the weak oscillator, a Fano-type (Fano 1961) transmission resonance appears when the incident electron is  $\hbar\omega$  above a bound state in the static attractive potential (Cai 1990). Fano resonances were originally observed in atomic physics (Madden 1963), and may also exist in GaAs/AlGaAs resonant tunneling structures due to the  $\Gamma - X$  valley coupling (Ko 1988). For a weak oscillator combined with a static repulsive barrier (not shown), we recover the results of Gelfand (1989).

For a stronger oscillator shown in Fig. 5(b), the transmission zero has moved lower in energy ( $E < \hbar\omega$ ), indicating the formation of a quasi-bound state. A classical particle can be trapped in an oscillating potential, so that the Bohr-Sommerfeld quantization rules applied to its classical trajectory would produce a quantum mechanical bound state. This idea is nearly correct, except that a quantum mechanical particle can gain enough  $\hbar\omega$  energy quanta to escape from the oscillator.

The complex energy poles of  $T_{00}(E)$  are shown in Fig. 6(a). These poles all lie off the real energy axis, indicating damping. Indeed, for a weak (small  $V_d$ ) oscillator operating at high frequency, we find these 'quasi-bound' states at

$$E_R \simeq n\hbar\omega \quad , \quad E_I \simeq -\frac{1}{16\hbar\omega} \left[ \frac{mV_d^2}{2\hbar^2} \right]^2 \quad , \quad (7)$$

so that lower frequencies or stronger oscillators increase the escape rate. A transmission zero exists next to the pole near  $E \simeq \hbar\omega$  (Fig. 6(b)), similar to the donor in a waveguide.

## 5. CONCLUSION

Transmission resonances for the donor in a waveguide and the oscillating barrier differ in detail, due to different couplings between their bound states and the continuum, but both scattering potentials trap electrons in cutoff channels near the defect. By locating the complex energy poles of  $T(E)$ , one can find the natural eigenstates of the scattering potential. Locally attractive potentials are required to form these poles, and the oscillating barrier is a special case where the potential is attractive over half its cycle. When the oscillator is combined with a strong static repulsive potential its transmission resonances disappear. It appears a basic feature of multiple channel quantum scattering problems is that, even when the Fermi energy is large, attractive versus repulsive potentials give rise to a very different energy dependence of the transmitted flux.

**Acknowledgements** - We thank Supriyo Datta and Muhammad Alam for discussion.

Bagwell P F 1990a *Phys. Rev. B* **41** 10354  
 Bagwell P F 1990b *J. Phys: Condens. Matter* **2** 6179  
 Bagwell P F and Lake R 1992 preprint  
 Cai W, Hu P, Zheng T F, Yudanin B, and Lax M 1990 *Phys. Rev. B* **41** 3513  
 Chu C S and Sorbello R S 1989 *Phys. Rev. B* **40** 5941  
 Fano U 1961 *Phys. Rev.* **124** 1866  
 Gelfand B Y, Schmitt-Rink S, and Levi A J F 1989 *Phys. Rev. Lett.* **62** 1683  
 Ko D Y K and Inkson J C 1988 *Semicond. Sci. Tech.* **3** 791  
 Kumar A and Bagwell P F 1991a *Phys. Rev. B* **43** 9012  
 Kumar A and Bagwell P F 1991b *Phys. Rev. B* **44** 1747  
 Madden R P and Codling C 1963 *Phys. Rev. Lett.* **10** 516  
 Oppenheim A V and Willsky A S 1983 *Signals and Systems* (London, Prentice-Hall)  
 Thouless D J 1977 *Phys. Rev. Lett.* **39** 1167

## Plasmon-phonon coupling and depolarization effects in quantum well wires

L. Wendler and R. Haupt<sup>(1)</sup>

Institut für Theoretische Physik, Technische Universität Merseburg, Geusaer Straße,  
D/O-4200 Merseburg, Germany

<sup>(1)</sup>Institut für Festkörpertheorie und Theoretische Optik, Friedrich-Schiller-Universität  
Jena, Max-Wien-Platz 1, D/O-6900 Jena, Germany

**ABSTRACT:** The coupled plasmon-phonon collective excitations of a quantum well wire are investigated in the random-phase approximation. It is obtained that in dependence on the density of the quasi-one-dimensional electron gas of a parabolic quantum well wire the depolarization shift of the (1-0) intersubband plasmon increases. For an effective parabolic potential the frequency of this mode increases with increasing density of the electron gas whereas for an initial parabolic potential it is pinned to the bare harmonic oscillator frequency.

Modern integrated circuits are increasingly based on semiconductor devices in which the electronically active channel is an electron gas with reduced dimensionality. This reduced dimensionality is caused in semiconductor microstructures by a confinement potential. In a quantum well wire (QWW) the confinement potential is in two spatial directions and the width of the well is in the order of the de Broglie wavelength of the electrons. Hence, the collective and single-particle excitations of the quasi-one-dimensional electron gas (Q1DEG) are splitted into intra- and intersubband excitations (Li and Das Sarma 1989, Cui et al 1989, Chaplik 1989, Gold and Ghazali 1990, Mendoza and Schaich 1991, Hu and O'Connell 1991, Wendler et al 1991, Haupt et al 1991). One important collective excitation of the Q1DEG measured with far-infrared (FIR) spectroscopy is the intersubband plasmon (Hansen et al 1987, Demel et al 1991). Such an excitation is connected with electron motion between different subbands. In general, caused by many-particle effects, the optical intersubband transition energies are shifted from the subband separation energies. But it was shown by Brey, Johnson, and Halperin (1989) that in an initial ideal parabolic QW the FIR absorption spectrum is independent of the number of electrons in the well, and also independent of the electron-electron interaction. This is called the generalized Kohn's theorem.

In this paper we calculate the dispersion curves of the intersubband plasmons and plasmon-phonons. Special attention is directed to the depolarization shift which is the difference between the energy  $\hbar\omega_p^{LL'}(q_z)$  of the (L-L') intersubband plasmon and the subband separation energy  $E_{LL'} = \hbar\Omega_{LL'} = \mathcal{E}_L - \mathcal{E}_{L'}$ . Because of the spatial dispersion the considered problem deviates from the originally generalized Kohn's theorem. We study the QWW by a model in which the electrons are confined in a zero thickness x-y plane along the z-direction at  $z=0$ . In the y-direction a parabolic quantum well is

assumed. Following in the effective-mass approximation the one-electron envelope wave function  $\xi_L(y)$  and the one-electron subband energy  $\mathcal{E}_L$  is given by the one-dimensional effective Schrödinger equation, where the electron is confined in an effective potential  $V_{\text{eff}}(y)$ . The lateral effective confinement potential  $V_{\text{eff}}(y)$  is a sum of the initial potential  $V_0(y)$  and the Hartree-potential  $V_H(y)$ . It is necessary to distinguish two different cases for this effective potential: (i) The first case is realized in semiconductor microstructures with electrostatic confinement. It is shown by the self-consistent solution of Schrödinger and Poisson equation (Laux et al 1988) that the resulting effective self-consistent confinement potential  $V_{\text{eff}}(y)$  is parabolic for small electron densities. At higher electron densities  $V_{\text{eff}}(y)$  changes from a parabolic shape to a square-well-like one. (ii) The second case is realized in semiconductor microstructures with an initial ideal parabolic confinement potential  $V_0(y) = m\Omega^2 y^2/2$ . Electrons, which arise from donor impurities located away from the quantum well, enter the well and screen this initial parabolic potential changing the shape of the resulting potential  $V_{\text{eff}}(y)$ . The dispersion relation of the collective excitations of the Q1DEG, intra- and intersubband plasmons, follows from Wendler et al (1991)

$$\sum_{L,L'} (\delta_{LL_1} \delta_{L'L_2} - W_{L_1 L_2 L' L}(q_x) P_{L L'}^{(1)}(q_x, \omega)) W_{L' L_3 L_4}^{SC}(q_x, \omega) = 0 \quad (1)$$

where  $W_{L_1 L_2 L_3 L_4}^{SC}(q_x, \omega)$  is the screened interaction potential,  $W_{L_1 L_2 L_3 L_4}(q_x, \omega)$  is the bare interaction potential which is a sum of the direct Coulomb potential and the bare electron-phonon interaction potential. To the bare electron-phonon interaction potential we only include 3D bulk longitudinal-optical (LO) phonons.  $P_{L L'}^{(1)}(q_x, \omega)$  is the RPA polarization function of the Q1DEG. For numerical work we have chosen a  $\text{GaAs}-\text{Ga}_{1-x}\text{Al}_x\text{As}$  QWW with  $\hbar\Omega = 2\text{meV}$ . Due to the symmetric effective potential  $V_{\text{eff}}(y)$  the algebraic equation system (1) splits into the dispersion relation of symmetric intersubband and intrasubband plasmons and the dispersion relation of antisymmetric intersubband plasmons. Here we are only concerned with the second type of collective and single-particle excitations.

In Fig. 1 the full RPA dispersion curves of the antisymmetric modes are plotted, i.e. dispersion curves of the mixed (1-0)-(3-0) coupled plasmon-phonons. The dispersion curves are plotted for case (ii). In the case (ii) of an initial ideal parabolic quantum well, the effective confinement potential must be calculated by solving self-consistently the coupled Schrödinger and Poisson equation. With the resulting eigenfunctions and eigenvalues the dispersion relation is to be solved. For the case (i) the eigenfunctions are given by the harmonic oscillator ones. The results for the case (i) can be considered in connection with case (ii) as the approximation  $V_H(y) = 0$ , i.e. the ground-state is not renormalized by many-particle effects. It is seen that we have two intersubband plasmon branches  $\omega_p^{10*}$  and  $\omega_p^{30*}$ . There exist four single-particle intersubband continua. If one compares Fig. 1 with the case (i) one can see that the renormalization of the ground state due to many-particle effects doesn't result in a dramatically change of the mode spectrum concerning the dependence on the wave vector  $q_x$ . Only the frequency scale is shifted. We note that there exists an additional  $\omega_p^{10*}$ -like mode in the region between the boundaries  $\omega_4^{10}$ ,  $\omega_3^{10}$  and  $\omega_2^{21}$  which is free of Landau damping. For typical QWW's the subband separation energy ( $\hbar\Omega = 2\text{meV}$ ) is much smaller than the energy of the LO phonon ( $\hbar\omega_{LO} = 36.2\text{meV}$ ). Hence, dynamical plasmon-phonon coupling plays nearly no role for the collective excitations under consideration.

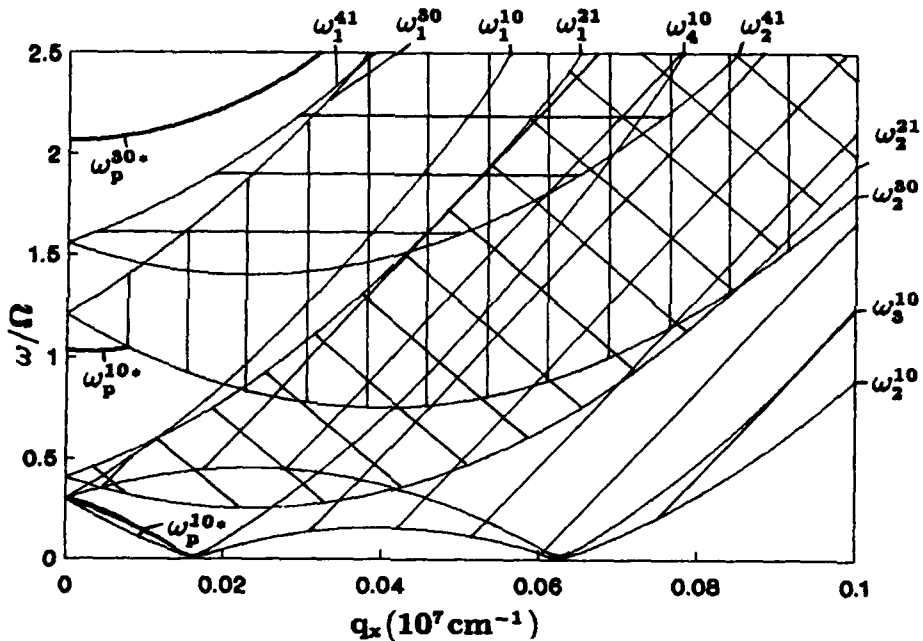


Fig. 1. Dispersion relation of the mixed (1-0)-(3-0) coupled plasmon-phonons (thick lines) for the case (ii) where two subbands are populated ( $n_{1DEG} = 0.04 \times 10^7 \text{ cm}^{-1}$ ). The boundaries of the single-particle continua (shaded regions) are given by  $\omega_1^{LL'}$ ,  $\omega_2^{LL'}$ ,  $\omega_3^{LL'}$ ,  $\omega_4^{LL'}$  as defined by Wendler et al (1991).

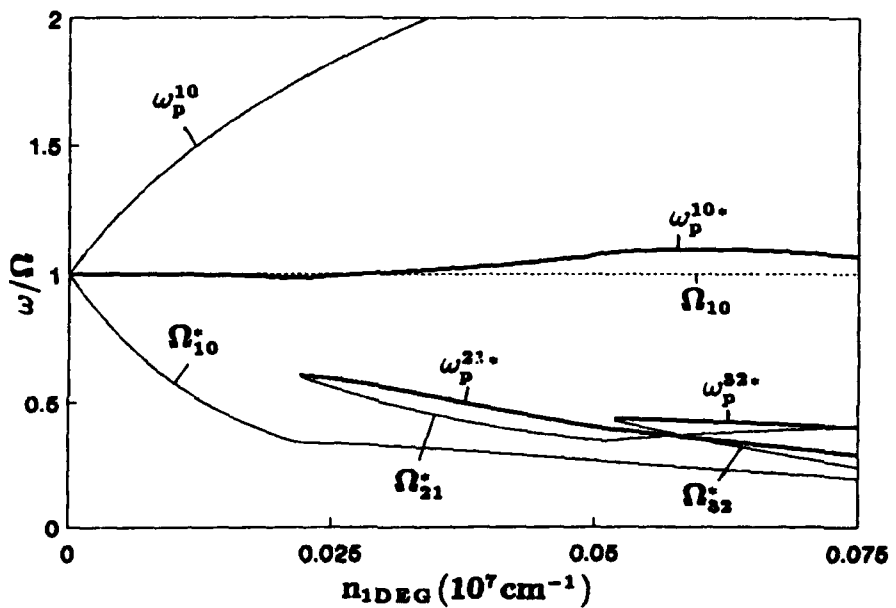


Fig. 2. Frequencies of the coupled collective (case (i):  $\omega_p^{LL'}$ ; case (ii):  $\omega_p^{LL'*}$ ) and single-particle (case (i):  $\Omega_{LL'}$ ; case (ii):  $\Omega_{LL'}^*$ ) antisymmetric intersubband resonances for  $\hbar\Omega = 2 \text{ meV}$  and a wave vector  $q_x \approx 0$ .

Now we look for the depolarization shift. In the following we investigate the energy difference between the energy of the (L-L') intersubband plasmon  $\hbar\omega_p^{LL'}(q_x)$  and the subband separation energy  $\hbar\Omega_{LL'}$  for the antisymmetric intersubband resonances:  $L \rightarrow L + (2n + 1)$ . As shown recently by Haupt et al (1991) for the case (i) where the effective confinement potential is parabolic, the strong interaction between the several excitations leads to the appearance of bands, each of them consists of M-1 resonances, where M is the number of populated subbands. These bands occur near the corresponding single-particle transition frequency. Hence, the depolarization shift of these coupled excitations is very small. Additionally, from each band one separate curve is splitted, corresponding to the mode  $\omega_p^{0+(2n+1),0}$  for lower electron densities, where only the lowest subband L=0 is occupied. This is to be seen in Fig.2 for the (1-0) intersubband plasmon  $\omega_p^{10}$ . In the case (ii) where the initial confinement potential is parabolic the situation is changed. In this case both, the single-electron energies and the frequencies of the collective excitations are shifted by many-particle effects. Consequently we have to define the depolarization shift between the renormalized subband separation energy  $\hbar\Omega_{LL'}^*$  and the corresponding energy of the renormalized (L-L') intersubband plasmon  $\hbar\omega_p^{LL'*}$ . In Fig.2 the frequencies of the (1-0), (2-1) and (3-2) intersubband plasmons and the corresponding subband separation frequencies for the case (ii) comparing to the (1-0) intersubband plasmon for case (i) are plotted. The calculation is done for small but finite wave vectors. It is to be seen that for the fundamental (1-0) transition the depolarization shift increases with increasing density of the Q1DEG. This is valid for both cases (i) and (ii). But the basic difference between the case of an effective parabolic confinement potential and an initial parabolic confinement potential is that in the first case the frequency of the intersubband plasmon increases with increasing electron density. In the second case this frequency is nearly fixed on the initial subband separation frequency  $\Omega$ . The higher resonances start at that densities, where the corresponding subband is occupied and they are also shifted to lower frequencies.

We note that the generalized Kohn's theorem is an exact result for optical dipole transitions in the FIR region. Here we have investigated the depolarization shift of the antisymmetric collective intersubband plasmons. Hence, there are two basic differences to the validity of Kohn's theorem: (i) We have a finite wave vector  $q_x$  and (ii) we solve the ground-state problem in the Hartree appoximation, neglecting exchange and correlation effects and we have therefore not the exact renormalized ground-state properties.

#### REFERENCES:

Brey L, Johnson N F, and Halperin B I 1989 Phys. Rev. B40 10647  
 Chaplik A V 1989 Superlatt. and Microstructures 6 329  
 Cui H L, Lu X J, Horing N J M, and Lei X L 1989 Phys. Rev. B40 3443  
 Demel T, Heitmann D, Grambow P, and Ploog K 1991 Phys. Rev. Lett. 66 2657  
 Gold A and Ghazali A 1990 Phys. Rev. B41 7626  
 Hansen W, Horst H, Kotthaus J P, Merkt U, Sikorski Ch, and Ploog K 1987 Phys. Rev. Lett. 58 2586  
 Haupt R, Wendler L, and Pechstedt R 1991 Phys. Rev. B44  
 Hu G Y and O'Connell R F 1991 Phys. Rev. B44 3140  
 Laux S E, Frank D J, and Stern F 1988 Surface Sci. 196 101  
 Li Q and Das Sarma S 1989 Phys. Rev. B40 5860  
 Mendoza B S and Schaich W L 1991 Phys. Rev. B43 9275  
 Wendler L, Haupt R, and Pechstedt R 1991 Phys. Rev. B43 14669

## Magnetophonon resonances in quantum wires

N. Mori, H. Momose and C. Hamaguchi

Department of Electronic Engineering, Osaka University,  
2-1, Yamadaoka, Suita City, Osaka 565, Japan

**ABSTRACT:** Magnetophonon resonances are studied in quantum wires with parabolic confinement potential. The conductivity  $\sigma_{xx}$  in quantum wires consists of two types of contributions; one is related to the current carried by electron hopping motion between the localized cyclotron orbits,  $\sigma_{ep}$ , and the other is caused by the effect of the confinement potential to flow electrons along the wire,  $\sigma_{po}$ . Magnitude of both the conductivity and the oscillatory part of the conductivity is calculated as a function of the strength of the confinement potential. In the case of strong confinement, *i.e.* in narrow quantum wires,  $\sigma_{xx}$  is found to be dominated by  $\sigma_{po}$ , resulting minima of the oscillatory part of the conductivity at resonances.

### 1. INTRODUCTION

Recent developments in microfabrication technology have made it possible to produce electron confined structures, namely, quantum wires, in which new quantum effects are expected to occur because the size of the structures is the order of the de Broglie wavelength of electrons. The structures with high electron mobility at low temperatures are proposed to have potential device applications, on the grounds that the large momentum transfer of back-scattering reduces the impurity scattering rate (Sakaki 1980). At high temperatures, however, optical-phonon scattering is dominant in compound semiconductors commonly used in microfabrication, and we have to know about the role of electron-optical-phonon interaction in such structures to improve the device performance. The magnetophonon resonance (MPR) consists of the oscillatory variation of conductivity with high magnetic field and it is known to be a powerful tool for the study of electron-optical-phonon interaction in semiconductors. Over the past few decades a considerable number of studies have been made on MPR in three- or two-dimensional systems (Hamaguchi and Mori 1990). However only few attempts have so far been made to investigate MPR effects in quasi-one-dimensional electron gas (Q1DEG) systems. Vasilopoulos *et al.* (1989) have studied MPR in quantum wires with a parabolic confinement potential of frequency  $\Omega$  and their calculations revealed that the usual resonance condition  $\omega_0 = P\omega_c$  is modified by  $\omega_0 = P\tilde{\omega}_c$ , where  $P$  is an integer,  $\omega_0$  and  $\omega_c$  are the longitudinal-optical-phonon (LO phonon) frequency and cyclotron frequency, respectively, and  $\tilde{\omega}_c$  is given by  $(\omega_c^2 + \Omega^2)^{1/2}$ . Recently we have studied MPR of Q1DEG in the case of the strong confinement potential by using the model adopted by Vasilopoulos *et al.* and found that the transverse conductivity  $\sigma_{xz}$  consists of two types of contributions; one is related to the current carried by electron hopping motion between the localized cyclotron orbits through electron-phonon interaction, and the other is caused by the current carried by electron motion affected by the confinement potential (Mori *et al.*). The former,  $\sigma_{ep}$ , is directly proportional to the coupling constant  $\alpha$  of the electron-optical-phonon interaction, whereas the latter,  $\sigma_{po}$ , is found to be inversely proportional to  $\alpha$ . Therefore, at resonances,  $\sigma_{ep}$  exhibits maxima and  $\sigma_{po}$  exhibits minima.

In this paper we calculate the conductivity and its oscillatory part (the second derivative) in quantum wires as a function of the strength of the confinement potential and show how  $\sigma_{xx}$  changes with the width of the wire. We proceed as follows. First, model for quantum wires are shown, and the formula of the conductivity is derived using Kubo formula. These procedures are the same in our recent paper, but for the sake of completeness we describe them briefly. Then we calculate the magnitude of  $\sigma_{xx}$  and its second derivative as a function of the strength of the confinement potential  $\Omega$  to show how  $\sigma_{xx}$  in narrow quantum wires is different from that in wide quantum wires or two-dimensional systems.

## 2. FORMALISM

We employ a simple model for a quantum wire as treated by Vasilopoulos *et al.*, in which two-dimensional electron gas formed in heterostructures are confined by the narrow-gates or split-gates, and electrons are free along only one direction. We assume that a heterointerface is normal to the  $z$  axis, and that the confinement in the  $y$  direction is characterized by a parabolic potential of frequency  $\Omega$ . A magnetic field  $\mathbf{B}$  is applied along the  $z$  axis. Using the Landau gauge  $\mathbf{A} = (-By, 0, 0)$ , the one-electron Hamiltonian  $\mathcal{H}_e$ , eigenstates  $|\lambda\rangle$  and eigenvalues  $\varepsilon_\lambda$  are written as

$$\mathcal{H}_e = (\mathbf{p} + e\mathbf{A})^2/2m^* + V(y) + H(z), \quad (1)$$

$$(\mathbf{r}|\lambda) = (\mathbf{r}|Nks) = e^{ikx} \phi_N(y - \tilde{Y}) \xi_s(z), \quad (2)$$

$$\varepsilon_\lambda = \varepsilon_{Nks} = (N + \frac{1}{2})\hbar\tilde{\omega}_c + \hbar^2 k^2/2\tilde{m}^* + \varepsilon_s, \quad (3)$$

where  $V(y) = \frac{1}{2}m^*\Omega^2 y^2$ ,  $H(z)$  is the confinement potential in the  $z$  direction,  $N$  is the Landau-level index,  $k$  is the wave vector in the  $x$  direction,  $s$  is the subband index associated with the quantized  $z$ -motion,  $\tilde{\omega}_c = (\omega_c^2 + \Omega^2)^{1/2}$  with  $\omega_c = eB/m^*$ ,  $\tilde{Y} = (\omega_c/m^*\tilde{\omega}_c^2)\hbar k$  and  $\tilde{m}^* = m^*(\tilde{\omega}_c/\Omega)^2$ . The wave functions  $\phi_N(y)$  are well-known simple harmonic-oscillator-like solutions. In the present calculations we consider such a case that only the lowest subband ( $s = 0$ ) is occupied. The wave function  $\xi_0(z)$  is assumed to be  $|\xi_0(z)|^2 = \delta(z)$  for the sake of simplicity. This approximation, *i.e.* neglecting the form factor, introduces negligible error qualitatively, although it overestimates the electron-phonon interaction.

We evaluate the Kubo formula for the electrical conductivity  $\sigma_{xx}$ : (Mahan 1981)

$$\sigma_{xx} = -\lim_{\omega \rightarrow 0} \left[ \frac{\Im \pi(\omega + i0)}{\omega} \right], \quad (4)$$

where  $\pi(\omega)$  is the correlation function:

$$\pi(i\omega) = - \int_0^\beta d\tau e^{i\omega\tau} \langle T_\tau j_x(\tau) j_x^\dagger(0) \rangle, \quad (5)$$

and  $\beta = 1/kT$ . At high magnetic fields, the conductivity  $\sigma_{xx}$  is determined by the change in the center of cyclotron motion  $X$  (Kubo *et al.* 1965). Therefore  $\sigma_{xx}$  is calculated by Eqs. (4) and (5) with  $j_x$  equal to

$$j_x = -e \int \Psi^\dagger(\mathbf{r}) \dot{X} \Psi(\mathbf{r}) d^3r, \quad (6)$$

where  $\Psi(\mathbf{r})$  is the field operator for electrons. Since  $\dot{X}$  is determined by the gradient of potential along the  $y$  direction, the term  $\dot{X}$  for electrons in the quantum wires is caused by the following two factors. One is the electron-phonon interaction potential  $U_{ep}(\mathbf{r})$  and the other is the confinement potential  $V(y)$ . In other words, the term  $\dot{X}$  is given explicitly by the equation of motion and we have

$$\dot{X} = \frac{1}{eB} \frac{\partial U_{ep}(\mathbf{r})}{\partial y} + \frac{1}{eB} \frac{\partial V(y)}{\partial y}. \quad (7)$$

Since the cross-term between the electron-phonon part and the potential part vanishes in the correlation function, we can divide the conductivity into two parts as follows:

$\sigma_{xx} = \sigma_{ep} + \sigma_{po}$ , where the two terms on the right hand side correspond the respective contributions stated above.

### 3. RESULTS AND DISCUSSION

In the following we present numerical results for quantum wires of GaAs, in which we assume  $\hbar\omega_0 = 36.2\text{meV}$ ,  $\alpha = 0.07$  and  $m^* = 0.07m_0$ . In Fig. 1 we show  $\sigma_{ep}$  and  $\sigma_{po}$  as a function of cyclotron frequency  $\omega_c$  for  $T = 100\text{K}$ . The strength of the confinement potential  $\Omega$  is 1meV. We assume that width of the density of states  $\Gamma$  is 1meV and independent of the magnetic field. The conductivity is normalized by  $\sigma_0 = ne^2/\alpha\hbar\omega_0 m^*$ , where  $n$  is the electron density. The confinement potential is so weak that a small amount of electrons is affected by the confinement potential, and thus  $\sigma_{xx}$  is dominated by  $\sigma_{ep}$ . Therefore we find that the oscillatory structures are very similar to two-dimensional case, exhibiting maxima at resonances. However, the resonance is weaker in quantum wires, where some electrons can absorb optical-phonons at off-resonance condition and make a transition to an excited state. When the strength of the confinement potential becomes stronger, more and more electrons are forced to flow along the wire by the confinement potential and therefore the current is mainly carried by electrons affected by the confinement potential. We show the magnitude of conductivity as a function of  $\Omega$  at off-resonance condition of  $\omega_0 = 1.5\tilde{\omega}_c$  in Fig. 2. The magnitude of  $\sigma_{ep}$  decrease as  $\Omega$  increase, whereas  $\sigma_{po}$  increases. The crossover occurs around  $\Omega = 2\text{meV}$ . We have omitted the form factor of quantized  $z$ -motion as stated above, and if we take into account of the effect of the form factor, the crossover point moves to somewhat lower value.

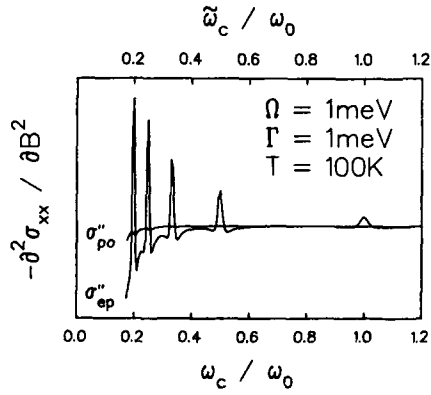


Fig. 1  $\sigma_{xx}$  as a function of  $\omega_c$  for  $T = 100\text{K}$ ,  $\Gamma = 1\text{meV}$  and  $\Omega = 1\text{meV}$ .

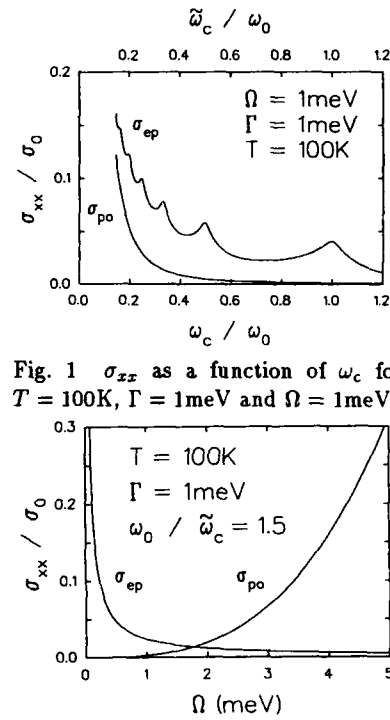


Fig. 2 The magnitude of  $\sigma_{xx}$  as a function of  $\Omega$  at off-resonance condition. If we take into account of the effect of the form factor, the crossover point moves to somewhat lower value.

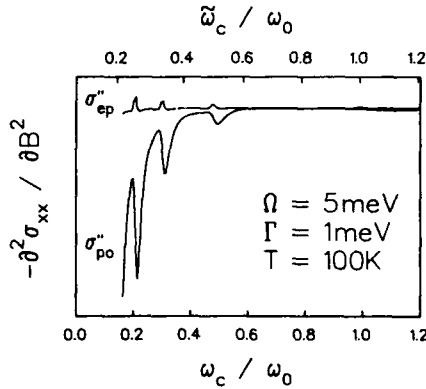


Fig. 3 The second derivative of  $\sigma_{po}$  and  $\sigma_{ep}$  as a function of  $\omega_c$  for  $T = 100\text{K}$ ,  $\Gamma = 1\text{meV}$  and  $\Omega = 1\text{meV}$ .

Fig. 4 The same as Fig. 3 for  $\Omega = 5\text{meV}$ .

Next we calculate the second derivative of the conductivity to see the oscillatory structure clearly. In Figs. 3 and 4 we show the second derivatives of  $\sigma_{po}$  and  $\sigma_{ep}$  as a function of  $\omega_c$ . For a weak confinement potential as shown in Fig. 3, the current mainly carried by the electron hopping motion ( $\sigma_{ep}$ ), resulting in a feature similar to the three- or two-dimensional systems. For strong confinement potential as shown in Fig. 4, the second derivative of  $\sigma_{xx}$  is also dominated by  $\sigma_{po}$ , resulting in a minima at resonances. The conductivity is expected to change from maxima to minima as the wire width is decreased. This crossover is also induced by the change in magnetic field under a certain condition of confinement potential. For example, in Fig. 4, the  $P = 4$  peak of  $\sigma''_{po}$  is one order of magnitude greater than that of  $\sigma''_{ep}$  although the  $P = 2$  peaks have almost the same magnitude. It is for this reason that electrons tend to localize with increasing the magnetic field and at sufficiently high magnetic field the current is mainly carried by the electron hopping motion with electron-phonon interaction.

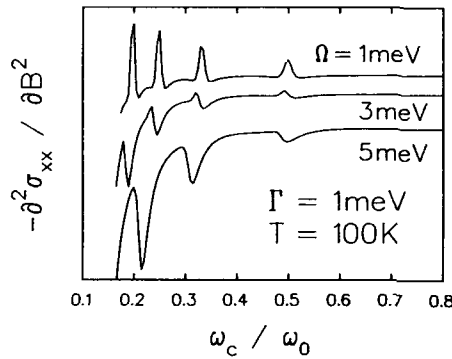


Fig. 5 The second derivative of  $\sigma_{xx}$  as a function of  $\omega_c$  for  $T = 100K$  and  $\Gamma = 1meV$ .

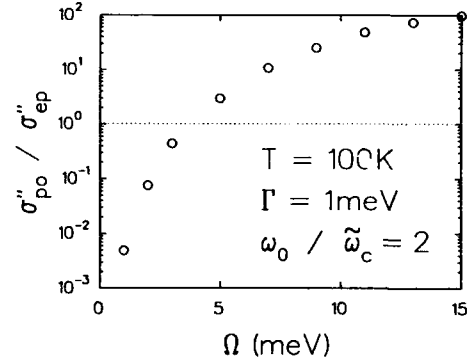


Fig. 6 The ratio of the peak height of the second derivative of  $\sigma_{po}$  and  $\sigma_{ep}$  as a function of  $\Omega$  at resonance condition.

Finally we show the second derivative of total conductivity as a function of  $\omega_c$  for different confinement potentials (Fig. 5) and the ratio of the peak height of the second derivative of two types of contributions as a function of  $\Omega$  (Fig. 6) to see how MPR peaks converts from maximum to minimum. The MPR peak of  $P = 2$  converts from maximum to minimum around  $\Omega = 4meV$  neglecting the form factor. The crossover points expected to move to higher values as temperature raises or magnetic field increases. In order to give a definite crossover point, however, we have to perform more elaborate calculations with appropriate confinement potential and electron states.

This work was supported in part by a Grant-in-Aid for Scientific Research on Priority Area "Electron Wave Interference Effects in Mesoscopic Structures" from the Ministry of Education, Science and Culture.

#### REFERENCES

Hamaguchi C and Mori N 1990 *Physica B* **164** 85, and references therein.  
 Kubo R, Miyake S.J and Hashitsume N 1965 *Solid State Physics*, edited by Seitz F and Turnbull D (Academic, New York) Vol. 17 p. 279.  
 Mahan G.D 1981 *Many-Particle Physics* (Plenum, New York).  
 Mori N, Momose H and Hamaguchi C, to be published in *Phys. Rev. B*.  
 Sakaki H 1980 *Jpn. J. Appl. Phys.* **19** L735.  
 Vasilopoulos P, Warmenbol P, Peeters F.M and Devreese J.T *Phys. Rev. B* **40** 1810.

## The influence of the Coulomb interaction on the electronic spectrum of quantum dots

W. Häusler and B. Kramer

Physikalisch-Technische Bundesanstalt Braunschweig  
Bundesallee 100, 3300 Braunschweig F. R. G.

January 22, 1992

### Abstract

The spectral properties of up to *four* interacting electrons confined within a quasi-one dimensional system of finite length are determined by numerical diagonalization. The ground state energy as a function of the number of the electrons and the lengths of the system is investigated. The energetically lowest lying excitations are identified with vibrational and tunneling modes of the charge distribution. The limits of a dilute, Wigner-type arrangement of the electrons, and a dense, more homogeneous distribution are discussed.

## 1 Introduction

Interaction effects play a crucial role in the understanding of the electric transport in very small condensed matter systems [1]. Most prominent are the Coulomb blockade and the single-electron oscillations in quantum mechanical tunneling of electrons through very small tunnel junctions [2], and the resonance-like oscillations of the conductance of quantum dots at milli-Kelvin temperatures [3]. They are commonly discussed in terms of the tunneling resistances and capacitances [4, 5]. However, the microscopic justification of the latter is not obvious [6, 7].

One possibility to investigate whether or not a capacitance can be defined for small systems is to compare the quantum mechanical ground state energy  $E_0$  of several,  $N$ , interacting confined electrons with the charging energy of a capacitor. In this paper we present results for  $E_0$  obtained by numerical diagonalization of the corresponding Hamiltonian. In contrast to previous work for harmonic confinement [8, 9] which was restricted to  $N \leq 2$  we consider rectangular confinement and  $N \leq 4$ .

In addition we discuss the spectral properties, especially in the asymptotic regions of low (Wigner electron lattice) and high density (almost homogeneous charge distribution). We identify two kinds of elementary excitations, namely vibrational and tunneling modes that are related to the Coulomb repulsion, and the exchange interaction, respectively.

We conclude from our microscopic results that for the system parameters realized in inversion layer based quantum dots the quantum mechanics of the electron-electron interaction cannot be neglected.

## 2 Interacting electrons in a square well potential

We consider  $N$ -electrons within a 1D square well of length  $L$ . We use the interaction potential

$$V(x, x') \propto \frac{1}{\sqrt{(x - x')^2 + \lambda^2}}. \quad (1)$$

which behaves Coulombically at large distances.  $\lambda$  is a measure for the width of the electron wave functions in transversal direction. For most of our results  $\lambda/L = 2 \cdot 10^{-4} \ll 1$ . Then, the energy eigenvalues of the Hamiltonian

$$H = E_H \frac{a_B}{L} \left( \frac{a_B}{L} H_0 + H_I \right) \quad (2)$$

depend only weakly on  $\lambda$ .  $E_H = e^2/a_B$  is the Hartree energy,  $a_B = \epsilon \hbar^2/m e^2$  the Bohr radius,  $\epsilon$  the relative dielectric constant and  $m$  the electron mass. The relative importance of the the kinetic energy of the electrons within the square well,

$$H_0 = \sum_{n,\sigma} \epsilon_n c_{n,\sigma}^\dagger c_{n,\sigma} \quad (3)$$

( $\epsilon_n \propto n^2$ ), and the interaction energy,

$$H_I = \sum_{n_1 \dots n_4, \sigma_1, \sigma_2} V_{n_4 n_3 n_2 n_1} c_{n_4 \sigma_1}^\dagger c_{n_3 \sigma_2}^\dagger c_{n_2 \sigma_2} c_{n_1 \sigma_1} \quad (4)$$

changes with the system length. The total electron spin  $S$  is conserved. All eigenvalues have degeneracy  $2S + 1$ .

The interaction matrix elements  $V_{n_4 n_3 n_2 n_1}$  are real, and do not depend on the spin state  $\sigma$ . They fulfill the symmetry relations  $V_{n_4 n_3 n_2 n_1} = V_{n_4 n_2 n_3 n_1} = V_{n_1 n_3 n_2 n_4} = V_{n_3 n_4 n_1 n_2}$ . Furthermore,  $V_{n_4 n_3 n_2 n_1} = 0$  if  $\sum_i n_i = \text{odd}$ . For  $\lambda/L \ll 1$

$$V_{n_4 n_3 n_2 n_1} \approx -8\pi \int_0^\infty dq (\ln(q\lambda/L) + C) \hat{f}_{14}(q) \hat{f}_{23}(q) .$$

$\hat{f}_{ij}$  is the Fourier transform of the product  $\varphi_{n_i}^*(x) \varphi_{n_j}(x)$  of the one-electron eigenfunctions of  $H_0$ , and  $C = 0.577$  the Euler constant.

The numerical diagonalization requires a restriction of the number of considered one particle states  $c_{n\sigma}^\dagger |0\rangle$  to  $1 \leq n \leq M$ . Their anti-symmetrized products form a complete  $N$ -particle basis, which includes also the spin degree of freedom. It can easily been generated for arbitrary  $N$  using a binary code representation. Although the size of the Hamiltonian matrix, given by the binomial coefficient  $R = (2M)!/N!(2M - N)!$ , is rapidly increasing with  $N$  there are only relatively few non-vanishing elements. It is very economic to determine only the latter. Applying two creation operators to a certain  $(N-2)$ -particle state, generates an  $N$ -particle state with proper sign, which corresponds to a certain row of the Hamiltonian matrix. Creating from the same  $(N-2)$ -particle state a (different or the same)  $N$ -particle state identifies a certain column. Independent summation over all possible two-particle excitations and subsequent summation over all  $(N-2)$ -particle states generates eventually all non-vanishing elements of the Hamiltonian matrix. In our calculations  $R \leq 10^4$  even when using Lanczos procedures.

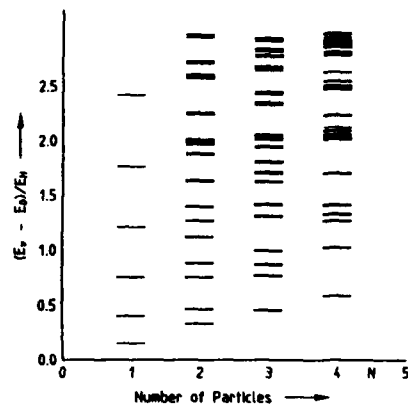


Figure 1: Energy spectra for different electron numbers for a system of length  $9.45a_B$  in atomic energy units  $E_H$ . The ground state energies  $E_0$  are subtracted. The low lying eigenvalues form multiplets with very small internal level separations which are not resolved in the figure. The corresponding states differ in the total spin quantum number.

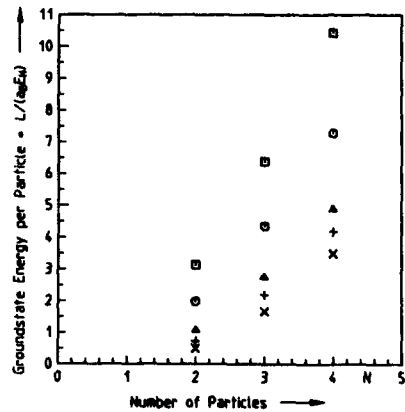


Figure 2: Ground state energies per particle  $E_0/N$  multiplied by  $L/a_B$  versus the particle number  $N$  in atomic units for  $L = 6.61a_B$  ( $\square$ )  $L = 16.1a_B$  ( $\circ$ )  $L = 94.5a_B$  ( $\Delta$ )  $L = 944.8a_B$  (+). ( $\times$ ) denote the energy of  $N$  electrons at fixed, equally spaced positions,  $L/(N-1)$ . They are the limiting values of  $E_0$  as  $L \rightarrow \infty$ .

### 3 The Eigenvalue Spectrum

Typical examples of  $N$ -electron spectra are shown in Figure 1. Not only the average total number of levels per energy interval is considerably increasing with  $N$ , but also their density within certain energy regions. The lowest eigenvalues form *multiplets* that are energetically extremely narrow when  $L \gg Na_B$ . The total number of states within each multiplet, including degeneracies, is  $2^N$ .

Figure 2 shows the dependence of  $E_0/N$  on  $N$  for different  $L$ . The data are multiplied by  $L$  in order to eliminate the trivial  $L$ -dependence.  $E_0(N)$  is not proportional to  $N(N-1)$ , as expected for the classical charging model. For the smaller systems the contribution of the kinetic energy leads to considerable deviations. On the other hand, for very large  $L$ , one can approximate  $E_0(N)$  by the Coulomb energy of  $N$  electrons at equal distances  $r_s = L/(N-1)$  (Wigner lattice).

In Figure 3  $E_0/N$  is shown as a function of  $r_s$ . Pronounced deviations from the Coulombic  $1/L$  behavior occur below  $r_s \lesssim r_1 \approx 50a_B$ . These deviations cannot be attributed to a simple additive influence of the kinetic part of the Hamiltonian.

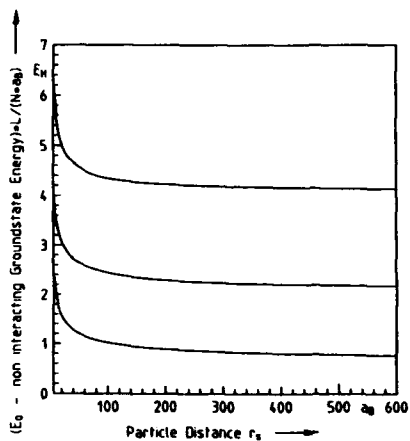


Figure 3: Ground state energy per particle  $E_0/N$  multiplied by  $L/a_B$  versus the mean particle distance  $r_s = L/(N-1)$ . Ground state energies of the corresponding non-interacting systems were subtracted. Data for  $N = 2$ ,  $N = 3$  and  $N = 4$  are shown (from bottom to top). Deviations from Coulombic behavior occur for  $r_s \lesssim 50a_B$ .

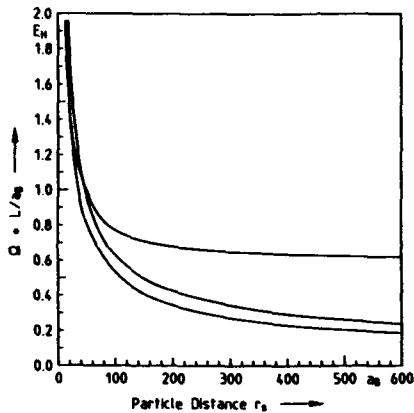


Figure 4: Energy difference between the two lowest multiplets,  $\Omega$ , multiplied by  $L/a_B$  versus the mean particle distance  $r_s$ . Data for  $N = 2$ ,  $N = 3$  and  $N = 4$  are shown (from bottom to top).  $\Omega$  decreases stronger than  $\sim r_s^{-1}$  for  $N = 2$  and 3.

For  $L \gg Na_B$  certain aspects of the spectra can be understood using the Wigner crystal picture. In this limit, the electron density shows  $N$  approximately equidistant peaks within  $L$ . One type of excitation is phonon like due to the Coulomb forces between these charge density maxima.

For charge clouds at equal distance  $r_s$ , the typical phonon frequencies should behave  $\sim r_s^{-\nu}$  with  $\nu = 3/2$  or  $= 1$  if  $\delta$ -function like or Gaussian charge distributions with a variance inversely proportional to the phonon frequency, respectively, are assumed. The energy of the lowest excitation of vibrational type is given by the distance  $\Omega$  between the lowest two multiplets in our spectra. Figure 4 shows  $\Omega L/a_B$  as function of  $r_s$  for different  $N$ . The behavior at large  $r_s$  is consistent with  $\nu \gtrsim 1$ , indicating that the charge density distributions are more localized than Gaussians. For  $r_s \lesssim r_2 \approx 100a_B$  the strong deviations from the asymptotic behavior signalize the breakdown of the Wigner crystal.

Each of the multiplets consists of a series of energy levels that are  $(2S + 1)$ -fold degenerate since the corresponding states are simultaneously eigenstates of  $\hat{S}^2$ . They transform according to the irreducible representation  $A_2$  of the permutation group  $P_N$

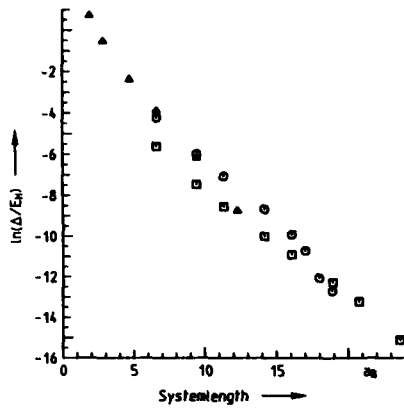


Figure 5: Logarithm of the energy difference  $\Delta$  between the ground state and the first excited state within the lowest multiplet versus the system length for  $N = 2$ ,  $M = 11$  ( $\square$ ),  $N = 3$ ,  $M = 13$  ( $\circ$ ), and  $N = 4$ ,  $M = 10$  ( $\Delta$ ). From the slope of the data we estimate  $L_\Delta \approx 1.5a_B$ .

(Pauli principle). However, when exchanging spatial coordinates only, they transform according to *any* irreducible representation of  $P_N$  since  $H$  does not contain spin operators.

In general, the states are not simple products of spatial and spin parts, as is shown for  $N = 3$  in [10]. The quantum number of the total spin increases with increasing energy within each multiplet, in agreement with the theorem of Lieb and Mattis [11] for 1D interacting electrons.

For a better understanding of the level structure within one multiplet we consider the configuration space of dimensionality  $L^N$ . The modulus of the  $N$ -particle probability amplitude has maxima there at  $N!$  different points corresponding to the number permutations of  $N$  particles. The eigenfunctions can be approximately identified with linear combinations of states  $|j\rangle$ , with  $1 \leq j \leq N!$ , each of them corresponding to one of the  $N!$  maxima. The coefficients for the linear combination are determined by the respective irreducible representation of  $P_N$ . The differences between the energy expectation values are proportional to the finite overlap integrals between the states  $|j\rangle$ . Assuming an asymptotic exponential decay of the  $|j\rangle$  wave functions suggests  $\Delta \propto \exp(-L/L_\Delta)$ , where  $\Delta$  is the energy difference between the ground state and the first excited state within the lowest multiplet.  $L_\Delta$  is a characteristic length scale beyond which the non-interacting spectrum is changed into the multiplet structure characteristic for the influence of the Coulomb interaction. The tunneling energies  $\Delta$  depend on  $\lambda$ , due to the finiteness of the height of the potential barrier between different maxima of the  $N$ -electron probability amplitude given approximately by  $V(x, x) \propto \lambda^{-1}$  (eq. (1)).

In Figure 5 the  $L$ -dependence of  $\ln(\Delta/E_H)$  is plotted for different  $N$ . From the slope of the linear part of the data we obtain  $L_\Delta \approx 1.5a_B$ .

#### 4 Conclusion

We have calculated numerically the energy spectra of up to  $N = 4$  electrons confined within a quasi-one dimensional potential well of finite length. We demonstrated that the  $E_0(N)$  deviates from the classically expected  $N^2$ -behavior due to the quantum mechanical influences of the kinetic energy, and the formation of a Wigner-lattice like structure for small and large  $L$ , respectively. For low electron numbers it is only a limited range

of variables where a capacitance-type of behavior can be obtained.

We discussed the dependence of the energies for the lowest (vibrational and tunneling mode) excitations. Deviations from the Wigner-type arrangement due to the influence of the kinetic energy part is found for quite large system sizes  $r_2$ . The ground state energy cannot be obtained by adding kinetic and potential energy eigenvalues separately. It turns out that exponentially decaying states  $|j\rangle$  describe our data well down to system lengths  $L \approx L_\Delta \approx 1.5a_B$  (Figure 5), although the single particle charge density can be expected to be more or less homogeneous for  $L \lesssim N \cdot 100a_B$  (Figure 4).

Given the geometry and the electron numbers in the AlGaAs/GaAs-based quantum dots showing the resonance-like conductance oscillations [3] (area of the dot  $\approx 2 \cdot 10^5 \text{ nm}^2$ , number of electrons  $\approx 10^2$  effective mass  $\approx 0.07m$ , dielectric constant  $\approx 10$ ) one can estimate a mean distance of  $r_s \approx 2a_B$  such that  $L_\Delta \approx r_s \ll r_1, r_2$ . Although in general, especially at lower electron density [12], quantum mechanical effects cannot be discarded for the understanding of the conductance oscillations, we conclude from the results of our investigations (Fig. 2) that for this relatively high density the physical situation can be approximately described by a semi-classical picture taking into account only the Coulombic part of the electron-electron interaction.

*Acknowledgement* : We thank Kristian Jauregui for enlightening discussions and constructive criticism.

## References

- [1] Kramer B. (ed.), *Quantum Coherence in Mesoscopic Systems* NATO ASI Series B **254**, (Plenum Press, New York 1991)
- [2] van der Zant H. S. J., Geerligs L. J., Mooij J. E. in ref. 1, pp 511-530; a collection of recent papers on this subject can be found in the Special Issue on *Single Charge Tunneling* of Z. Phys. B **85** (1991) edited by H. Grabert
- [3] Meirav U., Kastner M. A., Wind S. J., Phys. Rev. Lett. **65**, 771 (1990)
- [4] Averin D. V., Schön G. in ref. 1, pp 531-570
- [5] Beenakker C. W. J., Phys. Rev. B **44**, 1646 (1991-II)
- [6] Eckern U., Schön G., Ambegaokar V., Phys. Rev. B **30**, 6419 (1984)
- [7] Häusler W., Kramer B., Mäsek J., Z. Phys. B **85**, 435 (1991)
- [8] Merkt U., Huser J., Wagner M., Phys. Rev. B **43**, 7320 (1991)
- [9] Bryant G. W., Phys. Rev. Lett. **59**, 1140 (1987)
- [10] Stevens K. W. H., J. Phys. C **16**, 5765 (1983)
- [11] Lieb E., Mattis D., Phys. Rev. **125**, 164 (1962)
- [12] Heitmann D., this conference

## Spin scattering effect in metallic quantum dots

Shun-ichi Kobayashi, Hidenori Goto and Shingo Katsumoto  
Faculty of Science, University of Tokyo, 7-3-1 Hongo, Bunkyo-ku, Tokyo 113

**ABSTRACT:** The effect of spin scattering on the coherence of electron waves in metallic particles of mesoscopic size was investigated. By measuring the Knight shifts of Cu NMR in mesoscopic particles of Cu-Mn alloys with mean diameter of 60Å, we showed that the anomaly in the spin susceptibility due to the level quantization of conduction electrons can be suppressed by the spin scattering. The condition for the sufficient suppression was  $\tau_s \ll h/\delta$  where  $\tau_s$  is the spin scattering time and  $\delta$ , the mean level spacing.

The energy spectrum of electrons in a finite volume is, in principle, discrete. For the systems of mesoscopic size, the mean level spacing can be comparable to or larger than the thermal energy  $k_B T$  and the life time width of the levels due to inelastic scattering (Halperin 1986, Kobayashi 1990). We have studied the anomalies in metallic small particles arising from this discreteness as those of the spin susceptibility and of the nuclear spin relaxation by using the NMR method at low temperatures (Kobayashi et al. 1987, Goto et al. 1989). When the number of electrons is even in a particle, the paramagnetic susceptibility tends to zero as the temperature is lowered below  $\delta/k_B$ , while for the odd number of electrons, the susceptibility diverges. The susceptibility can be detected as the Knight shift of the NMR of the nuclear spins situated in the particles. Because the resonance line width is very large for the particles with odd number electrons, the steady state NMR can detect the signal from the particles with even number electrons. In copper particles, there remains the residual Knight shift at  $T=0$  because of the sizable strength of the spin orbit interaction (Yee et al. 1975).

Since inelastic scatterings by thermal phonons and the electron-electron interaction are the direct perturbation to the orbital states, they naturally broaden the kinetic energy levels which are discrete. Therefore, the anomalies disappear when  $\delta \ll h/\tau_p$  or  $\delta \ll h/\tau_e$ , where  $\delta$  is the mean spacing of levels, and  $\tau_p$  and  $\tau_e$  are the electron-phonon and the electron-electron scattering times. On the other hand, the spin scattering by the localized impurity spins,

which is certainly inelastic, is the perturbation to the spin state, and it is not self-evident that  $\tau_s \ll \hbar/\delta$ ,  $\tau_s$  being the spin scattering time, is the condition to suppress the anomalies. The purpose of the present study is to investigate how the discreteness is smeared by the spin scattering.

We performed the NMR experiment of the metallic small particles in which the spin scattering by the magnetic impurities is introduced. The system is the ensemble of very small Cu particles containing Mn impurities. The mean diameter of particles is 60 Å. The mean level spacing  $\delta$  estimated as  $\delta = (N(\epsilon_F)V)^{-1}$  is about 9.3 K. The particle samples were prepared in the following manner. First, a mother alloy containing 3.4 at.% of Mn was prepared by melting Cu and Mn metals in a plasma jet furnace. Then the mother was diluted successively by adding Cu to obtain desired concentrations. The rest of the process is the same as that described in (Kobayashi et al, 1987). We prepared three samples #1-#3. Because of the large difference of the vapor pressures between Cu and Mn, the Mn concentration in final product of particles can be very much different from that of the starting alloy. We analyzed the concentrations of Mn in particles using a X-ray micro-analyzer, and found that the Mn concentration of the most concentrated sample is about three times larger than the nominal concentration. For less-concentrated ones, the Mn signals were below the noise level, so that the concentrations were estimated by using the ratio observed for the most concentrated one. The analysed concentrations are shown in Fig.2 by the arrows.

A bridge spectrometer using a rf hybrid junction was used for the steady state detection of the NMR signals in the magnetic field of 6.8 kG. A one-shot  $^3\text{He}$  cryostat was used to cool the samples down to 0.5 K. The shifts were determined by using the resonance signal of the reference pure Cu located outside the  $^3\text{He}$  bath. The Knight shifts are plotted in Fig.1. The shift of the pure Cu particles with the same diameter (Kobayashi 1987) are shown together. The gradual restoration of the shift toward the Pauli value with the increasing concentration of Mn is clearly seen.

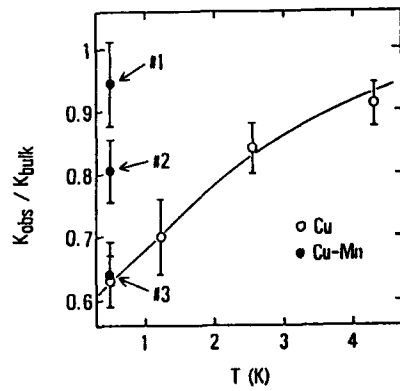


Fig.1 The Knight shifts of Cu-Mn alloy particles (solid circles), and pure Cu particles (open circles) with average size 60 Å. The shifts are normalized to the bulk value.

Cu-Mn alloy is one of the well known spin glass systems. The glass transition temperature  $T_g$  for 100 ppm Mn bulk alloy is about 0.2 K (Beck 1978). Therefore, our samples #1 and #2 are in glass states at 0.5 K. Generally, in magnetically ordered metals, the mutual flip of the conduction electron spin and the localized spin is not possible, so that the presence of the magnetic impurities does not mean the short  $\tau_s$ . However, the glass state allows many spins to be nearly free because of its complexity, and  $\tau_s$  can be very short.

Actually,  $\tau_s$  in Cu-Mn alloys were measured in the Anderson weakly localized films, which consisted of the lightly oxidized 30 Å particles of Cu-Mn connected to form a random two-dimensional networks (Komori et al. 1983). In Fig.2, we plotted the relation between the Mn concentration and the values of  $\tau_s$  taken from (Komori et al. 1983). The result that the eye-guide line for  $\tau_s$ 's intersects  $h/\delta$  near the concentration of sample #1 supports the idea that the relevant spin scattering time to destroy the level discreteness is  $h/\delta$ .

We can explain this result as follows. To establish sharp energy levels in a particle, an electron should travel the whole space in it, and collect the whole information about the potential. In a particle, the motion of the electron is ballistic, so that the electron can sweep a volume of  $\pi\lambda_F^2 v_F t$  in a time  $t$ , where  $\lambda_F$  and  $v_F$  are the Fermi wave length and velocity. The time required to see the whole space  $V$  in the particle is then  $t = V/(\pi\lambda_F^2 v_F)$ .<sup>1)</sup> It can be easily shown after simple manipulation that this  $t$  is equal to  $h/\delta$ . If the phase memory of the electron, regardless of the orbital state or the spin state, is lost before this  $t$  is finished, the orbital levels cannot be established, resulting in the broadening of the levels. As a consequence, we obtain the condition  $\tau_s \ll h/\delta$ .

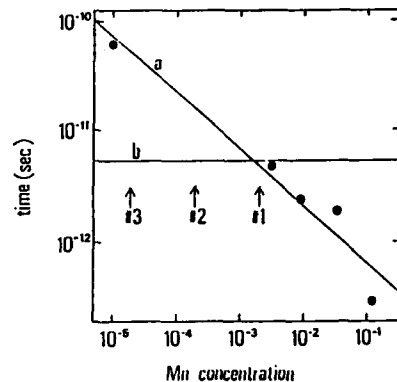


Fig.2 Mn concentration dependence of two characteristic time scales; a:  $\tau_s$  of Cu-Mn alloy films obtained by the Anderson localization experiments. b:  $\tau_d (=h/\delta)$  of pure Cu particles with diameter of 60 Å.

1) The idea of this electron "tube" is originally used to explain the Anderson localization by Aronov A G and Yu. V. Sharvin 1987 Rev. Mod. Phys. **59** 755. We thank Y. Ootuka for discussion.

This work is partly supported by Grant-in-Aid for Scientific Research on Priority Areas, Physics of Mesoscopic Systems from Minisitry of Education Culture and Science.

Beck P A Progr. Mat. Sci. 1987 **22** 3 1.

Halperin W P 1986 Rev. Mod. Phys. **58** 533.

Goto T, Komori F and Kobayashi S 1989 J. Phys. Soc. Jpn. **58** 3788.

Kobayashi S 1990 Phase Transitions **24-26** 463.

Kobayashi S and Katsumoto S 1987 J. Phys. Soc. Jpn. **56** 2256.

Komori F, Kobayashi S and Sasaki W 1983 J. Phys. Soc. Jpn. **52** 4306.

Yee P and Knight W D 1975 Phys. Rev. **B11** 3261.

## Green's function in magnetic fields

Tsuyoshi Ueta <sup>1</sup>

Department of Physics, Faculty of Science and Technology, Keio University,  
3-14-1 Hiyoshi, Kohoku-ku, Yokohama 223, Japan

**Abstract.** It is shown that only the phase factor breaks the translational symmetry of Green's function for a charged particle in a uniform magnetic field, even if the system contains periodic potential. In the absence of the periodic potential, the exact Green's function is derived and applied to practical problem.

### 1. Introduction

In the ballistic transporting regime, the electron focusing (van Houten *et al* 1989) and Hall resistance anomalies (Ford *et al* 1989) have been observed. These experimental results have qualitatively been explained in terms of the classical model called "Billiard Model". However, it is important to deal with them by quantum theory, since the boundaries of the structure confining the electron gas determine the eigenstates taking part in transport. Then, it is very advantageous to represent the wave functions in terms of boundary integration involving Green's function of a charged particle in uniform magnetic fields.

### 2. Translational symmetry breaking

In present section, it is investigated how the translational symmetry of the single particle Green's function  $G(r_2, r_1)$  is broken in the presence of a magnetic fields. We consider a charged particle moving under the influence of the periodic potential  $V(r) = V(r + R)$  and the homogeneous magnetic field  $B$ .

The Hamiltonian for a particle of electric charge  $q$  and magnetic translation operators (Brown 1964) are taken to be

$$\mathcal{H} = \frac{1}{2m}(\mathbf{P} - q\mathbf{A})^2 + V(\mathbf{r}) \quad \text{and} \quad T(\mathbf{R}) \equiv \exp\left(\frac{i}{\hbar}\mathbf{R} \cdot (\mathbf{P} + q\mathbf{A})\right). \quad (1)$$

We employ the vector potential  $\mathbf{A} = \frac{1}{2}\mathbf{B} \times \mathbf{r}$ .

<sup>1</sup> E-mail: ueta@rk.phys.keio.ac.jp (junet).

Then, calculations yield  $[\mathcal{H}, T(\mathbf{R})] = 0$  for arbitrary  $\mathbf{R}$  and so the retarded Green's function  $G = (E - \mathcal{H} + i\delta)^{-1}$  commutes with  $T(\mathbf{R})$  for arbitrary  $\mathbf{R}$ .

Therefore,

$$\langle \mathbf{r}_2 | G | \mathbf{r}_1 \rangle = \langle \mathbf{r}_2 | T(\mathbf{R}) G T^\dagger(\mathbf{R}) | \mathbf{r}_1 \rangle = e^{i \frac{q}{\hbar} \mathbf{B} \cdot \{\mathbf{R} \times (\mathbf{r}_1 - \mathbf{r}_2)\}} \langle \mathbf{r}_2 + \mathbf{R} | G | \mathbf{r}_1 + \mathbf{R} \rangle. \quad (2)$$

Putting  $\mathbf{R} = -\mathbf{r}_1$ , we obtain

$$\langle \mathbf{r}_2 | G | \mathbf{r}_1 \rangle = e^{i \frac{q}{\hbar} \mathbf{B} \cdot (\mathbf{r}_1 \times \mathbf{r}_2)} \langle \mathbf{r}_2 - \mathbf{r}_1 | G | 0 \rangle, \quad (3)$$

where  $\mathbf{r}_2$  is always arbitrary, whereas  $\mathbf{r}_1$  has to be taken an arbitrary lattice vector in the presence of a periodic potential.

Performing the gauge transformation  $\mathbf{A} \rightarrow \tilde{\mathbf{A}} = \mathbf{A} + \nabla \Lambda$  on Eq.(3) gives

$$\langle \mathbf{r}_2 | \tilde{G} | \mathbf{r}_1 \rangle = \exp \left( i \frac{q}{\hbar} \int_{\mathbf{r}_1}^{\mathbf{r}_2} \tilde{\mathbf{A}} \cdot d\mathbf{r} \right) \langle \mathbf{r}_2 - \mathbf{r}_1 | G | 0 \rangle. \quad (4)$$

where  $\tilde{G}$  denotes the Green's function for  $\tilde{\mathbf{A}}$  and for convenience we have used the fact that the integration of  $\mathbf{A}$  from  $\mathbf{r}_1$  to  $\mathbf{r}_2$  along the straight path gives  $\frac{1}{2} \mathbf{B} \cdot (\mathbf{r}_1 \times \mathbf{r}_2)$  (Ueta 1992).

### 3. Exact Green's function for the free case

We evaluate Green's function of a charged particle in a homogeneous magnetic field in absence of a periodic potential. Here, we choose the vector potential as  $\mathbf{A} = \frac{B}{2}(-y, x, 0)$  and we introduce a dimensionless variables  $\mathbf{r} = \mathbf{r}_2/\ell$ ,  $\mathbf{r}' = \mathbf{r}_1/\ell$ ,  $\varepsilon = \frac{E+i\delta}{\hbar\omega}$ ,  $z = \frac{1}{2}(\mathbf{r} - \mathbf{r}')^2$  where  $\omega$  is the cyclotron frequency and  $\ell$  represents the magnetic length  $\sqrt{\frac{\hbar}{m\omega}}$ .

In the present unit,  $G_0(\mathbf{r} - \mathbf{r}')$  ( $\equiv \langle \mathbf{r}_2 - \mathbf{r}_1 | G | 0 \rangle$ ) obeys the reduced Schrödinger equation,

$$\left[ \frac{\partial}{\partial z} \left( z \frac{\partial}{\partial z} \right) - \frac{1}{4} z + \varepsilon \right] G_0(z) = \frac{m}{2\pi\hbar^2} \delta(z). \quad (5)$$

We here note that the differential operator on the left-hand side of Eq.(5) has the Sturm-Liouville form. Therefore, on making use of the general procedure to obtain Green's function (Courant and Hilbert 1961), our Green's function is written

$$G_0(z) = -\frac{m}{2\pi\hbar^2} \Gamma \left( \frac{1}{2} - \varepsilon \right) e^{-z/2} U \left( \frac{1}{2} - \varepsilon, 1, z \right), \quad (6)$$

where  $U(z)$  is one of Kummer's functions which diverges logarithmically when  $z \rightarrow 0$  (Abramowitz and Stegun 1970).

From the geometrical symmetry, we obtain  $G(\mathbf{r}_2, \mathbf{r}_1; -B) = G(x_2, -y_2, x_1, -y_1; B)$ . Therefore  $G_0(z; -B) = G_0(z; B)$ , since  $G_0$  is a function of  $z = \frac{1}{2}(\mathbf{r} - \mathbf{r}')^2$ . This means that  $G_0$  does not include the information of the direction of the magnetic field, and that whether the motion is clockwise or counterclockwise is determined by only the phase factor.

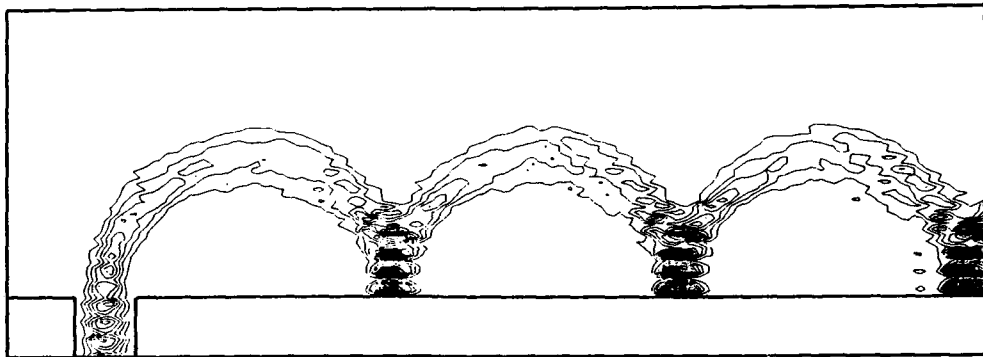


**Figure 1.** Contours of the modulus squared of the electron wave injected from the wave guide attached on the left-hand side of the bottom. The incident wave belongs to the fundamental mode. The width of the wave guide  $d = 3$  and  $\epsilon = 25$ .

#### 4. Numerical calculation

The practical method to obtain the numerical values of the Green's function is to solve the homogeneous equation corresponding to Eq.(5), that  $U(z)$  obeys, numerically. Necessary boundary conditions are given by asymptotic expansions of Eq.(6) at sufficiently large  $z$ . This method has an advantage that calculation for the differentiation of  $G_0(z; \epsilon)$  is not necessary, since it is simultaneously evaluated in the intermediate step of the calculation of  $G_0(z; \epsilon)$ . It has been found that the 4-th order Runge-Kutta method is sufficient to calculate it even for large  $\epsilon$ .

#### 5. Application

The Kirchhoff-Huygens theorem in the presence of a magnetic field,

$$\begin{aligned} \varphi(\mathbf{r}) = & -\frac{\hbar^2}{2m} \int [G(\mathbf{r}, \mathbf{r}') \nabla' \varphi(\mathbf{r}') - \varphi(\mathbf{r}') \nabla' G(\mathbf{r}, \mathbf{r}')] \cdot \mathbf{n}' dS' \\ & + \frac{i\hbar q}{m} \int [G(\mathbf{r}, \mathbf{r}') \mathbf{A}(\mathbf{r}') \varphi(\mathbf{r}')] \cdot \mathbf{n}' dS', \end{aligned}$$

is very useful to study wave propagation with arbitrary geometry of boundaries. Here the integral is performed on an arbitrary closed boundary surface which encloses the point  $\mathbf{r}$ . The method of numerical calculation of such a equation is well known as boundary element method (B.E.M.) (Bebbia 1978). It enables us to research the influence of geometry in ballistic wires on conductance fully by quantum theory.

As a example, a wave function of an electron injected into semi-infinite two-dimensional region has been computed. The electron wave which has energy  $\epsilon = 25$  and belongs to the fundamental transverse mode in the wave guide of the width  $d = 3$  is shown in Figure 1. The most probable path is a circle which agrees with corresponding classical trajectory.

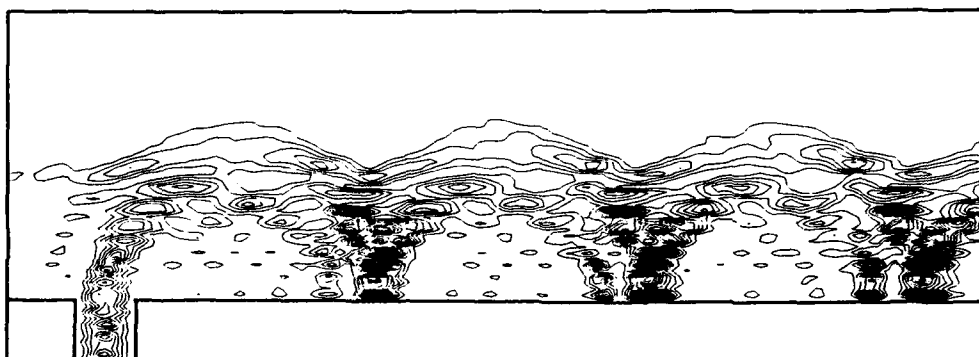


Figure 2. Contours of the modulus squared of the wave function belonging to the fundamental transverse mode with  $\epsilon = 16$  and  $d = 2.5$ .

For fundamental transverse mode with  $\epsilon = 16$  and  $d = 2.5$  (Figure 2), we can see complex structures which is considered to be the effects of diffraction and/or interference as Nakamura *et al* (1991) reported.

#### Acknowledgments

The author would like to thank Professor K. Kawamura for discussion, encouragement and continuous interest in this work.

This work was supported in part by a Grant-in-Aid for Scientific Research on Priority Area, "Electron Wave Interference Effects in Mesoscopic Structures" from the Ministry of Education, Science and Culture.

#### References

Abramowitz M and Stegun I A 1970 *Handbook of mathematical functions* (New York: Dover Publ.) pp 504-510

Brebbia C A 1978 *The boundary element method for engineers* (London: Pentech Press)

Brown E 1964 *Phys. Rev.* **133** A1038-A1044

Courant R and Hilbert D 1961 *Methods of mathematical physics* Vol 2 (New York: Interscience)

Ford C J B, Washburn S, Büttiker M, Knoedler C M and Hong J M 1989 *Phys. Rev. Lett.* **62** 2724-2727

Nakamura A, Maki Y and Okiji A 1991 *J. Phys. Soc. Japan* **60** 749

Ueta T 1992 *Proc. Int. Symp. on Science and Technology of Mesoscopic Structures, Nara Nov. 6-8, 1991* (Tokyo: Springer Verlag) to be published

van Houten H, Beenakker C W J, Williamson J G, Broekaart M E I and van Loosdrecht P H M 1989 *Phys. Rev. B* **39** 8556-8575

## Nanofabrication: challenges and opportunities

D.P.Kern

IBM Research, T.J. Watson Research Center, Yorktown Heights, NY 10598

**ABSTRACT:** Fabrication of structures for investigation of quantum effects frequently involves the use of MBE/CVD type growth processes to achieve control on an atomic scale in vertical direction and a wide range of combinations of lithography and pattern transfer techniques for control in lateral directions. The challenges ahead lie in the degree of lateral control with which the lithography can be performed, i.e. resolution and placement accuracy, but also in the throughput of the lithography equipment once technological applications are considered. Electron beam resolution can certainly extend to the 1nm regime, in the case of the STM even to 0.1nm, appropriate resist materials have to be found, however. Parallelism may be introduced into nanolithography through contact printing with x-rays, electron, ion, or x-ray projection, or arrays of miniaturized scanning electron or ion columns. Pattern transfer relies on a broad spectrum of subtractive and additive processes ranging from wet and dry etching to selective growth techniques. Pattern fidelity and damage to the material are the key issues.

### 1. INTRODUCTION

While the electronics industry has been dominated by silicon technology, evolving along an aggressive path of scaling with resultant performance improvements which is very likely to continue for a few decades, the past ten years have seen an explosion in both the amount and depth of work on electronic systems with reduced dimensionality, driven by desire to explore the physics of quantization in confined geometries and the hope of their future technological applications, and inspired by the significant advances in fabrication technology. The results indicate clearly that there will be limits to conventional scaling of devices but at the same time that there are novel effects such as non-equilibrium transport, quantum size effects, Coulomb blockade and possibly others which offer opportunities to overcome this barrier. However, devices based on these effects will not simply replace transistors but will require all new architectures where single electronics and arrays of quantum dots as cellular automata are emerging examples. Research will have to continue to explore the limits of scaling of conventional devices, search for novel effects, find novel ways to combine devices and evaluate their suitability for information processing.

On the fabrication side, the key issues remain to make things small and precise. This is true whether one works on scaling conventional technology, requiring sub-100nm gates, contacts, isolation trenches, shallow junctions, to name a few elements, or whether quantum effects are to be explored. Energy level spacings increase and their effects become more prominent when the confined systems become smaller, capacitances decrease and therefore Coulomb charging effects become more clearly visible. Reduced dimensions also allow for higher device density and therefore decrease the distance over which devices have to communicate with each other reducing time-of-flight delays. On the other hand, fabrication also

has to address the need for small scale prototyping of novel systems to explore novel interconnection and interaction mechanisms and strategies as well as the functionality of logic schemes. This requires that small structures can also be made in reasonably large quantities, not to mention that for real applications one would need millions and billions of them. Besides resolution and accuracy, potential fabrication techniques also should have extendability to high throughput.

The fabrication process typically starts with the growth of specifically tailored materials using MBE or CVD type processes for control on an atomic scale in vertical direction. A wide range of combinations of lithography and pattern transfer techniques is then used for control in lateral directions (Chang et al. 1988). In the following two sections we will take a closer look at the options available.

## 2. LITHOGRAPHY

The relevant feature sizes in nanofabrication range from about  $0.25\mu\text{m}$ , where the very early stages of silicon technology development have arrived, to 10nm, the typical size of the smallest structures which have been useful for electrical or optical experiments, to 0.1nm - 1nm where nanostructures may form the interface to the molecular and atomic world. Most of the patterning techniques rely on high resolution electron beam lithography performed with scanning electron beam systems, while some work has been reported based on x-ray nanolithography, on lithography or machining and implantation using focused ion beams or on holographic techniques for periodic structures. The challenges ahead lie in the degree of lateral control with which the lithography can be performed, i.e. resolution and placement accuracy, but also in the throughput of the lithography equipment once technological applications are considered. We have found that with proper attention to system aspects such as electron optical performance, mechanical stability and accuracy, electromagnetic interference, with the ability to correct for proximity effects close to theoretical limits, with proper choice of resist material and process integration, scanning electron beam lithography can yield reliable and flexible patterning on a close to 10 nm scale for resolution and placement. Equipment of that sort is fully engineered with high speed controls integrated into an engineering design system for pattern layout, laser interferometer based metrology and capable of handling 125mm - 150mm diameter substrates (as well as experimental pieces as small as a few millimeters). The performance of the IBM VS-6 system as an example is summarized in table 1 (Rishton et al 1989). A similar system but with a 25keV thermal field emission source achieves 10nm spot size at InA beam current (Gesley et al. 1988).

While this has proven adequate for most applications so far, in particular since damage from pattern transfer or depletion effects happen on an even larger scale, there is increased interest in pushing that limit further, e.g. from the work on luminescence from small Si-particles or transport controlled by Coulomb-blockade. Electron beam resolution can certainly extend to the 1nm regime, however appropriate resist materials have to be found. Work on metal-halide and  $\text{SiO}_2$  based resists may lead the way. Holes in LiF-films as small as 2nm have been generated using a 100keV STEM (Muray et al. 1985). The atomic resolution obtained with the scanning tunneling microscope and the surface modifications on an atomic scale e.g. by Eigler 1990 indicate that fabrication can reach the sub-1nm regime. Suitable "resist" materials and interaction processes are required for practical applications

and essentially any attempt of the latter has resulted in structures that can be readily attained using conventional electron beam techniques.

Some degree of parallelism has to be introduced into the nanolithography process in order to make it feasible for technological applications. Variable shaped electron beam systems typically projecting about 50 resolution elements at a time are in use for a while (Pfeiffer 1979) but they have not reached the 100nm resolution regime. Masked demagnifying electron projection has received renewed attention with the development of a novel mask (e.g. Berger 1991), but difficulties related to control of electron optical distortions and level to level overlay remain. A novel approach is based on microscopic electron optical columns. Recognizing that electron optical aberrations scale with the dimensions of the system, microscopic columns measuring a few millimeters in size and with critical feature sizes in the  $1\mu\text{m}$  regime have been designed (Chang et al. 1991) using a selective scaling technique. This way the small probe size and high brightness of the vacuum tunneling process in an STM can be essentially maintained without the extremely severe tip-sample interaction. Experimental evaluation is in progress (Muray et al. 1991). Due to their small size and the fact that many of the fabrication processes are derived from semiconductor processing, these micro-columns are very suitable for array applications, e.g. one or more columns per chip, and thus have the potential for considerable parallelism (Chang et al. 1992). A summary of the main advantages and disadvantages of the various electron beam techniques is given in table 2.

X-ray lithography with a mask in close proximity to the sample - about  $10\mu\text{m}$  to  $40\mu\text{m}$  separation - is one of the techniques being explored for semiconductor manufacturing. With a very small or vanishing gap (contact), features as small as 20nm have been printed

#### VS-6 Electron Beam Lithography System

- Fully equipped e-beam lithography tool
  - 8nm spot size
  - full proximity correction capability
  - 125mm wafer handling capability
  - field sizes:  $50\ \mu\text{m}$  to  $700\mu\text{m}$
  - laser Interferometer controlled stage and beam servo
  - scan linearity  $< 8\text{nm}$  (for  $100\ \mu\text{m}$  field)
  - scan calibration  $\sim 10^{-4}$  of field size
- TEM - like stability
  - piezo - locking stage with 2.5nm peak-peak residual motion
  - 60 Hz Interference  $< 3\text{nm}$  p-p
  - electronic noise  $< 3\text{nm}$  for small fields
- Detectors: backscattered and transmitted electrons

Table 1: Performance of IBM VS-6 electron beam lithography system

#### Types of Electron Beam Lithography Systems

	PRO	CON
STM (mod.)	high resolution ( $\sim 0.5\text{nm}$ ) high current (FE) high voltage (100kV)	limited control small field size limited sample handling capab.
Conventional Gaussian beam system	fully engineered high speed controls large samples	medium res. (2.5-8 nm) voltage $\leq 50\text{kV}$ (125mm)
Shaped Beam System	high speed high current	spot size ( $>100\text{nm}$ ) complexity
Projection	parallelism/ throughput	distortions/mask overlay
STM	small probe high current dens. simple	slow tip/sample interaction
Micro-Column	small probe high current dens. amenable to arrays	not yet available small field prob. low voltage

Table 2: Comparison of different types of electron beam lithography systems

(Flanders 1979) and work addressing the issues in mask making using electron beams at these dimensions is going on (Chu et al. 1992). Nevertheless, making accurate 1x masks at sub-100nm dimensions and accuracy with aspect ratios larger than ~4:1 on membranes transparent to x-rays is still a difficult task. Projection x-ray lithography which utilizes reflective optics coated with dielectric multilayers to enhance x-ray reflection (e.g. Hawryluk and Seppala 1988) may overcome some of these difficulties since a reflective (solid) mask may be used and the projection optics incorporates demagnification. Designing, building and assembling these multilayer mirror optics, however, remains a formidable, unproven task.

### 3. PATTERN TRANSFER

For the pattern transfer a variety of techniques can be used depending on the application and materials involved. Additive processes include lift-off and plating (mainly used for metals), beam assisted deposition, and selective growth epitaxy. Subtractive processes involve chemical etching (wet and gas phase), ion milling, and reactive ion etching. Local modification of physical properties due to ion implantation represents an additional successfully applied technique.

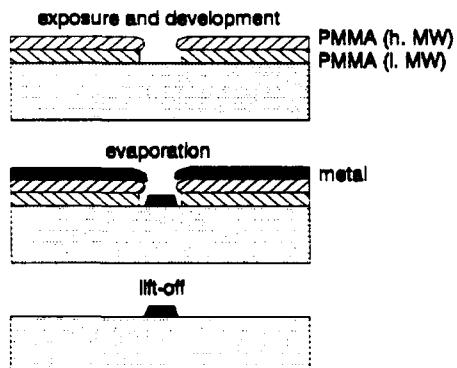


Fig. 1: Principle of lift-off

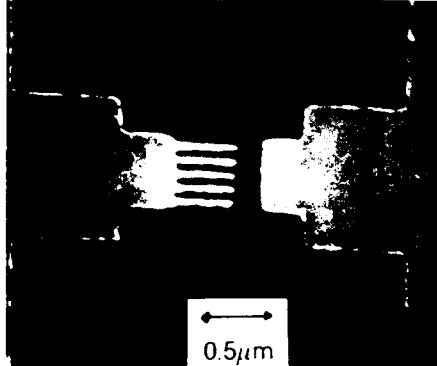


Fig. 2: Lifted off Schottky gate (Au/Pd on NiCr on GaAs)

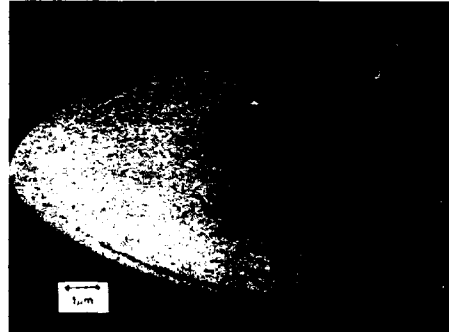


Fig. 3: Fresnel zone plate with 30nm zones made by electroplating of gold

Lift-off involves the formation of a resist stencil with undercut profile which can be achieved by electron beam lithography on a double layer resist system (c.f. fig. 1), and deposition of the desired material (typically evaporation of metal at normal incidence from a point source) so that the films on top of the resist and on the substrates are not connected. Subsequent dissolution of the resist lifts off the material on top. Due to the need for undercut

resist profile and for separation of the materials deposited on top of the resist and on the substrate, the technique has its limits with dense and high aspect ratio structures, but it is very widely used for fabrication of Schottky gates for point contacts, one- and zero-dimensional lateral superlattices and Coulomb-blockade structures. Fig. 2 shows such a gate configuration lifted off on a hall bar, exhibiting fingers with 100nm period. In cases where a plating base can be deposited on the substrate the resist stencil of fig. 1 can be filled by electroplating to the top of the resist without requiring the undercut profile. This allows the formation of high resolution, high aspect ratio structures such as x-ray masks. Fig. 3 shows a Fresnel zone plate consisting of 30nm wide and 60nm high gold rings, used as a lens in soft x-ray microscopy (Anderson and Kern 1992).

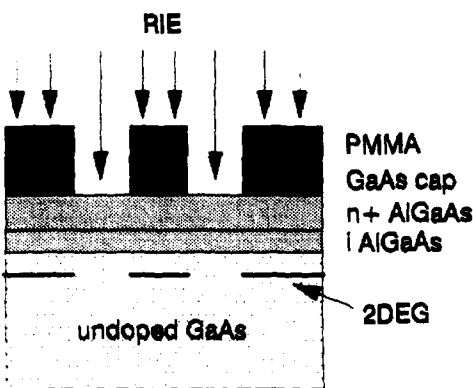


Fig. 4: Confinement through cap etch in typical GaAs/AlGaAs heterostructure

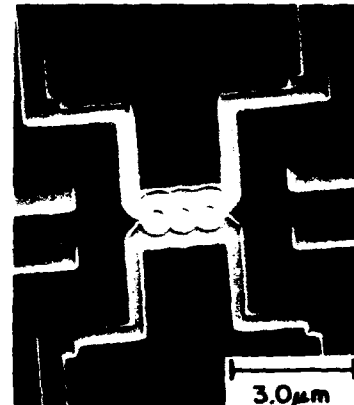


Fig. 5: Confinement through trench etching

Etching the GaAs cap layer of typical GaAs/AlGaAs heterostructures as indicated in fig. 4 has proven to be another widely used technique. We first developed it to fabricate arrays of quantum dots and wires (Smith et al. 1988) and in the form of trenches it represents a simple general isolation scheme (Lee et al. 1989). Fig. 5 shows an example where a string of three 0.6 $\mu$ m diameter rings with associated current leads and voltage probes have been formed using the trenching technique. With dry etching processes, etch damage poses significant problems. In particular, RIE with ECR-RF excited  $CCl_2F_2/He$  plasmas has proven to yield low damage, good anisotropy and selectivity between GaAs and AlGaAs (Cheung et al. 1989). Recently, wet etching controlled on a 10nm scale has been applied successfully to fabricate lateral surface superlattices with periods as small as 100nm (Lee et al. 1990). Transport structures fabricated this way exhibit quantized conductance over lengths up to 4  $\mu$ m (Ismail et al. 1991).

#### 4. CONCLUSION

High resolution electron beam lithography combined with appropriate pattern transfer techniques enables fabrication of a multitude of structures and devices with dimensions close to 10nm. A wealth of information on the physics of small structures has been gained this way over the past 5 - 10 years. Exploring the technological relevance of these devices

is the task ahead. Fabrication technology has to address higher resolution, understanding and control of damage, and parallelism in defining small geometries.

### 5. ACKNOWLEDGEMENT

I would like to acknowledge my colleagues T.H.P. Chang, J.M. Hong, K. Ismail, K.Y. Lee, Y.H. Lee, L. Muray, S. Rishton, U. Staufer, S. Wind from the IBM T.J. Watson Research Center, E. Anderson and V. Boegli from Lawrence Berkeley Laboratory and H.I. Smith and W. Chu from MIT whose collaboration and comments made this work possible.

### REFERENCES

Anderson E and Kern D P 1992 X-ray Microscopy Springer Verlag Michette, Morrison, Buckley Eds.

Berger S D, Gibson J M, Camarda R M, Farrow R C, Huggins H A, Kraus J S, and Liddle J A 1991 *J. Vac. Sci. Technol.* B9 2996

Chang T H P, Kern D P, Kratschmer E, Lee K Y, Luhn H E, McCord M A, Rishton S A, and Vladimirska Y 1988 *IBM J. Res. Develop.* 32 pp 462-493

Chang T H P, Kern D P, and Muray L P 1991 *IEEE Trans. El. Dev.* ED-38 2284

Cheung R, Lee Y H, Lee K Y, Smith III T P, and Kern D P 1989 *J. Vac. Sci. Technol.* B7 1462

Chu W, Rishton S A, Schattenburg M L, Kern D P, and Smith H I 1992 *J. Vac. Sci. Technol.*, submitted

Eigler D M and Schweizer E K 1990 *Nature* 344 534

Flanders D C 1979 *J. Vac. Sci. Technol.* 16 1615

Gesley M A, Hohn F J, Viswanathan R G, and Wilson A D 1988 *J. Vac. Sci. Technol.* B6 2014

Hawryluk A M and Seppala L G 1988 *J. Vac. Sci. Technol.* B6 2162

Ismail K, Washburn S, and Lee K Y 1991 *Appl. Phys. Lett.* 59 1998

Lee K Y, Smith III T P, Ford C J B, Hansen W, Knoedler C M, Hong J M, and Kern D P (1989) *Appl. Phys. Lett.* 55 625

Lee K Y, Kern D P, Ismail K, Haug R J, Smith III T P, Masselink W T, and Hong J M 1990 *J. Vac. Sci. Technol.* B8 1366

Muray A, Scheinfein M, Isaacson M, and Adesida I 1985 *J. Vac. Sci. Technol.* B3 367

Muray L P, Staufer U, Bassous E, Kern D P, and Chang T H P 1991 *J. Vac. Sci. Technol.* B9 2955

Pfeiffer H C 1979 *IEEE Trans. El. Dev.* ED-26 663

Rishton S A, Kern D P, Kratschmer E, and Chang T H P 1989 *Microelectronic Engineering* 9 pp 183-186

Smith III T P, Lee K Y, Knoedler C M, Hong J M, and Kern D P 1988 *Phys. Rev B* 38 2172

## Neutral atom nanolithography

K.K. Berggren, M. Prentiss  
Harvard University, Cambridge, MA 02138  
and  
G. Timp, and R.E. Behringer  
AT&T Bell Laboratories, Holmdel, New Jersey 07733

### ABSTRACT

Recently, we demonstrated that an optical standing wave at 589nm could be used as an array of cylindrical lenses to focus an atomic beam into a grating on a substrate, with a periodicity of  $294.3 \pm 0.3 \text{ nm}$ . This result was the first direct evidence of submicron focusing of atoms by light, and raised the possibility of a fundamentally new type of submicron lithography. Below we discuss the prospects for nanometer-scale lithography using this technique.

### 1. INTRODUCTION

Neutral atom optics are now technologically possible. For example, it has been demonstrated that a neutral atomic beam can be focused either by diffraction or refraction with high resolution. Specifically, using diffraction from a microfabricated Fresnel zone plate, Carnal et al. (1991) demonstrated a focal spot size only  $18 \mu\text{m}$  in diameter. However, the resolution of a Fresnel zone plate is limited by the outer ring spacing, and so ultimately the resolution is determined by conventional microfabrication technology. Alternatively, neutral atomic beams have been refractively focused using light as a lens. Nearly-resonant light exerts a net average force on a two-level atom which is proportional to the gradient in the light intensity and the detuning from resonance (Gordan and Ashkin 1980). When the laser frequency is greater than the natural resonant frequency of the atom, the average force is directed toward regions of lower intensity. Using the intensity gradient in a Gaussian beam, Bjorkholm et al. (1980) observed a focal spot size of  $28 \mu\text{m}$ . Subsequently, Balykin and Letokhov (1987), and Gallatin and Gould (1991), proposed that subnanometer-diameter spots might be achieved using the gradient light force.

We demonstrated recently that an optical standing wave at 589nm could be used as an array of cylindrical lenses to focus a collimated atomic beam into a grating on a substrate, with a periodicity of  $294.3 \pm 0.3 \text{ nm}$ . (Timp et al. 1992) In an optical standing wave (SW), the intensity oscillates spatially every half wavelength, and the corresponding oscillations in the average (gradient) force on an atom can be used as an array of lenses. If the frequency of the SW is detuned above (below) the two-level resonance, the atoms are focused toward the SW intensity nodes (antinodes). Such an array of lens might be suitable for certain submicron lithography applications. In what follows, we tersely review this result and examine the prospects for nanometer-scale lithography using neutral atomic beams.

### 2. EXPERIMENTAL RESULTS

Figure 1 is a schematic of the experimental apparatus. The experimental details are fully described elsewhere. (Timp et al. 1992) A well collimated sodium atomic beam, propagating along

$\hat{y}$ , interacts with a perpendicular SW with wavevector  $|k| \hat{z}$ , and is ultimately deposited onto a silicon substrate. The wavevector  $k=2\pi/\lambda$ , where  $\lambda$  is the optical wavelength. The atomic beam has a velocity,  $v_y$ , and interacts with the SW for a time,  $t_i=L_i/v_y$ , where  $L_i$  is the interaction length. The laser frequency,  $\omega_L$ , is nearly resonant with the sodium  $3^2S_{1/2}(F=2) \rightarrow 3^2P_{3/2}(F=3)$  transition at 589nm, which has a line width of  $\Gamma/2\pi=10MHz$ . Typically, the laser is detuned  $\Delta=\omega_L-\Omega=60MHz$  from the atomic frequency  $\Omega$ . The intensity in the SW is measured by the local Rabi frequency,  $\omega_R(z)=\mu E(z)/2\pi$  which is proportional to the product of the dipole moment,  $\mu$ , and the electric field,  $E \sim \sin[kz]$ . Typically,  $\omega_R \approx 100MHz$ . After emerging from the SW, an atom undergoes free flight for a distance  $L_f < 75\mu m$  before it hits the substrate.

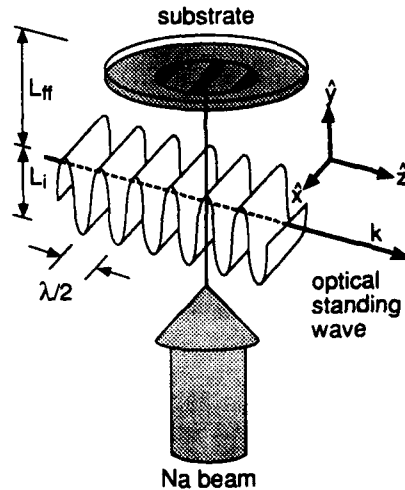


Figure 1. A schematic representation of the experiment. An optical standing wave is interposed between an atomic beam and a substrate to deflect or focus atoms during deposition.

The sodium film, which is deposited in about 10 minutes onto a silicon substrate, is shiny and colored gold. Close inspection showed that the surface morphology of the film is different in the position where the SW cut across the substrate. We used first order optical diffraction to investigate in-situ the region where the film was modified by the SW.

Figure 2 is a schematic representation of the diffraction geometry. An incident beam with  $560nm < \lambda < 580nm$  at an angle between  $8^\circ < \theta_i < 15^\circ$  from the surface back-scatters at an angle of  $6^\circ < \theta_m < 17^\circ$ . According to the formula:

$$-d(\cos\theta_m + \cos\theta_i) = m\lambda, \quad (1)$$

we observed the first order,  $m=-1$ , diffraction peak. In Eq. (1),  $\theta_i$  is the angle between the surface and the incident wavevector,  $\theta_m$  is the angle between the surface and the diffracted light, and  $d$  is the grating period. We observed diffraction only over the area associated with the position of the SW. In correspondence with Eq. (1), the position of the diffraction spot was sensitive to the incident wavelength, i.e. for fixed  $\theta_i$ , the angle  $\theta_m$  increases for shorter wavelength. Figure 2 also

shows a photograph of three  $m=1$  diffraction peaks corresponding to three different incident wavelengths: 574.99nm, 576.00nm, and 577.05nm. The photograph was obtained with the diffraction geometry shown in the top of Fig. 2 using three different exposures at the same position for the three wavelengths. The diffraction spots are separated by about 7mm and were observed approximately 40cm from the grating for  $\theta_i=10^\circ$  and  $\theta_m=13^\circ$ . We found an  $m=1$  diffraction spot for  $\Delta=-140MHz$  and 60MHz detunings with  $\omega_R=80, 100$ , and 150MHz.

We measured  $d$  at a variety of wavelengths and angles for all the variations of  $\Delta$  and  $\omega_R$  that we found diffraction. Using the condition:  $\theta_i=\theta_m=11.56^\circ$  when  $\lambda=577.05nm$ , we found  $d=294.3\pm0.3nm$  for all of the SW intensities and detunings used in our experiments. We also measured the diffraction efficiency, i.e. the ratio,  $\eta$ , of the intensity found in the  $m=1$  diffraction peak to the incident intensity, and found a weak dependence on the detuning and the power in the SW. The largest  $\eta$  we found was less than 0.04%.

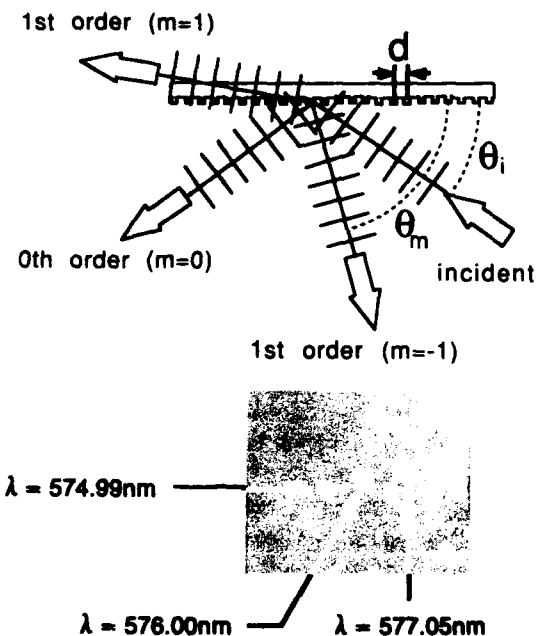


Figure 2. A schematic of the diffraction geometry used to detect the grating and a photograph of three  $m=1$  diffraction spots obtained using this geometry for three different wavelengths incident on the grating.

### 3. THEORETICAL DISCUSSION.

The net average force exerted by a SW on a two-level atom with negligible transverse velocity (i.e.  $v_z, v_x=0$ ) can be derived from the gradient of the pseudo-potential:

$$U(z) = \frac{1}{2} \hbar \Delta \log[1 + 2\omega_R^2(z)/(4\Delta^2 + \Gamma^2)]. \quad (2)$$

Since the Rabi frequency is proportional to the product of the dipole moment,  $\mu$ , and the electric field,  $E \sim \sin[kz]$ , the periodic variation in the square of the Rabi frequency gives rise to a potential which is periodic in  $\lambda/2$ . Typically, the depth of the potential is about 1–5 μeV.

The potential  $U(z)$  in Eq. (2) acts as an array of weak cylindrical lenses, focusing the atomic beam into a grating on the substrate, with a period of  $\lambda/2$ . If the potential within each half wavelength of the SW was harmonic with an oscillation period  $T$  then, when  $t_i = (2n+1)T/4$  where  $n$  is an integer, a perfectly collimated monoenergetic atomic beam would be focused to an array of lines. Ideally, each line would have a delta-function distribution along  $\hat{z}$ . Actually, the harmonic approximation is valid only near the nodes (antinodes) of the SW for  $\Delta > 0$  ( $\Delta < 0$ ). Semi-classical calculations of the atomic trajectories (see below) show that the width of the distribution can be less than 10 nm. A finite transverse velocity ( $v_z \neq 0$ ) and the Boltzmann spread in  $v_y$  will increase the width of the distribution further, as will mechanical vibrations of the substrate relative to the position of the SW. The contributions to the width of the line from the initial velocity and the mechanical vibration of the substrate can be controlled experimentally, however. (Timp et al., 1992)

The value of  $d$  and the small backscattered diffraction efficiency are consistent with either a weak, broad modulation of the sodium film thickness periodic in  $\lambda/2$ , or with very narrow lines periodic in  $\lambda/2$ . The latter possibility corresponds with the results of our semi-classical numerical simulations of the profile of the film. In our calculations, we suppose that the atoms in the beam are fully polarized the instant they enter the SW. The atoms are assumed to have a uniform spatial distribution along  $\hat{z}$ , with  $v_z = 0$  and a Boltzmann distribution for  $v_y$ . In the calculations we include the force associated with Eq. (2). Under the experimental conditions, the final distribution is not affected by the first order velocity-dependence. The atomic coordinates of roughly 100,000 two-level atoms are updated every 100 ps. The resolution of the final position of the atoms on the substrate is  $\approx 0.3 \text{ nm}$ . We assume that there is no diffusion once the atom hits the substrate.

Figure 3 illustrates the calculated effect of varying the interaction length  $0 < L_i < 500 \text{ μm}$  on the film profile over a distance of  $0 < z < \lambda/2$ . The narrow peak found in the simulation near  $z = \lambda/4$  Fig. 3 for  $L_i = 100 \text{ μm}$  is approximately 10 nm wide (FWHM), and is indicative of the focusing which can be achieved for particular longitudinal velocities in the Boltzmann distribution. The background corresponds to the remaining atoms in the Boltzmann distribution, and to atoms which have an initial position outside the range where the potential is harmonic.

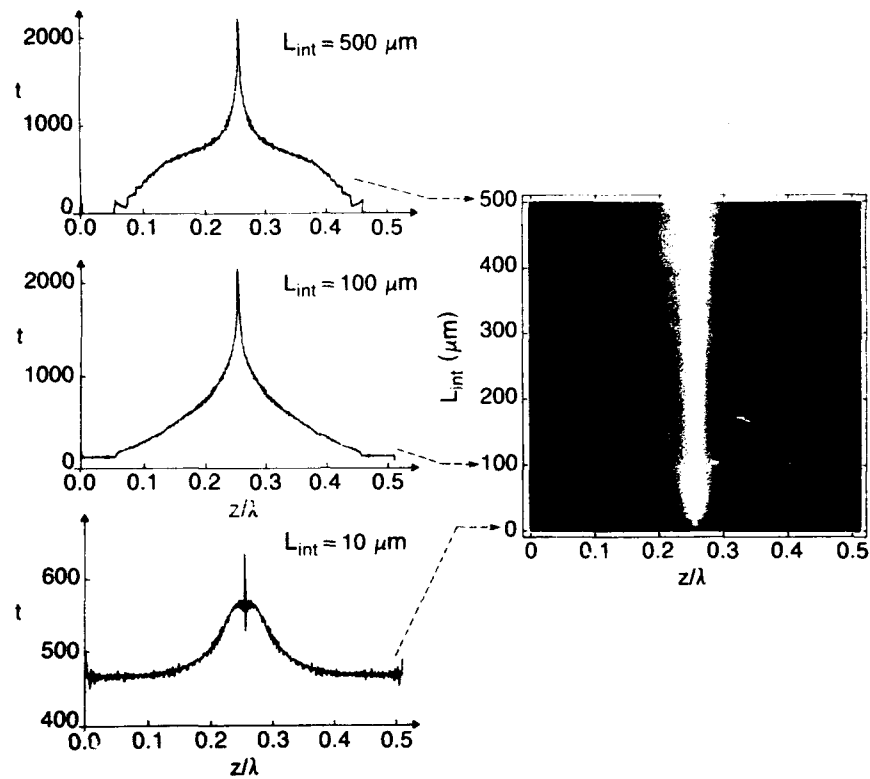


**Figure 3.** Semi-classical numerical simulations showing the thickness,  $t$ , of the film over a half wavelength field as a function of the interaction length,  $L_i$  for  $L_f=0$ ,  $\omega_k=100MHz$ , and  $\Delta=100MHz$ . On the right side of the figure is a density plot of the thickness as a function of  $z$  and  $L_i$ . On the left side of the figure there are three cross sections of  $t$  versus  $z$  taken at  $L_i=500$ ,  $100$ , and  $10\mu m$ . The narrow peak near  $z=\lambda/4$  is a result of the focusing action of the optical standing wave.

It may be possible to achieve lines even narrower than 10nm, however. For example, if the atomic beam is monoenergetic, the deleterious dispersion associated with a range of initial velocities would be minimized. (Light pressure forces could also be used to make a monoenergetic atomic beam; see Phillips et al.(1985).) Figure 4 compares the calculated profile of a film deposited by a Boltzmann beam and a monoenergetic atomic beam focused by a SW under the similar conditions. In Fig. 4(b),  $v_i=500m/s$  and  $L_i$  is chosen so that  $t_i=T/4$  exactly. Under these conditions, the width of the line is can be extremely narrow - less than 2nm!

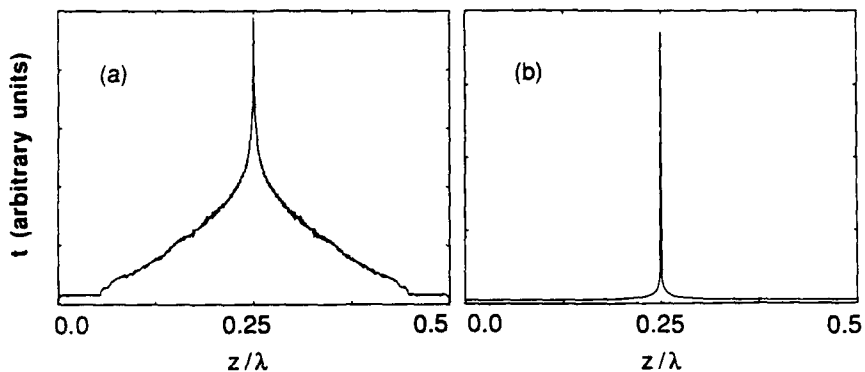


Figure 4. Semi-classical numerical simulations showing the thickness,  $t$ , profile of the film over a half wavelength field for: (a) an atomic beam with a Boltzmann distribution of the initial longitudinal velocities and (b) a monoenergetic atomic beam. The detuning of the SW is  $\Delta=100MHz$ ,  $L_i=100\mu m$ ,  $L_f=0$ , and  $\omega_R=100MHz$ . In (a) the average velocity is  $\bar{v}_i=500m/s$ , while in (b)  $v_i=500m/s$  exactly. The width (FWHM) of the narrow peak near  $\lambda/4$  is about  $10nm$  in (a), while in (b)  $FWHM<2nm$ .

In summary, we have focused an atomic beam into a  $294.5nm$  grating using the force exerted by an optical SW. Ultimately, our calculations show that the resolution of this type of optic is limited to about  $10nm$  for a thermal beam in the absence of surface diffusion. In principal, arbitrary features, within an area of  $\lambda/2 \times \lambda/2$ , could be made by manipulating the position of the nodes of a two-dimensional SW relative to the substrate during deposition. Finally, subnanometer resolution might be achieved using a monoenergetic atomic beam.

#### REFERENCES

Balykin V.I. and Letokhov V.S. (1987), Opt. Commun. 64, 151.  
 Bjorkholm J.E., Freeman R.R., Ashkin A., and Pearson D.B. (1980) Opt. Lett. 5, 111.  
 Carnal O., Sigel M., Sleator T., Takuma H., and Mlynek J. (1991), Phys. Rev. Lett. 67, 3231.  
 Gallatin G.M. and Gould P.L. (1991), J. Opt. Soc. Am. B8, 502.  
 Gordon J.P. and Ashkin A. (1980) Phys. Rev. A 21, 1606.  
 Phillips W.D., Prodan V., and Metcalf J. (1985), J. Opt. Soc. Am. 2, 1751.  
 Timp G., Behringer R.E., Tennant D.M., Cunningham J.E., Prentiss M., Berggren K.K. (1992), submitted to Physical Review Letters.

## Focused ion beam processing of mesoscopic quantum structures

P.M.Petroff, Z.Xu, Y.J.Li, M.Miller and M.Wassermeier. Materials Department and Electrical and Computer Engineering Department. University of California. Santa Barbara. CA 93106.

**ABSTRACT:** In this paper some of the fundamental aspects of ion implantation in III-V compounds semiconductors are revisited with the aim of processing mesoscopic devices using focused ion beam implantation. The spatial distribution and activation of implanted species(Ga and Si) in GaAs-AlGaAs quantum well structure are investigated and methods for controling them are introduced. Modulation doping and lateral band gap modulation on a mesoscopic scale are demonstrated. In situ processing of mesoscopic structures is also used to fabricate buried stressor structures and resonant tunneling devices.

### INTRODUCTION:

Focused ion beam implantation is a promising yet relatively unexplored technology with potential applications in the field of mesoscopic and nanostructures. It provides for a simpler processing approach of complex integrated structures since it is relatively easy to interface with an epitaxial growth system. In addition, the small ion probe size(50-100nm) is adequate for reaching mesoscopic or even quantum structure sizes.

In many respect, focused ion beam(FIB) is similar to conventional ion implantation(CII). It is surprising yet that CII processing has been used in only very few mesoscopic structures experiments. Indeed, the integration of various device types on the same wafer is routinely achieved with CII in the Si technology. This absence of CII processing applications in the field of quantum structures in compounds semiconductors may be traced to the complexity of the ion implantation process in these materials and to its poor understanding and control.

This paper reviews some of the fundamental processes of ion implantation. In particular, methods are proposed and demonstrated for controlling the nature of the damage, and the extent and spatial distribution of the implanted ions. Some specific applications to mesoscopic structure processing are then discussed.

### I) IMPLANTATION PROCESSES RELEVANT TO THE PROCESSING OF MESOSCOPIC AND QUANTUM STRUCTURES.

#### A) Spatial distribution of the implanted ions:

In CII implantation, the traditional approach has been to consider the ion projected range,  $R_p$  and localize the active part of the device at a depth close to  $R_p$ . This approach suffers from the inherent difficulty of completely annealing the implanted damage in a region of the material where maximum damage to the lattice was induced by the ion implantation.

We have avoided this approach since in most mesoscopic devices long elastic and inelastic mean free path as well as high luminescence efficiency are desirable. By using channeled ions which have lost most of their energy along the channel through electronic processes, we make use of the low damage to the lattice in that subsurface region corresponding to the channeling range  $R_c$ . By locating the active part of our devices near  $R_c$ , there is a reasonable chance of obtaining improved transport and luminescence characteristics because of the greater ease of annealing the lattice damage near  $R_c$ . An additional advantage associated with the use of channeled ions in such experiments is due to the fact that probe broadening due to ion straggling is no longer relevant since only ions which have not undergone straggling are effectively channeled..

The probe size conservation effect was demonstrated in a series of experiments where a 100nm  $\text{Ga}^+$  ions(100KV) probe was preserved 2500Å below the surface in a GaAs-AlGaAs quantum well structure [Laruelle et al.(1990 a and b)]. The stochastic nature of the ion implantation process and ion range in a solid may be a problem in mesoscopic structures where the depth as well as the lateral positioning of the ions must be achieved with a high degree of control.

This problem was made clear in a series of experiments aimed at using implantation enhanced interdiffusion for making quantum wires [Cibert et al (1986) and Hirayama et al ( 1988)]. The ion induced damage is used for enhancing locally the interdiffusion of Al and Ga across the interface of a GaAs-AlGaAs quantum well structure. The interdiffusion produces a wider band gap quantum well region which is used as a carrier confining barrier. The luminescence studies of interdiffused quantum wells show a confinement potentials as large as 90 meV [Laruelle et al (1990b) and Beinstingl et al (1991)]. The luminescence intensity of interdiffused quantum wells is as large as those of as grown quantum wells, however a broadening of the line is observed and excitation photoluminescence experiments fail to show the various expected excited quantum states recombination processes. This has been attributed to the non uniformity of the interdiffused quantum well thickness and to the depth distribution of the point defects generated near the quantum well interfaces.

To avoid this problem, we have proposed and demonstrated the use of a dechanneling layer [Beinstingl et al (1991)] that is pseudomorphically grown in the structure of interest. For example Figure 1 shows the type

of structures that were used in a series of experiments that are aimed at producing quantum wires and boxes using FIB induced interdiffusion. Layers 1 and 2 in Figure 1A are respectively  $\text{Al}_{0.3}\text{Ga}_{0.7}\text{As}$  and  $\text{GaAs}$  while layer 3 in Figure 1B is a pseudomorphic layer of  $\text{InGaAs}$  that is 1 or 2 or 3 monolayer thick.

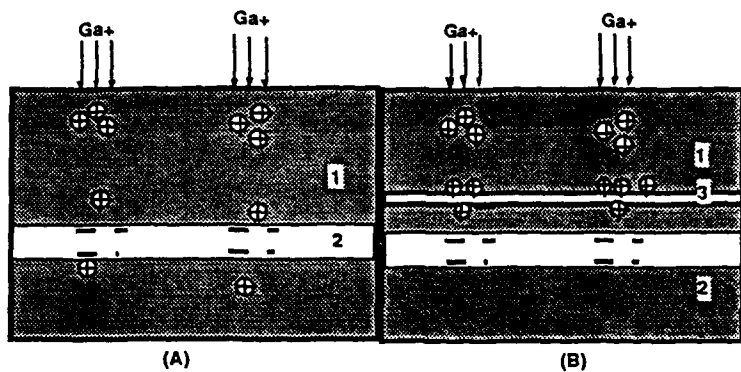


Fig. 1: Schematic of the channeling-dechanneling approach for ion or defect localization in a quantum well heterostructure. A) Implantation conditions where only channelled ions are used. B) The dechanneling layer(3) is increasing the dechanneling probability of those channelled ions near the channeling range  $R_c$ .

The elastic strain induced by this layer and the different mass of the atoms forming the channel are thought to be responsible for the dechanneling action [Petroff et al (1991)]. The pseudomorphic dechanneling layer is located at the channeling range  $R_c$ .

A clear indication that implantation enhanced interdiffusion was taking place more uniformly in the quantum well structure containing a pseudomorphic dechanneling layer was obtained from the measurements of the cathodoluminescence line width of the interdiffused quantum well region that were obtained after the  $\text{Ga}^+$  implantation and rapid thermal annealing. These results are shown in Figure 2.

The greatly reduced line width in the CL spectrum of the interdiffused regions is associated with a more uniform distribution of the point defects.

The effects of a pseudomorphic dechanneling layer are also supported by modulation doping experiments in a  $\text{GaAs-AlGaAs}$  quantum well structure identical to that shown in Figure 1.

In these experiments, the implanted species was  $\text{Si}^+$  ions. The modulation doped field effect transistors fabricated from the structures containing the dechanneling layers showed an increased mobility and carrier density over those of samples (without dechanneling layers) processed simultaneously which showed a

mobility of  $10^4$  cm $^2$ /Vs for a carrier density of  $5 \times 10^{12}$  cm $^{-2}$ . The improvement in the mobility (30%) is still modest and this is attributed to non optimized rapid annealing conditions during the activation of the Si $^{+}$  implanted ions.

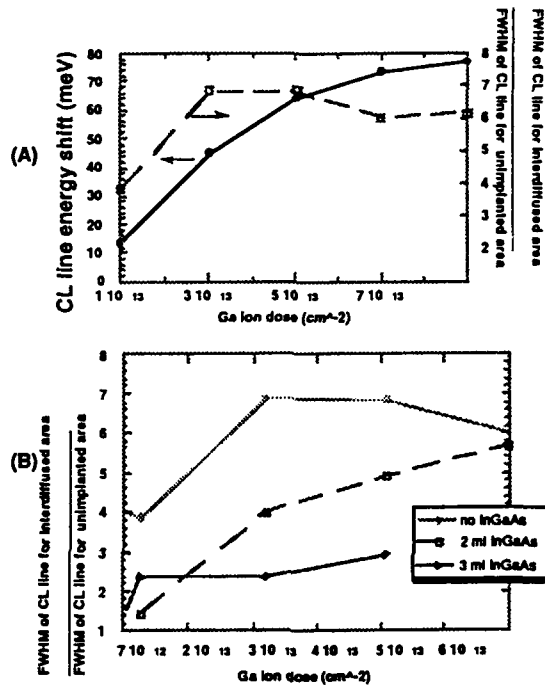


Fig. 2: A) Cathodoluminescence line energy shift measured at 10 $^0$ K in an implanted-interdiffused AlGaAs-GaAs quantum well structure as a function of Ga $^{+}$  (150KV) ion dose. Also shown in this panel is the CL line width increase from the implanted interdiffused region relative to that of the unimplanted region. B) Relative Cathodoluminescence line width for an interdiffused structure identical to that of A) but containing in addition 0, 2 or 3 monolayers of In $_{0.3}$ Ga $_{0.7}$ As as a function of implantation dose (After Beinstingl et al 1991).

The other important component to the spatial distribution of the ions is the lateral redistribution that is introduced by: a) the FIB probe current distribution and b) diffusion of point defects or implanted species during the rapid thermal annealing of the ion induced damage. Computation of the later show that it is dependent upon the point defect concentration i.e. the implantation dose and on the annealing temperature and times [Cibert et al (1987)]. An upper limit value for a dose of  $10^{13}$  cm $^{-2}$  and annealing at 900 $^{\circ}$ C for 10s is of the order of 500 $\text{\AA}$  for Ga $^{+}$  ions implanted in GaAs [Cibert et al (1987)]. This is a

fairly large increase in the effective spatial distribution of implanted ions. However, this quantity can be substantially minimized by using lower implantation doses and shorter annealing times. The FIB probe current distribution is composed of two gaussians and at high implanted dose, the effective probe size can be increased by as much as 200% because of this effect [Kubena et al (1991)]. It is clear that using low dose implants and low emission currents yield better defined and smaller implant regions.

**B) Defect annealing and dopant activation:**

Defect annealing is best achieved by rapid thermal annealing. Transmission electron microscopy studies indicate that the defect production rate is highly material dependent. For example several studies have confirmed that AlAs is more damage resistant to ion implantation than GaAs. There are some indications that interfaces and build in interfacial fields at heterojunctions may also play a role in the damage production and annealing [Bode et al (1991) and Ralston et al (1986)]. TEM studies have also established that no observable point defect clusters are observed in the channeling range region of the material. This suggests that annealing of individual point defects is effective near the end of the channeling range. In fact the simpler annealing kinetics near  $R_c$  are probably responsible for the relatively high dopant (Si) activation (25-30%) that have been observed in our experiments.

**IN SITU FOCUSED ION BEAM EXPERIMENTS FOR MESOSCOPIC STRUCTURES:**

We have used at UCSB both in situ FIB processing and conventional FIB processing for the fabrication of several types of mesoscopic structures in III-V compounds. The experiments are based on two coupled Varian GEN 2 Molecular Beam Epitaxy reactors and a high energy (150KV) focused ion beam implanter which are connected by a UHV shuttle that is used for transporting samples back and forth between the MBE systems and the FIB implanter. Figure 3 shows a schematic of the in situ processing FIB-MBE systems which also includes a reactive ion etching chamber. The base pressure in the system is below  $5 \times 10^{-10}$  Torr.

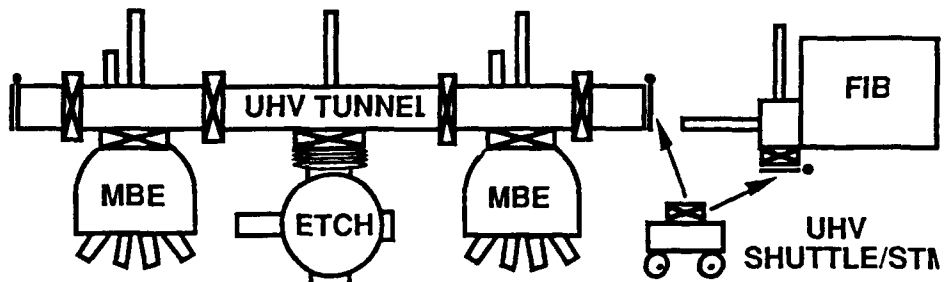


Fig. 3: Schematic of the UHV in situ FIB-MBE processing system. The UHV shuttle allows transfer of wafers back and forth between the MBE and UHV-FIB system. The MBE assembly also includes a reactive ion beam etching chamber.

The merits of such an approach are illustrated in the possible integration of complex electronic devices with optical devices on the same wafer [Wang et al (1990)].

The implementation of modulation doping for the manufacturing of a zero dimensional resonant tunneling device is demonstrated [Xu et al (1992)]. The processing which consists in a first MBE AlGaAs layer followed by a Si<sup>+</sup> FIB implant and a second regrowth step during which the resonant tunneling part of the structure is grown. A rapid thermal annealing at 850°C for 30s is applied before the final mesa etching and ohmic contacts to the emitter and collector parts of the device which is shown in Figure 4.

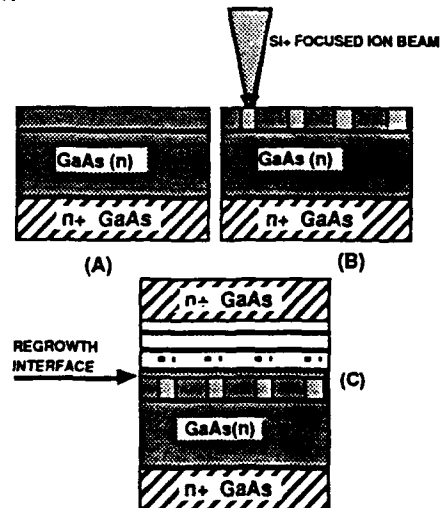


Fig. 4: Schematic of the processing sequence of mesoscopic tunneling diodes. Processing involves a regrowth step as indicated by the arrow in 4C) after the FIB implantation of Si<sup>+</sup> ions in 4B). The quantum well, spacer layer and collector layer thicknesses are respectively 50Å,

200Å and 250Å. The bottom GaAs near the n+ doped substrate is doped with Si ( $2 \cdot 10^{18}/\text{cm}^3$ ). The implanted dots are implanted with Si+ ions ( $2.5 \cdot 10^{13}/\text{cm}^2$ ) at an energy of 250KV.

The Si+ is implanted as dots by FIB. The Si+ ion lateral spreading is estimated at 1500Å including the lateral spread due to the annealing. The dot lattice period is 2000 Å for the sample with the I-V characteristics shown in Figure 5. The measured current peak to valley ratio at resonance are respectively 3.33 at 300°K and 10 at 77°K. Such values compare favorably to those obtained with devices entirely fabricated by molecular beam epitaxy.

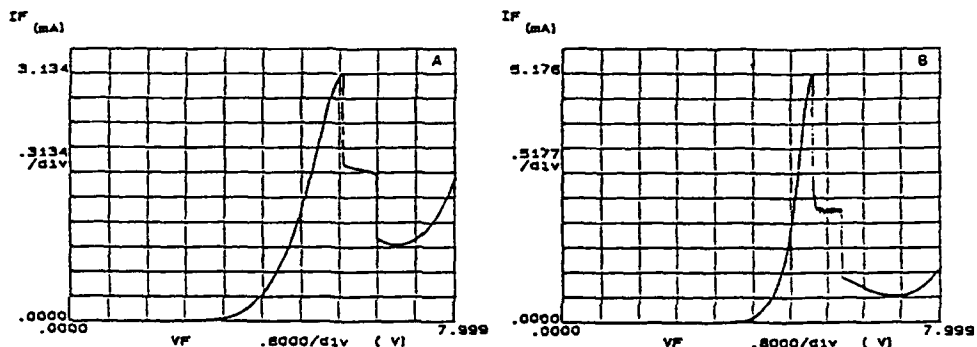


Fig. 5: I-V characteristics of a resonant tunneling device fabricated by in situ processing using a Si+ FIB implantation. A) Room temperature and B) Liquid nitrogen characteristics.

Reversed interface modulation doped FET have been also fabricated by using the FIB in situ processing [Xu et al (1992)]. Mobilities of  $2 \cdot 10^4 \text{ cm}^2/\text{Vs}$  at 4.2°K have been obtained for a carrier density of  $2 \cdot 10^{11}/\text{cm}^2$ . These results are encouraging and open interesting prospects for the fabrication of mesoscopic wire or dot channel modulation doped FET. We have also succeeded in fabricating the heavily doped source and drain regions as well as voltage probe contact regions using the FIB in situ implantation, thus opening future prospects with ultra short channels.

We have also developed an in situ processing method for buried stressor structures [Xu et al (1991)]. With such structures, a highly localized stress field generates a shrinkage of the materials band gap in a quantum well structure. The strain induced red shift has been demonstrated using surface stressors on GaAs-AlGaAs structures and applied towards demonstrating quantum wire confinement [Kash et al (1989)]. Theoretical calculations for buried stressors predict an

appreciable band gap shrinkage and 60-80 meV lateral confinement [Xu et al (1991)].

Figure 6 shows the schematic of the UHV processing for the fabrication of a buried stressor. First the growth of a pseudomorphic layer of  $\text{In}_{0.3}\text{Ga}_{0.7}\text{As}(60\text{\AA})$  on an  $\text{AlGaAs}$  epitaxial layer is carried out by MBE. The FIB is used for sputtering the  $\text{In}_{0.3}\text{Ga}_{0.7}\text{As}$  layer and leaves parts of this film as long thin wire strips ( $0.8\mu\text{m} \times 200\mu\text{m}$ ). The sputtering is carried out with  $100\text{KV Ga}^+$  ions. The sample is subsequently transferred back to the MBE reactor to grow a  $\text{Al}_{0.3}\text{Ga}_{0.7}\text{As-GaAs}$  quantum well structure. Quantum wells with thicknesses of  $60$  and  $80\text{\AA}$  are grown at different distances from the stressor interface. The stressor effects and quality are tested by low temperature cathodoluminescence(CL). A rapid thermal annealing at  $900^\circ\text{C}$  for 1 minute, was necessary to obtain a good luminescence from the parts of the quantum wells that were grown on top of the sputtered areas. As shown in Figure 7, the red shift in the band gap luminescence for an  $80\text{\AA}$  quantum well located at various distances above the stressor varies accordingly to the theoretical predictions [Xu et al (1991)].

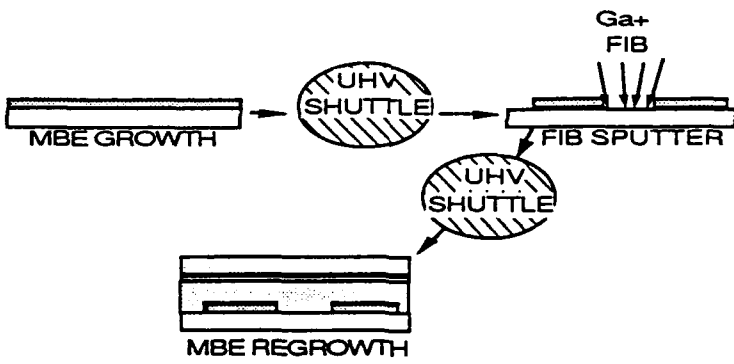


Fig. 6: Schematic of the processing sequence for stressor fabrication.

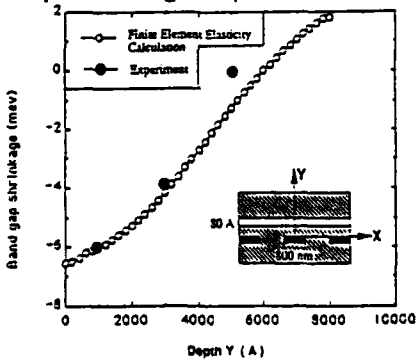


Fig. 7: Band gap shrinkage as a function of the distance between the stressor and the quantum well. The black circles are the experimental

points and the open ones are the computed values after reference by Xu et al (1991)

The total lateral confinement(electron and holes) for an 80Å quantum well located 1000Å above the stressor was 12.6meV. Larger lateral confinement energies (up to 80meV) should be easily achieved by using narrower stressors located closer to the quantum well[Xu et al (1991)].

**CONCLUSIONS:**

Focused ion beam implantation in III-V compounds semiconductors offers the prospect of a high resolution processing technology with potential applications for processing mesoscopic structures and ultimately quantum structures. Combined with in situ processing, modulation doping based MODFET devices, and resonant tunneling devices have been demonstrated. An essential component of the better performance of this type of devices using this technology is the preservation of the FIB probe size as well as the minimization of the implantation damage. We have presented a channeling-dechanneling approach which satisfies these two requirements.

**Acknowledgements:** The authors wish to acknowledge the support through out this work of the AFOSR and DARPA agencies and of "QUEST", an NSF Science and Technology Center.

**REFERENCES:**

W.Bainstingl, Y.J.Li, H.Weman, J.Merz and P.M.Petroff. *J.Vac Sci. Technol. B*, 9, 3479, (1991).  
M.Bode, A.Ourmazd, J.Cunningham, and M.Hong *Phys. Rev. Lett.* 67, 7, 843 (1991).  
J. Cibert, P. M. Petroff, G. J. Dolan, S. J. Pearton, A. C. Gossard and J. H. English. *Appl. Phys. Lett.*, 49, 1275 (1986).  
J.Cibert and P.M.Petroff *Phys. Rev. B* 36, 3243, (1987).  
Y. Hirayama, S.Tarusha, Y.Suzuki, and H.Okamoto *Phys. Rev. B* 37, 2774 (1988).  
K.Kash, R.Bhatt, D.D.Mahoney, P.S.D.Lin, A.Scherrer, J.M.Worlock, M.Koza, and P.Grabbe, *Appl. Phys. Lett.* 55, 681, (1989).  
R.Kubena and J.W.Ward *Appl. Phys. Lett.* 51, 1960 (1991).  
F. Laruelle., A. Bagchi, M. Tsuchiya, J. Merz and P.M.Petroff *Appl. Phys. Lett.* 56,1561(1990 a).  
F.Laruelle, P.Hu, X. Qian, R.Simes, W.Robinson, J.Merz and P.M.Petroff. *Surf. Science*,228, 306, (1990 b).  
P.M.Petroff et al. *J.Vac. Scien. Technol. B*, 9, (1991).

J.Ralston, G.W.Wicks, L.F.Eastman, B.C.DeCooman and C.B.Carter, J.Appl. Phys. 59, 1, 120, (1986).  
Z.Xu, M.Wassermeier, and P.M.Petroff (to be published (1992).  
Z.Xu and P.M.Petroff. Appl. Phys. Lett.69,9,6564 (1991).  
Y.L.Wang, H.Temkin, L.R.Herriot, R.A.Hanon, and J.S.Wiener Appl. Phys. Lett. 57, 1672, (1990).

## **Fabrication and spectroscopic studies of InP/GaInAs/InP and GaAs/GaInAs/GaAs quantum-well wire structures**

**L Samuelson, K Georgsson, A Gustafsson, I Maximov, L Montelius, S Nilsson, M-E Pistol,  
W Seifert and A Semu**

**Department of Solid State Physics and the Nanometer Structure Consortium  
University of Lund, Box 118, S-221 00 LUND, Sweden**

**ABSTRACT:** Quantum-well wire (QWW) structures have been fabricated by electron-beam lithography and etching. The original sample structures consisted of 30 Å thick quantum wells of GaInAs embedded in either InP or GaAs. Methane plasma based etching was used for fabrication of wires in the InP/GaInAs system while wet etching was used for the GaAs/GaInAs system. In both cases were obtained wires with effective widths less than 100 nm. Proof of the existence of the wires in the processed material was obtained and spectroscopic studies on individual wires have been made using low-temperature cathodoluminescence by which individual wires have been directly imaged. These studies demonstrate the fabrication of well-defined  $\leq 50$  nm wide wires having properties suitable for optical applications.

### **1. INTRODUCTION**

In the strive towards the realization of quantum-dominated semiconductor materials (Weisbuch and Vinter (1991)) whose properties have the advantages of quantum-wires two main approaches are taken; either direct growth of wires on vicinal or patterned surfaces or etching in pre-fabricated quantum-wells which, in this way, are carved into wires. This paper deals with the latter approach in which we first grow a sample with a well-characterized quantum-well positioned within a few hundred nm from the surface. Patterns of wires are made on top of the surfaces using electron-beam lithography with either polymethylmethacrylate (PMMA) or copolymer as resist. This resist mask is used directly as an etch mask and the different etching processes are optimized for controlled fabrication of narrow wires and for low-damage conditions. In all studies of low dimensional structures it is absolutely essential to prove the existence of these structures and to be able to image them and control the material quality after processing. We have, besides high-resolution scanning-electron microscopy (SEM), applied low-temperature cathodoluminescence (CL) by which we are able to observe and image the individual wires. CL has also allowed us to take spectra on such wires and to track the luminescence along the length of a single wire.

## 2. EXPERIMENTAL

Three different processing steps enter into this study:

(i) the epitaxial growth of single- or multi-layer epitaxial structures. Reduced pressure metal-organic vapour phase epitaxy (MOVPE system VP 502RP from Epiquip) has been used for growth of thin QW structures either of the type GaAs/Ga<sub>0.85</sub>In<sub>0.15</sub>As/GaAs or InP/Ga<sub>0.53</sub>In<sub>0.47</sub>As/InP. These starting materials are selected for their very efficient QW luminescence and low defect densities (Seifert *et al.* 1990). In order to further improve the possibilities for imaging of the QWWs, effects of minority carrier diffusion could be further reduced by placing a thicker GaInAs-layer under the QWW to be studied, thereby avoiding, or at least reducing, capture of carriers generated within a diffusion length from the QWW.

(ii) electron-beam lithography with PMMA as electron sensitive resist for InP-based structures and with copolymer for GaAs-based structures. The thicknesses of the resist was typically 200 nm and 50-100 nm, respectively. Exposure doses of around 400 and 20  $\mu\text{C}/\text{cm}^2$ , respectively, were employed using 40 keV acceleration in a JEOL 6400 SEM equipped with LaB<sub>6</sub>-emitter and Raith ELPHY pattern generation system.

(iii) etching using

(a) a CH<sub>4</sub>/H<sub>2</sub> plasma in both RIE (Semu and Silverberg (1991)) and ECR modes for the InP/Ga<sub>0.53</sub>In<sub>0.47</sub>As/InP system with special emphasis on the minimization of etching induced damage, as evaluated from the diode quality factor in I/V-curves of Schottky-diodes made on processed surfaces and from the PL intensity. Special care was taken to run the plasma process in a mode such that the developed PMMA-mask could be used directly as a plasma etching mask. Features as small as 30 nm in width after the etching process with straight side walls and with smooth etched surfaces have been fabricated by ECR-plasma etching.

(b) a wet etching solution of 1000:1:8 of

H<sub>2</sub>O/H<sub>2</sub>SO<sub>4</sub>/H<sub>2</sub>O<sub>2</sub> for Ga<sub>0.85</sub>In<sub>0.15</sub>As/GaAs. In this case a process was developed (see Figure 1) in which the under-cutting of the wet etch and the development of low etch rate surfaces were used for the fabrication of pyramid-shaped ridges with the QWs forming buried layers inside the pyramids. Depending on the etch-depth, the wire width defined by the width of the pyramid at the height of the buried QW varies from  $\sim 40$  nm down to zero width.

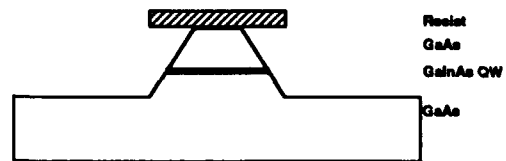
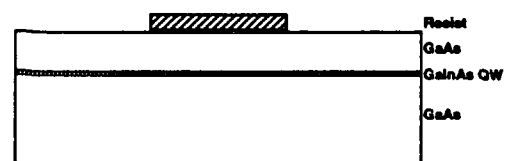


Figure 1. Simplified description of the methods used for fabrication of QWWs in GaAs/Ga<sub>0.85</sub>In<sub>0.15</sub>As/GaAs using, for definition of buried QWs in the top of the pyramids, H<sub>2</sub>O/H<sub>2</sub>SO<sub>4</sub>/H<sub>2</sub>O<sub>2</sub> as etchant.

The fabricated wire material was characterized in a secondary-electron detection mode using a scanning electron microscope equipped with a field-emission gun (JEOL 6400F) and by low-temperature photoluminescence (PL) and cathodoluminescence (CL). In this paper we restrict the optical studies to CL, the system for CL-studies described in Figure 2. The temperatures used were  $\approx 20$  K, which is sufficiently low for thermal quenching and broadening to be negligible. The photons emitted as a response to the electron-beam excitation were dispersed by a 0.5 m monochromator and detected either by a LN<sub>2</sub>-cooled Ge-detector or by a thermoelectrically cooled GaAs photomultiplier.

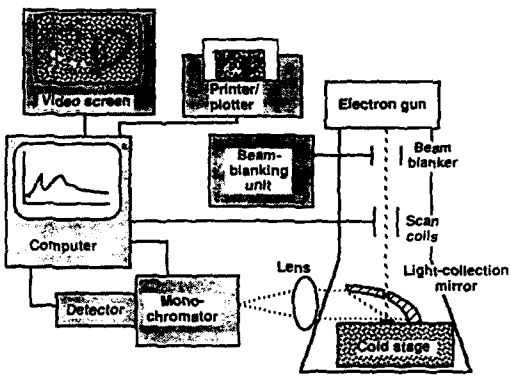


Figure 2. The CL detection system.

### 3. RESULTS AND DISCUSSION

(a) Wires were fabricated in InP/Ga<sub>0.53</sub>In<sub>0.47</sub>As/InP using CH<sub>4</sub>/H<sub>2</sub> RIE, giving reasonably straight walls and not too large damage. Using a trend of increasingly larger doses we have been able to make wires of good optical quality having geometrical dimensions down to 150 nm and with the effective electron confinement widths going down to  $\leq 50$  nm. This effective width can be estimated from the depletion widths from the etched side-walls forming a shallow parabolic well (see insert below). Figure 3a shows a CL image where the resolution is sufficiently good (better than 200 nm) for imaging of individual wires. This resolution is enhanced by the presence of a thicker GaInAs blocking layer below the QW, preventing carrier diffusion into the QW. In Figure 3b is shown a set of CL spectra obtained from wires of decreasing width going from (top curve) the unprocessed original QW to progressively smaller wire-widths for the lower curves, ending with 150 nm wires.

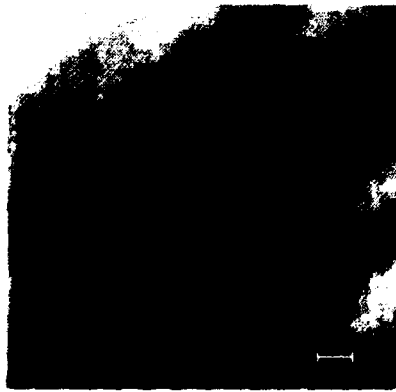


Fig. 3a. CL image of the fabricated wires.

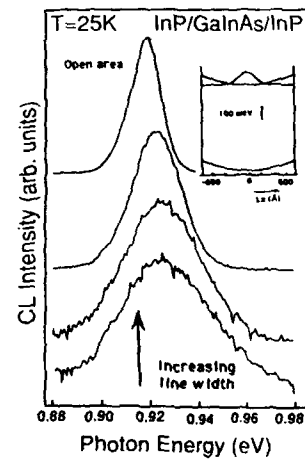


Fig. 3b. CL spectra for different wire widths.

(b) For GaAs/Ga<sub>0.85</sub>In<sub>0.15</sub>As/GaAs we have developed wet etching as described in Section 2. The top layer of GaAs is first removed using PL to evaluate the etch depth as a function of time. With the H<sub>2</sub>O/H<sub>2</sub>SO<sub>4</sub>/H<sub>2</sub>O<sub>2</sub> etchant we were able to control the formation of triangularly shaped surface features. Since the original sample contained four QWs of thickness  $\approx$ 30 Å with GaAs barriers of thickness 250 Å in-between, we expect that the top of the pyramid will contain between four and zero remaining QWWs. Three wire widths are shown in Figure 4, obtained from sections of the wafer with different design widths and different exposure levels. The left column shows CL images, the central column shows SEM-images and, finally, the third column shows the corresponding spectral distributions of the CL. To explain the absence of a clear blue-shift, which is expected for the QW closest to the peak of the pyramid, we note that the QWs positioned below this squeezed QW will preferentially be excited from the CL excitation and dominate. In future experiments this will be avoided by the use of similar blocking layers as used for InP/GaInAs/InP QWWs.

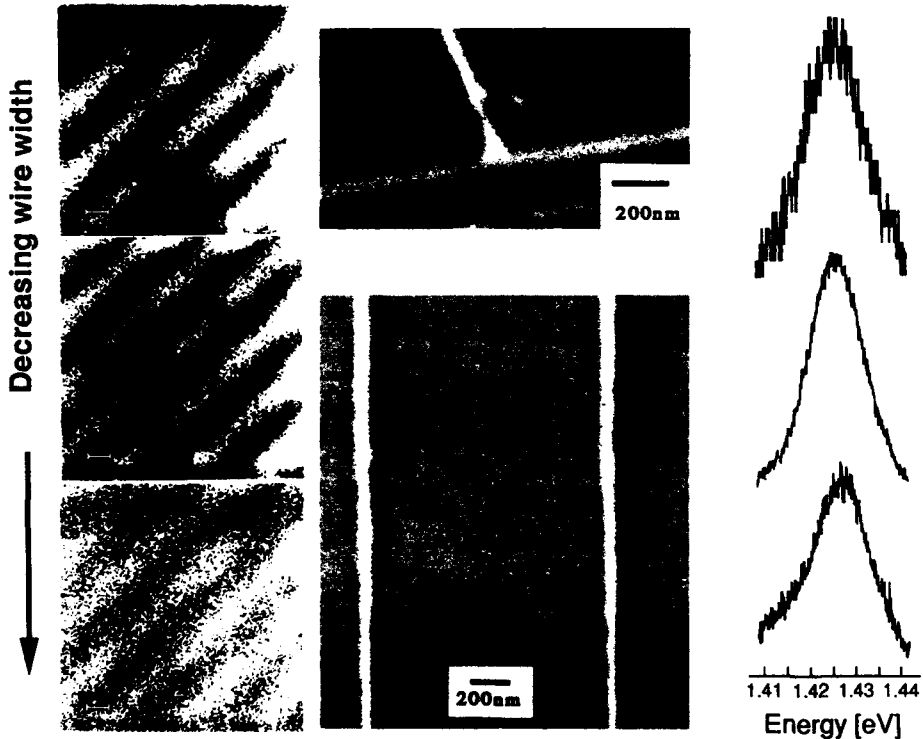


Fig. 4a. CL images of wires. Fig. 4b. SEM-images of wires. Fig. 4c. CL spectra of wires.

ACKNOWLEDGEMENTS: This work was supported by grants from NUTEK and NFR.

#### REFERENCES:

Gustafsson A 1991 Thesis, Lund University  
 Seifert W, Fornell J-O, Ledeborg L, Pistol M-E and Samuelson L 1990 *APL* **56**, 1128  
 Semu A and Silverberg P 1991 *Semicond. Sci. and Technol.* **6**, 287  
 Weisbuch C and Vinter B 1991 *Quantum Semiconductor Structures* (London, Acad. Press)

## **Observation of quantum confinement in strain-induced quantum wires/dots**

I-Hsing Tan, Takashi Yasuda, Richard Mirin, David Lishan, Evelyn Hu, John Bowers, and James Merz

Electrical and Computer Engineering Department  
University of California, Santa Barbara, CA93106, U.S.A.

**Abstract:** Low-damage dry and wet etching techniques were used to fabricate the quantum wires and dots structures using strain-induced lateral band edge modulation. By patterning the compressively strained InGaAs layer into a series of wires and dots, which overlie the GaAs quantum well, we have observed the lateral confinement of carriers in the photoluminescence (PL) spectra with high luminescence efficiency.

### **1. INTRODUCTION**

Much recent research has focused on electrical transport and optical properties of quantum wires and dots. A variety of techniques have been proposed and utilized in the fabrication of these quantum structures. Kash et al. have suggested that the introduction of modulated strain to a material structure could be used to achieve lateral quantum confinement of carriers. The lateral modulation of the band gap of a quantum well (QW) is achieved by patterning an overlayer of compressively strained material into arrays of wires or dots. The actual quantum structures are therefore buried beneath the surface and have a greater immunity from process-induced damage. We report here on the use of both low-damage dry and wet etching techniques to fabricate strain-induced quantum wires (SIQWs) and strain-induced quantum dots (SIQDs) with high quantum efficiency. We have studied their subband transition probability due to lateral quantum confinement and valence band-mixing effects.

### **2. FABRICATION AND PL STUDY OF SIQWS**

The starting material was a compressively strained  $In_{0.35}Ga_{0.65}As$  layer, 6 nm in width, which overlies a GaAs QW, 6 nm in width. Holographic lithography and low-damage HCl radical beam etching were used to define the grating patterns which had a 230 nm pitch. The slow (~2.5 nm/min), well-controlled HCl etch essentially stopped on the AlGaAs layer, but continued in the lateral direction. The wire width therefore depends on the etch time. Figure 1(a) is a schematic representation of a quantum wire structure.

Because of the strain release on the side walls of the etched InGaAs stressors, a pattern of inhomogeneous strain forms in the underlying GaAs QW. Solving both the elasticity equation and the Luttinger four-band model with strain allows us to model the effect of the strain on the energy band edges of the GaAs QW and the subband transitions. The band edge modulation for a wire width of 75 nm is shown in Figure 1(b). Our calculations show that for wire widths greater than 65 nm, the mixing of the valence band by shear strain components results in a double well in the valence band edge. We identify subband transition peaks P<sub>2</sub> and P<sub>3</sub>, the peak P<sub>0</sub> corresponding to the as-grown sample, and P<sub>1</sub> from the QW beneath the etched surface. Because of volume dilation at the center of wire stressor inside the QW, P<sub>2</sub> and P<sub>3</sub> are calculated to be red-shifted in energy by 19.7 and 12.5 meV, respectively, relative to P<sub>0</sub>, while P<sub>1</sub> is relatively unshifted.

We have carried out excitation intensity-dependent PL measurements on arrays of SIQWs of 75 nm width at 1.4 K to confirm the subband transitions. The spectra are shown in Figure 2. Curve (a) of Figure 2 is the spectrum for the as-grown sample taken at an excitation intensity of 0.1 W/cm<sup>2</sup>. The peak position, P<sub>0</sub>, is not substantially changed through variation of the excitation intensity from 0.1 to 100 mW/cm<sup>2</sup>, using the 488 nm excitation of an argon ion laser. Curve (b) is the spectrum for the etched sample, also taken at 0.1 W/cm<sup>2</sup> excitation intensity; the low-energy peak, P<sub>2</sub>, corresponds to the transition from the SIQW area; the higher-energy peak, P<sub>1</sub>, is from the QW beneath the etched surface. The integrated intensity over the PL spectrum for the etched sample is

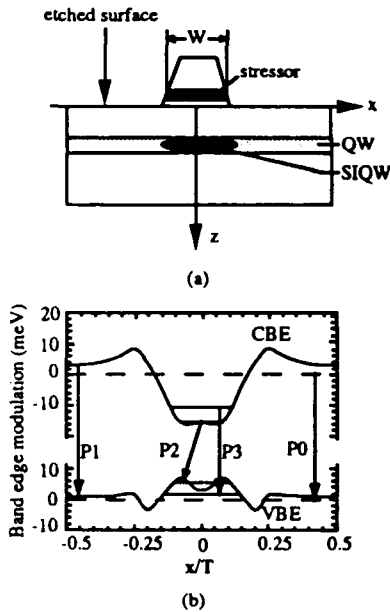


Figure 1 (a) material structure. W is the width of wire stressor. (b) Band edge modulation diagram. The solid curves indicate the modulation for conduction band edge (CBE) and valence band edge (VBE), while the dashed lines indicate the energy levels before perturbation. T is the pitch of grating.

nearly the same as that for the as-grown sample, confirming the low-damage nature of the HCl radical beam etching. We calculate an oscillator strength of the first subband transition that is smaller than that of the second subband transition. This result is borne out by the PL data. The SIQWs display only two peaks (P1 and P2) at lower excitation intensity; at higher excitation energy, P3 becomes visible, in addition to P1 and P2. Figure 2 indicates that the peak P2 shifts to the red by  $19.5 \pm 0.5$  meV relative to P0, and the subband splitting between P2 and P3 is  $7.5 \pm 0.5$  meV, consistent with our modelling.

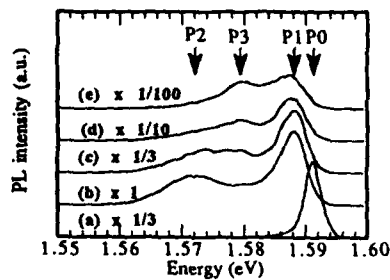


Figure 2 Excitation intensity-dependent PL spectra. (a) is for the as-grown sample, taken at  $0.1 \text{ W/cm}^2$ . (b)-(c) are for the etched sample taken at different excitation intensity: (b) 0.1, (c) 0.3, (d) 1, (e)  $10 \text{ W/cm}^2$ .

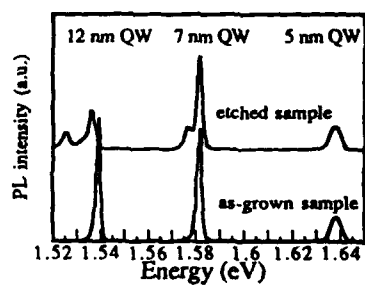


Figure 3 PL spectra for the as-grown sample and the SIQD sample. The excitation intensity is  $0.5 \text{ W/cm}^2$ . The bottom curve is the spectrum for the as-grown sample.

Although the PL spectra give evidence of lateral carrier confinement and subband transitions with high luminescence efficiency, the peak linewidths are broad. The possible reasons for this broadening include misfit dislocations generated in the highly strained material, pattern non-uniformity, and the effect of oxides formed on the etched surface of the AlGaAs layer.

### 3. FABRICATION AND OPTICAL STUDY OF SIQDS

The starting material for the SIQDs comprised a 6 nm strained layer of  $\text{In}_{0.3}\text{Ga}_{0.7}\text{As}$  overlying three QWs, 12, 7, and 5 nm in width, which were separated by 22, 54, and 154 nm, respectively, from the stressor. This material structure was adopted in order to improve the linewidth of the PL spectrum, to more clearly observe strain-induced shifts and to understand how deeply the strain can propagate into the material. A holographic grating was first formed along one direction in the photoresist-coated substrate; the substrate was subsequently rotated  $90^\circ$  for a second grating exposure. The dot photoresist grating then served as a mask for etching. To further simplify the processing, we used saturated bromine water/ $\text{H}_3\text{PO}_4$ /deionized water to etch the material. The etch rate for all the material is about 15 nm/min. The lateral dimension

of the dot is about 120 nm, after having been etched for two and a half minutes. The bottom curve in Figure 3 shows the PL spectrum for the as-grown sample. The peak positions of those excitonic transitions are 1.5393, 1.5815, and 1.6380 eV, corresponding to the 12, 7, and 5 nm QWs, respectively. The upper curve in Figure 3 is the spectrum for the etched sample. The excitons from the two QWs closest to the stressor are split into two peaks; the lower-energy peak is from the SIQD area and the higher-energy one is from the QW beneath the etched surface. The redshifts of the lower-energy peak from the first two wells are 14.0 and 4.8 meV, respectively, relative to the peak positions from the as-grown sample. The linewidths from the 12 nm QW for the etched sample are only ~1.5 meV broader than the peak linewidths of the as-grown sample. The linewidths from the other two wells in the SIQD structure remain the same as for the as-grown sample. The integrated intensity over the spectrum for the 12 nm well in the SIQD structure degrades by 20%; the intensities corresponding to the other two, deeper wells in the SIQDs do not show any degradation, compared to the as-grown sample.

#### 4. CONCLUSION

We have demonstrated the use of compressively strained InGaAs layer as stressors to laterally modulate band edges of GaAs QWs. For the SIQW structures, we have taken the advantage of etch selectivity of HCl radical beam to study the wire width-dependence of strain-induced redshift. The subband transitions observed were in good agreement with simulation results, calculated using the Luttinger four-band model with strain. The proper design of the material structure used in the SIQD structures, allowed greater resolution in the determination of strain-induced confinement. The high luminescence efficiency of the PL spectra of our SIQWs and SIQDs confirm the low-damage nature of our fabrication techniques.

#### REFERENCES

Kash K, Worlock J M, Sturge M D, Grabbe P, Harbison J, Scherer A, and Lin P S D, *Appl. Phys. Lett.* **53**, 782 (1988).  
Kash K, Van der Gagg B P, Mahoney D D, Gozdz A S, Florez L T, and Harbison J P, *Phys. Rev. Lett.* **67**, 1326 (1991).  
Gershoni D, Weiner J S, Chu S N G, Baraff G A, Vanderberg J M, Pfeiffer L N, West K, Logan R A, and Tanbun-Ek T, *Phys. Rev. Lett.* **65**, 1631 (1990).  
Tan I-H, Lishan D, Mirin R, Jayaraman V, Yasuda T, Hu E L, and Bowers J, *Appl. Phys. Lett.* **59**, 1875 (1991).  
Tan I-H, Lishan D, Mirin R, Jayaraman V, Yasuda T, Prater C B, Hu E L, Bowers J, and Hansma P K, to be published in *J. Vac. Sci. Tech. B*, Nov/Dec.  
Luttinger J M and Kohn W, *Phys. Rev.* **97**, 869 (1955).  
Baheler T B, *Phys. Rev. B*, **42**, 11992 (1990).

## **Lateral barrier modulation—a new technique for the definition of high quality quantum wires and dots for optical investigations**

Ch Gréus, A Orth, J Straka, K Pieger, A Forchel

Technische Physik, Universität Würzburg, Am Hubland, D-8700 Würzburg, Germany

**ABSTRACT:** We have developed a new approach for the definition of low dimensional semiconductor structures. Using a selective wet etch process the top barrier material of a quantum well substrate is removed between masked regions to obtain a lateral confinement. We have fabricated buried InGaAs/GaAs quantum wires with geometrical widths down to 25 nm. We obtain high quantum efficiencies from all wires and observe a strong blue shift of the emission energy for the smallest wires.

### **1. INTRODUCTION**

Effectively one- and zero-dimensional semiconductor structures have been intensely investigated recently because the physical properties can be controlled by changing the dimensions of these structures.

For the realization of quantum wire and dot structures for optical studies and future optoelectronic applications showing lateral confinement most commonly a semiconductor quantum well substrate is patterned by dry or wet etching (Izrael et al., Clausen et al.) or impurity induced disordering (Hiramoto et al.). In particular for etched structures the quantum efficiency of the nanometerstructures is severally limited by surface recombination and process induced defects (Maile et al.).

In this paper we report a new and simple approach for the definition of effectively buried nanostructures. Using a selective etchant the top barrier material of a quantum well is locally modulated leading to a confinement of the carriers. The optical investigation of the structures yields high quantum efficiencies for all wire widths and a significant blue shift of the emission for the smallest wires.

### **2. CONCEPT OF LATERAL BARRIER MODULATION**

We have developed a simple approach to define buried InGaAs quantum wires. The essential technological step is a single selective etch process by which the material of the top barrier layer

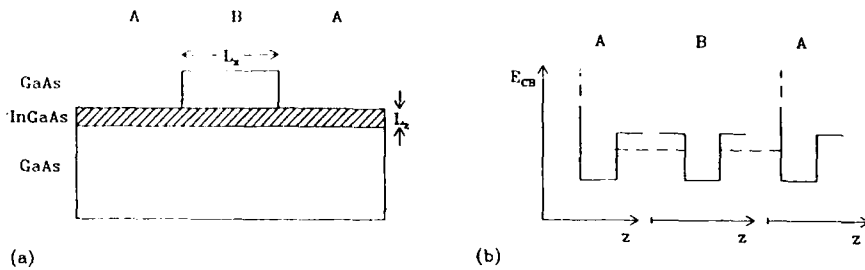


Fig. 1. Schematic design of a quantum wire or dot structure defined by a modulation of the top barrier. The modulation of the top barrier material (surface quantum well region (A), semiconductor covered region (B)) induces a change of the quantization energy along the quantum well plane, which provides a lateral confinement of the carriers.

is locally removed. Figure 1 displays schematically the layer structure of the processed sample. Due to the selective removal of the top barrier material of the quantum well the symmetrical potential well of the starting material is locally replaced by a quantum well with a vacuum barrier on one side. For sufficiently thin quantum wells the quantization energy depends on the energy band discontinuity between well and barrier material. Therefore the high energy barrier at the quantum well - vacuum interface is expected to lead to a significant increase of the quantization energy in the etched regions compared to the semiconductor covered structures. Due to the different quantization energies the InGaAs layer itself serves as lateral barrier which leads to a lateral confinement of the carriers in the masked regions.

As shown in figure 1 the mesoscopic structures can be regarded as electron hole waveguides in close analogy to conventional waveguide structures. The most obvious difference to optical waveguides is given by the waveguide widths. The width of the electron hole waveguides is determined by the de Broglie wavelength of the carriers whereas the width of the optical waveguides is determined by the wavelength of the light. This results in typical widths of the electron hole waveguides on the order of 30 nm or below.

We would like to point out that the strain present in our pseudomorphic structures does not provide the lateral confinement. Due to the used etch process only the lattice matched top barrier layer is locally patterned, whereas the stressed InGaAs layer remains over the whole plane.

Compared to the conventional deep etching our approach has a number of advantages: (i) Due to the use of wet etching our process does not induce defects. There is no patterning of the active material which is therefore maintained in the high quality realized by the epitaxy. (ii) Our technique provides effectively buried wires by using a change of the energy band structure of the quantum well material due to the modulation of the barrier material. (iii) By using overgrowth of the selectively etched structures with a high band gap semiconductor the lateral confinement due to the barrier modulation can be maintained and at the same time the wire or dot pattern can be integrated in e.g. a waveguide.

### 3. INVESTIGATION OF SEMICONDUCTOR WIRES DEFINED BY LATERAL BARRIER MODULATION

The starting material for the quantum structures are undoped (Al)GaAs/InGaAs/GaAs single quantum wells grown by molecular beam epitaxy on (100) oriented GaAs substrates. The 5 nm thick  $In_{0.18}Ga_{0.82}As$  quantum well is covered by a 20 nm GaAs top barrier layer. By high resolution electron beam lithography and selective wet etching with  $H_2O_2$  buffered with  $NH_4OH$  (Gréus et al.) wires with geometrical width between 1  $\mu m$  and about 25 nm have been defined. For comparison, deep etched wires were fabricated by using  $H_2O:H_2SO_4:H_2O_2 = 1200:1:8$ .

We have investigated the luminescence spectra of wires defined by the barrier modulation technique in comparison with deep etched wires at different temperatures. At a temperature of 2 K the emission intensity of the open wires decreases by about an order of magnitude if the wire width is reduced from 1  $\mu m$  to 170 nm. In the same width range the barrier modulated wires show, in contrast, a significantly increased quantum efficiency which decreases only slightly for smaller wire widths. Figure 2 shows the ratio of the emission intensity of the barrier modulated structures and the deep etched wires versus the geometrical wire width. For a temperature of 2 K the quantum efficiency of the barrier modulated wires is higher by more than one order of magnitude than the efficiency of the deep etched structures for wire widths below about 150 nm. For higher temperatures the open wires show a stronger decrease of the emission intensity with decreasing wire width than at 2 K due to increased sidewall recombination. The emission efficiency of the buried wires defined by selective barrier modulation is significantly less affected by the temperature increase. Therefore the ratio of the emission intensities shows a stronger increase with decreasing wire width for higher temperatures.

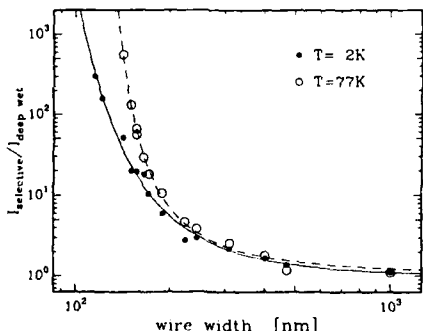


Fig. 2. Ratio of the emission intensity of barrier modulated wires and deep wet etched wires vs geometrical wire width. Full symbols: 2 K, open circles: 77 K (lines are guides for the eye only).

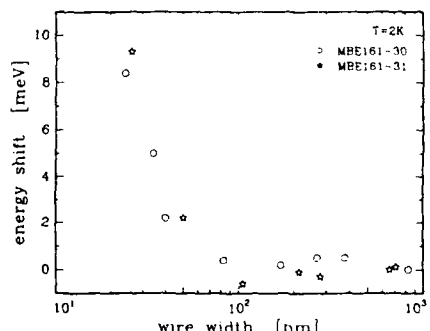


Fig. 3. Blue shift of the emission energy vs geometrical wire width.

For the smallest wires defined by barrier modulation we observe a significant shift of the emission energy to higher values compared to the two-dimensional reference sample. Figure 3 displays the shift of the emission energy as a function of the wire width. For geometrical wire

widths above 100 nm no shift of the emission energy is seen, which is consistent with theoretical expectations. For wires with widths below 100 nm the emission energy shifts continuously to higher values with decreasing wire width. In the case of the smallest wires (geometrical width 25 nm) the shift amounts to about 9 meV. We attribute this blue shift to the lateral quantum confinement of the carriers in the barrier modulated wires. Simple theoretical estimates of the quantization effects yield an energy shift of about 6.5 meV for 25 nm wire width. In the lateral barrier regions about 1.5 nm of the InGaAs quantum well are removed due to the finite selectivity of the etch process used (Gréus et al.). Taking into account these reduction of the layer thickness of the lateral barrier our simple model yields a shift of about 8.5 meV for the 25 nm wires which is in good agreement with the experimental observed value.

#### 4. CONCLUSIONS

We have fabricated InGaAs/GaAs quantum wires using a selective wet etchant. Due to the corresponding modulation of the barrier the active layer itself serves as a lateral barrier. Therefore our process leads to effectively buried structures with high quantum efficiency showing confinement effects for the smallest wires with geometrical width of 25 nm. We would like to point out that the geometrical dimensions of the present structures are comparable or even significantly smaller than the widths of previously prepared deep etched wires (Kohl et al., Maile et al.). Different to a number of previous approaches we are able to correlate the emission energy shift to the geometrical width of the structures, i.e. we observe no indications of optically inactive ("dead") sidewall layers. In conjunction with the rather weak variation of the quantum efficiency with the wire widths we therefore expect that wires with geometrical width in the 10 nm range may be realizable by our approach.

We gratefully acknowledge the financial support of this work by the Deutsche Forschungsgemeinschaft.

#### REFERENCES

Clausen E M, Jr, Craighead H G, Worlock J M, Harbison J P, Schiavone L M, Florez L and Van der Gaag B, *Appl. Phys. Lett.* **55**, 1427 (1989).  
Gréus Ch, Forchel A, Straka J, Pieger K and Emmerling M, submitted to *J. Vac. Science Technol. B*.  
Hiramoto T, Hirakawa K, Iye Y and Ikoma T, *Appl. Phys. Lett.* **54**, 2103 (1989).  
Israel A, Sermage B, Marzin J Y, Ougazzada A, Azoulay R, Etrillard J, Thierry-Mieg V and Henry L, *Appl. Phys. Lett.* **56**, 830 (1990).  
Kohl M, Heitmann D, Grambow P and Ploog K, *Phys. Rev. Lett.* **63**, 2124 (1989).  
Maile B E, Forchel A, Germann R, Straka J, Korte L and Thanner C, *Appl. Phys. Lett.* **57**, 807 (1990).

### **Ultra-fine AlGaAs/GaAs quantum-well wire fabrication combining electron beam lithography and wet chemical etching**

Y. Shiraki, S. Fukatsu, and R. Ito

*RCAST, The University of Tokyo, Komaba, Meguro-ku, Tokyo 153*

E. Ishikawa and K. Onabe

*Dep. of Applied Physics, The University of Tokyo, Bunkyo-ku, Tokyo 113*

K. Momma and N. Ogasawara

*Dep. of Electronics Engineering, University of Electro-Communications, Chofu-shi, Tokyo 182, Japan*

Ultra-fine AlGaAs/GaAs quantum-well wires with smooth sidewall surfaces were successfully fabricated by combining electron beam lithography and two-step wet etching techniques. Photoluminescence measurement revealed that the thickness of the non-radiative surface layer formed during processing was remarkably reduced even for the wires in the quantization regime and the blue shift in photoluminescence due to quantum confinement was observed.

One-dimensionality and zero-dimensionality receive growing attention due to their modified optical and electrical properties. The vertical confinement is easily realized by epitaxial growth of quantum wells by such methods as MBE and MOCVD. One-dimensional (wire) and zero-dimensional (dot) confinement can be generated by patterning using sophisticated lithography techniques like electron beam (EB) and focused ion beam (FIB) or specially-designed epitaxial growth on tilted or patterned surfaces. Although the latter method can provide small-scale dimension, versatility or flexibility in patterning is lacking. The former method, that is, lithography technique, on the other hand, is much flexible to generate patterns. Especially, EB lithography can provide the finest patterns where quantum confinement effects can be sufficiently expected. Generally, the pattern transfer from the resist to semiconductor substrates is carried out by dry etching. However, dry etching generates severe problems, especially serious in quantization regime, that is, radiation damage and surface roughening. In fact, open wires of AlGaAs/GaAs system hardly give rise to photoluminescence (PL) in the quantum confinement regime. In order to cope with these problems, we previously proposed a new wet etching technique especially useful for fine pattern generation and demonstrated the realization of GaAs narrow wires in the dimension of 25 nm combining the improved EB lithography technique. The wet etching consists of two kinds of etchants, one of which is not sensitive to surface contamination and adequate for rough patterning and the other is good for smoothing of clean surfaces. Here we applied this technique to fabrication of one-dimensional quantum structures of AlGaAs/GaAs system and ultra-fine wires with smooth sidewall

surfaces which have never been obtained by the conventional dry etching.

MBE grown  $\text{Al}_{0.3}\text{Ga}_{0.7}\text{As}/\text{GaAs}$  double quantum well structures were used as starting materials. The sample consisted of a GaAs buffer layer, a 50nm-thick  $\text{Al}_{0.3}\text{Ga}_{0.7}\text{As}$  barrier, a 20nm-thick GaAs quantum well, a 180nm-thick barrier, a 10nm-thick quantum well, and a 10nm cap layer of GaAs. Only the 10nm quantum well was patterned into wire structures and the 20nm well was used as a standard for PL measurement. The line-and-space features were fabricated by using a high-resolution electron beam lithography system (JEOL JBX-5DII) at an accelerating voltage of 50 keV. Poly-methyl-methacrylate (PMMA) with a thickness of 50nm was used as a positive resist for EB lithography. The orientation of patterns was chosen so that the wire goes along the  $\langle 100 \rangle$  direction, that is, it is tilted 45° from the cleavage direction. This was found to be essential to fabricate wire structures with high quality sidewalls. It is known that the ordinary-mesa and reversed-mesa structures are obtained if the wire runs parallel to the  $\langle 110 \rangle$  and  $\langle \bar{1}\bar{1}0 \rangle$  directions, respectively, when the wet chemical etching is employed on (100) GaAs surfaces. It was, therefore, expected and was confirmed that nearly perpendicular sidewalls can be obtained when the wire axis is rotated by 45° with respect to the  $\langle 110 \rangle$  direction.

The pattern transfer from the resist to the quantum well substrate was carried out by the two-step wet chemical etching. The first etching was performed in a mixture of  $\text{H}_2\text{SO}_4:\text{H}_2\text{O}_2:\text{H}_2\text{O}$  with a volume ratio of 8:1:20 for 30 sec. at 3.5 °C, which provided coarse erosion of the contaminated GaAs surface. After  $\text{CH}_3\text{OH}$ -dipping, the second etching was done in a  $\text{Br}_2:\text{CH}_3\text{OH}$  (1:1000) solution for 20 sec. at 20 °C, resulting in smoothing the sidewall surface. Figure 1 shows a cross-sectional view of the array of the 35nm quantum wires fabricated here. It was found that the  $\langle 110 \rangle$  and  $\langle \bar{1}\bar{1}0 \rangle$  facets are preferentially eroded by the first etching. As seen in this figure, however, the second  $\text{Br}_2$  etching was found to be very much effective for smoothing the sidewall surface. The sidewalls are nearly perpendicular to the (100) plane in the vicinity of the surface and the quantum well structure.

Figure 2 shows the well width dependence of the normalized PL intensity for the wet-etched wires. PL experiments were carried out at 20 K with



Fig.1 Cross-sectional view of the array of the 35nm AlGaAs/GaAs quantum wires.

the Ar ion laser as an excitation source. The PL intensity was scaled by taking account of the actual areal filling factor and normalized to the intensity of the 20nm quantum well reference. For comparison, results on the dry-etched samples obtained by Maile et al.<sup>4</sup> are also shown in this figure. It can be seen that for both the wet-etched and dry-etched wires PL intensity decreases by more than the five orders of magnitude as the size is reduced to the quantum regime. This strong feature-size dependence of the luminescence intensity is most likely due to the surface recombination of the carriers at the wire sidewalls, that is, the formation of the deteriorated "dead layer". However, it should be noticed that the luminescence intensity of the wet-etched sample is always larger than that of the dry-etched sample. Moreover, the decay slope of the intensity is significantly small in the wet-etched sample compared with that of the dry-etched one. The feature size dependence of the wire luminescence can be understood based on a simple model in which photogenerated carriers diffused to the dead layer recombine nonradiatively. The lines are calculated results and the agreement between experimental and calculated ones is quite good. By proper fitting, the least squares method,  $2S\tau = 250\text{nm}$  and  $d=6\text{nm}$  were obtained for the wet-etched wires, where  $S$  is the nonradiative surface recombination velocity,  $\tau$  is the carrier life time, and  $d$  is the dead layer width of both sides of the wire. The effective wire width which is optically active for light emission is therefore given by  $(w-2d)$ . This dead layer thickness, 6nm, is significantly small compared with that of the dry-etched wires reported previously, 50–60nm<sup>4</sup>. Therefore, it can be concluded that the present wet etching technique provides big advantages for nanofabrication requiring less damage on the surface over conventional methods reported so far.

The peak position of the luminescence was examined as a function of the wire width. The filled circles in Fig. 3 represent the observed peak position as a function of the actual wire size. Since the quantum well thickness has a distribution in this sample due to the growth-related origin, mapping in the entire sample was carried out to avoid ambiguity in

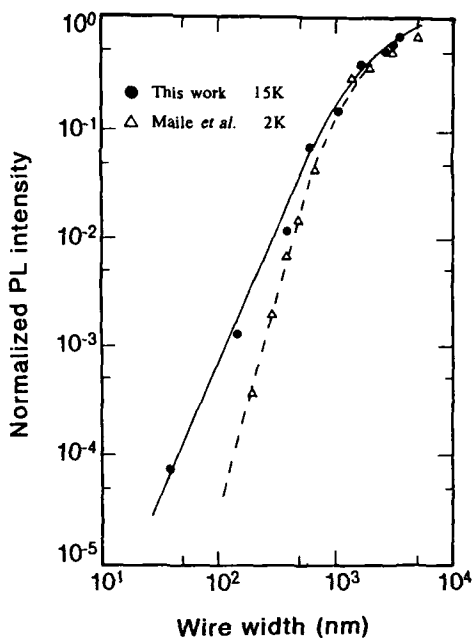


Fig.2 Well width dependence of PL intensities of wires

the peak shift and the region bounded by broken lines in Fig. 3 shows the energy variation of the quantum well fabricated here. The solid line in this figure represents the blue shift in the PL energy expected for wires in the quantum regime. The peak energy of the finest wire, 35nm, is clearly above the bound region and gives rise to a finite blue shift, while the peak position of wider wires remains within the bound region. Thus it can be said that the two-dimensional confinement of electrons which has not been observed in dry-etched wires is realized in the finest wire fabricated by the two-step wet chemical etching method. Although the lateral confinement energy is calculated to be 5.2meV for the 35nm wide wire, quantitatively discussion can hardly be conducted at the present stage. Further study is now in progress.

In conclusion, we have successfully fabricated ultrafine quantum well wire structures as small as 35nm by combining the EB lithography and the two-step wet chemical etching. The dead layer thickness of the sidewalls was dramatically reduced by this method in contrast to the dry-etched method. For the wire with a lateral dimension of 35nm, the substantial blue shift of the excitonic emission due to two-dimensional quantum confinement of electrons was observed for the first time in open AlGaAs/GaAs quantum wire structures.

The authors acknowledge the support of M. Morioka, A. Fujiwara, and S. Ohtake. This work was supported in part by a Grant-in-Aid for Scientific Research on Priority Area, "Electron Wave Interference Effects in Mesoscopic Structures" from the Ministry of Education, Science and Culture.

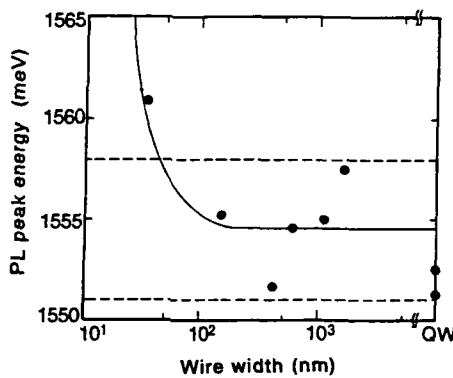


Fig.3 PL peak position as a function of the wire width

#### References

- 1 P. M. Petroff, A. C. Gossard, R. A. Logan and W. Wiegmann; *Appl. Phys. Lett.* **41**, 635 (1982)
- 2 B. E. Maile, A. Forchel, R. Straka, L. Korte, and C. Thanner; *Appl. Phys. Lett.* **57**, 809 (1990)
- 3 T. Katoh, Y. Nagamune, G. P. Li, S. Fukatsu, Y. Shiraki, and R. Ito; *Appl. Phys. Lett.* **57**, 1212 (1990)
- 4 B. E. Maile, A. Forchel, R. Germann, A. Menschig H. P. Meier and D. Grutzmacher; *J. Vac. Sci. Technol.* **B6**, 2308 (1988)

### **Side gating for $\delta$ -doped quantum wires**

T J Thornton, Y Feng

Imperial College of Science, Technology & Medicine, Dept. of Electronic & Electrical  
Engineering, Exhibition Road, London SW7 2BT, UK

J J Harris

IRC for Semiconductor Materials, Blackett Laboratory, Prince Consort Road,  
London SW7 2BZ, UK

D Williams

Hitachi Cambridge Laboratory, Cavendish Laboratory, Madingley Road,  
Cambridge CB3 0HE, UK

**ABSTRACT:** We have used side gating to change the width of narrow wires made from  $\delta$ -doped GaAs. The high electron density in the  $\delta$ -layer ensures that the depletion from the etched surfaces is negligible permitting a high degree of control of the channel width.

#### **1. INTRODUCTION**

Side gating is a method for reducing the width of a narrow 2DEG by applying an electric field across an insulating boundary. In the devices considered so far the boundaries have been defined by ion damage from a focused ion beam (Wieck and Ploog 1990), p-type implants (Blaikie et al 1991) or by deep trench etching (Takagaki et al 1990). We have used the latter method to define narrow wires and point contacts in  $\delta$ -doped GaAs. The width and electron density in the wires were determined by low temperature magnetoresistance measurements. Unlike similar structures made from modulation doped GaAs:AlGaAs heterojunctions the edge depletion in the  $\delta$ -doped wires is very small, presumably because of the much higher electron density.

© 1992 IOP Publishing Ltd

## 2. DEVICE FABRICATION

The details of the fabrication have been presented elsewhere (Feng et al 1992) and only a brief summary is included here. Our starting material was GaAs with a silicon  $\delta$ -doped layer buried  $0.25\mu\text{m}$  below the surface. The doping level in the layer was  $1 \times 10^{13} \text{ cm}^{-2}$ . We patterned trenches  $0.3\mu\text{m}$  deep by a combination of electron beam lithography and reactive ion etching (see figure 1). The trenches were approximately  $0.5\mu\text{m}$  wide and were either side of a conducting channel as shown schematically in the inset to figure 2.

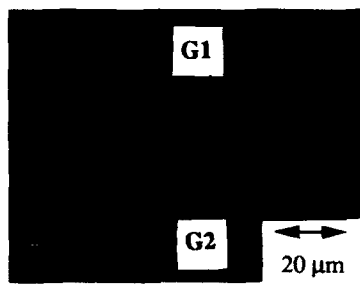


Figure 1: An electron micrograph showing the wire, voltage probes and side gates.

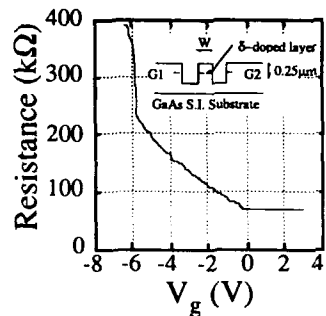


Figure 2: The resistance of the wire as a function of side gate voltage. The inset is a schematic cross section through the device

## 3. PINCH-OFF CHARACTERISTICS

The resistance of the devices was measured by conventional lock-in amplifier techniques using a constant current of frequency  $10\text{Hz}$  and amplitude  $10^{-8}\text{ A}$ . A typical pinch-off characteristic for a wire  $20\mu\text{m}$  long with a structural width of  $\sim 1\mu\text{m}$  is shown in figure 2. For gate voltages in the range  $-5\text{V} \leq V_g \leq 0\text{ V}$  the wire resistance increases almost linearly before pinching off very rapidly when the reverse bias is increased above 5 volts. The wire resistance is almost constant for forward gate biases suggesting that the wire width cannot be increased beyond that at zero volts. This is consistent with our overall conclusion that the depletion from the etched surfaces is very small.

$$\delta g = (We^2/2\pi^2\hbar L) [ Y(1/2 + \hbar/4eBL_g^2) + \ln(4eBL_g^2/\hbar) ] \quad (1)$$

To determine the mechanism of the side gate action we measured the magnetoresistance of the wires at low temperatures. For small magnetic fields the resistance decreases because of the suppression of two dimensional weak localisation (see figure 3). Data similar to that in figure 3 can be used to determine the electrical width of the wires from a least squares fit to equation 1

(Hikami et al 1980) which gives the magnetoconductance,  $\delta g$ , in terms of the digamma function,  $\Psi$ , the wire width,  $W$ , and the phase coherence length  $L_\phi$ .

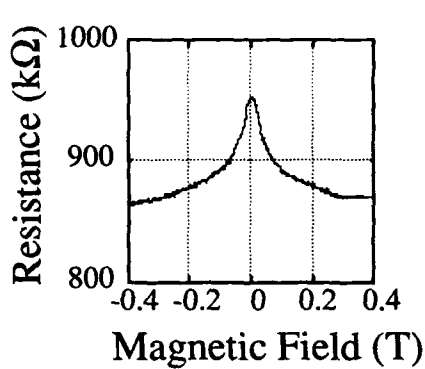


Figure 3: The low field magnetoresistance of an 80  $\mu\text{m}$  long 0.2  $\mu\text{m}$  wide wire. The temperature was 4.2 K.

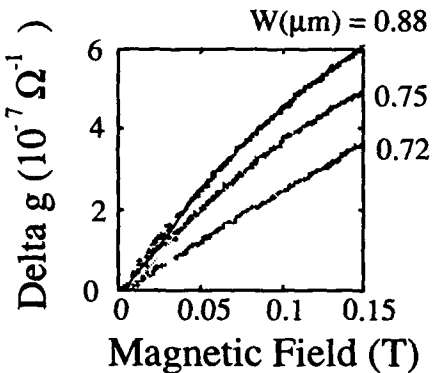


Figure 4: The magnetoconductance for three different side gate biases. The data has been fitted to equation (1).

We have performed this fitting procedure for a 20  $\mu\text{m}$  long wire of structural width  $\sim 1 \mu\text{m}$  over a range of side gate voltages as shown in figure 4 and have plotted the corresponding values of  $W$  and  $L_\phi$  in figure 5. The wire width decreases almost linearly as the gate voltage is made more negative. From this result we conclude that the pinch-off shown in the linear region of figure 2 is primarily due to a reduction in the wire width.

At zero gate voltage the wire width determined from the best fit to the data in figure 5 is 1.1  $\mu\text{m}$  which is the same as the structural width to within our experimental uncertainty. It would therefore appear that the depletion from the etched surfaces is negligible in these heavily doped wires in sharp contrast to the large depletion lengths observed in heterojunction wires (Demel et al 1988).

To confirm that the side gating effects primarily the width of the wire we measured the electron density in the channel from the Shubnikov - de Haas oscillations which appear at high magnetic fields (see figure 6). There are two pronounced periods in the magneto-oscillations each of which is due to an occupied 2D subband. From a fourier transform analysis (Yamada and Makimoto 1990) we estimate a total electron density of  $3.6 \times 10^{16} \text{ m}^{-2}$ , somewhat lower than the nominal doping density. There may well be more than two subbands occupied which would be resolved at magnetic fields higher than 9 T and therefore our estimate of the density represents a lower bound. The effect of applying a reverse bias to the gate is just to offset the curves to higher resistance (see figure 6). Although the amplitude of the oscillations gradually decrease their magnetic field position remains the same indicating that the electron density in the channel remains constant over a fairly wide range of side gate bias.

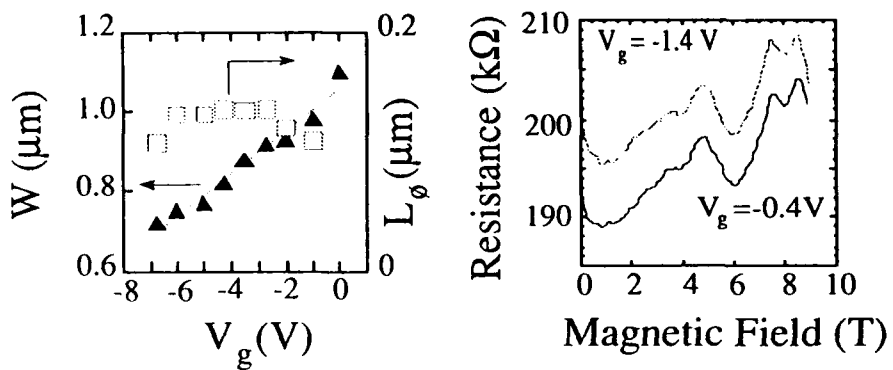


Figure 5: The wire width and phase coherence length as a function of side gate bias.

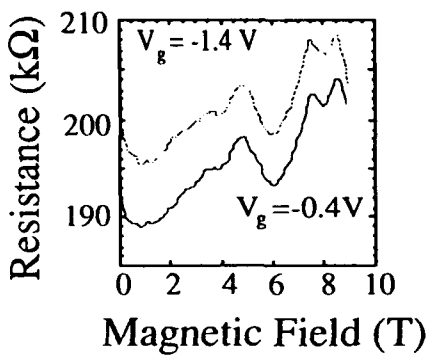


Figure 6: Shubnikov - de Haas oscillations for two side gate biases. The temperature was less than 100mK.

#### 4. CONCLUSIONS

We have shown that the pinch-off mechanism in side gate  $\delta$  - doped quantum wires is due mainly to a reduction in the wire width, the electron density in the channel remaining constant. At zero gate bias the depletion from the etched surfaces is negligibly small in this system making  $\delta$  - doped wires very attractive for further studies of side gate devices.

It is a pleasure to acknowledge the support of this work by the Japan Foundation for the Promotion of Materials, Science and Technology.

#### 5. REFERENCES

Blaikie R, Cleaver J R A, Ahmed H, Nakazato K 1992 to be published in *Appl. Phys. Letts.*  
 Demel T, Heitmann D, Gammow P, Ploog K 1988 *Appl. Phys. Letts* **53**, 2176  
 Feng Y, Thornton T J, Green M, Harris J J 1992 *Superlattices and Microstructures* **11**, 281  
 Hikami S, Larkin A L, Nagaoka Y 1980 *Prog. Theor. Phys.* **63**, 707  
 Takagaki Y, Gamo K, Namba S, Takaoka S, Murase K 1990 *Appl. Phys. Letts.* **57**, 2916.  
 Wieck A D and Ploog K 1990 *Surf. Sci.* **229**, 252  
 Yamada S and Makimoto T 1990 *Appl. Phys. Letts.* **57**, 1022

## Control of surface and interface Fermi level pinning for compound semiconductor nanometer scale structures

H. Hasegawa, H. Fujikura, M. Akazawa and H. Tomozawa

Research Center for Interface Quantum Electronics  
and Department of Electrical Engineering  
Hokkaido University, Sapporo, 060 Japan

**ABSTRACT:** A novel approach to control the surfaces and interfaces of GaAs and InGaAs nanometer-scale structures using an ultrathin MBE Si interface control layer (Si ICL) is presented. Details of the Si ICL technique and its application to InGaAs wire structures are discussed.

### 1. INTRODUCTION

One of the key processing issue related to realization of quantum effect devices lies in that surfaces and interfaces play far more important role than the present-day devices. Except for a few nearly ideal semiconductor hetero-interfaces, compound semiconductor surfaces and interfaces generally exhibit the so-called Fermi level pinning phenomena. It is highly probable that the ultimate functionality, performance and integration level of quantum devices will be severely limited the states causing Fermi level pinning and the resultant far-reaching depletion layers.

The purpose of the present paper is to describe a novel approach to control the surfaces and interfaces of GaAs and InGaAs nanometer-scale structures using an ultrathin MBE Si interface control layer (Si ICL, Hasegawa et al, 1989). Processing details of the Si ICL technique and its application to InGaAs quantum wire structures are discussed.

### 2. FORMATION OF Si ICL AND CONDITIONS FOR UNPINNING OF FERMI LEVEL

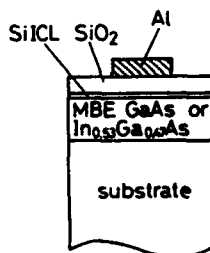
The sample, shown in Fig.1, was prepared as follows using a system having MBE, CVD and XPS chambers connected by a UHV transfer chamber.

(1) MBE growth of GaAs and InGaAs layers on GaAs(100) and InP(100) substrates.

(2) Growth of a Si ICL by MBE from a Knudsen cell at 1200°C.

(3) Deposition of a thick outer SiO<sub>2</sub> layer at 250°C by a photo-CVD process using a gas mixture of SiH<sub>4</sub>, N<sub>2</sub>O and Ar and an ArF excimer laser (193 nm).

During Si ICL formation up to about 10 Å, the RHEED pattern showed (3x1) surface reconstruction for Si/GaAs and (3x3) reconstruction for Si/InGaAs. Above 10 Å, the RHEED intensity rapidly decreased and the pattern finally became a halo. Decay of the XPS core level signals indicated that the growth proceeds in a two-dimensional fashion up to about 10 Å which is roughly equal to the critical thickness after Matthews-Blakeslee. The Fermi level position measured by in-situ XPS showed shifts towards the conduction band edge with Si coverage for both n- and p-type samples, indicating that Fig.1 Sample Structure.



pseudomorphic Si ICL alone does not remove Fermi level pinning. However, pinning could be removed after deposition of the  $\text{SiO}_2$  layer on the Si ICL and subsequent annealing. This was found to depend critically on the Si ICL thickness. Figure 2 plots the interface state density distributions measured by the C-V method for samples having the ICL thickness of 0, 10 and 20 Å. The optimum thickness was found to be 10 Å.

### 3. INTERFACE CONTROL OF AIR-EXPOSED SURFACES

Since nanostructure fabrication often involves use of electron beam lithography, X-ray lithography or selective regrowth, where the sample surface is exposed to air at a certain stage of processing, it is desirable that the Si ICL technique is applicable to the air-exposed surface. To explore such a possibility, various surface treatments to remove natural oxides were tried which included chemical etching by  $\text{H}_3\text{PO}_4:\text{H}_2\text{O}_2:\text{H}_2\text{O}=1:1:38$ , thermal cleaning in MBE chamber under As overpressure and immersion into HF solution in  $\text{N}_2$  atmosphere. The thermal cleaning removed the oxide efficiently, but deteriorated the stoichiometry very much. The HF treatment efficiently removed the  $\text{In}_2\text{O}_3$  and  $\text{Ga}_2\text{O}_3$  components of the surface oxide, leaving  $\text{As}_2\text{O}_3$  and elemental As. The subsequent deposition of the Si ICL then removed these As components almost completely, leaving an oxide-free and stoichiometric surface. The C-V analysis indicated that the interface Fermi level was unpinned. The results of C-V measurements are included in Fig.2. Thus, the HF treatment was found to be most effective.

### 4. APPLICATION TO InGaAs WIRES

An attempt to form InGaAs wire structures by a laser interference lithography and MBE growth was made for the first time using the following sequence. A similar approach has been reported for AlGaAs/GaAs system (Karam et al, 1991).

(1) A corrugated surface with  $(110)$  oriented grooves is formed on  $(100)$  InP substrate by an Ar laser interference lithography and wet chemical etching.

(2) An InAlAs buffer layer is grown on the corrugated surface by MBE.

(3) InGaAs wires are formed by MBE.

(4) A top InAlAs layer or  $\text{SiO}_2$  layer with or without a Si ICL is grown.

Fig. 3 shows dependence of the observed cross-sectional shapes on the MBE growth temperature. Thus, wire structures can be formed at a fairly low temperatures whereas the MOVPE approach requires a much higher temperature which causes the deterioration of the InP surface corrugation (Fujii et al, 1991). Figure 4(a) shows an SEM microphotograph of the cross-section of an InAlAs/InGaAs/InAlAs wire structure for  $t_{\text{PL}} = 50$  Å and a

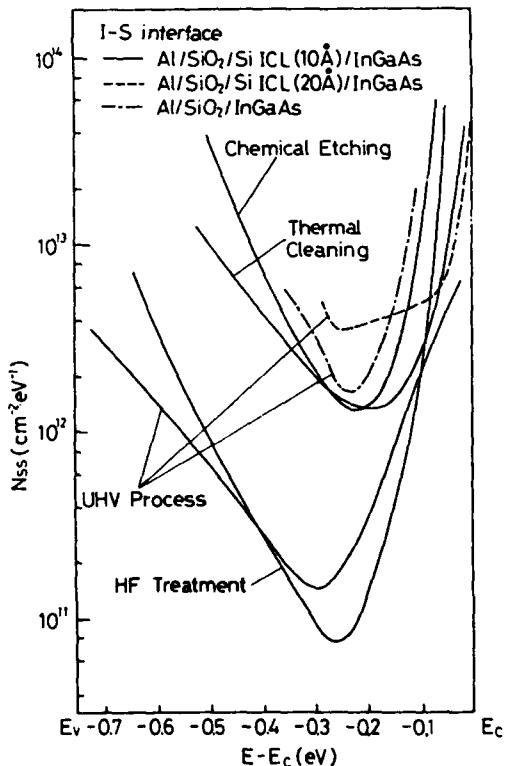


Fig.2  $N_{\text{ss}}$  distributions of various InGaAs interfaces.

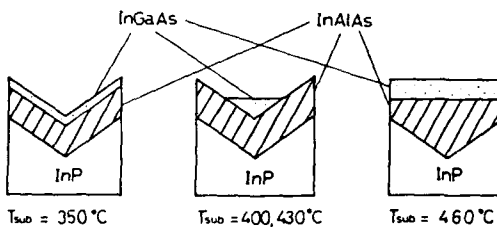


Fig.3 Dependence of cross-sectional structure on MBE growth temperature.

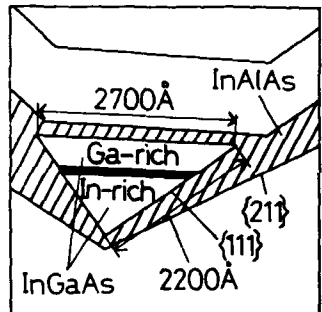
wire pitch of 10,000 Å. Here,  $T_{FL}$  is the amount of InGaAs used to form wires as expressed in terms of the equivalent flat layer thickness. A triangular shaped wire structure with a dark bisecting band is clearly seen. The PL spectra observed in this sample is shown in Fig.5. Three peaks were seen. The energy position of the peak ② agrees with that from the non-patterned flat sample, and thus originates from the reference flat portion of the sample.

The size of the present wire is still too large to expect large blue shifts due to quantum confinement. The interpretation of the remaining two peaks, ① and ③ in Fig.5, is as follows. Since the migration length of In is larger than that of Ga, the bottom portion of the wire tends to be In-rich whereas the top portion tends to be Ga-rich, resulting in a phase separation in the middle of the wire, as schematically shown in Fig.4(b). This produces a blue-shifted peak ③ and a red-shifted peak ①. Since the boundary portion of the two phases most likely contains a high density of defects due to high stress involved, Fermi level pinning may occur. Then, some quantum confinement effect may be present due to enhanced confinement by the resultant depletion layers. A further work is necessary to clarify this point.

Figure 6 shows a comparison of the PL intensity of the top Ga-rich portion of the wire for the InAlAs/InGaAs/InAlAs,  $\text{SiO}_2/\text{Si}$  ICL/InGaAs/InAlAs and  $\text{SiO}_2/\text{InGaAs}/\text{InAlAs}$  samples. They have the same wire size corresponding to  $t_{FL} = 50\text{\AA}$ . Spectra from flat structures are also shown by dashed curves for comparison. It is seen that both wire and flat samples having



(a)



(b)

Fig.4 Cross section of an InAlAs/InGaAs/InAlAs wire :  
(a) SEM photograph,  
(b) schematic representation.

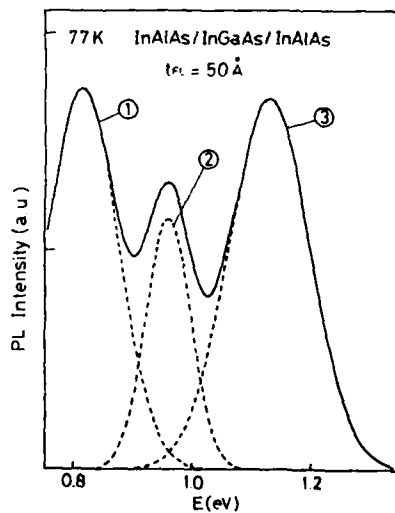


Fig.5 Observed PL spectrum of an InAlAs/InGaAs/InAlAs wire.

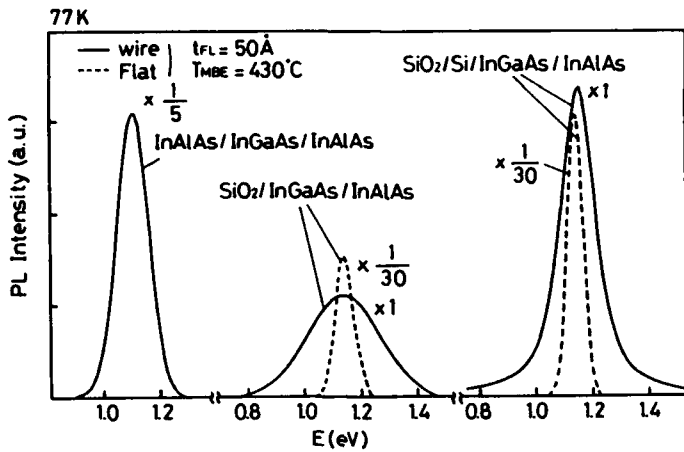


Fig.6 Comparison of PL spectra from Ga-rich portions of various wires

Si ICL show an much enhanced PL intensity as compared with samples having  $\text{SiO}_2$  layer only without Si ICL. This is consistent with result of the electrical measurement shown in Fig.2, and can be interpreted in terms of the reduction of interface state. It is also noted that the PL halfwidth is narrower in the sample with Si ICL. As for the comparison with the sample having an InAlAs overlayer, the wire with Si ICL has nearly the same PL halfwidth, but the PL intensity is still about 5 times smaller.

##### 5. CONCLUSION

- (1) For successful unpinning of Fermi level, the Si ICL should maintain an ordered pseudomorphic structure and should be covered with a  $\text{SiO}_2$  film.
- (2) Pinning at the air-exposed surfaces can be removed by combining an HF surface treatment with the Si ICL technique.
- (3) Feasibility of fabricating InGaAs quantum wire structures using interference lithography and selective MBE was demonstrated for the first time. The wire seems to involve a phase separated structure.
- (4) The Si ICL technique can be applied to the wire structure without difficulty and that the Si ICL technique was shown to be promising for interface control of quantum confined structures.

##### ACKNOWLEDGMENT

The present work is financially supported in part by a Grant-in-Aid for Scientific Research on Priority on Electron Wave Interference Effects in Mesoscopic Structures from Ministry of Education, Science and Culture.

##### REFERENCES

Fujii T, Aoki O and Yamazaki S, Proc. of 18th Int. Symp. on GaAs and Related Compounds(Sept.9-12,1991,Seattle,USA) to be published.  
 Hasegawa H, Akazawa M, Ishii H, Matsuzaki K and Ohno H, 1988 Jpn. J. Appl. Phys. **27**, L2265.  
 Karam N H, Mastrovito A, Haven V, Ismail K, Pennycook S and Smith H I, 1991 J. Crystal Growth **107**, 591.

## Nanometer x-ray mask created using precise crystal growth

Kazuhito FURUYA, Yasuyuki MIYAMOTO and Daisuke YAMAZAKI  
Department of Electrical and Electronic Engineering, Tokyo Institute of Technology  
2-12-1 Ookayama, Meguro-ku, Tokyo 152 Japan

**ABSTRACT:** Fabrication possibility of X-ray masks with nanometer size patterns by precise crystal growth techniques is discussed. As a preliminary experiment, using GaInAs/InP layered structure grown by OMVPE, 100nm-patterns were transferred by X-ray.

### 1. INTRODUCTION

X-ray lithography(Spears et.al., 1972) is one of promising methods for the fabrication of quantum-size structures, such as the interference transistor(Warren et.al., 1986) and the electron diffraction transistor(Furuya et.al., 1988). In this technique, creation of the nanometer-size pattern is one of key points. When the mask pattern is drawn by the electron beam, the electron scattering limits the down-sizing of the pattern(Inamura et.al., 1988).

On the other hand, crystal layers of the nanometer thickness have been obtained by using precise crystal growth techniques, OMVPE and MBE. It is very interesting to apply these techniques for the X-ray mask fabrication. Flanders fabricated X-ray mask by the deposition of the metal film(Flanders 1980). However, applications of the crystal growth technique for the X-ray mask were not reported yet.

In this paper, we discuss fabrication possibility of X-ray mask using precise crystal growth techniques. As a demonstration, masks of InP/Vacuum/InP structure were fabricated by OMVPE and the material selective etching. Then mask patterns were transferred by Cu-L X-ray.

### 2. X-RAY MASK BY CRYSTAL GROWTH

The method to be considered is as follows. A heterostructure of ultrathin layers consist of crystals A and B is grown by a crystal growth technique, for example, OMVPE and MBE. We can use the grown sample as the mask so that X-ray is irradiated along the crystal layers. One method to irradiate the X-ray along the crystal layer is to cut the crystal layer into a narrow stripe and turn it by 90 degrees as shown in Fig.1(a). The alternative is to grow the crystal on the vertical wall as shown in Fig.1(b).

When the difference in the absorption coefficient between the crystals A and B is large enough, we can use the crystal wafer as the mask directly after the growth (Fig.1(b)) or after the cutting and thinning (Fig.1(a)). When the difference in the absorption is not large enough, the material selective etching is used to remove crystal totally or partially(Fig.1(a)). The method is analogous to Flanders' 1980 where a metal film is deposited by the evaporation on the side wall of the mesa structure. The present method has following merits. The first is high controllability of the thickness. The second is a possibility of the growth on side walls in trenches with high aspect ratio using ALE(Usui et.al.,1990), for example, more than 10, which are required for

the creation of dense patterns with nanometer size.

### 3. X-RAY ABSORPTION BY SEMICONDUCTOR

To use growth technique of the semiconductor crystal for the X-ray mask fabrication, absorption coefficients of typical semiconductors are evaluated using data reported by Henke et.al., 1973 (Table 1). When GaP/AlP and Al-L line are used as the material and X-ray, respectively, large difference in absorption is obtained. Lattice constants of these materials match each other as shown in Table 1. This combination provides contrast of 10 when the mask thickness is  $1.6\mu\text{m}$  at the attenuation of 1/3. If we can use the material combination lattice-mismatched, GaAs/Ge or GaP/Si provides high contrast under irradiation of Al-L line.

By material-selective etching, we can get high contrast with thin mask. The absorption coefficient of GaAs for C-K line is as high as that of gold for Cu-L line,  $13/\mu\text{m}$ , which provides contrast of 10 by  $0.17\mu\text{m}$ -thick mask.

The thickness of the semiconductor absorber is typically more than  $0.2\mu\text{m}$  to obtain enough contrast in the X-ray intensity. Thus for the mask of feature size of  $20\text{nm}$  order, aspect ratio more than 10 is required for the absorber profile. The situation is more or less similar for the metal mask when the pattern is quantum-size.

### 4. X-RAY PROPAGATION THROUGH MASK

As the ratio of a thickness  $t$  to an aperture of X-ray mask is high, it is appropriate to consider X-ray passage through an aperture as a wave propagation along a waveguide (Fig.2(a)). The waveguide consists of a core of the vacuum and a cladding of a substance. The refractive index of the substance for the X-ray is given as (Aigner et.al., 1986 and Landau et.al., 1984);

$$n = 1 - e^2 \lambda^2 N / (8\pi^2 \epsilon_0 c^2 m) = 1 - 2.7 \times 10^8 \lambda^2 Z \rho / A$$

where  $-e$  and  $m$  are the charge and mass of the electron, respectively,  $\epsilon_0$  is dielectric constant of the vacuum,  $c$  is the light velocity,  $N$  is the electron density,  $Z$  is the atomic number,  $\rho$ ,  $A$  and  $\lambda$  are density, the atomic weight and X-ray wavelength in MKS units, respectively. The index of InP at the wavelength of  $1.3\text{nm}$ , is  $1 - 0.001$ . The imaginary part of the index is  $\alpha\lambda/(4\pi)$  ( $\alpha$ : the absorption coefficient) and is  $0.0003$ . In comparison with the core/cladding difference in the real part, the imaginary part is small enough to be neglected in the mode analysis.

As shown in Fig.2(b), the intensity profile of the X-ray extends substantially outside the aperture. The full width at 1/10 maximum of the intensity profile is at the minimum and  $0.7 \lambda / \sqrt{2\Delta}$  when the value of  $\pi\sqrt{2\Delta}w / \lambda$  ( $\Delta$ : index difference,  $w$ : the core width) is  $0.3\pi$ . In InP/Vacuum/InP waveguides, the minimum width is  $20\text{nm}$ , while  $12\text{nm}$  for Au/Vacuum/Au waveguides. These are considered as the minimum transferable pitch of the grating pattern. As  $\Delta$  is proportional to  $\lambda^2$ , the minimum width is independent of the wavelength of the X-ray.

### 5. EXPERIMENT

GalnAs/InP layered structures were grown by organometallic vapor phase epitaxy

(OMVPE) (Miyamoto et.al., 1988). GaInAs layers on a cleaved facet were selectively etched with  $H_2SO_4$  to form grooves. As shown in Fig.3, a semiconductor comb of 60nm-pitch was created at an edge where two cleaved facets meet.

For pattern-transfer experiments, we used layered structures including GaInAs layers of thicknesses of 100 and 200 nm at pitches of 200 and 400 nm, respectively. The mask with the thickness of 350 $\mu m$  was placed directly on a 200nm-thick PMMA resist layer so that the grooves on the cleaved facet were normal to the resist surface as shown in Fig.4.

To increase the alignment tolerance, we reduced an effective thickness of the mask by making angle as shown in Fig.4. The effective mask thickness is the groove depth/ $\sin\theta$ . We set  $\theta = 45$  degree so that the contrast was more than 5 and the tolerance of the angle alignment is more than several degrees.

To suppress the gap between mask and substrate, a bottom face of the mask was prepared by the cleavage. Adhesion between the bottom face and the surface of the PMMA layer was promoted by using a liquid as in the epitaxial lift-off technique(Yablonovitch et.al., 1990).

As to the X-ray source, an electron gun of 6KV/50mA and a Cu target were used. The distance between the target and the mask was 35cm. The exposure time was 5mins. After the exposure, the resist was developed with MIBK. Figure 5 shows the transferred pattern. Clear dips were observed at 400nm-pitch and slight dips were observed at 200nm-pitch.

## 6. CONCLUSION

Fabrication of ultrafine pitch mask for X-ray lithography by precise crystal growth was discussed. From the X-ray absorption coefficient, sufficient contrast can be obtained by appropriate combination of substances. From the waveguide consideration, the minimum pitch transferable by X-ray is determined by the index of the substance to be 20nm and 12nm for typical semiconductor and metal masks. As a preliminary experiment, using OMVPE grown GaInAs/InP multilayer structure, 60nm-pitch grating mask was fabricated. 100nm-pattern was successfully transferred by X-ray.

## ACKNOWLEDGMENTS

Authors acknowledge president Y. Suematsu for his continuous support, and Profs. S. Arai and M. Asada for fruitful discussions. K.F. thanks Prof. K. Iio for kind explanation about refractive index. They thank Dr. K. Komori and Mr. M. Ishida for technical support. This work was supported by a Scientific Research Grant-in-Aid and Special budget for "Ultra- High Speed Electronics" at Tokyo Institute of Technology and the Joint Project "Mesoscopic Electronics", all from the Ministry of Education, Science and Culture.

## References

- Aigner H and Wobrauschek P 1986 *Adv. X-ray Anal.* 28 1
- Flanders D C 1980 *Appl.Phys.Lett.* 36 93
- Furuya K, Kurushima K and Yamamoto T 1988 *Trans. IEICE* E71 286
- Henke B L and Ebisu E S 1973 *Adv. X-ray Anal.*, 15 150
- Inamura E, Miyamoto Y, Tamura T, Takasugi S and Furuya K 1989 *Proc. of Int. Symp. on*

Microprocess Conf., 209

Landau L D, Lifshitz E M and Pitaevskii L P 1984 *Electrodynamics of Continuous Media*, Pergamon Press, Oxford

Miyamoto Y, Uesaka K, Takadoh K, Furuya K and Suematsu Y 1988 *J. Cryst. Growth* 93 353

Spears D L and Smith H I 1972 *Electron Lett.* 8 102

Usui A, Sunakawa H, Stutzler F J and Ishida K 1990 *Appl. Phys. Lett.* 56 289

Warren A C, Plotnik I, Anderson E H, Schattenburg M L, Antoniadis D A and Smith H I 1986 *J. Vac. Sci. Technol. B4* 365

Yablonovitch E, Hwang D M, Gmitter T J, Florez L T and Harbison J P 1990 *Appl. Phys. Lett.* 56 2419

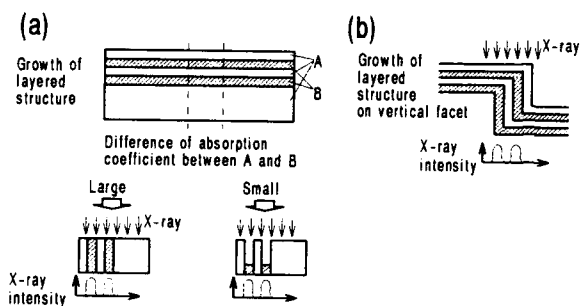


Fig.1 X-ray mask fabricated by crystal growth.

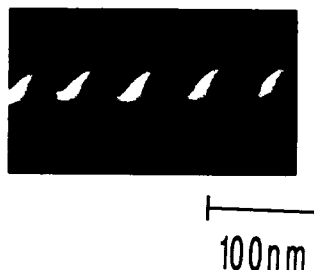


Fig.3 Scanning electron micrograph of 60nm-pitch comb shape.

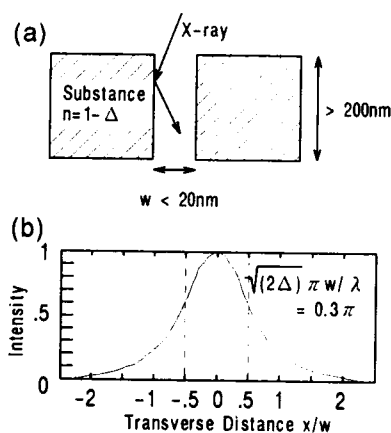


Fig.2 X-ray propagation through aperture. (a) waveguide structure. (b) intensity profile of mode in waveguide.

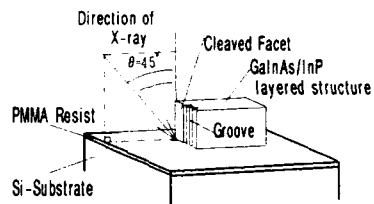


Fig.4 Schematic diagram of X-ray exposure experiment.

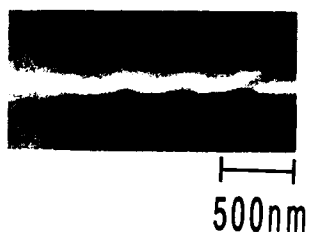


Fig.5 Transferred pattern. Pitch are 200nm and 400nm.

Table.1 X-ray absorption coefficient of semiconductors.

	GaAs	AlAs	InP	GaInAs	GaP	AlP	Ge	Si	unit
8.3 Å Al-L	2.85	1.53	1.27	2.54	1.6	0.13	0.21	0.13	
13.3 Å Cu-L	1.2	0.83	3.7	2.67	0.87	0.47	1.1	0.46	$\mu\text{m}^{-1}$
44.7 Å C-K	13.7	10.7	6.5	10.6	11.9	8.6	16.1	8.6	
Lattice constant	5.65	5.66	5.87	5.87	5.45	5.45	5.65	5.43	Å

## Si super-heteroepitaxy and its application to new structure FETs

Masanobu MIYAO and Kiyokazu NAKAGAWA,  
Central Research Lab., Hitachi Ltd., Kokubunji, Tokyo 185, JAPAN

**ABSTRACT:** New methods to fabricate atomic layer doping structures, strain controlled  $Ge/Si_{1-x}Ge_x$  heterostructures and Si / silicide / Si double heterostructures are developed using Si molecular beam epitaxy. Characterization and device applications of these Si super-heterostructures are comprehensively studied.

### 1. Introduction

Formation of high quality heterostructures and superlattices combined with Si technology attracts current interest because this can open possibilities for new future device applications. In the past decade, Hitachi Central Research Laboratory has been proceeding with basic and applied research on Si molecular beam epitaxy (MBE).

The present paper describes several typical results, including atomic layer doping (ALD), SiGe/Si and Si/silicide/Si heteroepitaxy [1~4,6,7]. Novel applications for new structure FET's are also discussed.

### 2. Atomic Layer Doping (ALD) Structure in Si

A new method to perform atomic layer doping in Si [1] is developed using a combination of MBE and solid phase epitaxy (SPE). In the process, Sb is deposited on the Si substrate at a temperature of  $\sim 650^\circ C$ , which gives a monolayer (ML) adsorption of Sb on Si (100). And then, Sb concentrations are reduced using a thermal desorption process at  $750^\circ C$ . Finally, amorphous Si is deposited and crystallized ( $550^\circ C$ ) through SPE to suppress the surface segregation of Sb atoms.

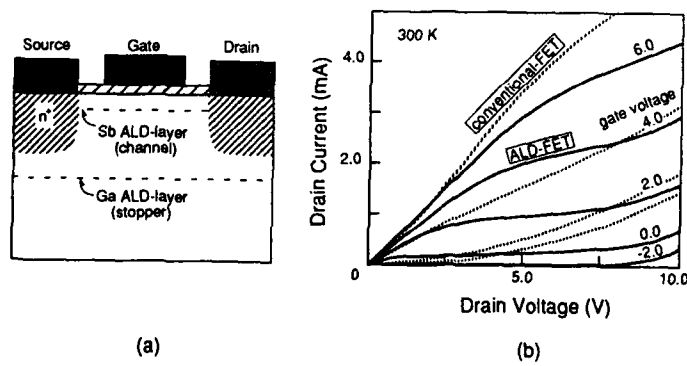


[Fig.1] (a) Cross-sectional view of ALD-FET. (b) Current voltage characteristics of ALD-FET and conventional FET (dotted line).

Experiments indicate that Sb dopants are restricted to a region thinner than the resolution limit of secondary ion mass spectroscopy (SIMS), and exhibit extremely sharp C-V carrier profiles less than 2nm for an Sb ML. In addition, Hall and SIMS data show full activation of Sb dopants up to  $\sim 0.1$ ML and saturation at  $8 \times 10^{13}$  electrons/cm<sup>2</sup>.

The ALD-FET's are fabricated [2] and shown in Fig.1. Here the Sb ALD region and the Ga doped region are used as the conductive channel and potential barrier to electrons (punch-through stopper), respectively. This structure can suppress punch-through current sufficiently, indicating that the device is promising as a short channel FET in the sub one-tenth micron region.

### 3. Modulation-Doped p-Si<sub>0.5</sub>Ge<sub>0.5</sub>/Ge/Si<sub>1-x</sub>Ge<sub>x</sub> Heterostructures

A schematic illustration of a new Si-Ge heterostructure (p-Si<sub>0.5</sub>Ge<sub>0.5</sub>/Ge/Si<sub>1-x</sub>Ge<sub>x</sub>/(100)substrate) is shown in Fig.2, where the strain fields in Ge channel layers are controlled by the Si composition (1-x) of the Si<sub>1-x</sub>Ge<sub>x</sub> buffer layers. In the MBE growth, thick ( $\sim 1.0 \mu m$ ) Si<sub>1-x</sub>Ge<sub>x</sub> buffer layers are grown incommensurately (520°C) on the substrate, and then thin ( $\sim 50$ nm) modulation doped p(Ga)-Si<sub>0.5</sub>Ge<sub>0.5</sub>/Ge layers are grown commensurately (400°C) on the buffer layers [3].

Strains ( $\epsilon$ ) in the grown layers are measured using Raman spectroscopy and evaluated to be  $\epsilon$  (%) =  $4.0[1-X]$ . Electrical properties in the Ge channel measured at 77K are summarized in Fig.3. Both hole concentrations and hole mobilities increase with the strain in the low strain region ( $\leq 1.0\%$ ). This is because the strain fields in the Ge channel layers cause a large energy discontinuity in the valence band (0.20eV at  $\epsilon = 1\%$ ) at the hetero-interface between p-Si<sub>0.5</sub>Ge<sub>0.5</sub> and the Ge channel, which enables sufficient confinement of the two dimensional hole gas. However, in the high strain region ( $\geq 1.0\%$ ), hole mobilities decrease with strain. This is attributed to the generation of interface roughness as well as threading defects caused by the high strain field. To achieve higher mobility values, new techniques such as selective area MBE growth and/or oxygen controlled CVD growth should be investigated to improve crystallinity.

Modulation doped, p-channel FET's are fabricated [4] and it is shown that the devices have ultra-high field effect mobilities (10000 cm<sup>2</sup>/Vs, 77K). These values are ten times higher than those of previously reported SiGe heterostructures (600 cm<sup>2</sup>/Vs, 77K) [5].

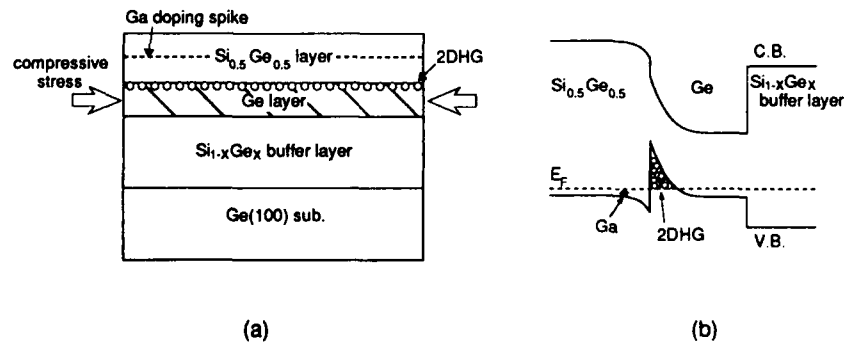


[Fig.2] (a) Cross-sectional view of a new heterostructure consisting of p-Si<sub>0.5</sub>Ge<sub>0.5</sub>/Ge/Si<sub>1-x</sub>Ge<sub>x</sub>. (b) Band diagram of the new heterostructure.

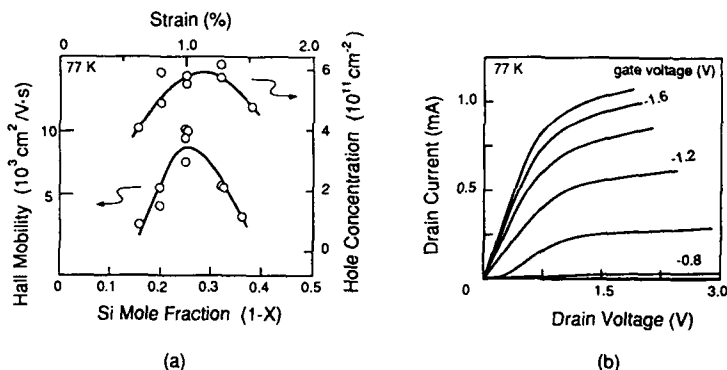


[Fig.3] Electrical properties of a new SiGe heterostructure; (a) Two dimensional hole mobilities at the p-Si<sub>0.5</sub>Ge<sub>0.5</sub>/Ge interface obtained by Hall effect measurements. (b) Current-voltage characteristics of the SiGe MODFET.

#### 4. Fine-Patterned Si/Silicide/Si Double Heterostructures

A new sub-micron patterning method of single crystal silicide (CoSi<sub>2</sub>) films is developed using self aligned and selective MBE growth. As the first step, grooves of submicron scale ( $0.5 \mu\text{m}$  line and space) are formed on Si (111) substrates. Then, single-crystalline CoSi<sub>2</sub> is grown by MBE. The CoSi<sub>2</sub> films deposited on the side walls of the grooves drain away ( $\geq 400^\circ\text{C}$ ), and pin-hole-free CoSi<sub>2</sub> films are obtained on the (111) Si surfaces ( $\leq 500^\circ\text{C}$ ). This is because the interface energy is greater on Si {112} and {110} surfaces than on a Si (111) surface. In this way, submicron patterning of CoSi<sub>2</sub> films is established in a self-aligned fashion by choosing a proper growth temperature ( $400\text{--}500^\circ\text{C}$ ).

In addition, a high-quality double heterostructure (Si/silicide/Si) is formed by two-step MBE of the Si overlayer on CoSi<sub>2</sub>/Si. Here very thin Si (2 nm) layers are grown at low temperature ( $\sim 350^\circ\text{C}$ ) to stabilize the surface atoms of CoSi<sub>2</sub>. Then on top, thick Si (200 nm) layers are grown at high temperature ( $\sim 550^\circ\text{C}$ ). A schematic illustration and a cross sectional TEM observation are shown in Fig.4, which reveals that both the upper and lower interfaces between the CoSi<sub>2</sub> and Si are atomically abrupt and smooth.

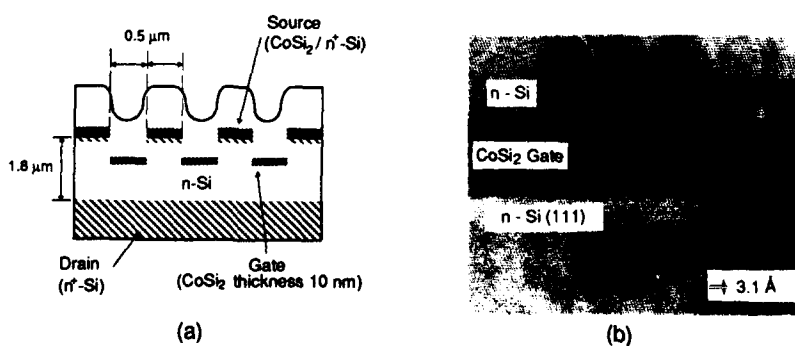


[Fig.4] (a) Cross sectional view of PBT. (b) Cross-sectional lattice image of the Si/CoSi<sub>2</sub>/Si double heterostructure observed by TEM.

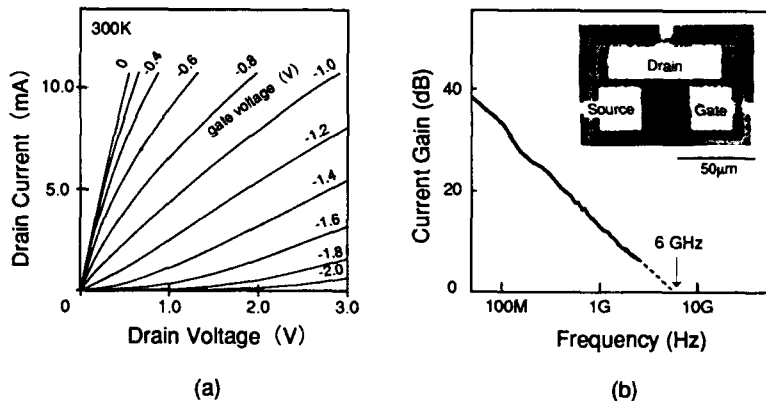


[Fig.5] (a) Current-voltage characteristics of PBT. (b) High-frequency characteristics of PBT. The plan view of PBT is also shown.

Using these new techniques, permeable base transistors (PBT) with buried gate ( $0.5 \mu\text{m}$  width) are fabricated [6,7]. Electrical characteristics are shown in Fig.5, which indicate a high performance, i.e. transconductance ( $g_m$ ) of  $50 \text{ mS/mm}$  and unity gain frequency ( $f_T$ ) of  $6 \text{ GHz}$ . The  $g_m$  value and the I-V characteristics agree well with the results of computer simulations. More significant improvement in  $f_T$  ( $\sim 100 \text{ GHz}$ ) is possible by using a deep submicron patterned gate ( $\leq 0.1 \mu\text{m}$ ).

### 5. Summary

Recent progress of Si heteroepitaxy is reviewed. Si super-structures realized by MBE are effectively used for the formation of new structure FET's, i.e. ALD-FET, strain controlled SiGe MODFET and PBT. These devices are attractive and promising as novel devices for the next ULSI generations and/or future quantum devices.

A part of this work was performed under the management of the R&D Assoc. for Future Elec. Dev. as a part of the R&D of Basic Tech. for Future Indus. supported by New Ener. and Indus. Tech. Devel. Organ.

### References

- [1] A.A. van Gorkum, K. Nakagawa, and Y. Shiraki; *J. Appl. Phys.* **65**, 2485, (1989)
- [2] K. Nakagawa, A.A. van Gorkum, and Y. Shiraki; *Appl. Phys. Lett.* **54**, 1869, (1989)
- [3] E. Murakami, H. Etoh, K. Nakagawa, and M. Miyao, *Jpn. J. Appl. Phys. Part2*, **29** (7), (1990)
- [4] M. Miyao, E. Murakami, H. Etoh, K. Nakagawa and A. Nishida; *J. Cry. Growth* **111**, 912, (1991)
- [5] T.P. Pearsall and J.C. Bean; *IEEE Trans. Electron Device Letters* **EDL-7**, 308, (1986)
- [6] T. Ohshima, N. Nakamura, K. Nakagawa, and M. Miyao, *Thin Solid Films*, **184**, 275, (1990)
- [7] M. Miyao, K. Nakagawa, N. Nakamura, and T. Ohshima; *J. Cry. Growth* **111**, 957, (1991)

## **Ballistic transport and low-frequency noise in high mobility two-dimensional electron systems**

S. Tarucha, T. Saku, Y. Hirayama, J. R. Phillips, K. Tsubaki, and Y. Horikoshi

NTT Basic Research Laboratories, Musashino-shi, Tokyo 180, Japan

**ABSTRACT:** Ballistic transport and low-frequency noise are studied for two-dimensional electrons of very high electron mobility. Using macroscopic-scale devices, we reveal two major properties of ballistic transport: long-distance ballistic transport of electrons and size-independent resistance. These behaviors are well reproduced by the Landauer-Büttiker formula in the classical limit. We observe critical noise generation for a large injection current in a wide channel device. This arises from nonequilibrium electron heating under high electric field.

### **1. INTRODUCTION**

Ballistic transport characteristics have been revealed in "mesoscopic" scale devices whose critical dimension is around 1  $\mu\text{m}$  or less since the electron mean free path is generally a few  $\mu\text{m}$ . Four-terminal devices consisting of sub- $\mu\text{m}$  wide intersecting wires exhibited negative bend resistance (Takagaki et al 1989, Timp et al 1990) and nonlinear Hall resistance (Chang et al 1989, Ford et al 1989). These characteristics have been successfully analyzed using the Landauer-Büttiker (L-B) formula (Landauer 1970, Büttiker 1986), which holds for a ballistic conductor with one-dimensional (1D) propagating channels in each lead. In such small devices, however, the conductance is affected by boundary scattering and quantum interference. Recent development of high electron mobility heterostructures enabled "macroscopic" scale ballistic devices of 10  $\mu\text{m}$ -order (Spector et al. 1990, Hirayama et al. 1991, Fukai et al. 1992). Such large devices allow us to study the transport properties of two-dimensional electron systems (2DESs) free from the diffusive boundary scattering. This paper describes recent experimental studies on ballistic transport properties and low-frequency noise in very high mobility 2DESs. Macroscopic ballistic transport is exemplified by long-distance ballistic transport of electrons and size-independent resistance, both of which are observed in large-scale (10 to 150  $\mu\text{m}$ ) devices. We discuss the resistance characteristics using the L-B formula in the classical limit. For a large injection current,

high mobility is degraded by electron heating. We find that nonequilibrium electron heating gives rise to a critical increase of low-frequency noise.

## 2. LONG-DISTANCE BALLISTIC TRANSPORT

A high mobility Al<sub>0.35</sub>Ga<sub>0.65</sub>As/GaAs modulation doped wafer was chemically mesa-etched into four-terminal square devices (Fig. 1). The initial wafer had an electron mobility  $\mu$  of  $7.8 \times 10^6$  cm<sup>2</sup>/Vs and an electron density  $n_s$  of  $2.8 \times 10^{11}$  cm<sup>-2</sup> at 1.5K after illumination. The corresponding elastic mean free path  $l_e$  was 69  $\mu\text{m}$ .

Figure 2 shows the bend resistance  $R_B = R_{12,43} = V_{43}/I_{12}$  vs. magnetic field  $B$  characteristics observed for devices having various values of  $L$  and  $W$ .  $R_B$  exhibited a pronounced negative peak at  $B=0$ , which is due to a direct ballistic injection into the opposite voltage lead. The smaller peak observed in the larger  $L$  device was due to the reduced ballistic injection probability. Our observation of the  $R_B$  peak for the  $L=150 \mu\text{m}$  device, indicates the existence of ballistic electrons travelling a distance of over  $\sqrt{2} L = 210 \mu\text{m}$ . The L-B formula gives  $R_B$  as

$$R_B = \frac{h}{2e^2} \frac{T_{41}T_{32} - T_{42}T_{31}}{D}, \quad (1)$$

where  $T_{ij}$  is the transmission probability of electrons from lead  $j$  to  $i$ ,  $N$  is the propagating 1D channel number in each lead, and  $D$  is a sample-specific constant. We assume that  $T_{ij} \approx N/4$  due to the scrambling effect (Beenakker and van Houten 1989), and that  $T_{ij}$  with  $i \neq j$  is larger than  $T_{ij}$  due to the direct ballistic injection. This assumption leads from eq. (1) to

$$R_B \approx \frac{h}{e^2} \frac{1}{N^2} \left( \frac{T_f + T_d}{2} - T_d \right), \quad (2)$$

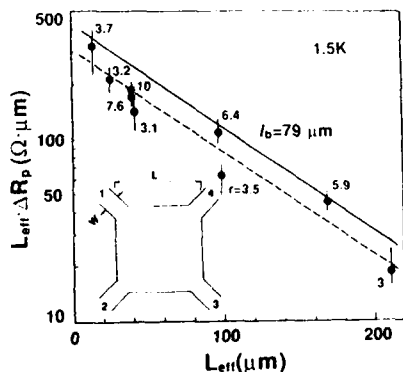


Fig. 1. Plots of  $L_{\text{eff}} - \Delta R_p$  vs.  $L_{\text{eff}}$  for various devices.

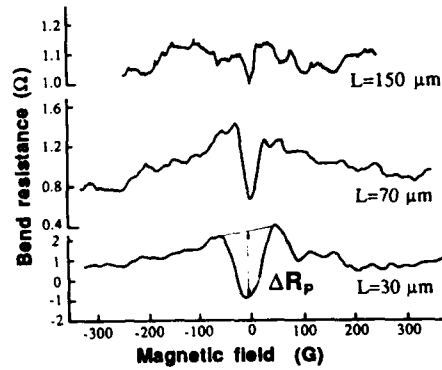


Fig. 2.  $R_B$  vs.  $B$  characteristics for various devices having  $r=3$ .

where the subscripts d, r, and l represent the injection trajectories into the opposite, right, and left corner leads, respectively.  $T_l + T_r$  is nearly constant in the low field region while  $T_d$  goes to zero with increasing B. Therefore, eq.(2) predicts a zero-field negative  $R_B$  peak with amplitude  $\Delta R_p$  given by  $\frac{h}{e^2} \frac{1}{N^2} T_d$ . When we assume a cosine-like angular distribution for the injection trajectories and a 1D channel number N given by an infinite square well model,  $\Delta R_p$  follows

$$L_{\text{eff}} \Delta R_p = \frac{h}{e^2} \frac{\sqrt{\pi}}{2} n_s^{-1/2} \exp(-L_{\text{eff}}/l_b), \quad (3)$$

where  $L_{\text{eff}} = \sqrt{2} L$  and  $l_b$  is the ballistic length. Figure 1 shows the  $L_{\text{eff}} \Delta R_p$  plots as a function of  $L_{\text{eff}}$  measured for various devices. The data points fall along the same line, the dashed line, which is independent of W or r ( $=L/W$ ) values as expected from eq.(3). This line has a slope as given by eq. (3) with  $l_b = 79$  mm, which agrees well with  $l_e$  of 69  $\mu\text{m}$ . The agreement between  $l_b$  and  $l_e$  was found to be good for various electron densities (Tarucha et al. 1991). The solid line indicates the calculated  $L_{\text{eff}} \Delta R_p$  by substituting  $l_b = 79$  mm and  $n_s = 3.0 \times 10^{11} \text{ cm}^{-2}$  into eq.(3), and agrees fairly well with the broken line. This means that the resistance of a ballistic wide channel is equivalent to the value deduced from the occupied number N of 1D subbands although N is rather continuous. The billiard-ball model analysis, which assumes rather continuous N, well reproduces the resistance characteristics of *mesoscopic-scale* ballistic devices (Beenakker and van Houten 1989). Consistently our result demonstrates that the L-B formula holds for *macroscopic-scale* ballistic devices in the classical limit.

### 3. LENGTH-INDEPENDENT CHANNEL RESISTANCE

Figure 3 schematically shows wide channel devices prepared from a modulation doped wafer having  $\mu = 6.4 \times 10^6 \text{ cm}^2/\text{Vs}$  and  $n_s = 2.8 \times 10^{11} \text{ cm}^{-2}$  at 1.5 K. The corresponding  $l_e = 56 \mu\text{m}$ . The prepared devices had the voltage leads of the same spacings of  $L_{34} = 12 \mu\text{m}$ ,  $L_{45} = 20 \mu\text{m}$ , and  $L_{56} = 40 \mu\text{m}$ , and widths of  $W = 3.7 \mu\text{m}$ , but various current channel width D ranging from 1.7 to 15.7  $\mu\text{m}$ . The effective widths  $D_e$  and  $W_e$  were given by  $D_e = D - d$  and  $W_e = W - d$ , where  $d$  is the sidewall depletion depth of  $0.2 \pm 0.1 \mu\text{m}$ .

Figure 4 shows the channel resistances  $R_{12,34} (=V_{34}/I_{12})$ ,  $R_{12,45} (=V_{45}/I_{12})$ , and  $R_{12,56} (=V_{56}/I_{12})$  as a function of temperature measured for devices having  $D = 1.7$ , 3.7, and 9.7  $\mu\text{m}$ . At high temperatures, all devices were in the diffusive regime, so that the longitudinal resistance was proportional to the channel length, i.e.  $R_{12,34} : R_{12,45} : R_{12,56} = L_{34} : L_{45} : L_{56}$ . The length factor became quenched as the temperature was lowered. Particularly, the ratio of  $R_{12,45}/R_{12,34}$  decreased down to  $\approx 1$  below 3 to 5 K, indicating

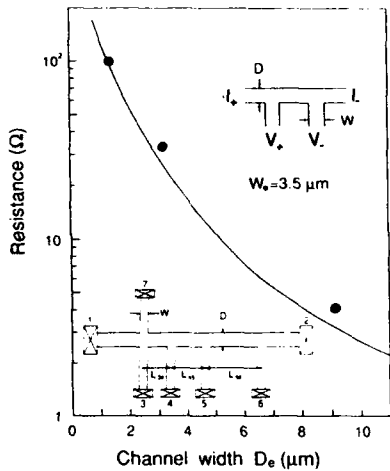


Fig. 3. Channel resistances at various temperatures.

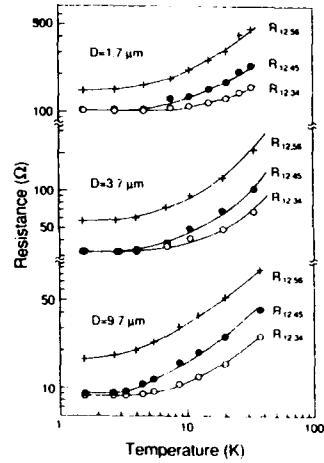


Fig. 4. Length-independent channel resistance.

that  $l_b \gg L_{23}(=20 \mu\text{m})$  although  $l_e=35$  to  $45 \mu\text{m}$  in this temperature range. This size-independent resistance appeared more pronounced for a device having a smaller value of  $D$ . The device of  $D=1.7 \mu\text{m}$  exhibited significant quenching of the length factor for  $R_{12,56}$  with  $L_{56}=40 \mu\text{m}$ . These results imply that the wide channels of  $D=1.7$  to  $10 \mu\text{m}$  significantly restrict the transverse momentum and enhances the apparent ballistic length, even though the calculated subband separation is much smaller than  $3kT$ . Figure 3 shows the length-independent resistance  $R_0$  of  $R_{12,45}(=R_{12,34})$  for various devices. The L-B formula gives a four-terminal resistance  $R_{xx}=(V_+-V_-)/(I_+-I_-)$  (Fig. 3) as

$$R_{xx} = \frac{\hbar}{2e^2} \cdot \frac{T_{14} - T_{15}}{2 T_{14} T_{15} + (T_{12} + T_{45})(T_{14} + T_{15}) + 2 T_{12} T_{45}},$$

where  $\sum_i T_{ij} = N_j$ .  $N_1=N_2=N_D$  and  $N_4=N_5=N_W$ , where  $N_D$  and  $N_W$  are the occupied 1D subband numbers in the current channel and voltage leads, respectively. For calculation of  $T_{ij}$ , we assumed the effect of scrambling where  $N_D \neq N_W$ . (Tarucha) The calculated  $R_{xx}$  is shown by the solid line, which well reproduces the experimental data of  $R_0$ . This means that our wide ballistic current channel is referred to a 1D channel rather than to a 2D channel.

#### 4. LOW-FREQUENCY NOISE UNDER HIGH ELECTRIC FIELD

1/f noise has been observed in most semiconductor devices and generally is attributed to fluctuation of resistance, because the noise power increases quadratically with current (Weissman 1988). We have studied noise generation in a high mobility 2DES using a four-terminal channel device with a Schottky gate. (Fig. 5) Observable noise appeared near

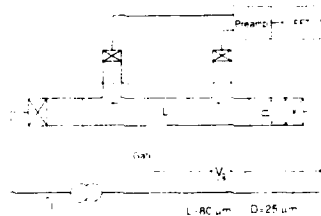


Fig. 5. Configuration of noise measurement.

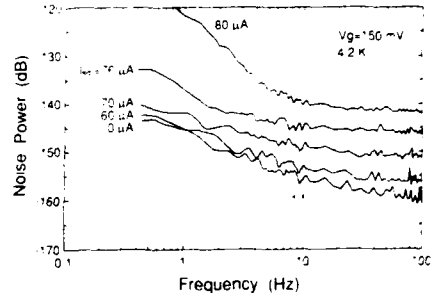


Fig. 6. Noise power vs. frequency curves for various channel current.

a diffusive regime rather than in the ballistic regime.  $\mu$  and  $n_s$  at 4.2 K of the device varied from  $\mu = 1.6 \times 10^6 \text{ cm}^2/\text{Vs}$  and  $n_s = 1.9 \times 10^{11} \text{ cm}^{-2}$  to  $\mu = 4.0 \times 10^5 \text{ cm}^2/\text{Vs}$  and  $n_s = 0.75 \times 10^{11} \text{ cm}^{-2}$  as a function of gate voltage  $V_g$  from 150 to -150 mV.

Figure 6 shows the noise power  $S_v$  vs. frequency  $f$  characteristics at  $V_g = 150 \text{ mV}$ . For a small injection current, there appeared no noise above the equilibrium level, where the channel current  $I_{sd} = 0$ . A significant noise generation was observed for  $I_{sd} > 60 \mu\text{A}$ . The noise power  $S_v$  followed the  $1/f$  line for  $f < 10 \text{ Hz}$ . A pronounced deviation from the  $1/f$  line appeared when  $I_{sd} = 80 \mu\text{A}$ . Figure 7 shows  $S_v$  at 1 Hz as a function of  $I_{sd}$  at various  $V_g$ . Above a critical level of  $I_{sd}$ ,  $S_v$  exhibited a steeper increase rather than the  $I_{sd}^2$  line, suggesting a nonlinear channel resistance. The critical current became large with increasing  $V_g$ , and compared well to the current range where an abrupt degradation of electron mobility occurred as indicated in the inset of Fig. 7. From DC and pulsed current measurements of electron mobility, we found that such an abrupt mobility degradation was caused by nonequilibrium electron heating under high electric field rather than by lattice heating. (Phillips) The electron mobility is restricted by optical and acoustic phonon scattering. The steep increase of  $S_v$  observed in the high mobility case ( $V_g = 150 \text{ mV}$ )

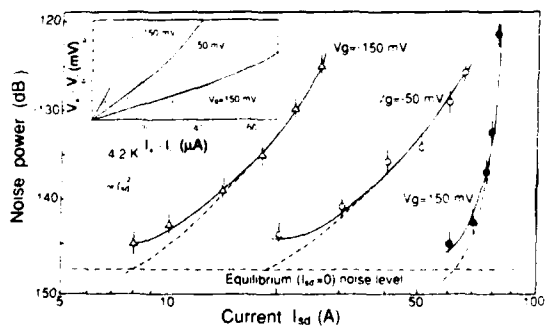


Fig. 7. Noise power vs. channel current measured at various  $V_g$ .

suggests a strong heating effect of nonequilibrium electrons in a high mobility 2DES. The dashed lines in Fig. 7 represent  $S_V$  after subtraction of the nonequilibrium noise level. This  $S_V$  may follow the 1/f line in the low-current limit.

## 5. SUMMARY

Macroscopic ballistic transport and low-frequency noise are studied for very high mobility 2DESS. Large-scale (10 to 150  $\mu\text{m}$ ) devices show two major properties of ballistic transport: long-distance ballistic transport of electrons and size-independent resistance. An abrupt increase of low-frequency noise appears for a large injection current. This arises from nonequilibrium electron heating giving rise to a strong mobility degradation.

**ACKNOWLEDGEMENT:** The authors are grateful to Y. Tokura and M. Stopa for valuable discussion on ballistic transport.

Büttiker M 1986 *Phys. Rev. Lett.* 57 1761  
Beenakker C W J and van Houten H 1989 *Phys. Rev. Lett.* 63 1857  
Chang A M, Chang T Y and Baranger H V 1989 *Phys. Rev. Lett.* 63 996  
Ford C J B, Washburn S, Büttiker M, Knoedler C M and Hong J M 1989 *Phys. Rev. Lett.* 62 2724  
Fukai Y K, Tarucha S, Hirayama Y, Tokura Y and Saku T 1992 *Appl. Phys. Lett.* (to be published)  
Hirayama Y, Saku T, Tarucha S and Horikoshi Y 1991 *Appl. Phys. Lett.* 58 2672  
Phillips J R (unpublished)  
R. Landauer 1970 *Philos. Mag.* 21 863  
Spector J, Stormer H L, Baldwin K W, Pfeiffer L N and West K W 1990 *Appl. Phys. Lett.* 56 1290  
Takagaki Y, Gamo K, Namba S, Ishida S, Takaoka S, Murase M, Ishibashi K and Aoyagi Y 1989 *Solid State Comm.* 69 881  
Timp G, Berringer R, Sampere S, Cunningham J E and Howard R E 1990 *Nanostructure Physics and Fabrication* (New York: Academic Press) p. 331  
Tarucha S, Hirayama Y, Saku T and Horikoshi Y 1991 *Proc. Int. Symp. Nanostructures and Mesoscopic Systems* (Santa Fe, New Mexico 1991) (to be published)  
Tarucha S (unpublished)  
Weissman M B *Rev. Mod. Phys.* 60 537

## Non-linear electron focusing in 2DEG systems with an applied DC current

K Nakazato, † R I Hornsey, ¶ T J Thornton, † J R A Cleaver and † H Ahmed

Hitachi Cambridge Laboratory, Madingley Road, Cambridge, CB3 0HE, United Kingdom  
† Microelectronics Research Centre, Cavendish Laboratory, Madingley Road, Cambridge, CB3 0HE, United Kingdom

¶ Department of Electrical Engineering, Imperial College of Science, Technology and Medicine, Exhibition Road, London, SW7 2BT, United Kingdom

Electron focusing has been observed in a GaAs/AlGaAs heterojunction, patterned into single and double grids by a combination of electron beam lithography and ion implantation. We report for the first time that the focusing peaks split and separate when a dc current is forced through the double grid. A possible cause of this effect is the acceleration and deceleration of electrons through the grids. Theory of electron focusing has been developed in terms of microscopic transmission probability, with a good agreement between measured and calculated magnetic and electric field dependences.

### 1. INTRODUCTION

Electron focusing in a high-mobility two-dimensional electron gas (2DEG) has been observed in laterally patterned AlGaAs/GaAs heterojunctions (van Houten et al. 1989, Nakamura et al. 1990). The electrons that initially pass through the grid return due to their cyclotron motion (Fig. 1); those electrons which are then incident on a gap in the grid return to the injector side and reduce the transmission probability, resulting in an increase in the longitudinal magnetoresistance. A resistance peak was therefore observed at the magnetic field for which the cyclotron diameter coincided with the spacing of the grid ( $n=1$  in Fig. 1b). Because the grid consisted of multiple openings, several higher-mode peaks ( $n=2, 3, 4, \dots$ ) were also observed. The purpose of the present paper is to show that this electron focusing contains various information about such nanostructures.

### 2. EXPERIMENTS

The structures used in this work were made from a GaAs/AlGaAs heterojunction grown by molecular beam epitaxy. The mobility at liquid helium temperatures was around  $5.0 \times 10^5 \text{ cm}^2/\text{Vs}$  at a sheet concentration of  $1.8 \times 10^{11} \text{ cm}^{-2}$  measured with no illumination.

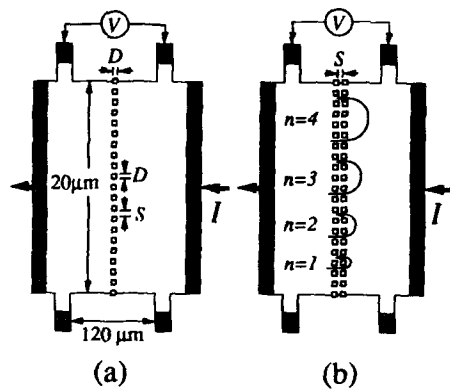


Fig. 1. Schematic diagram of the devices used in this work. (a) Single-grid structure, (b) Double-grid structure.  $D = S = 0.5 \mu\text{m}$ . The electron trajectories corresponding to cyclotron radii equal to  $n L$  ( $n=1, 2, 3$  and  $4$ ), where  $L = (D+S)/2$ , are shown in the figure.

These values were changed to  $8.6 \times 10^5 \text{ cm}^2/\text{Vs}$  and  $3.3 \times 10^{11} \text{ cm}^{-2}$  after illumination. Hall bars were defined by wet etching and single and double grid patterns (see Fig. 1) were fabricated in the centre of the sample using electron beam lithography with a polymethylmethacrylate (PMMA) resist. Samples were then exposed to a rastered  $\text{Ga}^+$  focused ion beam with an energy of 30keV and a dose of  $1 \times 10^{13} \text{ cm}^{-2}$ , with no subsequent annealing. Areas of the 2DEG not protected by the PMMA were thereby rendered insulating. The width of the Hall bar was  $20 \mu\text{m}$  so that each  $1 \mu\text{m}$ -pitch grid consisted of 20 damaged regions.

Figure 2 shows the magnetoresistance of single and double grid structures at 1.8K. From the Shubnikov de Haas oscillations at high magnetic fields ( $H > 0.4\text{T}$ ), the sheet carrier concentration was estimated to be  $2.9 \times 10^{11} \text{ cm}^{-2}$ . Using this value, magnetic fields corresponding to a cyclotron radius of  $n L$  (where  $L = (D+S)/2 = 0.5 \mu\text{m}$ ) were calculated, and the index  $n$  is shown in Figure 2. It is apparent that this low-field resistance oscillation is due to electron focusing through the grid(s). At integer values of  $n$ , resistance maxima occur because electrons returning to the grid are transmitted back through and so reduce the current (Fig. 3bA). The resistance is therefore higher than the zero-field resistance (Fig. 3a). For half-integer values of  $n$ , those trajectories that have passed through the grid do not find an opening in the grid for the return passage and are scattered in the forward direction (Fig. 3cA). In addition, electrons that initially were scattered at the front side of the grid will be transmitted forward through it (Fig. 3cB). The resultant resistance minimum, lower than the zero-field resistance, has been observed clearly, as shown in Fig. 2. Furthermore, the difference between the magnetoresistances of single and double grid structures does not display oscillations but instead has a peak at a magnetic field of around  $0.27\text{T}$ . This behaviour may be explained by internal scattering between the two grids using a simple model of parallel *rough* quantum wires of approximate length  $2D+S$ . A model including diffuse scattering at the boundary shows that the magnetoresistance increases until it reaches a maximum at a field  $H_{\max}$ , which scales with the ratio of the cyclotron radius  $\ell_c$  to the effective wire width  $S'$  as  $S'/\ell_c = 0.55$  (Thornton et al. 1989). From the above value of  $H_{\max}$ , the effective width  $S'$  is estimated to be 180nm. This implies that the width of the depletion region around the implanted areas is 160nm.

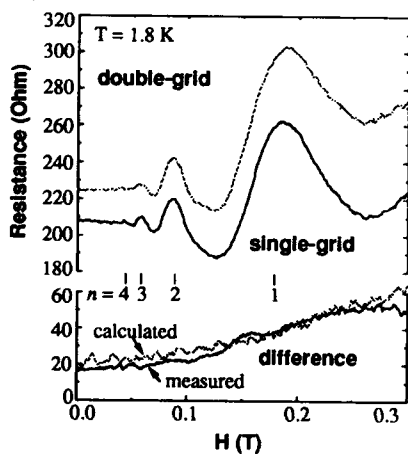


Fig. 2. Magnetoresistance of single-grid and double-grid structures. The index  $n$  from 1 to 4 for values of magnetic field is indicated in the figure. The difference in magnetoresistance between single-grid and the double-grid structures is compared with the calculation using a billiard ball model, in which the width of the depletion region is assumed to be 100nm.

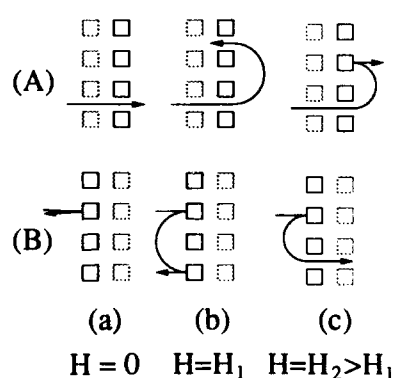


Fig. 3. Some of the various transmission mechanisms and scattering mechanisms possible with two grids, for a range of magnetic fields; (a) zero field (b) field enhancing the resistance (c) field decreasing the resistance.

The differential longitudinal magnetoresistance was measured with a constant dc current applied. Through a  $500\Omega$  load resistance, a dc voltage (0-5V) is applied to the sample, in addition to a low-frequency ac voltage with amplitude 50mV. The two-terminal resistance of the sample is around  $2\text{k}\Omega$ , much smaller than the load resistance, so that an approximately constant dc current condition is achieved. Figure 4 shows the result at temperature 0.15K. The measurement has been performed with no illumination and so the carrier concentration, estimated to be  $1.9 \times 10^{11}\text{cm}^{-2}$ , is lower than that in the linear electron focusing experiments. The electron focusing peaks split and separate when a dc current is forced through the double grid, shown by the dotted lines in Fig. 4. We propose that this split of electron focusing peaks can be interpreted by considering the acceleration and deceleration of electrons through the grids. Since the most resistive region is that of the grids, the main voltage drop in the circuit occurs across them. Electrons injected from the left-hand side are accelerated through the grids and the electron kinetic energy at the right-hand side is increased by an amount of  $-eV$ , where  $e < 0$  is the electron charge and  $V$  is a voltage drop across the grids. On the other hand, electrons injected from the right-hand side are decelerated by an amount of  $-eV$ . Since the cyclotron radius is proportional to the square root of the electron kinetic energy, these accelerated and decelerated electrons have different cyclotron radii, resulting in the observed splitting of the electron focusing peaks. This implies a phenomenological expression of differential magnetoresistance  $R(H, V)$  under a magnetic field  $H$  and a dc voltage  $V$ ;

$$R(H, V) = a(V) \left\{ R\left(\frac{H}{\sqrt{1 - \alpha_1(V)}}, 0\right) + R\left(\frac{H}{\sqrt{1 - \alpha_2(-V)}}, 0\right) \right\} + b(V) . \quad (1)$$

The parameter  $\alpha$  ( $\alpha_1$  and  $\alpha_2$ ) for negative voltage is defined by  $\alpha(-V) = -\alpha(V)$ ; the expected value of  $\alpha$  is  $-eV/E_F$  where  $E_F$  is the electron Fermi energy. Measured values of the differential magnetoresistance are fitted to the phenomenological expression (1) by the least-squares method and the obtained parameter  $\alpha$  is plotted as a function of dc current in the inset of Fig. 4. At currents less than  $2\mu\text{A}$ ,  $\alpha$  has linear dependence on the dc current, given by  $0.2 I[\mu\text{A}]$ . This dependence is stronger than the expected one,  $\alpha = -eIR/E_F = 0.08 I[\mu\text{A}]$  obtained using a measured average resistance  $R$  of  $550\Omega$  and Fermi energy  $6.8\text{meV}$ . Despite this, the initially linear dependence of  $\alpha$  upon dc current supports the acceleration and deceleration mechanism proposed above.

### 3. THEORY

The observed magnetoresistance can be classed as a semi-classical phenomenon and results from the characteristics in an extended region. A semi-classical theory of magnetoresistance in a quantum wire has been developed previously, based on the Büttiker-Landauer formula and a billiard ball model (Beenakker and van Houten 1989). However this model mainly considers the scattering at the boundary of the quantum wire. The characteristics in the extended region

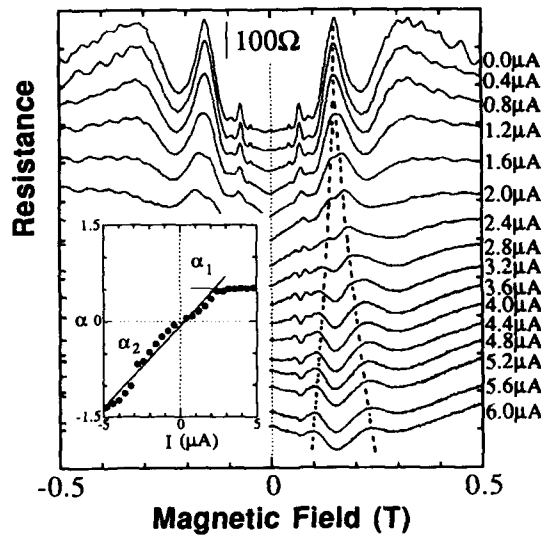


Fig. 4. Differential magnetoresistance of double-grid structure at  $T=0.15\text{K}$ . A constant dc current is forced into the sample from  $0\mu\text{A}$  to  $6\mu\text{A}$ . Resistance data are fitted by eq.(1) and the obtained parameter  $\alpha$  is plotted in the inset.

cannot be calculated in this way owing to the singularity encountered because the electron trajectories in the extended region consist of closed circles and do not contribute to the transport. One method to overcome this difficulty is to introduce impurity scattering. However the observed magnetoresistance seems to be independent on the details of scattering so a general theory has been developed, independent of the details of scattering mechanism in the extended region. We consider the probability  $P_f$  that an electron is injected from the left-hand side and transmitted across the grid to the right-hand side,

$$P_f = t_f / (t_f + t_g + t_b) , \quad (2)$$

where  $t_f$ ,  $t_g$ , and  $t_b$  are times for which an electron stays in the forward region (right-hand side), the grid region, and the backward region (left-hand side), respectively. This probability characterises the three primary components of electron trajectories related to electron focusing; forward scattering (Fig.3cA), trapping (Fig.3bA), and backscattering (Fig.3bB). Furthermore,  $P_f$  can be interpreted as a *microscopic transmission probability* through the grids. If an additional scattering is assumed due to random impurities, the probability that electrons are transmitted forwards is proportional to the time an electron stays in the forward region. In addition,  $P_f$  is a statistical mechanical definition of transmission probability in a system without any scattering mechanism except the grids. When electric potentials are applied between the grid(s) ( $V_L$  at the left-hand side electrode and  $V_R$  at the right-hand side electrode), the resulting electric current,  $I$ , is given by the Landauer formalism to be

$$I = \frac{2e}{h} \left[ \int T_{L \rightarrow R}(E) f_L(E) \{1 - f_R(E)\} dE - \int T_{R \rightarrow L}(E) f_R(E) \{1 - f_L(E)\} dE \right] , \quad (3)$$

where  $h$  is the Planck constant,  $f_L$  and  $f_R$  are local equilibrium distribution functions at the left and right-hand electrodes with chemical potentials  $E_F + eV_L$  and  $E_F + eV_R$ . The *macroscopic transmission probability*  $T_{L \rightarrow R}$  can be written in terms of microscopic transmission probability  $P_f$  defined by eq. (2) as

$$T_{L \rightarrow R} = \frac{P_f}{h} \int_0^W dx \int_{-\pi/2}^{\pi/2} d\theta P_f \cos \theta , \quad (4)$$

where  $W$  is the width of the quantum wire and  $\theta$  is the angle between the incident electron momentum  $p$  and the electron flow  $-I$ . Electrons (typically around  $2 \times 10^5$ ) are injected from the left-hand side of the grids and their trajectories are followed by solving the equation of motion until a time  $t_{total} = t_f + t_g + t_b$  is reached. This value corresponds to the mean free time in the starting GaAs/AlGaAs heterojunction and is typically 40ps. Specular reflection is assumed at the boundaries of the grid(s). The microscopic transmission probability  $P_f$  is then calculated by obtaining the electron time  $t_f$ . Figure 5 shows the calculation for the double-grid structure under a constant voltage condition. It is seen that the calculated resistance explains the experiments quite well.

## REFERENCES

Beenakker C W J and van Houten H 1989 *Phys. Rev. Lett.* **63** 1857  
 Nakamura K, Tsui D C, Nihey F, Toyoshima H and Itoh T 1990 *Appl. Phys. Lett.* **56** 385  
 Thornton T J, Roukes M L, Scherer A and van de Gaag B P 1989 *Phys. Rev. Lett.* **63** 2128  
 van Houten H et al. 1989 *Phys. Rev. B* **39** 8556

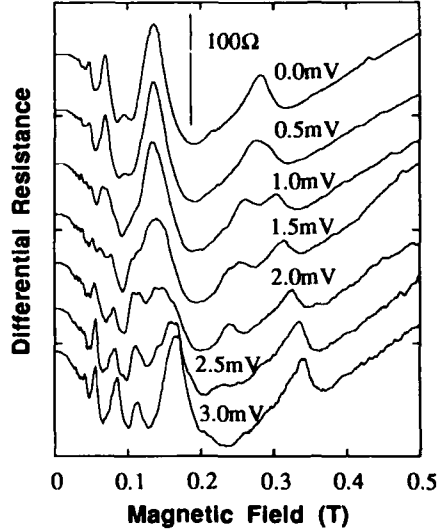


Fig. 5. Calculated differential magnetoresistance under a constant dc bias condition. The depletion width is assumed to be 100nm.

## Electron transport in the transition regime between 2D and 0D behaviour

G Berthold, J Smoliner, V Roßkopf, E Gornik, G Böhm and G Weimann

Walter Schottky Institut, TU München, Am Coulombwall, D-8046 Garching, Germany

**ABSTRACT:** The influence of strongly modulating potentials on the magnetotransport properties of a two dimensional electron gas is investigated. On anti-dot like lateral surface superlattices, a well defined negative differential magnetoresistance occurs at low magnetic fields, which is followed by a large peak. In addition, an anomalous temperature behavior is observed. Calculating the electron drift in the modulated potential by taking the external electric fields and the Hall field explicitly into account, the occurrence of the negative differential magnetoresistance and the negative temperature coefficient is explained for the first time.

Many magnetotransport experiments on low dimensional electron systems show that semi-classical effects (Weiss 1991, Beton 1989) are dominant if the cyclotron radius matches the dimensions of the system. In this paper, we investigate the transport properties of anti-dot type lateral surface superlattices (LSSL) in a regime where the Fermi energy is in the same order of magnitude as the potential modulation ( $\lambda = E_f/eV_m > 1$ ). At low magnetic fields, such LSSLs show a negative differential magnetoresistance, which is followed by a large peak, if the cyclotron diameter matches the period of the modulated potential. Also an anomalous temperature behavior is observed and explained within a semiclassical model.

The samples consist of an unintentionally p-doped GaAs layer grown on a semiinsulating substrate ( $N_A < 10^{14} \text{ cm}^{-3}$ ), followed by an undoped spacer ( $d = 120 \text{ \AA}$ ), and doped  $\text{Al}_x\text{Ga}_{1-x}\text{As}$  ( $d = 400 \text{ \AA}$ ,  $N_D = 2 \cdot 10^{18} \text{ cm}^{-3}$ ,  $x = 32\%$ ). The additional GaAs cap layer was also highly n-doped ( $d = 150 \text{ \AA}$ ,  $N_D = 3 \cdot 10^{18} \text{ cm}^{-3}$ ). The mobility of the samples is  $\mu = 4 \cdot 10^5 \text{ cm}^2/\text{Vs}$  at  $T = 4.2\text{K}$ . Bar-shaped mesas were etched into the sample and ohmic contacts were alloyed using AuGe. By means of wet chemical etching anti-dot structures having a period of  $a = 475 \text{ nm}$  and  $630 \text{ nm}$  were fabricated on the mesas using UV-laser holography.

To investigate the transport properties of these lateral surface superlattices, magnetoresistance measurements were performed in a configuration where the magnetic field is oriented perpendicular to the two dimensional electron gas. Fig. 1 shows the magnetoresistance curves for an anti-dot like superlattice (curve 1,2,3). At low magnetic fields

( $B < 0.2$  T), a clear NDMR is evident in all cases. In addition, a large maximum in the magnetoresistance is observed at  $B = 0.48$  T and  $B = 0.27$  T for the anti-dot like LSSL with the period  $a = 475$  nm (curve 1) and  $630$  nm respectively. (curve 2,3). This peak has also been observed by other groups (Lorke 1991). The NDMR was also observed earlier (Ensslin 1990), but it was never discussed. In addition, the magnetoresistance decreases with increasing temperature (NTC). Curve (2) and (3) show this behavior for  $T = 7$  K and  $T = 4.2$  K, respectively. For an unstructured 2DEG the resistance at  $B = 0$  T (curve 0sec in Fig.2) increases

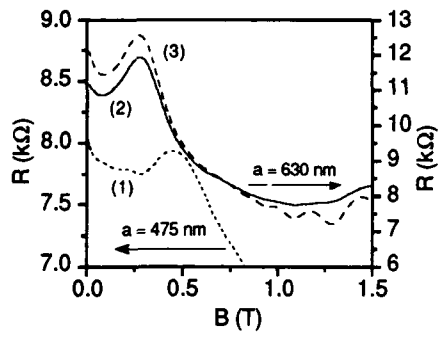


Fig. 1. Magnetoresistance of a 475 and a 630 nm sample. Curve 2 and 3 were recorded at  $T = 7$  K and  $4.2$  K respectively.

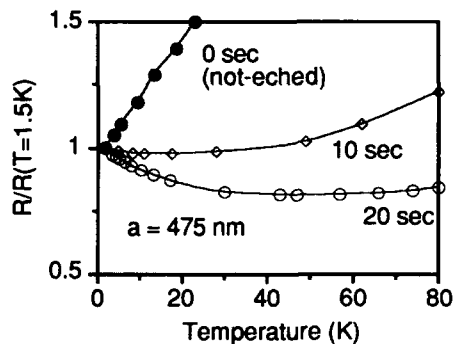


Fig. 2. Normalized sample resistance vs. temperature

with increasing temperature. For anti-dot like structures, however, a clear NTC is observed which is more pronounced if the grating is etched deeper into the sample (see Fig. 2 for different times of etching (10 sec, 20 sec)).

To explain these properties quantitatively, we now consider electrical transport in a two dimensional lateral surface superlattice in terms of a classical Drude model. The classical magnetoresistance is given by the expression  $\rho_{xx} = m^*/(Ne^2\tau)$ , where  $m^*$  denotes the effective mass,  $e$  the electron charge,  $\tau$  the scattering time and  $N$  the number of electrons per unit area which contribute to the current flow. In our model,  $N$  is obtained from :

$$N(B) = n_s P(B, E_f) \int_{E_f - kT}^{E_f + kT} \frac{1}{E_F} f(E) dE, \quad (1)$$

where  $n_s$  is the 2D electron concentration,  $f(E)$  the Fermi distribution and  $P(B, E_f)$  a magnetic field dependent percentage of electrons which contribute to the current flow.

To calculate  $P(B, E_f)$ , we now consider the trajectories of the electrons in a LSSL with magnetic field perpendicular to the modulated electron gas. In addition to the calculations performed by other groups, we also include the external electric field  $E_{ext}$  (x-direction) and the Hall field  $E_{Hall}$  (y-direction) which results in an effective potential:

$$V(x,y) = \frac{V_m}{4} \left( \cos\left[\frac{2\pi}{a} x\right] + \cos\left[\frac{2\pi}{a} y\right] + 2 \right) + eE_{ext}x + eE_{Hall}y, \quad (2)$$

The equations of motion including the effective potential  $V(x,y)$  and the magnetic field, were solved numerically for a set of 588 arbitrary initial starting points  $(x,y)$  and momentum vectors  $(p_x, p_y)$ . The corresponding kinetic energy was then obtained by  $E_{kin} = E_f - V(x,y)$ . As a result, we obtain two groups of electrons, which coexist in a detailed balance. The first group  $P(B, E_f)$  has a drift in the direction of the external field. The second group of  $(1 - P(B, E_f))$  electrons moves either perpendicular to the external field or on closed trajectories. This kind of orbits always exists as long as the integral  $\int (E_{int} + E_{ext} + E_{Hall}) dx$  is zero. Here, the integration is carried out along the trajectory.  $E_{int}$  is the internal field in the modulated potential.

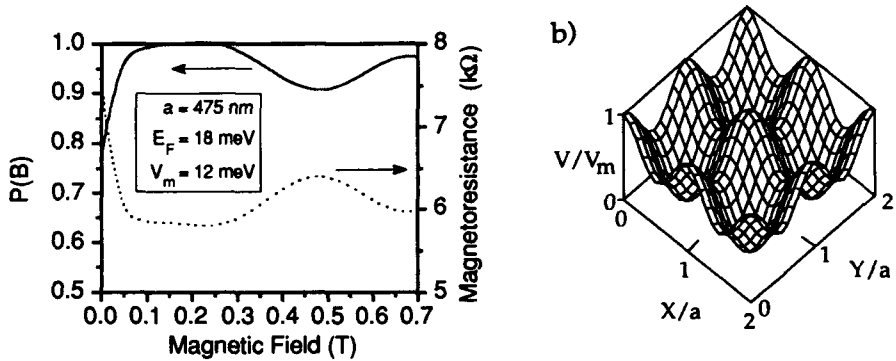


Fig. 3: a) The calculated relative number of electrons  $P(B)$  (solid line) which contributes to the current flow. The resulting magnetoresistance (dotted line) shows a clear negative differential magnetoresistance followed by a maximum at  $2R_c \approx a$ . The periodic potential is shown in b)

To evaluate the number of electrons contributing to the current flow  $P(B, E_f)$ , one has to know how many particles move in field direction. For a fixed Fermi level and  $B=0T$ , a significant amount of the electrons channel through the potential valleys perpendicular to the direction of the external field. If  $B$  is increased, a decreasing number of electrons  $(1 - P(B, E_f))$  moves perpendicular to the external electric field. Further, an increased number of electrons moves parallel to the external field  $E_{ext}$  or show some random walk like motion with an average drift velocity  $v_{drift}$  in the direction  $E_{ext}$ . This behavior explains the well defined NDMR observed in our experiment. As the electrons which move perpendicular to the external field  $E_{ext}$  do not contribute to the current flow, the  $B=0T$  resistance of the nanostructured samples is higher than on unstructured samples.

If  $B$  increases further ( $B > 0.2T$ ), the interplay between the Hall field  $E_{Hall} = \omega r E_{ext}$  and the Lorentz force  $eV \times B$  strongly influences the trajectories in the two dimensional modulated potential. In this regime, the Lorentz force induces an increasing number of closed

orbits. Simultaneously,  $P(B, E_f)$  is reduced due to a decreasing number of electrons drifting in the direction of the external field. Therefore, a maximum in the magnetoresistance is expected in the range, where the diameter of the cyclotron orbit matches the period of the LSSL. For an anti-dot like potential, which has a period of 475 nm, we obtain a value of  $B_p^{\text{calc}}=0.51\text{T}$  and an experimental value of  $B_p^{\text{exp}}=0.43\text{T}$ . The calculated maximum of the magnetoresistance is in good agreement with the experimental data. At even higher magnetic fields ( $B>0.5\text{T}$ ) the Hall field  $E_{\text{Hall}}$  is so large, that the closed trajectories are destroyed and a regular  $E_{\text{Hall}} \times B$  drift comes up. This means that  $P(B, E_f)$  increases until all electrons move in the direction of the external field  $E_{\text{ext}}$ .

If we average the relative number of participating electrons within  $kT$  around the Fermi energy, we get the following result :  $P(B, T) = c \cdot \int P(B, E) f(E, T) (1-f(E, T)) dE$ , with  $c=1/\int f(E, T) (1-f(E, T)) dE$  as a normalization constant. With increasing temperature, the effect of the 'guiding' potential decreases. Therefore, this yields an increased amount of electrons participating to the current and therefore a decreasing sample resistance with increasing temperature. This is shown in Fig. 4 for a potential modulation with  $V_m = 8\text{meV}$  and  $12\text{meV}$ .

In summary, we have investigated the transport properties of anti-dot like LSSL's in the presence of a low magnetic fields. On all samples, a well defined NDMR followed by a large resistance maximum is observed accompanied by a strong NTC. Taking explicitly the external electric field and the Hall field into account, the NDMR, the maximum of the magnetoresistance and the NTC are quantitatively explained through a purely classical model.

**Acknowledgements :** The authors are grateful to J.A. Brum and W. Demmerle for helpful discussions. This work was sponsored by Deutsche Forschungsgemeinschaft, project no. SFB 348 TPA2.

#### REFERENCES :

Weiss D, Roukes M.L., Menschig A., Grambow P, v. Klitzing K and Weimann G, 1991  
*Phys. Rev. Lett.* 66 p2790

Beton P H, Alves E.S, Main P.C, Eaves L, Dellow M.W, Henini M, Huges O.H, Beaumont S.P and Wilkinson C.D.W, 1989 *J. Phys. C* 1 p8257

Lorke A, Kothaus J P and Ploog K, 1991 *Phys. Rev. B* 44 p3447

Ensslin K and Petroff P.M, 1990 *Phys. Rev. B* 41 p12307

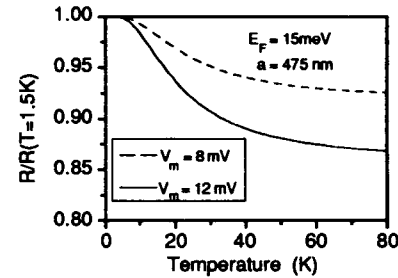


Fig. 4: Calculated normalized sample resistance vs. temperature.

## Superlattice effects on the weak localization of a grating gate Si-MOSFET

J.R. Gao<sup>1\*</sup>, C. de Graaf<sup>1</sup>, J. Caro<sup>1</sup>, S. Radelaar<sup>1</sup>, and K. Heyers<sup>2</sup>

<sup>1</sup> Delft Institute of Microelectronics and Submicron Technology,  
Delft University of Technology, Lorentzweg 1, 2628 CJ Delft, The Netherlands

<sup>2</sup> Institute of Semiconductor Electronics,  
Aachen Technical University, D-5100 Aachen, Germany

**ABSTRACT:** It is found that weak localization (WL) in a lateral superlattice is considerably enhanced compared to the homogeneous two-dimensional case. The maximum value of the enhancement as deduced from low field magnetoconductance measurements is 2.3. By varying the biasing of the grating gate of the superlattice device we also observed a clear cross-over from one-dimensional WL to two-dimensional WL.

### 1. INTRODUCTION

In this paper we report the first observation of superlattice effects on the weak localization (WL) of a lateral superlattice (LSL). The effects were observed in the low field magnetoconductance (LFMC) of a LSL induced in a grating gate MOSFET as a function of the strength of the potential modulation. The measurements also show a cross-over from 1D to 2D WL by changing the operation mode of the device from the multiple quantum wire mode to the LSL mode, and finally to the virtually homogeneous 2D EG mode.

The device used was a Si-MOSFET fabricated on a (100) wafer. Figure 1 shows a schematic cross-section of the device. The lower gate of the MOSFET is a polysilicon grating of period  $a=200$  nm. The 240 interconnected parallel grating lines extend from source to drain and cover a channel area  $L \times W_{2D}=24 \mu\text{m} \times 48 \mu\text{m}$  ( $L$ =channel length;  $W_{2D}=2D$  channel width). The upper gate is a continuous aluminium layer. For appropriate biasing of the gates, multiple quantum wires can be formed in the device. Starting from the quantum wire mode an electron gas with a modulated surface potential or a LSL can be formed by increasing the appropriate gate voltage to above threshold. The potential modulation is a function of both the upper gate voltage  $V_{GU}$  and the lower gate voltage  $V_{GL}$ .

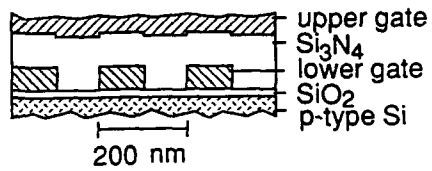


Fig. 1. Schematic cross-section of a grating gate MOSFET.

### 2. EXPERIMENTAL RESULTS

Our direct measurement results are shown in Figure 2a, which shows LFMC traces of a device taken at  $T=0.4$  K between  $-0.12$  T and  $0.12$  T and for  $V_{GU}=28$  V. The range of  $V_{GL}$  values between  $-0.4$  V and  $5.5$  V covers a range of device operation modes from quantum wire mode (electrons under the gaps between the grating lines) via superlattice mode with a strong modulation to superlattice mode with a weak modulation. For the quantum wire mode several (up to about five) 1D subbands are occupied (Gao et al., 1990 and Gao, 1991). The relative conductance increase for the field range used amounts to 14 % for  $V_{GL}=-0.4$  V and this value gradually decreased to 1 % for  $V_{GL}=5.5$  V.

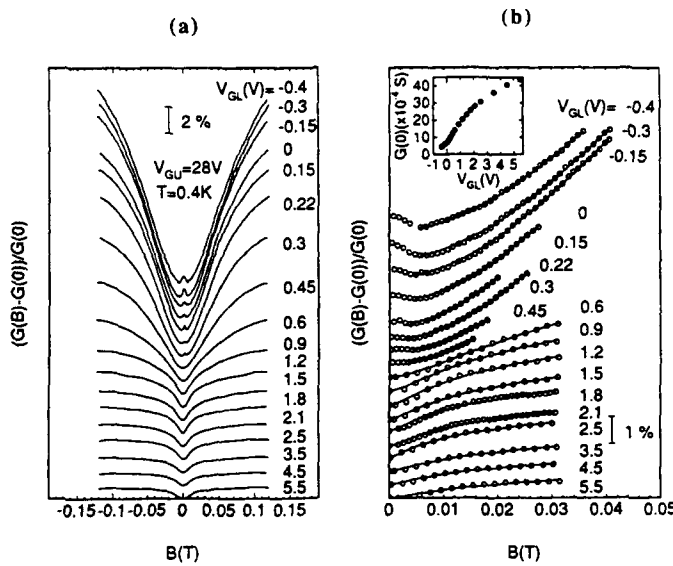


Fig. 2. Magnetoconductance for eighteen  $V_{GL}$  values and for fixed  $V_{GU}$ . Curves have a vertical offset. Raw data are shown in (a). In (b) a reduced data set is shown. The curves in (b) are fits of Eq. (1) or Eq. (2) to the data points. The inset shows a plot of  $G(0)$  vs  $V_{GL}$ .

### 3. ANALYSIS

We analysed the data of Figure 2a by fitting to the corresponding *absolute* magnetoconductances the standard expressions for the LFMC due to WL of Al'tshuler and Aronov (1981) and of Al'tshuler et al. (1980), for the 1D case ( $L_{in} > W_{1D}$ ,  $L_{in}$  being the inelastic diffusion length and  $W_{1D}$  the 1D channel width, and (naively neglecting superlattice effects) for the 2D case ( $L_{in} < W_{2D}$ ), respectively:

$$G(B,T) - G(0,T) = \frac{N_c}{L} \frac{e^2}{\pi \hbar} n_v \alpha \left[ L_{in} \left( \frac{1}{L_{in}^2} + \frac{e^2 W_{1D}^2 B^2}{3 \hbar^2} \right)^{-1/2} \right] \quad (1)$$

$$G(B,T) - G(0,T) = \frac{W_{2D}}{L} \frac{e^2}{2\pi^2 \hbar} n_v \alpha \left[ \Psi \left( \frac{1}{2} + \frac{\hbar}{4eBL_{in}^2} \right) - \ln \left( \frac{\hbar}{4eBL_{in}^2} \right) \right] \quad (2)$$

Here  $G(0,T)$  and  $G(B,T)$  are the conductances at temperature  $T$  and at zero and non-zero magnetic field, respectively. In Eq. (1)  $N_c$  is the number of channels ( $N_c = 240$ ) and  $n_v$  the valley degeneracy ( $n_v = 2$  for a (100) Si inversion layer). In Eqs. (1) and (2)  $\alpha$  is an empirical constant depending on the relative magnitude of the inelastic scattering time and the intervalley impurity scattering time (Fukuyama, 1982), and  $\Psi$  is the digamma function. Eq. (1) is valid only if the magnetic length  $l_B = (\hbar / 2eB)^{1/2}$  exceeds  $W_{1D}$ , while Eq. (2) is valid if  $l_B > l_c$ ,  $l_c$  being the elastic mean free path.

In the fitting procedure we used a reduced data set obtained by averaging for each  $V_{GL}$  the pair of points taken at positive and negative magnetic field and we first omitted the negative magnetoconductance around zero field, which occurs for  $V_{GL}$  in the range -0.40 V to 0.3 V and which resembles spin-orbit (SO) scattering effects observed in metal films (Santhanam et al., 1984).

We fitted the 2D equation to the data by adjusting  $\alpha$  and  $L_{in}$  under the condition  $l_B \approx 2l_e$  ( $l_e \approx 50$  nm). We found that using Eq. (2) only for  $V_{GL} \geq 0.6$  V satisfactory fits can be obtained (Eq. (1))

does not fit for  $V_{GL} \geq 0.6$  V; see below). Therefore, it is concluded that in this  $V_{GL}$  range the system seemingly follows the standard 2D behaviour, although we know that for  $V_{GL}$  immediately above 0.6 V the system is a LSL with a strong potential modulation. For this 2D case we found that  $\alpha=0.88$  for  $V_{GL}=0.6$  V and that  $\alpha$  decreases with  $V_{GL}$  up to 2.5 V, whereafter it remains at the constant value of about 0.39, which is very close to the recently reported experimental value  $\alpha=0.35$  for homogeneous (100) Si inversion layers (Paquin et al., 1988). The saturation of  $\alpha$  above 2.5 V at the level of a two-dimensional electron gas (2D EG) leads us to assume that the actual parameter we fitted is the product of  $\alpha$ , which takes the usual 2D EG value, and an enhancement parameter  $F$ , which takes into account the superlattice effects on the WL. In this way, the saturation region corresponds to a virtually homogeneous 2D EG. Eq. (1) was fitted to the data by adjusting  $W_{1D}$  and  $L_{in}$  under the condition  $l_B \geq 1.2W_{1D}$ , using the saturation value  $\alpha=0.39$  found in the 2D fits. This 1D equation fits well for  $V_{GL} \leq 0.45$  V but not beyond this range. Apparently for  $V_{GL} \leq 0.45$  V multiple 1D channels are formed.

In an attempt to analyse the negative magnetoconductance around zero field occurring in the 1D regime, we used the extended version of Eq. (1) usually employed to describe the effect of SO-scattering in metal wires (Santhanam et al., 1984). It was not possible, however, to obtain acceptable fits using this equation. Possibly, the vertical confinement of an electron gas in a MOSFET causes that the equation including the effect of SO-scattering applicable to 1D metal wires does not apply in our case.

The values of  $F$  obtained by normalizing the  $\alpha$  parameter to its saturation value (0.39) are plotted in Fig. 4a, together with  $W_{1D}$ . Superlattice effects apparently enhance the WL considerably above its strength in a homogeneous 2D EG (up to a factor 2.3), the enhancement becoming stronger with decreasing  $V_{GL}$ , i.e. increasing potential modulation. This qualitatively agrees with the recent theory of Szott et al. (1992) for WL in a LSL with the Fermi energy inside the first minigap. Szott et al. argue that the electronic diffusion constant in a LSL is an anisotropic quantity with components  $D_x$  and  $D_z$  for diffusion parallel and perpendicular to the "channels" of the superlattice, respectively.  $D_z$  depends on the superlattice period and the strength of the potential modulation (which determine the widths of the minibands and of the minigaps), but  $D_x$  almost does not. Further,  $D_z$  is smaller than  $D_x$ , the inequality becoming stronger for stronger potential modulations. The effect of all this becomes clear from the expression of Szott et al. for the parallel transport magnetoconductivity in the limit of

large  $D_z$  (i.e.  $L_{in,z} = (D_z \tau_{in})^{1/2} > a$ ,  $\tau_{in}$  being the inelastic scattering time and  $a$  the superlattice period), which takes a form essentially identical to Eq. (2) apart from a prefactor  $(D_x/D_z)^{1/2}$  and the replacement of  $L_{in}^2$  by  $L_{in,x}L_{in,z}$  (where  $L_{in,x} = (D_x \tau_{in})^{1/2}$ ). Thus, for their specific case Szott et al. predict an enhancement of the WL effect in a LSL compared to the homogeneous 2D EG case.

In our case the number of filled minibands is about ten. Nevertheless, we interpret our data in the light of the WL results of Szott et al. and assume that the properties they derive also hold qualitatively in case several minibands are filled. In this way  $F$  is a generalized function depending on the superlattice parameters and with properties similar to those of  $(D_x/D_z)^{1/2}$ . The  $F$  function interpolates between 1D and 2D WL. By turning on the potential modulation two

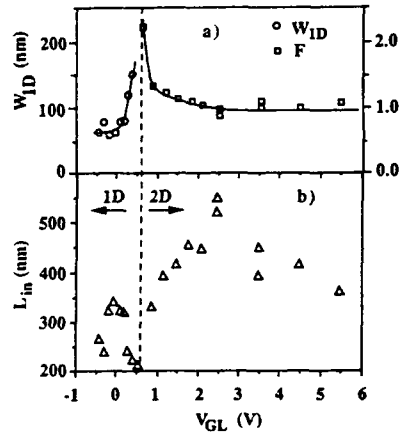


Fig. 3. Fit parameters  $W_{1D}$  and  $F$  both in (a), and  $L_{in}$  in (b) corresponding to the fits of Figure 2b. The right hand scale applies to the  $F$  parameter. Curves were drawn to guide the eye.

sets of communicating parallel "wires" of different electron density are formed. The dispersion relation  $E(k_z)$  for the motion perpendicular to the wire direction becomes a set of minibands separated by gaps of a width proportional to the strength of the potential modulation. As this strength increases the minibands flatten. As a result, the electron velocity in this direction is decreased and thus the electron diffusion is reduced. This resembles a system of weakly coupled wires, which are 1D with respect to WL in case  $L_{in} \geq a$ . Due to this 1D character, the coherent backscattering of electrons increases. Therefore, the absolute magnitude of the WL correction to the conductance is larger in the LSL than in the homogeneous 2DEG and increases with increasing modulation strength. In the extreme case of very strong modulation only one set of isolated wires remains and the minibands transform to dispersionless energy levels. Then the WL behaviour is 1D.

In the 1D regime the values of  $L_{in}$  (see Figure 3b) always exceed  $W_{1D}$ , which justifies the use of Eq. (1). On the average,  $L_{in}$  in the 2D regime is about two times as large as in the 1D regime. This qualitatively agrees with experimental data and a theoretical estimate of Wheeler et al. (1982). The initial increase of  $L_{in}$  in the 2D regime for low  $V_{GL}$  is probably also a superlattice effect, since here  $L_{in}$  actually stands for  $(L_{in,x}L_{in,z})^{1/2}$ , which increases with decreasing potential modulation due to the dependence of  $L_{in,z}$  on  $D_z$ .

$W_{1D}$  (see Fig. 4a) on the average increases with  $V_{GL}$ , as expected. For  $V_{GL}=0.30$  V and  $V_{GL}=0.45$  V the fitted  $W_{1D}$  exceeds the gap width between the lines of the grating gate. We attribute this effect to the breakdown of the 1D WL theory in the regime of the transition from quantum wires to superlattice.

#### 4. CONCLUSIONS

In summary, we have observed, for the first time, lateral superlattice effects on the weak localization (WL) by measuring the magnetoconductance of a superlattice MOSFET. In qualitative agreement with a recent theory of such effects, the WL is enhanced in a lateral superlattice, the enhancement increasing with increasing potential modulation.

#### 5. ACKNOWLEDGEMENTS

We thank W. Szott and W.P. Kirk for helpful discussions and for their preprint. This work is part of the research program of the "Stichting Fundamenteel Onderzoek der Materie (FOM)", which is financially supported by the "Nederlandse Organisatie voor Wetenschappelijk Onderzoek (NWO)".

#### 6. REFERENCES

- \*Present address: Laboratory of Applied Physics, Groningen University, Nijenborgh 18, 9747 AG Groningen
- Al'tshuler B L and Aronov A G 1981 JETP Lett. 33 499. These authors erroneously use a prefactor in their Eq. (10) which differs from the (correct) prefactor in Eq. (1). See also Santhanam et al. (1984)
- Al'tshuler B L, Kmechnitzkii D, Larkin A I and Lee P A 1980 Phys. Rev. B22 5142
- Fukuyama H 1982 Surf. Sci. 113 489
- Gao J R, de Graaf C, Caro J, Radelaar S, Offenberg M, Lauer V, Singleton J, Janssen T J B M and Perenboom J A A J 1990 Phys. Rev. B41 12315
- Gao J R 1991 Thesis (Delft University of Technology)
- Paquin N, Pepper M, Gundlach A and Ruthven A 1988 Phys. Rev. B38 1593
- Santhanam P, Wind S and Prober D E 1984 Phys. Rev. Lett. 53 1179
- Szott W, Jedrzejek C and Kirk W P 1992 to be published in *Nanostructures and Mesoscopic Systems* (eds. W.P. Kirk and M. Reed, Academic Press)
- Wheeler R G, Choi K K, Goel A, Wisniewski R and Prober D E 1982 Phys. Rev. Lett. 49 1674

## Magnetoresistance in GaAs-AlGaAs heterostructures under two-dimensional lateral potential modulation

F. Nihey and K. Nakamura

Fundamental Research Laboratories, NEC Corporation,  
34 Miyukigaoka, Tsukuba, Ibaraki 305, Japan

**ABSTRACT:** We have investigated magnetoresistance in two-dimensional electron gases modulated by two-dimensional periodic potential with various strength. When the modulating potential is weak, magnetoresistance oscillations are observed. Though they are similar to the magnetoresistance oscillations under one-dimensional modulation, the phase factor is almost reversed. When the modulating potential is strong exceeding the Fermi energy, magnetoresistance has a single peak implying the formation of orbits encircling a depleted region. As adjacent depleted regions come in touch with each other, the magnetoresistance peak shifts to a high magnetic field suggesting the deformation of the orbits.

### 1. INTRODUCTION

Two-dimensional electron gases (2DEGs) in modulation-doped GaAs-AlGaAs heterostructures have long mean free paths due to reduction of impurity scattering. Ballistic motion of the electron can be controlled by artificially imposed potential on the 2DEG. When one-dimensional (1D) periodic potential is applied, it has been reported that magnetoresistance oscillations periodic in  $1/B$  appear in addition to Shubnikov-de Haas (SdH) oscillations, reflecting the commensurability of cyclotron diameters and the modulation period (Weiss *et al.* 1989, Zhang *et al.* 1990). Similar oscillations have also been observed in the 2DEG under two-dimensional (2D) periodic potential (Alves *et al.* 1989, Fang *et al.* 1990, Gerhardts *et al.* 1991, Liu *et al.* 1991, Lorke *et al.* 1991). Although the periods of the oscillations are the same as that under 1D modulation, the phase values of the oscillations are different between those researchers listed above. On the other hand, when the modulating potential is strong enough to exceed the Fermi energy  $E_F$ , magnetoresistance peaks aperiodic in  $1/B$  have been observed, which imply formation of orbits encircling some depleted regions (Weiss *et al.* 1991).

In this paper, we report magnetoresistance under lateral arrays of potential hills, height of which can be controlled by gate voltage. We discuss magnetoresistance oscillations appearing for weakly modulated samples, especially phase factor of the oscillations. We perform classical calculation of the magnetoresistance for our samples and compare the results between 1D and 2D modulations. We also present magnetoresistance peaks observed for strongly modulated samples including depleted regions so called anti-dots, and the peak position dependence on the anti-dot diameters.

The samples are fabricated from a modulation-doped GaAs-Al<sub>0.3</sub>Ga<sub>0.7</sub>As heterostructure. Electron density  $n_e$  and mobility  $\mu_H$  at 4.2 K under illumination are  $2.4 \times 10^{15} \text{ m}^{-2}$  and  $97 \text{ m}^2/\text{V}\cdot\text{s}$ , respectively. Corresponding  $E_F$  and the mean free path are 8.6 meV and 7.8  $\mu\text{m}$ . We fabricated two types of samples. One is a weakly modulated sample with etched holes in the AlGaAs layer, and the other is a strongly modulated sample with a gate electrode on the previous holes. Figure 1 shows the schematic view of the sample with the gate electrode.

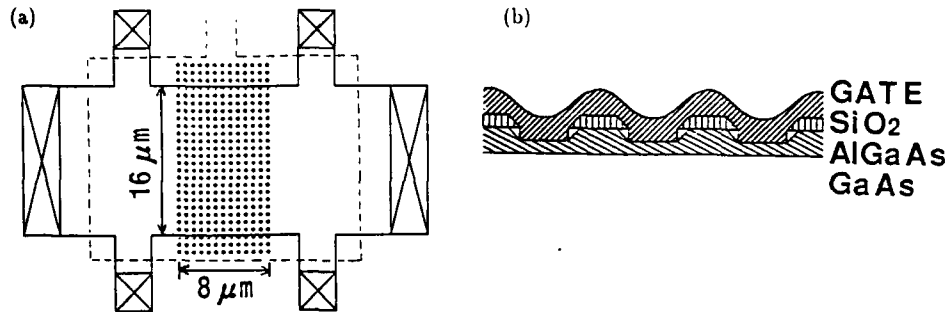


Fig. 1. (a) The top view of the schematic sample structure. The broken lines denote the boundaries of the gate electrode. (b) The cross-sectional view of the sample with the gate electrode for the strong modulation.

Between the voltage probes of the Hall bar, arrays of holes are chemically etched into the AlGaAs layer through a mask of SiO<sub>2</sub> layer which is deposited on the AlGaAs layer and patterned by electron beam lithography. The periods  $a$  of the arrays are 0.4 and 0.5 μm. The diameter of the holes (0.31 μm) is determined by a scanning electron microscopy. For the strongly modulated sample with the gate electrode, electrons under the holes are depleted due to increase of surface potential and anti-dots are formed. Voltage drops between two voltage probes are measured at 2K with a current of 100 nA.

## 2. WEAKLY MODULATED CONDITION

Figure 2 (a) shows the magnetoresistance for the weakly modulated samples with  $a = 0.4$  and  $0.5 \mu\text{m}$ , together with an unmodulated sample. At low magnetic fields, magnetoresistance oscillations are observed accompanied by SdH oscillations at higher magnetic fields. The low field oscillations are insensitive to temperature compared with the SdH oscillations. As observed in 1D modulation (Weiss *et al.* 1989), the oscillations are related to cyclotron diameters commensurate with the modulation periods. For the 1D modulation, peaks in the magnetoresistance occur at the magnetic field given by

$$2r_c = a(\lambda + \phi), \quad \lambda = 1, 2, 3 \dots, \quad (1)$$

where  $r_c = \hbar k_F/eB$  is the cyclotron radius at  $E_F$ , and  $\phi$  is the phase factor. For the 1D modulation,  $\phi = -1/4$ . For 2D modulation, there is no agreement for the experimental value of this phase factor. Liu *et al.* (1991) have claimed that they have observed the same oscillations as in 1D modulation, including the phase factor. Gerhards *et al.* (1991) have reported that amplitude of oscillations for 2D modulation is small and  $\phi = 1/4$ . They explain these feature quantum mechanically by the formation of Hofstadter-type energy spectrum. Lorke *et al.* (1991) have pointed out that the phase factor depends on potential structures. As for our data, the phase factor is closer to that by Gerhards *et al.* (1991). However, we cannot deny a possibility that our data can be classically explained.

We make classical calculation for the magnetoresistance in our samples. Billiard model is used to derive an electron diffusion tensor under a certain magnetic field (Lorke *et al.* 1991). The diffusion tensor is translated into resistivity by Einstein relation (Beenakker 1989). Scattering events are included as memory losses of velocity directions with a probability  $1/\tau$  per unit time, where  $\tau = m\mu_H/e$ , and is assumed to be independent of the density of states under magnetic fields. In order to derive the diffusion tensor, a mean square distance from initial points ( $t = 0$ ) to final points ( $t \sim 3\tau$ ) is calculated for typically 2000 electrons. Figure 2 (b) shows the

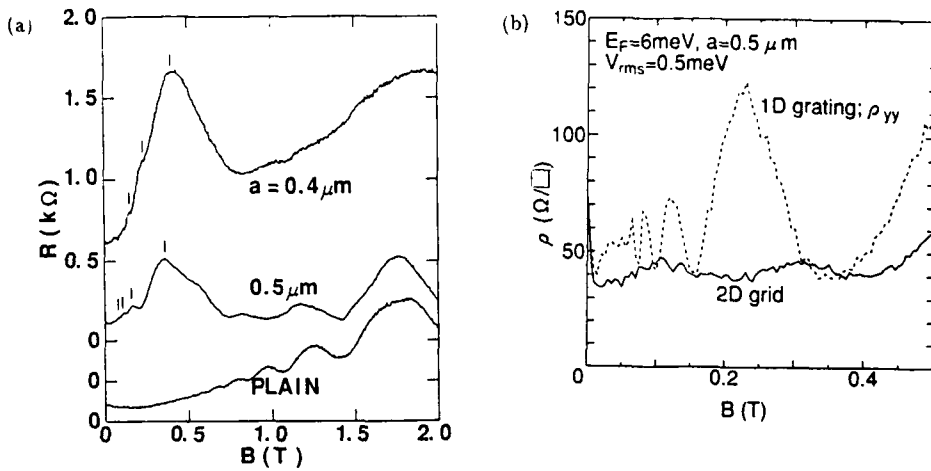


Fig. 2. Magnetoresistance for the weak modulated samples ( $a = 0.4 \mu\text{m}$ ,  $0.5 \mu\text{m}$ ) and the unpatterned sample (PLAIN). (b) Calculated resistivity vs magnetic field for 1D and 2D modulation

calculated magnetoresistance for 1D and 2D potential modulation. For 1D modulation, we can obtain large oscillations which are consistent with eq. (1), including the phase factor  $\phi$ . This seems to indicate validity of our calculation. However, for 2D modulation, we failed to obtain the oscillations observed in our experiment. As Lorke *et al.* (1991) have reported, we have also found that the oscillations sensitively depend on the potential shapes used in the calculation. Therefore, to reproduce the oscillations, it is needed to adjust the potential shape to a realistic one. Nevertheless, figure 2 (b) shows an interesting point. Intensity of the magnetoresistance is small compared to 1D case. Although the same reduction has been explained quantum mechanically by Gerhardts *et al.* (1991), our result indicates that it can be also explained by the classical calculation.

### 3. STRONGLY MODULATED CONDITION

Figure 3 (a) shows the magnetoresistance for the strongly modulated sample with  $a = 0.5 \mu\text{m}$  at different gate voltages  $V_g$ . In each magnetoresistance, a single peak appears around  $B = 0.4 \text{ T}$ , satisfying  $2r_c \sim a$ . These peaks originate from the formation of localized orbits which are impaled on an anti-dot (Weiss *et al.* 1991). Harmonics peaks are not observed because the anti-dot diameter is so large that the orbits encircling several anti-dots are blocked by the other anti-dots. Figure 3 (b) presents the gate voltage dependence of  $n_s$ , derived from SdH oscillations, the peak position  $B_p$ , and zero field resistance  $R(B = 0)$ . For  $V_g \geq 0.65 \text{ V}$ ,  $R(B = 0)$  increases as  $V_g$  decreases, while  $n_s$  is constant. This suggests that the gate voltage can change the anti-dot diameter, keeping the carrier density constant. It is reasonable that  $B_p$  is constant because the condition for the impaled orbits is only determined by the period and is independent of the anti-dot diameter.

For  $V_g \leq 0.65 \text{ V}$ , SdH oscillations vanish and  $R(B = 0)$  rapidly increases as  $V_g$  decreases. In this region, anti-dots begin to overlap each other and conducting channel between the anti-dots are squeezed. In the channels, electrons are likely to travel straightforward. Therefore, to complete the orbit encompassing an anti-dot, higher magnetic field is needed for electrons turning at the regions surrounded by four anti-dots.

When  $V_g$  is lowered further, magnetoresistance begins to fluctuate. The fluctuations depend on magnetic field and also on time. For the data with  $V_g = 0.55 \text{ V}$  in figure 3 (a), the fluctuation amplitude is  $\Delta G \sim 0.2(2e^2/h)$ . In this regime, anti-dots sufficiently overlap each

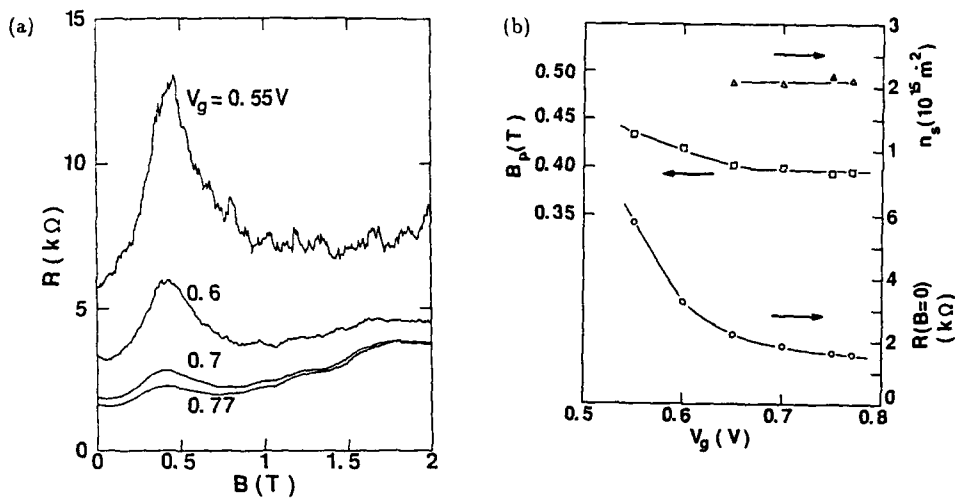


Fig. 3. (a) Magnetoresistance for the strongly modulated sample ( $a = 0.5 \mu m$ ) at different gate voltages  $V_g$ . (b) Carrier density  $n_s$  obtained by SdH oscillations, peak position  $B_p$ , and zero field resistance  $R(B = 0)$  versus  $V_g$ .

other, and electrons have to take hopping conduction through the extremely narrow channels. The fluctuations seems to be originated from sensitive dependence of the hopping conduction on magnetic fields and on the gate voltages.

#### 4. CONCLUSIONS

Magnetoresistance of two-dimensional electron gas under lateral arrays of potential hills is investigated. For weakly modulated samples, magnetoresistance oscillations are observed. The phase of the oscillations is almost reversed as compared with that in 1D modulation system. Our classical calculation shows that the oscillations are sensitive to the potential shape and that the intensity of the oscillations are greatly reduced in 2D modulation. For strongly modulated samples, magnetoresistance has a single peak corresponding to an impaled orbit on an anti-dot. As increase of the anti-dot diameter, deformation of the orbits can be made, and a precursor effect of quasi-zero dimensional confinement can be observed.

#### References

Alves E S, Beton P H, Henini M, Eaves L, Main P C, Hughes O H, Toombs G A, Beaumont S P and Wilkinson C D W 1989 *J. Phys.: Condens. Matter* **1** 8257  
 Beenakker C W J 1989 *Phys. Rev. Lett.* **62** 2020  
 Fang H and Stiles P J 1990 *Phys. Rev. B* **41** 10171  
 Gerhardts R R, Weiss D and Wulf U 1991 *Phys. Rev. B* **43** 5192  
 Liu C T, Tsui D C, Shayegan M, Ismail K, Antoniadis D A and Smith H I 1991 *Appl. Phys. Lett.* **58** 2945  
 Lorké A, Kotthaus J P and Ploog K 1991 *Phys. Rev. B* **44** 3447  
 Weiss D, von Klitzing K, Ploog K and Weimann G 1989 *Europhys. Lett.* **8** 179  
 Weiss D, Roukes M L, Menschig A, Grambow P, von Klitzing K and Weimann G 1991 *Phys. Rev. Lett.* **66** 2790  
 Zhang C and Gerhardts R R 1990 *Phys. Rev. B* **41** 12850

## Magnetic breakdown in a two-dimensional electron gas subjected to a periodic potential

P H Beton, M W Dellow, P C Main, L Eaves, E S Alves  
Department of Physics, University of Nottingham, Nottingham, NG7 2RD

**ABSTRACT:** We have measured the magnetoresistance of a two dimensional electron gas subjected to a periodic potential. At very low fields we observe a positive magnetoresistance which extends out to a critical field  $B_{\text{crit}}$ . At this field a classical form of magnetic breakdown effect occurs. Experimentally we find  $B_{\text{crit}} \propto V/a$  where  $V$  and  $a$  are respectively the amplitude and period of the potential. We can account for this behaviour within a semiclassical model of electron dynamics. A quantum mechanical treatment of this problem is presented which is equivalent to the semiclassical model for  $a > > 50$  nm. For  $a < 50$  nm electrons may tunnel through the maxima of the periodic potential and the semiclassical model breaks down.

In this paper we will review the main points of our recent work on the magnetic breakdown which occurs in a two dimensional electron gas (2DEG) subjected to a one dimensional periodic potential (Beton et al 1990, Beton et al 1991). This system has been extensively studied over the last three years following the observation by Weiss et al (1989) of a series of oscillations in the magnetoresistance which are periodic in  $1/B$  ( $B$  is the magnetic field). Also observed (Weiss et al, Winkler et al 1989, Beton et al 1990) at very low field is a positive magnetoresistance which extends out to a critical field  $B_{\text{crit}}$ . Figure 1 shows some typical data for a device in which the periodic potential is generated using a patterned gate. The critical field is indicated by an arrow. In the field interval  $B_{\text{crit}} < B < 0.7$  T the magnetoresistance is oscillatory in  $1/B$ . At low gate voltage for  $B > 0.7$  T Shubnikov-de Haas oscillations are observed. The patterned gate is formed by evaporating a Ti/Au layer over a set of regularly spaced lines of resist which are formed using electron beam lithography. A schematic diagram of the structure is shown in Figure 2. The current is passed perpendicular to the equipotentials formed by the patterned gate and the magnetic field is perpendicular to the plane of the 2DEG.

The origin of the low field oscillations is a commensurability which occurs when the cyclotron diameter  $2R_c = (n + 1/4)a$ , where  $R_c = 2mv_F/eB$ , where  $v_F$  is the Fermi velocity,  $a$  is the period of the potential and  $n$  is an integer. A detailed theory of the effects of this commensurability on the resistance has been given by Gerhardts et al (1989) and Winkler et al (1989) using the Kubo formalism (see also Vasilopoulos and Peeters (1989)), and by Beenakker (1989) who uses a semiclassical model. However, none of these theories predict the observed positive magnetoresistance which occurs for  $B < B_{\text{crit}}$ . The oscillations which occur when the current flows perpendicular to the equipotentials may be explained within a semiclassical model, but this model cannot account for the much weaker oscillations observed by Weiss et al (1989) when the current flows parallel to the equipotentials. We will follow Beenakker's semiclassical treatment and restrict our discussion to the case where the current is perpendicular to the equipotentials. A key point is

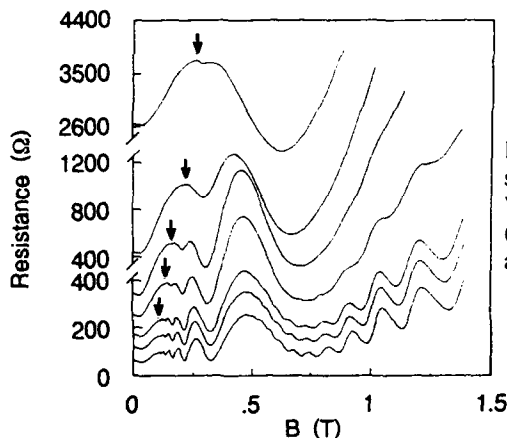


Figure 1 Magnetoresistance at 2K for a structure with  $a = 300$  nm. Gate voltage  $V_g = -1.0V$  (top),  $-0.8V$ ,  $-0.6V$ ,  $-0.5V$ ,  $-0.3V$  (displaced by  $100\Omega$ ),  $-0.2V$  (displaced by  $50\Omega$ ) and  $0V$  (bottom).

that the electric field, which arises from the periodic potential, and the magnetic field, which are oriented along the  $x$  and  $z$  directions respectively, give rise to an electron drift in the  $y$  direction, with a drift velocity  $v$ . For  $\mu B > > 1$  ( $\mu$  is the electron mobility) this drift gives rise to an increase in  $\rho_{xx}$  given by

$$\frac{\delta \rho_{xx}}{\rho_0} \sim \frac{\mu^2 B^2}{2} \frac{\langle v^2 \rangle}{v_F^2} \quad (1)$$

where  $\rho_0$  is the resistivity at zero field and the brackets  $\langle \dots \rangle$  denote an ensemble average. Beenakker (1989) showed that in the limit of a weak potential for a given magnetic field the electron trajectories may be considered as a superposition of a circular cyclotron orbit and a drift along the  $y$  axis. Within this approximation the ensemble average may be replaced by an average over orbit centre position and

$$\langle v^2 \rangle = \frac{v_F^2 (eV)^2}{2 (E_F)} \frac{R_c}{a} \cos^2(2\pi R_c a - \pi/4) \quad (2)$$

giving rise to a series of oscillations in  $\delta \rho_{xx}$  periodic in  $1/B$  where  $V$  is the amplitude of the potential and  $E_F$  is the Fermi energy.

However, even for a weak potential there is a sufficiently low field for which this approximation breaks down. This is because at very low field the Lorenz force  $ev_F B$  on the electron is less than the maximum force  $2\pi eV/a$  generated by the periodic potential, resulting in a gross distortion of the orbit. In fact when

$$2\pi eV/a > ev_F B \quad (3)$$

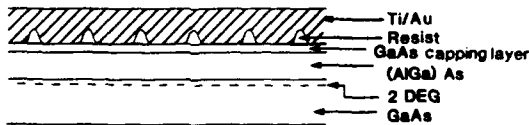


Figure 2 Schematic diagram of the sample fabrication process.

there exist 'streaming orbits' which remain in one minimum of the potential and stream in the  $y$  direction with a velocity  $v = v_F$ . Electrons in streaming orbits move much faster in the  $y$  direction than those in drifting orbits and so make a dominant contribution to  $\langle v^2 \rangle$ . Therefore, at low field  $\langle v^2 \rangle = f v_F^2$  where  $f$  is the fraction of electrons in streaming orbits, giving

$$\delta \rho_{xx}/\rho_0 \approx f \mu^2 B^2 \quad (4)$$

where  $f$  is a slowly varying function of magnetic field. At low fields we therefore expect a positive magnetoresistance to be generated by the streaming orbits. We have shown in a previous paper (Beton et al 1990) that  $f$  is zero above a value of magnetic field which satisfies the equality in equation (3). We associate this magnetic field with the critical magnetic field identified in the experimental data. Thus we predict  $B_{\text{crit}} = 2\pi V/a v_F$ . We have established that  $B_{\text{crit}}$  has the predicted dependence on  $V$  and  $a$  by varying the gate voltage for a sample with  $a = 300$  nm, and by comparing samples with periods  $a = 150, 300$  and  $500$  nm which are all fabricated from the same modulated heterostructure (Beton et al 1991).

The theories which were developed (Gerhardts et al 1989, Winkler et al 1989) to explain the low field oscillations using the Kubo formalism are unable to account for the low field magnetoresistance which occurs for  $B < B_{\text{crit}}$ . A theory developed by Streda and MacDonald (1990), which is an extension of the conventional theory of the magnetic breakdown observed in metals (see Pippard, 1989), predicts a positive magnetoresistance at low fields. However, a prediction of this model is that  $B_{\text{crit}} \propto V^2$ , which does not agree with the experimental data. Thus the semiclassical model we have described is the only theory which accounts for both the low field positive magnetoresistance and the oscillations originally observed by Weiss. To understand the essential differences between our work and the theories referred to above, we have developed (Beton et al, 1991) a quantum mechanical formulation of this problem which has the correct correspondence with our semiclassical model.

In the Landau gauge the Schrodinger equation for an electron moving a periodic potential and a magnetic field reduces to

$$\left[ \frac{-\hbar^2}{2m} \frac{\partial^2}{\partial x^2} + V_{\text{eff}}(x) \right] \psi(x) = E\psi(x) \quad (5)$$

where

$$V_{\text{eff}}(x) = m\omega_c^2 (x - x_0)^2/2 + eV[\cos(2\pi x/a) + 1], \quad (6)$$

where  $x_0 = -\hbar k_c/eB$  is the orbit centre and  $\omega_c = eB/m$  is the cyclotron frequency.

Thus the problem reduces to solving the one dimensional Schrodinger equation for a particle in a potential well given by  $V_{\text{eff}}(x)$ . This is the combination of a parabolic potential, the curvature of which is determined by the magnetic field, and the periodic potential. Figure 3 shows plots of  $V_{\text{eff}}(x)$  for various magnetic fields and typical values of  $V$  and  $a$ . We consider the nature of possible solutions for an energy  $E = 10$  meV (see dotted line in Figure 3) which is comparable with the typical Fermi energy. At high fields (Figure 3c) the potential (for  $E = 10$  meV) closely resembles a parabola so the eigenstates may be treated as perturbed simple harmonic states. This corresponds to the treatment of Gerhardts et al (1989) and Winkler et al (1989). However, at low field (Figure 3a) there is the additional possibility of local minima in the potential. At low field it is therefore not valid to treat the true eigenfunctions as perturbed eigenstates of a parabolic potential. In addition at low field there are local quasi-bound states associated with the local minima (see Figure 3a). We have shown (Beton et al 1991) that these quasi-bound states are equivalent to the semiclassical

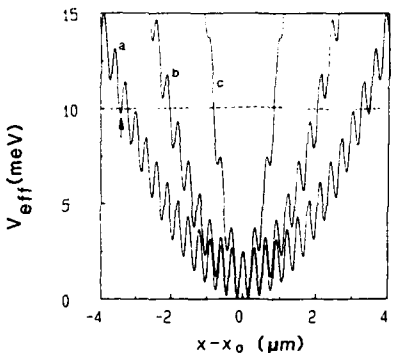


Figure 3 The effective potential for an electron moving in a periodic potential of amplitude 1.25 meV and period 300 nm, and a magnetic field 0.025T(a), 0.04T(b) and 0.1T(c).

streaming states discussed above in the limit where tunnelling through the barriers defining the local minima may be neglected. Note that within this formulation  $B_{\text{crit}}$  is the field above which there are no local minima, which for a given energy occurs when  $dV_{\text{eff}}(x)/dx > 0$  ( $x > 0$ ) for all orbit centres. This condition leads to the expression  $B_{\text{crit}} = 2\pi V/a\nu_F$ , which is identical to the semiclassical expression for  $B_{\text{crit}}$ .

Within the semiclassical theory there is a well defined condition for the existence of streaming orbits. However in the quantum mechanical formulation electrons may tunnel through the barriers forming the local minimum in potential. This tunnelling would be expected to blur the distinction between streaming and drifting orbits, leading to a consequent smearing of the value of  $B_{\text{crit}}$  over a field range  $\delta B$ . In a previous paper we have characterised this smearing in terms of the tunnelling probability of electrons with a characteristic energy calculated within the WKB approximation. For a field  $B = B_{\text{crit}} - \Delta B$ , the tunnelling probability  $T \sim \exp\{-4(\Delta B/B_{\text{crit}})^{5/4}(eV/E_G)^{1/2}\}$  ( $E_G = \hbar^2/2ma^2$  is the kinetic energy of an electron with a wavelength equal to  $a$ , the period of the potential) and the semiclassical model should be valid (ie  $\delta B \ll B_{\text{crit}}$ ) for  $16eV > > E_G$ . For typical values of  $V$  ( $\approx 1$  meV) this inequality is satisfied for  $a > 50$  nm. In the opposite limit ( $a < 50$  nm) the nearly free electron model holds and the theory of Streda and MacDonald (1990) is valid.

We have shown that a semiclassical model of electron dynamics can account for both the positive magnetoresistance and the low field magneto-oscillations which occur in a 2DEG subjected to a periodic potential. A criterion for validity of this model may be deduced from a quantum mechanical formulation of the problem.

The devices described in this work were fabricated at the Department of Electrical and Electronic Engineering at the University of Glasgow in collaboration with S P Beaumont and C D W Wilkinson. P H Beton thanks C R Leavens and G Aers (NRC Ottawa, Canada) for interesting discussions and the Royal Society for financial support. This work was founded by the UK SERC.

Beenakker C W J 1989 *Phys Rev Lett* **62** 2020

Beton P H, Dellow M W, Main P C, Alves E S, Eaves L, Beaumont S P and Wilkinson C D W 1991 *Phys Rev B* **43** 9980.

Beton P H, Alves E S, Main P C, Eaves L, Dellow M W, Henini M, Hughes O H, Beaumont S P and Wilkinson C D W 1990 *Phys Rev B* **42** 9229.

Gerhardts R R, Weiss D and V. Klitzing K 1989 *Phys Rev Lett* **62** 1173.

Pippard A B 1989, *Magnetoresistance in Metals*, published by Cambridge University Press.

Streda P and MacDonald A H 1990 *Phys Rev B* **41** 11 892.

Vasilopoulos P and Peeters F M 1989 *Phys Rev Lett* **63** 2120.

Weiss D, V. Klitzing K, Ploog K and Weimann G 1989 *Europhys Lett* **8** 179.

Winkler R W, Kotthaus J P and Ploog K 1989 *Phys Rev Lett* **62** 1177.

## Ballistic conductance steps and electron focusing in long samples

S Washburn<sup>a</sup>, K Ismail<sup>b</sup> and KY Lee<sup>c</sup>

*IBM Watson Research Center, Yorktown, NY 10598, USA, and*

*<sup>a</sup>Dept Physics and Astronomy, Univ North Carolina, Chapel Hill, NC 27599-3255, USA*

*<sup>b</sup>Dept of Telecommunication and Elec Eng, University of Cairo, Cairo, Egypt*

*<sup>c</sup>IBM East Fishkill, Hopewell Junction, NY 12533, USA*

**ABSTRACT:** Carefully controlled wet etching of high mobility GaAs-AlGaAs heterostructures has allowed us to make 2 micron long, globally gated quantum wires that exhibit quantized conductance steps. The steps have been observed previously only in very short "point contacts" whose width and length were comparable. The new wires have length to width ratios much greater than 10 near pinch off. The unusual result is attributed to very clean sidewalls that result from the gentle etching process. Loops exhibit quantized steps but with step heights that result from non-trivial addition rules of several contacts. The loops also exhibit a unique classical electron focussing when the cyclotron orbit matches the loop size and Aharonov-Bohm oscillations over a wide range of resistances.

In very pure GaAs/Al<sub>x</sub>Ga<sub>1-x</sub>As heterostructure crystals, a stunning variety of new and potentially useful effects have been observed (Timp 1990, Beenakker and van Houten 1991). Point contacts conduct according the number of independent transmitted modes (Imry 1986, Wharam, *et al* 1988, van Wees, *et al* 1988), and point contacts can also be used as mode selecting voltage probes (Timp, *et al* 1988, van Wees, *et al* 1988). Electron focussing appears when a magnetic field is used to bend the orbits of the electrons (van Houten, *et al* 1988). The response to a magnetic field or to an applied voltage or current bias can be tailored by judiciously chosen shapes of transistors (Ford, *et al* 1989), because the electrons in the transistors are guided by walls of the device and by the applied voltage (Baranger, *et al* 1991), rather than by random scattering from defects as in familiar electronics. Naively one would suppose that the simple mode counting formula for G would appear in almost any wire made from this material, but in fact the mode counting was observed in samples where the mean free path estimated from the Drude formula for the G was about a factor of 30 longer than the wire length (10  $\mu\text{m}$  compared with 0.3  $\mu\text{m}$ ) (Timp 1990).

To make such short wires, two large area conductors were connected by a pin-hole or point contact formed by bringing two sharp-pointed Schottky gates to within a few tenths of a micron of each other. A negative bias  $V_g$  applied to the gates first depletes the areas beneath the gate forming a pin-hole of width about equal to the gate separation. Further negative bias narrows and depletes the point contact because of the spreading capacitance. Gradually increasing the negative bias steadily reduces the width of the "wire" so that, one at a time, the modes are cut off producing a staircase-like structure in  $G(V_g)$ . Soon afterwards, it was observed that the steps in the conductance vanished if the wire was too long -- too long being  $L > 0.5\mu\text{m}$  (Timp 1990) -- more than a factor of 10 smaller than the mean free path length of the starting material from which the devices were made. It was suggested that the random potential of the donor atoms (that are responsible for the free electrons in the heterostructure) was the source of the small angle scattering that destroys the steps, and sophisticated device model calculations corroborated this assertion (Davies, *et al* 1991).

Very recently conductance steps have been observed in much longer wires of length 2 to 4  $\mu\text{m}$  (Ismail, *et al* 1991a). Representative device structures and data appear in figure 1. The data in the figure contain two sweeps of the conductance in a freshly cooled transistor.

The donor population was still relaxing from the room temperature distribution, so the two sweeps are not coincident. In both sweeps there are some plateaux, and the plateaux align between the two sweeps. The alignment indicates that the steps are associated with mode counting, and not with some random scattering.

In the new experiments a very gentle etching technique was used to fabricate small wires without any harsh processing environments for the high quality starting material. The wet etch is perfectly adequate to the demands of even these very small scale devices (Ismail, *et al* 1991b). We made samples using only a heavily diluted crystallographic wet etch to define the wires. Then while still passivated by the etch solution, the devices were moved to an evaporation chamber and the gate which covers the entire device region was deposited. We suppose that this provides two improvements on earlier technologies: (1) The etch process is very gentle and causes no strain or damage to the crystal except for that intrinsic to the vacuum interface, and (2) The global metal gate covering all portions of the device provides much better screening of the random electrostatic potential from the coulomb (DX) centers in the AlGaAs layer.

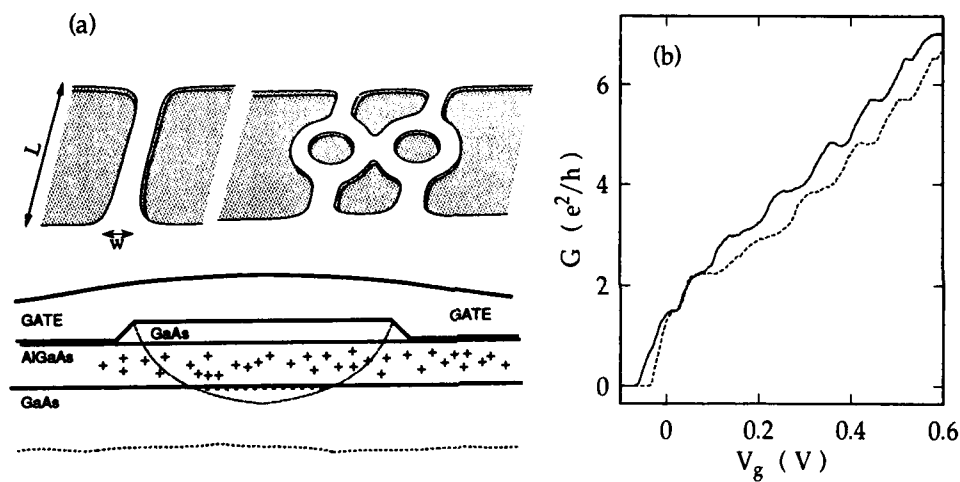


Figure 1. (a) Schematic profile for the devices. The perspective views illustrate the wire and loop etch profiles before the gates are deposited. (b) The conductance as a function of gate voltage contains steps of the same kind found in the quantum point contacts. The two sweeps [up (solid) and down (dashed)] were separated in time -- ie by the relaxation of some donor states (Ismail, *et al* 1991a).

Further evidence for ballistic transport appears in the magnetoresistance of loop samples, which contain evidence for magnetic focussing of the electrons as they circle the loop. In figure 2 we display some representative focussing data. The electron beam is split and recombined to form an interferometer. Electrons travel in either arm of the loop and interfere as they exit the device. In the magnetoresistance at 4.2K (too warm to observe any quantum interference), there are regularly spaced peaks in the resistance, and the spacing of the peaks for each carrier concentration (gate voltage) studied is just that needed to map the classical cyclotron orbits onto the loop diameter.

The peaks in the magnetoresistance arise when the cyclotron orbit size matches the loop diameter and so cause the electron paths to miss the inlet ports. In the loop sample, one might first suppose that there would be only one matching condition that would cause a peak in the magnetoresistance, namely when  $d = 2r = 2\hbar k_F/eB$ . From this viewpoint the experimental data, which contain a series of peaks, cannot be explained. This assumption is based on the focussing condition familiar from point contact experiments where the focussing involves reflections from a surface in a bulk conductor (van Houten 1988). Here, however, the carrier motion is confined to the loop, and part of the carriers' energy involves radial

"motion", ie perpendicular to the conduction path with wave vector  $k_{\perp}$ . Only the tangential motion along the conduction path figures in the focussing condition, so that here the criterion becomes instead

$$d = 2[\sqrt{2mE_F} - \hbar k_{\perp}] / e\Delta B,$$

where  $\Delta B$  is the spacing between the peaks. Since (approximating wire cross-section with an infinite-wall square-well) we expect  $k_{\perp} = j\pi/w$ , where  $j$  is a positive integer and  $w$  is the width of the channel: The focussing condition provides for equally spaced peaks. Each peak corresponds to a different transverse mode in the conducting path. This is confirmed if we plot the peak separation and the carrier density  $n_s = k_F^2/2\pi$  together as a cyclotron orbit size. These data are plotted in raw form and then as the cyclotron orbit diameter  $d$  in figure 2. In spite of the range of carrier densities,  $d$  is always about the outside diameter of the loop, ie  $d = 1.85$  microns.

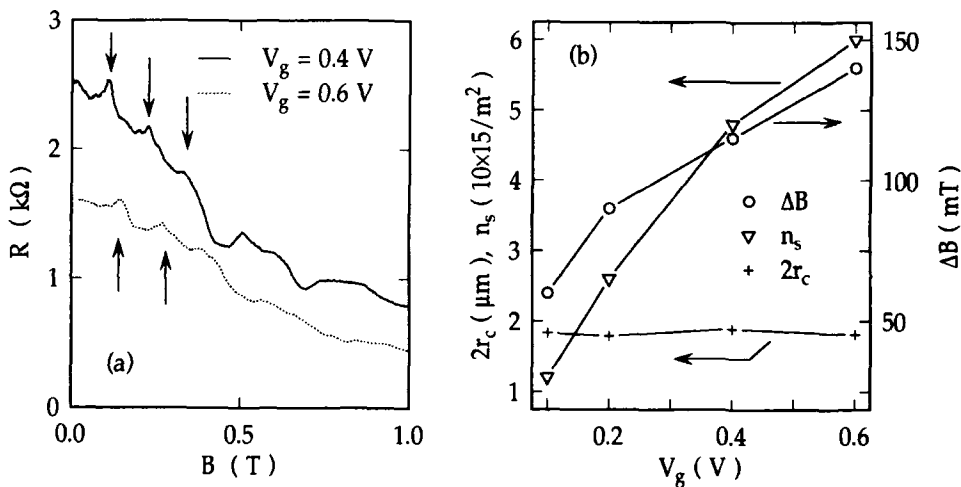


Figure 2 (a) The magnetoresistance at  $V_g = 0.4$  V (top curve) and  $V_g = 0.6$  V (bottom curve) contains peaks (marked by arrows). The separation of the peaks corresponds to the classical cyclotron orbits for each transverse mode  $k_{\perp}$  fitted to the loop. Similar data from other gate voltages always contain a few peaks at regular spacings, and (b) the peak spacing is such that the cyclotron orbit diameter matches that of the loop.

It is clear from the mere existence of magnetoresistance peaks that the transverse modes are not mixed in the loop. In principle, the conductance steps may arise from the inlet ports, but it is easier to explain the step heights if the steps arise from the loop arms (Büttiker, private communication)). The focussing data make this assignment perfectly plausible, since the peaks in the magnetoresistance prove that the modes are distinct in the loop. While electron focussing occurs in point contact devices van Houten, 1988), apparently nothing of this sort has been observed in transport through a ring, although many such geometries with about the same dimensions have been studied (Ford, *et al* 1988, Ishibashi, *et al* 1986, Timp 1990). Therefore these measurements provide another kind of evidence that the new etching process is much more benign than others.

At very low temperatures, quantum mechanical interference is apparent as an Aharonov-Bohm oscillation. For large wire widths (when several modes are transmitted) or for  $V_g$  in a "riser" in the  $G(V_g)$  staircase, the interference pattern is random, which does indicate some mode mixing scattering is still occurring. Typical data are in figure 3. In addition to the regular oscillation period there is an envelope function that governs the

oscillation amplitude, and this is a random function of the field. The random interference pattern is replaced by a much more regular pattern when only one channel is transmitted or when  $V_g$  is at the center of the "tread" in the  $G(V_g)$  staircase. It seems quite reasonable that this envelope function for the magnetoresistance in the tread, which comprises a regular series of nodes and antinodes at about the right spacings, results from the same classical focussing mentioned above. The question of what is causing the random interference pattern in the risers is unresolved. It is obvious that there is much more random scattering in the risers, because one mode is partly reflected and the scattering that reflects it is from random irregularities either in the device shape or in the electrostatic potential.

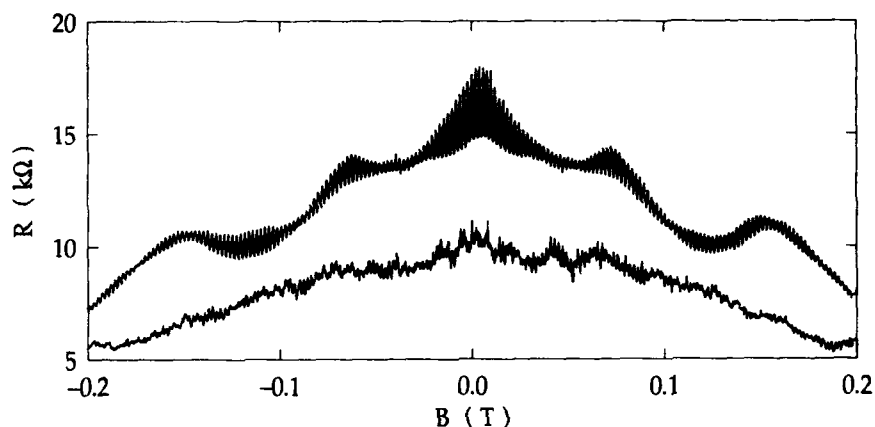


Figure 3. Very low temperature ( $T = 0.02\text{K}$ ) magnetoresistance data containing Aharonov-Bohm oscillations. The oscillations might be have random (lower curve for  $V_g = 0.22$ ) or regular (upper curve for  $V_g = 0.15$ ) envelope functions depending on the conditions in the sample (Ismail, *et al* 1991a).

Baranger HU, Divincenzo D, Jalabert R and Stone AD 1991 *Phys Rev B* **44** 10637, and references cited there  
 Beenakker CWJ and van Houten H 1991 in *Solid State Physics, Volume 44*, ed H Ehrenreich and D Turnbull (Academic: Boston)  
 Davies J, Nixon JA and Baranger HU 1991 *Phys Rev B* **43** 12638  
 Ford CJB, Thornton TJ, Newbury R, Pepper M, Ahmed H, Foxon CT, Harris JJ and Roberts C 1988 *J Phys C* **21** L325  
 Ford CJB, Washburn S, Büttiker M, Knoedler CM, and Hong JM 1989 *Phys Rev Lett* **62** 2724  
 Imry Y in *Directions in Condensed Matter Physics* 1986 ed E Mazenko and G Grinstein (New World: Singapore)  
 Ishibashi K, Takagaki Y, Gamo K, Namba S, Ishida S, Murase K, Aoyagi Y and Kawabe Mitsuo 1987 *Solid State Comm* **64** 573  
 Ismail K, Washburn S and Lee KY 1991a *Appl Phys Lett* **59**, 1998 (1991)  
 Ismail K, Burkhardt M, Smith HI, Karam NH and Sekula-Moise PA, 1991b *Appl Phys Lett* **58** 1539  
 Timp G 1990 in *Semiconductors and Semimetals*, ed MA Reed (Academic: New York); in *Mesoscopic Phenomena in Solids*, ed BL Altshuler, PA Lee and RA Webb (North Holland: Amsterdam)  
 Timp G, Baranger HU, deVegvar P, Cunningham JE, Howard RE, Behringer R and Mankiewich PM 1989 *Phys Rev Lett* **59** 732  
 van Wees BJ, van Houten H, Beenakker CWJ, Williamson JG, Kouwenhoven LP, vander Marel D and Foxon CT 1988 *Phys Rev Lett* **60** 848  
 van Wees B, Willems EMM, Harmans CJPM, Beenakker CWJ, van Houten H, Williamson JG, Foxon CT and Harris JJ 1989 *Phys Rev Lett* **62** 1181  
 van Houten H, van Wees BJ, Mooij JE, Beenakker CWJ, Williamson JG and Foxon CT 1988 *Europhys Lett* **5** 721  
 Wharam DA, Thornton TJ, Newbury R, Pepper M, Ahmed H, Frost JEF, Hasko DG, Peakcock DG, Ritchie DA and Jones GAC 1988 *J Phys C* **21** L209

## Electron scattering in AlGaAs/GaAs hetero-quantum wires

T. IKOMA, T. Odagiri and K. Hirakawa

The Institute of Industrial Science, The University of Tokyo  
22-1, Roppongi 7-Chome, Minato-ku, Tokyo, Japan 106

**ABSTRACT:** We investigated the phase breaking time of electron waves in AlGaAs/GaAs quantum wires by systematically studying the temperature and the electron density effects on the weak localizations. The phase breaking time  $\tau\phi$  increases with decreasing  $T$ , and saturates below  $\sim 3$ K. At relatively high temperatures, the electron-electron scattering with momentum preservation is dominant and Fukuyama and Abraham (1983) theory can well explain the temperature dependence but not the Fermi energy dependence. At lower temperatures, the phase coherent length is constant and has a strong Fermi energy dependence. This behavior can not be predicted by existing theories.

### 1. Introduction

In a mesoscopic electron system, both energy-loss and momentum-loss scatterings are important to determine the quantum transport of electrons. The former determines the phase coherence length and the latter does the boundary between ballistic and diffusive transport. The phase coherence length is an important physical parameter when quantum interference devices are considered. The prolongation of the phase coherence length is an interesting engineering from a view point of device application of mesoscopic phenomena. In so doing, first we have to understand what is a dominant scattering to break a phase memory.

In this context we have investigated the phase breaking time as a function of temperature in AlGaAs/GaAs narrow wires and shown that there exist three temperature regions: (1) the temperature region lower than 3 K, where the phase breaking time is constant, (2) the intermediate temperature region from 3 K to 8 K and (3) the temperature region higher than 8 K, where it decreases with  $T^{-2}$  (Hirakawa et al. 1989, Ikoma and Hiramoto 1990). In the high temperature region, the temperature dependence ( $T^{-2}$ ) is in good agreement with the Fukuyama and Abrahams (FA) calculation (1983), where the electron-electron scattering with momentum preservation is considered as a main mechanism. In the intermediate region, the so-called Nyquist scattering calculated by Altshuler, Aronov and Khmel'nitsky (AAK) (1981) fits well to the measurement. The boundary between FA and AAK is given by  $\hbar/k\tau_m$ , where  $\tau_m$  is the momentum scattering time. This boundary is 8 K in the present sample and agrees well with the experimental observation (Ikoma et al. 1989, Odagiri et al 1990).

In this work we systematically investigated the phase breaking time as a function of temperature and Fermi energy for various samples with different mobilities, electron densities and wire widths in order to find out which mechanism mainly determines the phase coherence in each of these temperature regions.

### 2. Sample preparation and experimental procedure

AlGaAs/GaAs single or double hetero-structure wafers with different mobilities and carrier densities were grown by the molecular beam epitaxy (MBE). The mobility among the wafers varies from approximately  $2000\text{ cm}^2/\text{Vs}$  to  $800000\text{ cm}^2/\text{Vs}$  at 4.2K. The low mobility samples have a double heterostructure with an active 50nm GaAs layer doped at a sheet electron density varying from  $1.7 \times 10^{12}\text{ cm}^{-2}$  to  $1.3 \times 10^{13}\text{ cm}^{-2}$ . The other samples have selectively-doped single hetero-structures.

A narrow channel was formed by the focused  $\text{Be}^{2+}$ -ion implantation at 100kV [Ikoma et al. 1989, Yamada et al. 1990]. The implanted dose was different according to the doping density. Without annealing the implanted regions are converted to high resistive and can confine electron conduction to a narrow channel. The spacing between the two implantations was varied from  $1.0\mu\text{m}$  to  $2.0\mu\text{m}$ , which gives an effective channel width from  $0.14\mu\text{m}$  to  $1.0\mu\text{m}$ . In order to change the Fermi energy, an Al gate was formed. The sample structure is similar to the one previously reported (Hiramoto et al. 1987, Hiramoto et al. 1989).

Magnetoresistance was measured both at low and high fields. The sheet carrier density was determined from the Shubnikov-de Haas oscillation and the phase coherence length from the weak localization effect. To derive the phase coherence length the AAK theory was used for low mobility samples and the Beenakker and van Houten (BvH) (1988) theory for intermediate mobility samples. Both theories deal with the diffusive transport case, but the latter holds for higher mobility samples when the boundary scattering becomes influential in the weak localization (Ikoma and Hiramoto 1990). Therefore we examined carefully a validity of fitting of the theory with the measured results and found all the samples presented here showed a good fitting with either of the two theories.

In these theories, the phase coherence length appears as an adjustable parameter and by best fitting of the calculated curve with the measured one, we determined the phase coherence length, from which the phase breaking time was derived

### 3. Phase Breaking Time

#### 3.1 Temperature dependence

The temperature dependence of the phase breaking time is summarized in Fig.1 for various samples with different mobilities( $\mu$ ) and electron densities( $N_s$ ). The specification of the samples is listed in Table 1. There are two groups: low and intermediate mobility samples.

In the low mobility samples, the phase breaking time saturates at temperatures lower than 3 K and the saturation value is 1 to 2 psec. At temperatures between 3K and 8K, it falls off with  $T^{-2/3}$ .

This fall off is well explained by the Nyquist scattering within a framework of the AAK theory, where the phase breaking time is proportional to  $N_s^{1/3}, \mu^{1/3}, W^{2/3}$  and  $T^{-2/3}$ . In the low mobility samples, the cross over temperature between AAK and FA is as high as 100K and is not observable.

In the intermediate mobility samples, the phase breaking time saturates at lower than 3K as is in the low mobility samples. The saturation value, however, ranges from 5 to 20 psec. In this group the samples have almost the same electron density of  $6.0 - 6.7 \times 10^{11} \text{ cm}^{-2}$  except nGA42 ( $1.7 \times 10^{11} \text{ cm}^{-2}$ ) and the mobility is  $26000 \text{ cm}^2/\text{Vs}$  (nGA12&nGA36),  $36'000 \text{ cm}^2/\text{Vs}$  (nGA23&nGA24) and before the process. At temperatures higher than 3K, the phase breaking time falls off rather rapidly. This decrease is well explained by combination of AAK and FA theories as shown in Fig.2. From 3K to 8K, the Nyquist scattering is dominant and at higher than 8K the electron-electron scattering with momentum preservation (the clean limit) becomes dominant as was already shown previously (Hirakawa et al. 1989, Ikoma et al. 1989).

The saturation of the phase breaking time at low temperatures is interesting because no reasonable explanation has been given so far. Experimentally all the samples tested here with different electron densities, mobilities and wire widths showed the saturation. We also examined if effects of electromagnetic noise during the measurement induce such saturation but found that this is not the case. Therefore this is not an artifact. This saturation is also reported by other authors (Fukai et al. 1990). The spin-orbit scattering is a possible cause as Fukai et al. (1990)

proposed. The spin-orbit scattering should induce positive magnetoresistance at low magnetic field as Kawaguchi et al. (1987) reported in an InAs inversion layer. However we did not observe such positive magnetoresistance related with the saturation. Furthermore, the curve shape of magnetoresistance calculated by using Hikami et al. (1980) formula by taking into account the spin-orbit scattering is very different from the observed curve. Therefore, in the present case, the spin-orbit scattering is not a cause for the saturation.

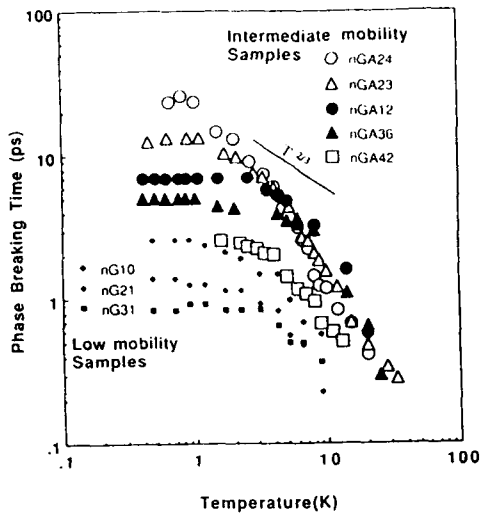


Fig.1 Temperature dependence of the phase breaking time for various samples. The specification of the sample is listed in Table 1.

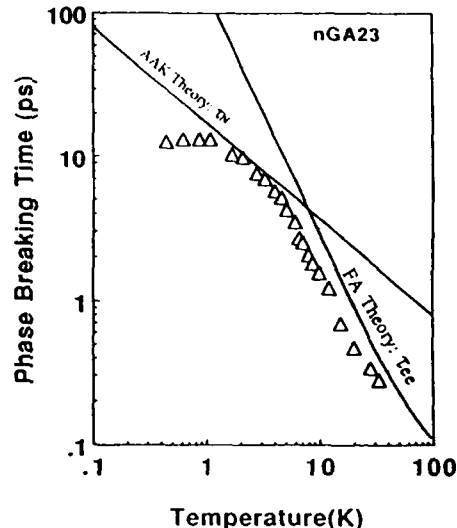


Fig.2 Temperature dependence of the phase breaking time. Calculated phase breaking times limited by electron-electron scattering is also shown; tcc:momentum-conserving electron-electron scattering (Fukuyama and Abrahams 1983) and tcf:scattering by electromagnetic fluctuation (Al'tshuler et al. 1982)

Table 1 The specification of the sample. Each wire width is derived by fitting weak localization theory to the data. S.D.S.H. stands for Selectedly Doped Single Heterojunction. S.D.D.H.: Selectedly Doped Double Heterojunction. D.D.H.: GaAs layer Doped Double Heterojunction.

	Material	Wire Width ( $\mu\text{m}$ )	Carrier Density ( $\text{cm}^{-2}$ )	Fermi Energy (meV)	Mobility ( $\text{cm}^2/\text{Vs}$ )	Momentum Scattering Time (ps)	Diffusion Coefficient ( $\text{m}^2/\text{s}$ )
nGA24	S.D.S.H	0.35	$6.3 \times 10^{11}$	22.2	$2.0 \times 10^4$	0.76	0.0453
nGA23	S.D.S.H	0.25	$6.7 \times 10^{11}$	23.5	$2.1 \times 10^4$	0.80	0.0506
nGA12	S.D.D.H	0.38	$6.0 \times 10^{11}$	21.1	$2.6 \times 10^4$	0.99	0.0557
nGA36	S.D.D.H	0.15	$6.0 \times 10^{11}$	21.1	$2.6 \times 10^4$	0.99	0.0557
nGA42	S.D.S.H	0.14	$1.7 \times 10^{11}$	6.07	$1.2 \times 10^4$	0.46	0.080
nG10	D.D.H	0.16	$3.4 \times 10^{12}$	120	$2.4 \times 10^3$	0.091	0.0294
nG21	D.D.H	0.14	$7.0 \times 10^{12}$	249	$2.4 \times 10^3$	0.091	0.0602
nG31	D.D.H	0.08	$1.3 \times 10^{13}$	457	$2.4 \times 10^3$	0.091	0.108

In Fig.1 we have found that the saturation value has a sample dependence and a higher mobility gives a higher saturation value. In the group of low mobility samples a higher electron density gives a lower saturation value.

This is contrast to the fact that the higher electron density gives a longer phase breaking time in the electron-electron scattering dominated region as shown in the next section. It should be noted that the present samples the conduction channel is formed by ion-implantation, which can introduce defects at the boundary of the channel and possibly into the channel. This was actually observed in magneto transport(Yamada et al. 1990). In the high electron density samples the dose of implantation is proportionally higher and accordingly the defect density induced is expected to be higher. This would suggest together with the mobility dependence that impurities or defects can contribute to phase breaking scattering as well as momentum-loss scattering at very low temperatures.

Magnetic impurities are known to break a phase of electron wave through the spin-flip scattering. Defects introduced by ion-implantation may have lone-pair electrons and behave as magnetic impurities. Then these defects, if they exist, can cause the saturation of phase breaking time and in this case the saturation value should have a sample dependence. Another possibility is the case where a defect has two energy states and when it is scattered by an electron it changes the state accompanied with energy change through an athermal process (Sols 1991). This also can give a saturation of the phase breaking time.

### 3.2 Fermi energy dependence

If the electron-electron scattering is dominant, the phase breaking time should be dependent on the electron density as

$$\frac{1}{\tau_{ee}} = \frac{\pi (k_B T)^2}{2 \hbar E_F} \ln \left( \frac{E_F}{k_B T} \right) \quad (\text{the FA theory})$$

$$\frac{1}{\tau N} = \left( \frac{\sqrt{2} D e^2 k_B T}{\sigma W \hbar^2} \right)^{2/3} = \left( \frac{\sqrt{2} e \pi k_B T}{\sqrt{E_F} \mu m^* W \hbar^2} \right)^{2/3} \quad (\text{the AAK theory})$$

To examine their validity, we measured the Fermi energy (carrier density) dependence of the phase breaking time at different temperatures. Fig.3 shows the results. In the intermediate mobility samples, the Fermi energy was varied by changing the gate voltage, while in the low mobility case, samples with different electron densities were used.

The electron density dependence is different between the two groups. In the sample (nGA23) with the intermediate mobility, the phase breaking time increases with the electron density as  $N_s^{1.2}$  at 15 K, while the sample (nGA42) shows the stronger electron density dependence ( $\tau\phi \sim N_s^{2.3}$ ) at 11K. These dependences are stronger than the prediction ( $\tau\phi \sim N_s^{\gamma}$   $0.5 < \gamma < 1$ ) by FA theory. In the intermediate temperature region, the dependence is stronger and  $\tau\phi \sim N_s^{3.0}$  holds at 4.8K. At lower temperatures where it saturates, the phase breaking time increases very rapidly with  $N_s$  as  $\tau\phi \sim N_s^{4.4}$ .

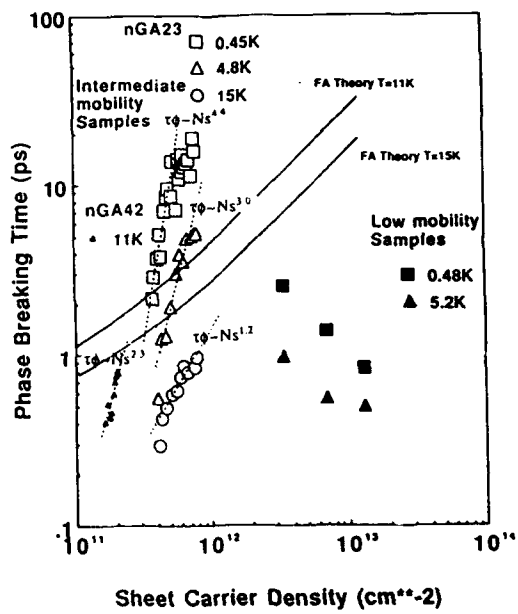


Fig.3 Carrier density dependence of the phase breaking time for various samples. Calculated phase breaking times by using Fukuyama and Abrahams (1983) theory at 11K and 15K are also shown in this figure.

This strong dependence of the phase breaking time on the electron density is not predicted by the existing theories and partly comes through the fitting procedure from the strong dependence of mobility on electron density which is shown in the next section. The BvH equation that was used for the fitting includes the momentum scattering time to represent less frequent backscattering events. When the momentum scattering time increases, it is expected that the quantum correction due to weak localization becomes smaller if the phase coherence length is constant. However, in the experiment, increase of the electron density leads to increase of the quantum correction or the negative magnetoresistance, indicating increase of the phase breaking time. By using the BvH equation, the increase of the phase breaking time is enhanced through the increase of the mobility or momentum scattering time. Therefore, when the momentum scattering time is comparable to the phase breaking time, the BvH equation may be re-examined.

At the high temperature region, the FA theory provides a proper prediction on the temperature dependence of the phase breaking time. However, the electron density dependence is not well explained by the FA theory. Moreover, it has a sample dependence as shown in Fig.3. Here the electron density is varied by applying gate voltage. This might induce a change of the wire width, which might cause an experimental error. Moreover, the sample nGA42 has a narrow wire width ( $0.14\mu\text{m}$ ), while the FA theory deals with two dimensional electron gas, which might be another explanation for the discrepancy. At this moment, however, we can not draw a decisive conclusion on this point. A strong electron density dependence of mobility in the present samples with narrow widths is peculiar and we need more experimental investigation.

In low mobility samples, the electron density dependence of the phase breaking time is opposite to that in the intermediate mobility samples. This dependence is not well understood but in these samples, the mobilities are almost the same although the electron density differs. This suggests that in these samples there exist unknown scatterers which affect both momentum and energy loss scatterings.

#### 4. Fermi Energy Dependence of Mobility

It is well known that the mobility of two dimensional electron gas changes with electron density as  $\mu \sim N_s^{1.0-1.5}$ . We investigated the electron density dependence of mobility in narrow wires by using the Shubnikov-de Haas oscillation and the conductance. In narrow wires, the boundary scattering becomes important in determination of conductance. Therefore, we separately determined the equivalent mobility due to boundary scattering and the inside-wire mobility due to impurity scattering of electrons (Thornton et al. 1989).

Fig. 4 shows the results. In the wide wire, the mobility changes with the electron density as  $\mu \sim N_s^{1.4}$ .

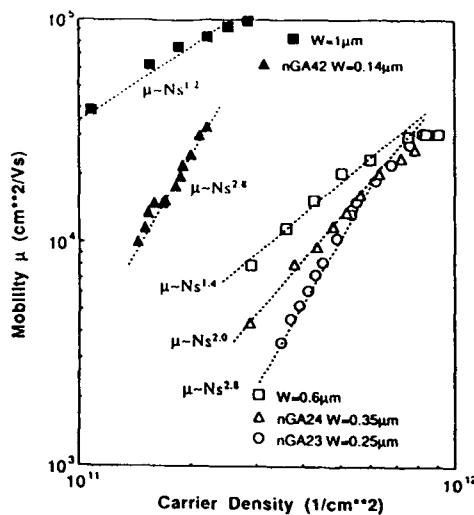


Fig.4 Carrier density dependence of the mobility for various width samples. In the narrow wires, the dependence becomes very large and the mobility changes with the carrier density as  $\mu \sim N_s^{2.8}$ . Each wide wire sample was made from the same wafer as nGA42 ( $W=1\mu\text{m}$ ) or nGA23 & nGA24 ( $W=0.6\mu\text{m}$ )

which is a little steeper than the two dimensional electron gas but in a reasonable range of agreement. However, in the narrow wires, the dependence becomes very large and the mobility changes with the electron density as  $\mu \propto N^{2.8}$ . This strong dependence was once observed and ascribed to fluctuations of electron density and mobility in MOS inversion layers (Brews 1975) and also in low electron density AlGaAs/GaAs heterostructures (Jiang et al. 1988). In the present samples, the strong dependence occurred in the electron density one order of magnitude higher than these cases. We tentatively ascribed to this strong dependence to a similar density fluctuations in the samples which were induced by scattered ions in the channel region. The introduction of defects in a channel was clarified previously (Yamada et al. 1990) and it is considered that the effect of such defects is enhanced in narrower wires.

The strong electron density dependence of mobility is reflected in the strong dependence of the phase coherence length on the electron density as described in the previous section. This again would suggest that the phase coherence length has some relation with mobility, and hence with impurity scattering.

### 5. Conclusions

By investigating magnetoresistance in AlGaAs/GaAs narrow wires, the phase breaking time was determined as a function of temperature and electron density. At relatively high temperatures, the electron-electron scattering with momentum preservation is dominant and the FA theory can well explain the temperature dependence but not the Fermi energy dependence. At lower temperatures, the phase coherence length is constant and has a strong Fermi energy dependence. This behavior can not be predicted by existing theories. It is suggested that the phase coherence length has a sample dependence and hence unknown scattering mechanisms should be involved. On this issue further study is needed.

This work was supported in part by University-Industry Joint Research Program on "Mesoscopic Electronics".

### REFERENCES

- Al'tshuler B L, Aronov A G and Khmelnitsky D E 1982 *J. Phys. C* **39** 7367
- Beenakker C W and van Houten H 1988 *Phys. Rev. B* **38** 3232
- Brews J R 1975 *J. Appl. Phys.* **46** 2181
- Fernando Sols's private communication 1991
- Fukai Y K, Yamada S and Nakano H 1990 *Appl. Phys. Lett.* **56** 2133
- Fukuyama H and Abrahams E 1983 *Phys. Rev. B* **27** 5976
- Hikami S, Larkin A I and Nagaoka Y 1980 *Prog. Theor. Phys.* **63** 707
- Hirakawa K, Odagiri T, Hiramoto T and Ikoma T 1989 *Proc. of Symp. on New Phenomena in Mesoscopic Structures Hawaii USA*
- Hiramoto T, Hirakawa H, Iye Y and Ikoma T 1987 *Appl. Phys. Lett.* **51** 1620
- Hiramoto T, Hirakawa H, Iye Y and Ikoma T 1989 *Appl. Phys. Lett.* **54** 2103
- Ikoma T, Hirakawa K, Hiramoto T and Odagiri T 1989 *The 21st Conf. on Solid State Devices and Materials, Tokyo, Japan*
- Ikoma T and Hiramoto T 1990 *NATO ASI (Proc. of Physics of Granular Nanoelectronics), IlCirocco, Italy*
- Jiang C, Tsui D C and Weimann G 1988 *Appl. Phys. Lett.* **53** 1533
- Kawaguchi Y, Takayanagi I and Kawaji S 1987 *J. Phys. Soc. Jpn.* **56** 1293
- Odagiri T, Hirakawa K and Ikoma T 1990 *20th International Conference on the Physics of Semiconductors, Thessaloniki, Greece 1990*
- Thornton T J, Roukes M L, Scherer A and van de Gaag B P 1989 *Phys. Rev. Lett.* **63** 2128
- Yamada M, Odagiri T, Thornton T J, Hirakawa K and Ikoma T 1990 *Japan-US Seminar on Focused Ion Beam Technology and Application, Portland, Oregon, USA*

## Boundary scattering in quantum wires fabricated using ion implanted gates

R J Blaikie\*, K Nakazato†, T J Thornton‡, J R A Cleaver\* and H Ahmed\*

\* Cavendish Laboratory, University of Cambridge, Cambridge CB3 0HE, U.K.

† Hitachi Cambridge Laboratory, Madingley Road, Cambridge CB3 0HE, U.K.

‡ Department of Electrical Engineering, Imperial College, London SW7 2BT, U.K.

**ABSTRACT:** We have fabricated multi-probe wires in GaAs/AlGaAs heterostructure material using implanted p-type regions to provide the lateral confinement. We observe two peaks in the weak field longitudinal magnetoresistance, together with a 'last plateau' in the Hall resistance and a negative zero-field bend resistance. Device simulations using diffuse boundary scattering in a semi-classical model agree with our experiments.

### 1. INTRODUCTION

In mesoscopic multi-probe wire structures boundary scattering can often dominate the device resistance, so that the geometry of the junction regions and the nature of the scattering of electrons from the device boundaries become very important. Effects due to specular scattering at junctions in multi-probe wires were first observed by Roukes *et al.* (1987) who found that the Hall resistance is 'quenched' at low magnetic fields and then exhibits a steep rise to a 'last plateau' at a field below the threshold for quantum Hall plateaux. The bend resistance of a narrow junction was measured by Timp *et al.* (1988) who found this to be negative in the absence of a magnetic field, contrary to the case of a macroscopic junction. Semi-classical ballistic modelling of multi-probe wires by Beenakker and van Houten (1989) predicted features in the Hall resistance and bend resistance in agreement with these experiments. Thornton *et al.* (1989) investigated the effects of diffuse boundary scattering on the magnetoresistance of narrow wires. They found a weak field longitudinal magnetoresistance maximum consistent with the classical calculations of Ditlefsen and Lothe (1966).

We have investigated boundary scattering in multi-probe wires fabricated in a GaAs/AlGaAs heterostructure using p-type implanted gates to provide the lateral confinement (Blaikie *et al.* 1991). We observed two peaks in the longitudinal magnetoresistance, one due to diffuse boundary scattering within the wire and the other due to specular scattering within the junctions. This junction scattering peak was predicted by Beenakker and van Houten (1989) but in previous experiments has not been distinguishable from the diffuse boundary scattering peak. When we extended the semi-classical model to include diffuse boundary scattering we obtained agreement between this new model and our experimental results.

### 2. DEVICE FABRICATION

The material used in this study (Fig. 1(a)) is a conventional GaAs/AlGaAs heterostructure which has a 4.2K electron density of  $3.4 \times 10^{11} \text{ cm}^{-2}$  and mobility of  $4.5 \times 10^5 \text{ cm}^2 \text{V}^{-1} \text{s}^{-1}$ . A schematic cross section of the completed device is shown in Fig. 1(b). The wire is formed in the region between two 20 keV Be p-type implants separated by a distance  $w_i$ . The electrical width of the wire  $w_e$ , and the electron density  $N_s$ , can be controlled by biasing these implanted gates. An electron beam induced current (EBIC) micrograph of a completed device is shown in Fig. 1(c). In this micrograph the device-defining depletion regions appear as bright bands surrounding the p-type implants, and the rounded nature of the junctions is clearly visible.

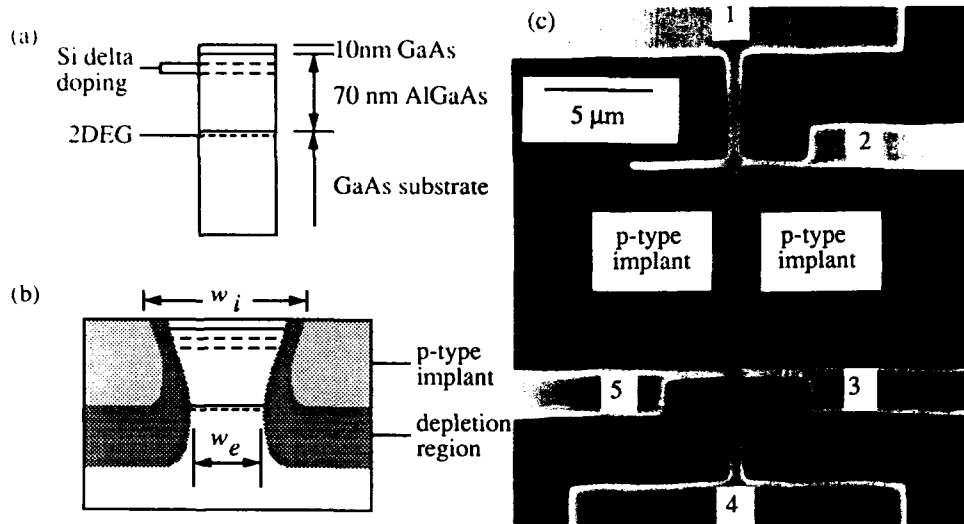


Fig. 1. (a) Material layer structure. (b) Schematic cross-section of a completed device. (c) EBIC micrograph of a multi-probe device having  $w_i = 0.4\mu\text{m}$  in the  $10\mu\text{m}$  long central channel and  $w_i = 0.8\mu\text{m}$  in all other probes.

### 3. EXPERIMENTAL RESULTS

We fabricated a series of multi-probe wires with  $10\mu\text{m}$  long central channels, having  $w_i$  values in the range  $0.4\mu\text{m}$  to  $1.5\mu\text{m}$ . Standard low frequency lock-in techniques have been used to measure four-terminal device resistances  $R_{ij,kl}$ , where current is passed between probes  $i$  and  $j$ , and voltage is measured between probes  $k$  and  $l$  (see Fig. 1(c) for probe labelling). Figure 2(a) shows the  $1.7\text{K}$  longitudinal magnetoresistance  $R_L \equiv R_{14,23}$ , of a device having  $w_i = 0.6\mu\text{m}$ , with a forward bias applied to the p-type gates,  $V_i = 1.40\text{V}$ . For fields below  $0.5\text{T}$  we observe two peaks, at  $B_1$  and  $B_2$ , and for higher fields Shubnikov de Haas oscillations emerge. The presence of two weak field peaks was unexpected since similar structures fabricated by other methods have shown only a single peak (Thornton *et al.* 1989, Nakata *et al.* 1991). We interpret these two peaks as follows. The peak at  $B_1$  is due to an increase in the transmission of electrons into the side-probes by a weak magnetic field as predicted by Beenakker and van Houten (1989), and is therefore expected only in devices with side-probes. The peak at  $B_2$  is due to diffuse boundary scattering within the wire itself as discussed by Thornton *et al.* (1989). Our interpretation was verified by measuring the magnetoresistance of a two-terminal wire with the same implant separation, shown also in Fig. 2(a). Whilst a peak at  $B_2$  remains, there is no peak at  $B_1$  since this device has no side-probes.

Since  $B_2$  is caused by diffuse boundary scattering within the wire the experimentally verified classical relationship (Thornton *et al.* 1989)  $B_2 = 0.55\sqrt{N_s/w_e}$  should be valid, where  $N_s$  is the electron density within the wire and  $w_e$  is the electrical width. We have used this relationship to determine  $w_e$  for the multi-probe device of Fig. 2, having calculated  $N_s$  from the  $1/B$  period of the Shubnikov de Haas oscillations. For an implanted gate bias  $V_i = 1.40\text{V}$  the electrical width is  $0.15 \pm 0.01\mu\text{m}$  and the zero field mobility is  $3.5 \pm 0.2 \times 10^5 \text{ cm}^2\text{V}^{-1}\text{s}^{-1}$ , as compared to the mobility of  $4.5 \times 10^5 \text{ cm}^2\text{V}^{-1}\text{s}^{-1}$  for the starting material.

We have also investigated the variation of  $B_1$  and  $B_2$  with implant separation  $w_i$  and implant bias  $V_i$ , Fig. 2(b). As expected from the classical theory,  $B_1$  and  $B_2$  are larger for devices with narrower implant separations; however  $B_1$  and  $B_2$  are independent of  $V_i$ . This implies that for these wires  $w_e \propto \sqrt{N_s}$ , which is consistent with the confining potential produced by the implants being parabolic. Modelling of a similar structure by Meirav *et al.* (1989) predicts a

parabolic confining potential between two implanted p-type regions in a GaAs/AlGaAs heterostructure but experimental evidence of this has not been reported previously.

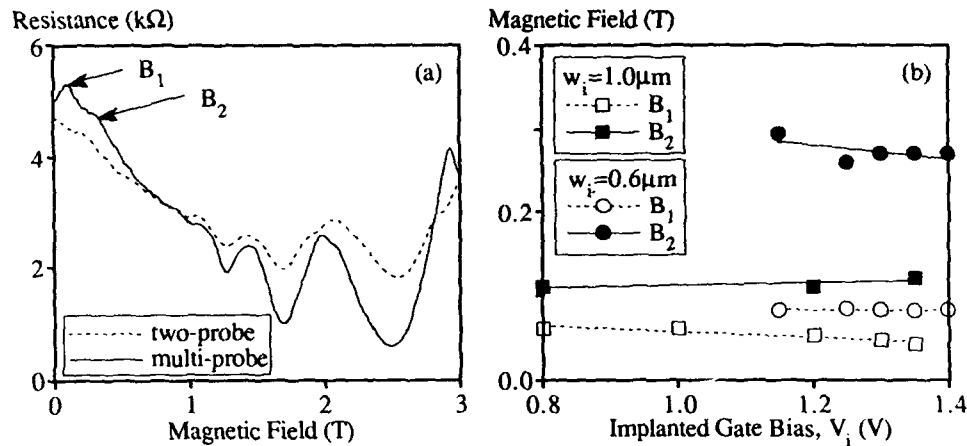


Fig. 2 (a) Magnetoresistance of 10  $\mu\text{m}$  long wires with  $w_i = 0.6 \mu\text{m}$ .  $V_i = +1.40\text{V}$ .  
 (b) Variation of  $B_1$  and  $B_2$  with p-type gate bias for multi-probe wires with  $w_i = 0.6 \mu\text{m}$  and  $1.0 \mu\text{m}$ .

As well as the longitudinal magnetoresistance  $R_L$  of the multi-probe wires, we have measured their Hall resistances  $R_H \approx R_{14,53}$  and bend resistances  $R_B \approx R_{15,34}$  as functions of magnetic field. Figure 3 shows  $R_L$ ,  $R_H$  and  $R_B$  for the  $w_i = 0.6 \mu\text{m}$  device with  $V_i = 1.35\text{V}$ . In the Hall resistance a 'last plateau' is observed, with the steep rise to this plateau being centred at  $B_1$ . The bend resistance is negative at zero field and then rises to a small positive peak near  $B_1$ . These features are consistent with the semi-classical modeling of Beenakker and van Houten (1989), and their positions confirm that the peak in the longitudinal resistance at  $B_1$  is caused by scattering into the side-probes.

#### 4. DEVICE MODELLING

In order to confirm further the nature of the magnetoresistance peaks at  $B_1$  and  $B_2$  we extended the semi-classical model of Beenakker and van Houten (1989) to include diffuse boundary scattering. In this model the probability for an electron injected into probe  $i$  to be transmitted into probe  $j$ ,  $T_{i \rightarrow j}$ , is estimated by following a large number of classical electron trajectories through the device. The resistance is then calculated from the Landauer-Büttiker formula (Büttiker 1986). Diffuse boundary scattering is introduced directly into the trajectory calculation through the specularity coefficient  $p$ . We model the device boundaries with a hard-wall potential and assume that for any collision between an electron and a wall the probability that the electron will scatter diffusely is  $(1-p)$ .

A set of results from this model are shown in Fig. 4. The device modelled is of length  $l = 20$ , with junctions having radii of curvature  $r = 2.0$  and for boundary scattering with a degree of specularity  $p = 0.8$ , where all device dimensions have been normalized by the wire and probe width  $w$ . In the simulation results resistances are normalized by  $R_0 = (h/2e^2)\pi k_F w$  where  $k_F$  is the Fermi wave vector, and magnetic fields are normalized by  $B_0 \equiv mv_F/ew$  where  $v_F$  is the Fermi velocity. A set of results for the same device but with perfectly specular boundary scattering ( $p = 1.0$ ) is shown by the dashed lines in Fig. 4. We see that when  $p = 0.8$  two peaks in the longitudinal magnetoresistance are predicted, but for the case of completely specular boundary scattering the broad peak centred at  $B_2$  disappears. For the diffuse boundary scattering case no new features appear in the Hall resistance and the bend resistance at  $B_2$  since these resistances are dominated by the electron trajectories within the junction, which will suffer fewer boundary collisions than the trajectories along the wire.

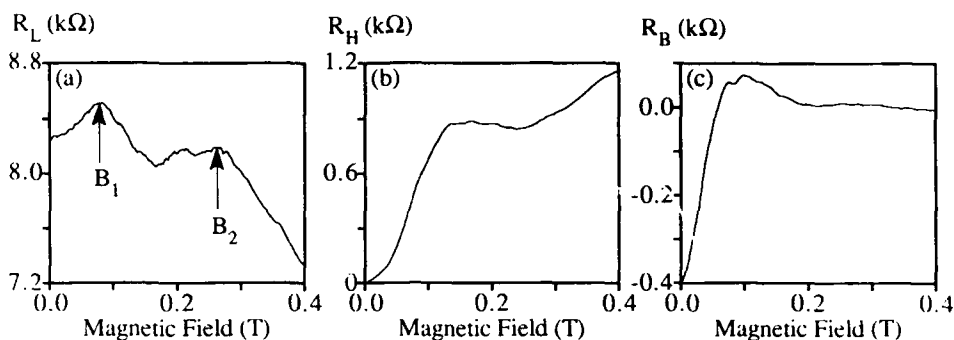


Fig. 3 (a) Longitudinal resistance  $R_L$  (b) Hall resistance  $R_H$  and (c) bend resistance  $R_B$  for the multi-probe wire with  $w_i = 0.6\mu m$ .  $V_i = +1.35V$ .

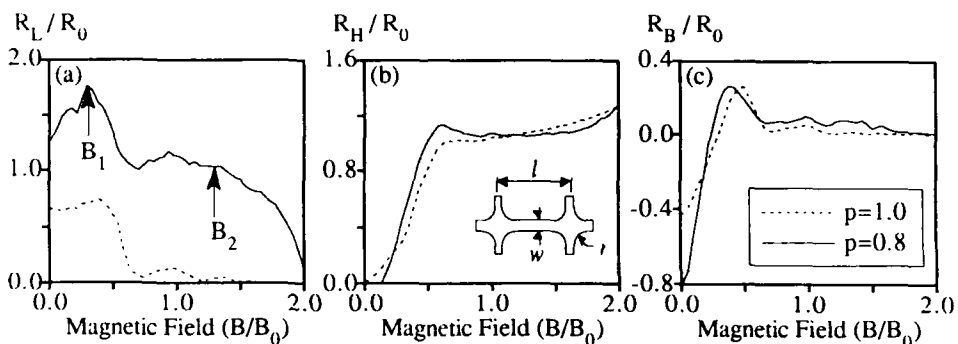


Fig. 4 Numerical simulations of  $R_L$ ,  $R_H$ , and  $R_B$  for the device layout shown inset in (b). Device dimensions:  $l/w = 20$  and  $r/w = 2$ . Solid line:  $p = 0.8$ . Dashed line:  $p = 1.0$ .

## 5. CONCLUSIONS

In conclusion, we have observed experimentally two weak field peaks in the longitudinal magnetoresistance of multi-probe wires fabricated in a GaAs/AlGaAs heterostructure using ion implanted p-type gates to provide the lateral confinement. By extending the semi-classical ballistic model to include diffuse boundary scattering we have been able to simulate this twin peak structure successfully.

We would like to thank T Tanoue for growing the starting material for this study and B Fraboni for help with the EBIC microscopy.

## REFERENCES

Beenakker C W J and van Houten H 1989 *Phys. Rev. Lett.* **63** 1857  
 Blaikie R J, Nakazato K, Fraboni B, Hasko D G, Cleaver J R A and Ahmed H 1991 *Microelectronic Engineering* **13** 373  
 Büttiker M 1986 *Phys. Rev. Lett.* **57** 1761  
 Ditlefsen E and Lothe J 1966 *Philos. Mag.* **14** 759  
 Meirav U, Kastner M A, Heiblum M and Wind S J 1989 *Phys. Rev. B* **40** 5871  
 Nakata S, Hirayama Y, Tarucha S and Horikoshi Y 1991 *J. Appl. Phys.* **69** 3633  
 Roukes M L, Scherer A, Allen S J, Craighead H G, Ruthen R M, Beebe E D and Harbison J P 1987 *Phys. Rev. Lett.* **59** 1011  
 Thornton T J, Roukes M L, Scherer A and Van de Gaag B 1989 *Phys. Rev. Lett.* **63** 2128  
 Timp G, Baranger H U, deVegvar P, Cunningham J E, Howard R E, Behringer R and Mankiewich P M 1988 *Phys. Rev. Lett.* **60** 2081

## **Fluctuations effects in the low temperature magnetoresistance of micron scale semiconductor junctions**

JP Bird (1), Y Ochiai (1), T Onishi (1), T Kitatani (1), M Kawabe (1), K Ishibashi (2), K Ishibashi (2), Y Aoyagi (2), and S Namba (2)

(1) Institute of Materials Science, University of Tsukuba, Tsukuba, Ibaraki 305, Japan.

(2) Frontier Research Program, RIKEN, Hirosawa 2-1, Wako, Saitama 351-01, Japan

We discuss the low temperature transport properties of small electrical devices defined using an electrostatic confinement technique. Electron beam lithography enables us to fabricate devices in which transport is intermediate between the pure ballistic and diffusive regimes. Fluctuations observed in the magnetoresistance exhibit a non universal scaling with sample size which we discuss in terms of the increased importance of sub band quantisation in small semiconductor structures.

### **1 INTRODUCTION**

The universal properties of the conductance fluctuations, observed in the low temperature magnetoresistance of disordered metal wires, are believed to result from a special correlation between the quantum mechanical transmission coefficients in metallic systems, Washburn and Webb (1987). This correlation is thought to arise from the diffusive nature of electronic motion and from the long range phase coherence of the electronic wave function at low temperatures. An interesting question is whether such correlation is also present in semiconductors, where the long mean free path means that the motion may no longer be clearly diffusive.

In this paper we discuss the conductance fluctuations observed in the low temperature magnetoresistance of semiconductor microdevices and show that they exhibit a non universal scaling with sample size. We believe this indicates that the correlation particular to metallic systems may no longer be present and discuss the increased importance of sub band quantisation in small semiconductor devices.

### **2 EXPERIMENTAL TECHNIQUES**

We have fabricated split gate microdevices, Ishibashi et al (1991), using lithographically defined aluminium gates deposited on to the surface of a GaAs/AlGaAs heterojunction.

Application of a suitable negative bias depletes electrons from underneath the gates, thereby defining a small conducting region connected to the measurement probes via large sections of two dimensional electron gas. In the experiments we discuss here, the lithographic length of the gates was defined to be  $2 \mu\text{m}$  while the gap between them was  $1.2 \mu\text{m}$ .

Measurements of the magnetoresistance and gate voltage characteristics were performed in a  $^3\text{He}$  cryostat in applied magnetic fields of up to 8 Tesla. The carrier density was obtained from the periodicity of the Shubnikov de Haas oscillations and was found to remain unchanged at gate biases suitably away from pinch off. The zero gate voltage mobility was of order 100,000  $\text{cm}^2/\text{Vs}$  and in the following we will assume that it remained independent of gate voltage. This seems to be a reasonable assumption away from pinch off, where the carrier density is constant and the resistance of the channel scales suitably with gate voltage, Ochiai et al (1991).

### 3 EXPERIMENTAL RESULTS

The low temperature magnetoresistance of the split gate samples exhibits universal conductance fluctuations (figure 1) whose amplitude varies both as a function of applied magnetic field and gate voltage.

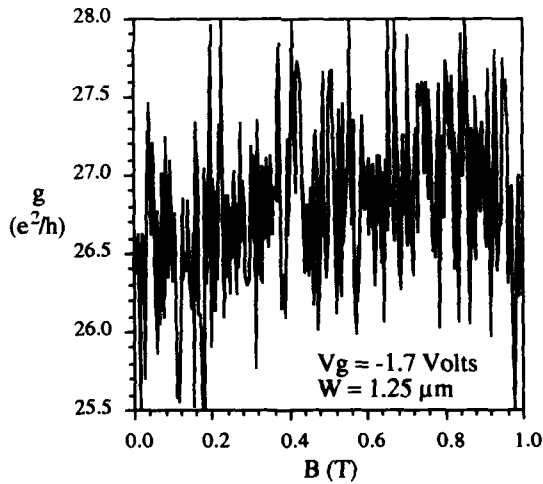


Fig. 1. Universal conductance fluctuations measured in a split gate sample at 0.3 Kelvin.

Although the average amplitude of fluctuation was reproducible between gate voltage sweeps, the exact magnetofingerprint was not. Such high sensitivity may reflect the ability of a single impurity to strongly modulate the conductance of the channel. Since in these devices the mean free path is comparable to the device dimensions, scattering should occur from only one or two impurities. As a result, the motion of just one impurity should be sufficient to completely alter the magnetofingerprint of the fluctuations. Feng et al (1986).

In figure 2 we show how the amplitude of the conductance fluctuations scales with gate voltage, or sample size. The first important feature is the observation that the amplitude of the fluctuations, measured over a range of 500 mT at 6 Tesla, is almost an order of magnitude smaller than that measured over the same range around zero field. The second is that as we increase the negative bias applied to the gates, and so decrease the conducting width of the channel, the amplitude of the fluctuations is seen to decrease by two orders of magnitude.

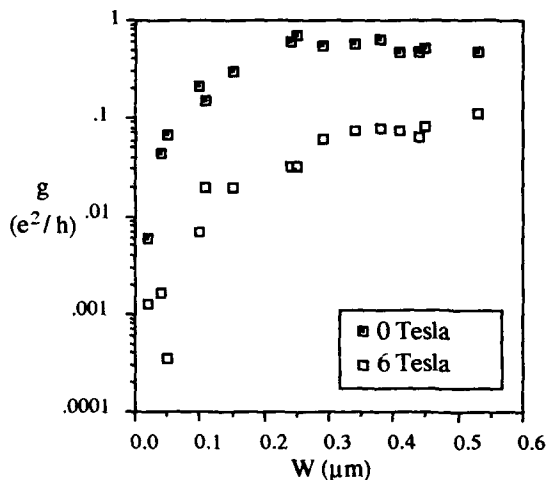


Fig. 2. The variation of the conductance fluctuations, observed in the split gate geometry, with channel width.

In terms of the universal conductance fluctuation theory this size dependence is unexpected and can only be explained by a gate-voltage dependent inelastic scattering length. However, to account for the magnitude of the effect in figure 2, the inelastic length would have to change by well over an order of magnitude. This seems unlikely since, as we have already mentioned, the transport properties of the channel seem insensitive to the applied gate voltage. We therefore propose that figure 2 provides evidence for a non universal scaling of the conductance fluctuations in the split gate device.

#### 4 DISCUSSION AND CONCLUSIONS

In metallic systems the mean free path is typically much smaller than the sample dimensions and the electronic motion can be considered to be diffusive. This diffusive motion is thought to be responsible for the universal properties of the conductance fluctuations in metals, establishing a special correlation between the transmission coefficients of the system, Imry (1986).

In small semiconductor devices the mean free path is often comparable to the device dimensions and the motion can no longer be considered to be diffusive. The confining potential quantises the motion into discrete sub bands, whose separation increases as the strength of the

confining potential is increased. Recent calculations indicate that a non universal scaling of the fluctuations can be expected when the number of occupied sub bands is small. Tamura and Ando (1991) find for small sub band occupancy that the localisation length is comparable to the mean free path. In this regime the fluctuations are not independent of sample size but instead show a strong scaling dependence. As the number of sub bands is increased, the localisation length eventually becomes larger than the sample length and in this regime the fluctuations are predicted to exhibit the universal characteristics common to metallic systems. Higurahi et al (1991) also find that as the number of sub bands is increased from the ballistic limit, the interference between modes, and so the amplitude of fluctuation, is dramatically increased. Although a direct comparison with theory, where the authors study the length dependence of the fluctuations at differing sub band occupancy, is not possible, the results of figure 2 at least appear to be in general agreement with the theoretical predictions: at low gate voltage, and so high sub band index, the amplitude of fluctuation is independent of gate voltage; at lower widths, the number of sub bands is small and the fluctuations scale non universally.

In conclusion, we have studied the conductance fluctuations in small, split gate devices in which scattering occurs from just a small number of impurities. At high negative biases, only a few sub bands are occupied and the amplitude of the fluctuations exhibits a non universal scaling dependence, not observed in metallic systems. Our results are in reasonable agreement with recent theoretical calculations which predict non universal scaling in semiconductor devices when the number of occupied sub bands is small. We therefore conclude that the special correlation properties particular to diffusive systems no longer persist in this particular regime of transport.

This work was partly supported by a grant from the Ministry of Education, Science and Culture of Japan (priority area: Electron Wave Interference Effects in Mesoscopic Structures). JPB would like to acknowledge the financial support of the Japan Society for the Promotion of Science and thanks H Zhao for stimulating conversations. The electrical measurements presented here were performed at the Cryogenics Center of the University of Tsukuba.

## 5 REFERENCES

- H Higurahi, S Iwabuchi and Y Nagaoka (1991) to appear in *Surf Sci.*
- Y Imry (1986) *Europhys Lett* **1** 249.
- K Ishibashi, Y Aoyagi, S Namba, Y Ochiai, JP Bird and M Kawabe (1991) to appear in *Surf Sci.*
- Y Ochiai, T Onishi, JP Bird, M Kawabe, K Ishibashi, Y Aoyagi and S Namba (1991) to appear in *Jap J Appl Phys.*
- H Tamura and T Ando (1991) *Phys Rev B* **44** 1792.
- S Washburn and RA Webb 1987 *Adv Phys* **35** 375.

## Experiments on mechanically controllable break junctions of niobium and platinum

C. J. Muller, J. M. van Ruitenbeek and L. J. de Jongh

Kamerlingh Onnes Laboratory, Leiden University  
P.O. Box 9506, 2300 RA Leiden, The Netherlands

A new technique is developed to obtain a controllable clean and stable junction. As a function of an externally applied force the normal resistance,  $R_N$ , of the junction can be adjusted in a wide resistance range. The stability of the system is such that the transition from weak link to tunnel junction can be studied.

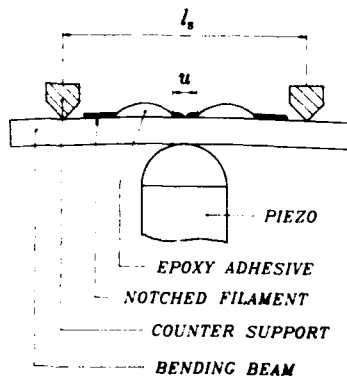
### Introduction

Mechanically controllable junctions may prove beneficial in various fields of physics. The possibility to change  $R_N$  in a continuous way allows systematic study of physical properties, moreover the  $R_N$ -range of applicability of various theories can experimentally be determined. An important step in the development of mechanically adjustable junctions was made by Moreland et al. (1984, 1985). With the use of an electromagnetic squeezer they were able to construct a "squeezable" tunnel junction which consists of two evaporated electrodes, pressed towards each other in vacuum until a gap of a few Å exists between the electrodes. The electromagnetic squeezer was also used by them in a different method whereby a small gap was established between two ends of a brittle  $Nb_3Sn$  filament which was broken in liquid helium.

We have developed a method which combines the advantages of both the squeezable tunnel junction (operation in vacuum) and the break junction (clean electrodes formed at 4.2 K) as used by Moreland et al. In this paper we report experiments on mechanically controllable break (MCB) junctions of niobium and platinum at 4.2 K. Part of this work is also described in the original paper on MCB junctions of niobium by Muller et al. (1992).

### Experimental techniques

In figure 1 the most important item, the sample mounting, of the MCB setup is shown in a three point bending configuration. The sample mounting consists of a notched metal filament which is glued on a glass bending beam in such a manner that the notched section remains unglued. The dimensions are:  $l_s \approx 15$  mm,  $u \approx 0.2$ – $0.5$  mm and the width of the notch is typically 5– $10$   $\mu$ m. With the use of a spindle driven by an electro-motor the piezo is directed towards the sample mounting. The counter supports form a part of a rigid construction, delivering the counter force when the piezo starts bending the beam. On bending, the length increase of the unglued section,  $u$ , is used to break the notched part of the filament. In this way it is possible to point bending configuration.



break metals which typically exhibit a maximum strain which is approximately five times larger than the strain of glass. When the metal filament is broken the motor is reversed in order to establish a contact between the broken ends. When the filament ends make contact the bending beam is still under strain because of the deformation and elongation of the notched part of the filament before it breaks. From this stage onward the piezo is used (instead of the motor) for fine adjustment of the junction. The length increase of the piezo is sufficient to study the cross-over from weak link to tunnel junction, and to obtain the highest resistance value (measured up to  $1\text{ G}\Omega$ ) in the tunnel regime. The displacement ratio *i.e.* the vacuum barrier increase in the tunnel regime divided by the length increase of the piezo has a typical value of  $5 \cdot 10^{-3}$  for the MCB junctions described here.

### Results of niobium MCB junctions

In the weak link regime the electrodes are in physical contact with each other. Although a multiple contact geometry cannot completely be excluded this is not likely to occur. Contact between the freshly broken filament ends is most probably established at two nearest opposite clean spots of the electrodes. The small constriction radius of  $40\text{ \AA}$  for a  $10\Omega$  weak link junction and  $4\text{ \AA}$  for a  $1000\Omega$  weak link obtained using the relation derived by Sharvin (1965) gives confidence that we are dealing with a single constriction like contact. In the weak link regime the  $I$ - $V$  curves exhibit a critical current,  $I_c$ , and an excess current,  $I_{ex}$ . The excess current is defined as the intersection of the extrapolated high voltage branch of an  $I$ - $V$  curve with the zero voltage axis. In normal superconducting (NS) structures an excess current results from Andreev reflection (1964) at the NS interface. Superconducting weak links can often be modelled as SNS structures where Andreev reflections also play an important role.

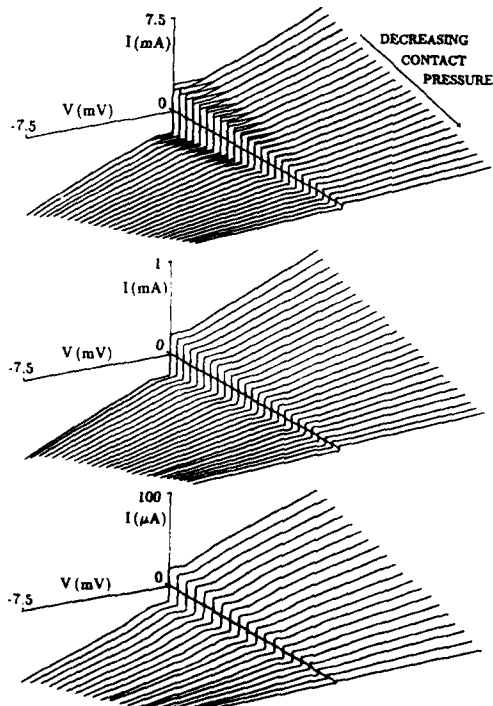


Figure 2:  $I$ - $V$  curves in the weak link regime as a function of decreasing contact pressure. The pressure scale is in arbitrary units. The vertical scales change between the graphs, indicating a change of  $R_N$  by three orders of magnitude.

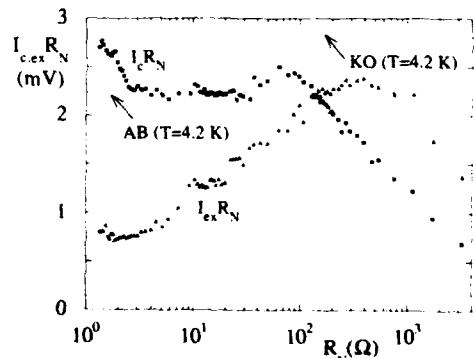


Figure 3: The  $I_c R_N$  and  $I_{ex} R_N$  values, derived from the  $I$ - $V$  curves of figure 2, as a function of the normal resistance. The predictions of AB for a tunnel junction and KO for a short clean weak link are indicated.

As a result of an increasing piezo voltage the contact pressure of the electrodes diminishes, resulting in a smaller constriction radius, and an increase of  $R_N$ . This is shown in figure 2 for the  $R_N$  range 1–3000  $\Omega$ . Figure 3 shows the  $I_c R_N$  and  $I_{ex} R_N$  values as a function of  $R_N$ . The  $I_c$  and  $I_{ex}$  values are derived from the curves in figure 2;  $I_c$  is defined as the current value at which a jump occurs to the voltage carrying state. The normal resistance and the excess current are derived from a linear fit to the 5 to 10 mV and –5 to –10 mV curve parts. The dotted lines in figure 3 indicate the theoretical predictions of the  $I_c R_N$  product at 4.2 K derived by Ambegaokar-Baratoff (AB, 1963) for a tunnel junction and by Kulik-Omelyanchuk (KO, 1977) for a short clean weak link. Surprisingly the AB result is in close agreement with the data over almost two orders of magnitude of  $R_N$ , while the KO prediction is too high over the whole  $R_N$  range. The larger  $I_c R_N$  values in the 1–3  $\Omega$  range coincide with the hysteretic I-V curves as can be observed in the upper graph of figure 2. Hysteresis in weak links is attributed to self heating effects (Gubankov et al. 1972, Fulton and Dunkleberger 1974) which suggests that the larger  $I_c R_N$  values for the hysteretic curves are a consequence of self heating. The logarithmic decrease of the  $I_c R_N$  product for the highest  $R_N$  values in the weak link regime might be due to a suppression of the critical current by fluctuations.

The  $I_{ex} R_N$  product increases where the  $I_c R_N$  product is constant and decreases for the highest  $R_N$  values in the weak link regime, as is expected due to the absence of an excess current in a tunnel junction. Also for the  $I_{ex} R_N$  product the AB result seems to impose a natural voltage limit. Theoretical predictions of the  $I_{ex} R_N$  product in clean short constrictions (Zaitsev 1980, Klapwijk et al. 1982) exceed the highest observed values in figure 3.

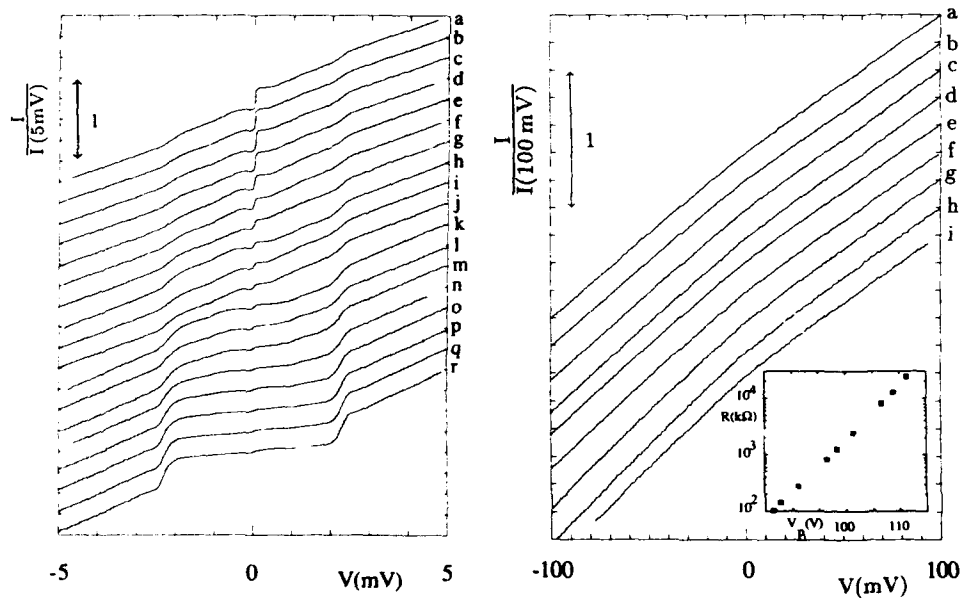


Figure 4: The transition from contact to vacuum barrier. The current is normalized to the positive 5 mV value. Successive curves have an offset of 0.25, the normal resistance in  $k\Omega$  reads: a: 1.67, b: 1.80, c: 1.97, d: 2.22, e: 2.69, f: 4.15, g: 5.68, h: 7.30, i: 8.77, j: 10.8, k: 13.0, l: 18.4, m: 21.7, n: 40.7, o: 63.6, p: 87.3, q: 111, r: 149.

Figure 5: I-V curves in the tunnel regime of a platinum MCB junction. Successive curves are normalized to the positive 100 mV value and have an offset of 0.2. The resistance in  $M\Omega$  reads: a: 23.8, b: 12.6, c: 8.16, d: 2.40, e: 1.26, f: 0.83, g: 0.27, h: 0.14, i: 0.10. In the inset the exponential dependence of  $R_N$  on  $\delta$  is expressed according to eq. 1.

In figure 4 *I-V* curves are shown of the transition from weak link to tunnel junction. The normal resistance changes continuously from  $1.67\text{ k}\Omega$  in the weak link regime to  $149\text{ k}\Omega$  in the tunnel regime. A smooth cross-over is observed from an infinite conductance at  $V = 0$  in the weak link regime (e.g. curve a) to a finite conductance at  $V = 0$  (e.g. curve h) in the transition regime. The zero voltage resistance equals  $R_N$  at approximately  $33\text{ k}\Omega$ .

### Results of platinum MCB junctions in the tunnel regime

In figure 5 results are shown of a platinum MCB junction with a vacuum barrier between the electrodes. The resistance  $R$  is obtained from the positive linear  $50\text{--}100\text{ mV}$  curve part and changes from  $100\text{ k}\Omega$  to  $22\text{ M}\Omega$  on increasing the piezo voltage. The asymmetry of the *I-V* curves amounts to 20% and scales with the resistance. The asymmetry is believed to be a result of the geometry of the electrodes, since it can be changed by deforming the electrode material by establishing a contact. The inset of figure 5 shows the resistance of the *I-V* curves as a function of the piezo voltage. The vacuum barrier distance,  $\delta$  is in first order approximation proportional to the piezo voltage,  $V_p$ . The exponential dependence of  $R$  on  $V_p$  agrees with the following relation:

$$R(\delta) \propto \exp\left(\frac{2}{\hbar}(2m\phi)^{\frac{1}{2}}\delta\right) \quad (1)$$

which is expected for vacuum barrier tunneling. Here  $m$  is the free electron mass and  $\phi$  is the work function of the platinum electrodes. With a measured  $R$  stability better than 1%, and using eq. 1 we claim an absolute stability of the distance between the electrodes which is better than  $0.5\text{ pm}$ . Under stable conditions we have already observed an  $R$  stability of 0.1% ( $\approx 50\text{ fm}$ ).

It is likely that tunneling in our MCB junction occurs somewhere between two nearest spots on the clean fractured electrodes. The *I-V* curves may be compared with e.g. experiments by van Bentum *et al.* (1988) who measured *I-V* curves with a STM tip a few Å above a metal surface. They however measured highly non-linear *I-V* curves. This non-linearity was attributed to a Coulomb blockade effect of the tunneling electrons induced by a small capacitance of the tip-plate tunnel junction configuration. In the experiments performed on platinum MCB junctions no evidence for such effects is found. Even on the scale of a few millivolts the *I-V* curves are linear.

### Acknowledgements

We wish to thank R. de Bruyn Ouboter for his interest and discussions. This work is part of the research program of the Leiden Materials Science Center (WFMO) and is financially supported by the Stichting voor Fundamenteel Onderzoek der Materie (FOM).

Ambegaokar V and Baratoff A 1963 *Phys. Rev. Lett.* 10 486; *Phys. Rev. Lett.* 11 104.  
 Andreev A F 1964 *Sov. Phys. JETP* 19 1228.  
 van Bentum P J M, van Kempen H, van de Leemput L E C and Teunissen P A A  
   1988 *Phys. Rev. Lett.* 60 369.  
 Fulton T A and Dunkleberger L N 1974 *J. Appl. Phys.* 45 2283.  
 Gubankov V N, Likharev K K and Margolin N M 1972 *Sov. Phys.-Solid State* 14 819.  
 Klapwijk T M, Blonder G E and Tinkham M 1982 *Physica* 109/110b 1657.  
 Kulik I O and Ormelyanchuk A N 1977 *Sov. J. Low Temp. Phys.* 3 459.  
 Moreland J and Hansma P K 1984 *Rev. Sci. Instrum.* 55 399.  
 Moreland J and Ekin J W 1985 *J. Appl. Phys.* 58 3888.  
 Muller C J, van Ruitenbeek J M and de Jongh L J 1992 to be published in *Physica C*.  
 Sharvin Yu V 1965 *Zh. Eksp. Teor. Fiz.* 48 984.  
 Zaitsev A V 1980 *Sov. Phys. JETP* 51 111.

## **High temperature operation of ballistic constrictions**

Gregory L. Snider\*, Mark S. Miller, Michael J. Rooks<sup>†</sup>, and Evelyn L. Hu

Department of Electrical and Computer Engineering,  
University of California, Santa Barbara CA 93106

\* Current Address: Department of Applied and Engineering Physics,  
Cornell University, Ithaca NY 14853

† National Nanofabrication Facility, Cornell University, Ithaca NY 14853

**ABSTRACT:** The limited temperature and drain bias performance of split-gate ballistic constrictions is addressed through a design giving large electron subband separations. Quantized conductance in a split gate structure is observed at a temperature of 30K. Plateaus are also seen with a drain bias of up to 12mV. This performance is made possible by placing the Two Dimensional Electron Gas (2DEG) 30nm below the surface, and a gate separation of 100nm.

### **1. INTRODUCTION**

A great deal of research has been performed on devices whose critical dimensions are on the order of the mean free path and Fermi wavelength of an electron in GaAs, K. Ismail et al (1989) and T.L. Cheeks et al (1988). At these scales an electron no longer behaves simply as a particle, but will begin to exhibit quantum mechanical effects. One of these effects is the quantized conductance observed in electrons traveling ballistically through one-dimensional constrictions, B.J. van Wees et al (1988) and D.A. Wharam et al (1988). If the width of the constriction can be varied, one can adjust the position of the one-dimensional electron energy subbands with respect to the Fermi level. At sufficiently low temperatures, this results in the appearance of discrete steps in the current conductance through the one-dimensional "wire", quantized in units of  $2e^2/h$ , where  $h$  is Planck's constant, and  $e$  is the electron charge. A severe limitation of these devices is the "delicacy" of the quantized conductance. A temperature which is too high or a drain bias which is too large will destroy the effect. Both of these limitations are due to the small energy separations between electron subbands in the constriction. A large subband separation addresses both limitations by reducing the thermally-induced partial occupation of higher subbands at high temperatures, and the intersubband

scattering at high drain bias. We report here measurements of quantized conductance at a temperature of 30K, and at a drain bias of 12mV, made possible by the specific design of a quantum wire structure having large subband spacings.

## 2. EXPERIMENTAL

We employ the technique of reverse biased Schottky barrier "split gates", as indicated in Fig.1, to form the constriction since it offers the advantages of relative simplicity and low process damage. To maximize the subband separations, the cross section of the one-dimensional wire should be as small as possible. However, the lower bound on the value of the minimum gate

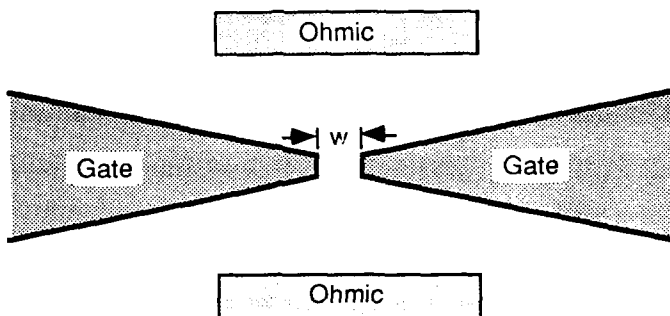


Fig. 1. Schottky barrier split-gate ballistic constriction.

separation,  $w$ , is not set by lithographic resolution limits, but by the electrostatic interaction of the gates with the underlying semiconductor. Due to fringing electric fields, the minimum separation is determined by the distance of the 2DEG from the surface and the sheet charge in the 2DEG. Bringing the 2DEG closer to the surface of the structure allows a smaller value of  $w$ , but with the disadvantage of increased sensitivity to damage from routine processing. To balance the effects of these restrictions and optimize a structure that will provide the largest subband spacings, we have carried out an analysis, using a self-consistent two-dimensional Schrödinger-Poisson solver, detailed in G.L. Snider et al (1990), which enables us to consider the effects of material structure and fabrication on the subband separations.

The structure used in this work employs a single delta-doped layer, placed 15nm from the heterojunction, to provide a high sheet concentration while avoiding parallel conduction. The total distance from the surface to 2DEG is 30nm. At 4.2K without illumination, the measured electron sheet concentration is  $5 \times 10^{11} \text{ cm}^{-2}$ , with a mobility of 290,000  $\text{cm}^2/\text{V}\cdot\text{s}$ . Ohmic contacts are formed using a standard AuGe/Ni process, and a mesa etch is used to isolate the devices. The split-gates are formed by high resolution electron beam lithography, where PMMA is used to lift-off 20nm of AuPd metalization, M.J. Rooks et al (1990). The split gate

separation is 100nm, and the length of the constriction is 200nm. Simulations of this structure suggest that three conductance steps should be seen, with subband separations of 10meV at the gate bias where the lowest subband is at the Fermi level.

To measure the temperature performance, a two-point conductance measurement of the constriction is performed using standard lock-in techniques. Fig. 2a shows the conductance of the constriction, and its derivative as a function of gate voltage at 4.5K. The conductance is normalized with respect to  $2e^2/h$ , and the measured series resistance has been removed. Four minima are visible in the derivative plot, corresponding to four plateaus in the conductance at

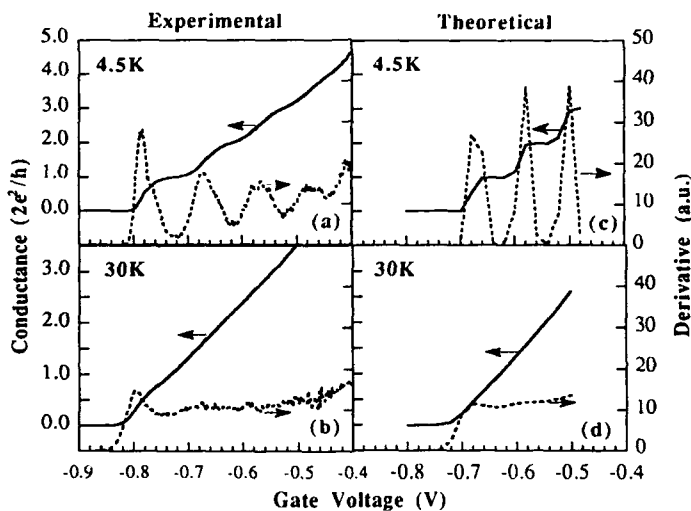


Fig. 2. Comparison of experimental and theoretical conductance vs. gate voltage.

integer multiples of  $2e^2/h$ . The position of the first step, corresponding to a peak in the derivative, is at -0.8V, in good agreement with the -0.7V predicted by the simulation. At 30K, Fig. 2b, the first plateau can be seen in the derivative. The theoretical conductances, calculated from the 2D Poisson-Schrödinger solutions, are shown in Fig. 2c and 2d. Remnants of the rising edge of the first step, denoted by the peak in the derivative, can be seen as high as 44K. Although the plateau of the first step is no longer apparent, we believe that the indication of the rising edge of the first step gives evidence of quantized behavior at this relatively high temperature.

Another advantage of the large subband separations afforded by this structure is the tolerance of electron heating due to bias voltage. If the kinetic energy gained as the electron traverses the constriction is close to the subband separation, inter-subband scattering can occur, eliminating the quantized conductance. High bias voltages are desirable because larger signal currents are

obtained, and again large subband separations are needed. To illustrate the high currents possible, Fig. 3 shows a DC measurement, taken without a lock-in amplifier, of the current at 4.5K with a bias of 6mV. The current at the first plateau is 420nA. The first plateau can be resolved to a bias voltage of 12mV, at a current of 800nA.

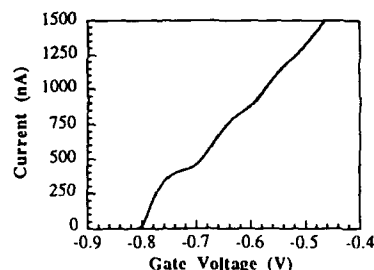


Fig. 3. Quantized conductance at a drain bias of 6mV.

### 3. CONCLUSIONS AND ACKNOWLEDGEMENTS

The ballistic constriction devices presented here exhibit conductance plateaus at 30K, the highest temperature reported for this type of device. In addition, by limiting inter-subband scattering, the large subband separation allows greater drain bias voltages than previously possible. Through a careful design to maximize the subband separations, the performance of these devices can be greatly enhanced.

This work was supported by the National Science Foundation under the QUEST Science and Technology Center, and was performed in part at the National Nanofabrication Facility which is supported by the National Science Foundation under Grant ECS-8619049, Cornell University, and industrial affiliates.

### REFERENCES

- K. Ismail, D.A. Antoniadis, and H. Smith 1989 *Appl. Phys. Lett.* 54 1130
- T.L. Cheeks, M.L. Roukes, A. Scherer, and H.G. Craighead 1988 *Appl. Phys. Lett.* 53 1964
- B.J. van Wees, H. van Houten, C.W.J. Beenakker, J.G. Williamson, L.P. Kouwenhoven, D. van der Marel, and C.T. Foxen 1988 *Phys. Rev. Lett.* 60 848
- D.A. Wharam, T.J. Thornton, R. Newbury, M. Pepper, H. Ahmed, J.E.F. Frost, D.G. Hasko, D.C. Peacock, D.A. Ritchie, and G.A.C. Jones 1988 *J. Phys. C* 21 L209
- G.L. Snider, I-H. Tan, and E.L. Hu 1990 *J. Appl. Phys.* 68 5922
- M. J. Rooks, G. Snider, E. Hu, C. C. Eugster, J.A. del Alamo 1990 *Materials Research Society Meeting*, Boston, MA

## Conductance oscillations in a quantum point contact of high-mobility hole gas

M. Noguchi, K. Hirakawa and T. Ikoma

Institute of Industrial Science, University of Tokyo

**ABSTRACT:** We have observed for the first time a conductance oscillation against gate voltage in a quantum point contact formed in a MBE grown p-type AlGaAs/GaAs heterostructure. The channel conductance, however, showed a monotonic increase with a threshold when increasing source-to-drain voltage. To explain this oscillation and the threshold behavior, examined are four models, which require potential fluctuations induced by residual impurities or defects near the channel. We also showed that potential fluctuations induced by remote dopants are relatively small because of the short screening length of a hole gas.

In quantum point contacts, many interesting physical phenomena have been observed, including conductance quantization (van Wees et al. 1988), resonant tunneling or single electron tunneling (Brown et al. 1990, Meirav et al. 1990). However, most of them have been made by using two-dimensional electron gas and no reports are available on a hole-gas quantum point contact. A two dimensional hole gas has some interesting features as compared with an electron gas because it has a larger effective mass and shorter screening length. Moreover, the valence band in a two dimensional structure becomes complex because of the band mixing and it makes an analysis of experimental observations very difficult.

As an example, a larger effective mass is advantageous for single carrier tunneling to be observed at higher temperatures, since the upper limit of temperature for single carrier tunneling in a quantum dot structure with a diameter  $l$  is given by  $k_B T \ll e^2/2C^*$ , where  $C^*$  is an effective capacitance given by  $C^* \sim C/(1 + e^2/2me^2l)$  (Pasquier et al. 1991) when the Pauli repulsion is taken into account. Furthermore, the single particle energy separation,  $\Delta E = \pi \hbar^2/m l^2$  should be smaller than  $k_B T$ . The shorter screening length also reduces possible potential fluctuations in a channel. All these make a hole-gas quantum point contact worthy being tested, although it is rather difficult to obtain a high-mobility hole gas.

In this work, we fabricated for the first time point contacts by using a high-mobility hole gas in a p-type AlGaAs/GaAs hetero-structure, and observed periodic conductance-oscillations as a function of gate voltage. A possible origin of oscillations and a source of potential fluctuations are discussed in this paper.

An AlGaAs/GaAs single-heterostructure was grown by molecular beam epitaxy (MBE) on a semi-insulating GaAs (100) substrate. A 0.9  $\mu\text{m}$ -thick undoped GaAs buffer layer was grown first, followed by a 20 nm-thick undoped  $\text{Al}_{0.5}\text{Ga}_{0.5}\text{As}$  spacer layer, a 40 nm-thick Be-doped  $\text{Al}_{0.5}\text{Ga}_{0.5}\text{As}$  layer, and a 5 nm-thick Be-doped GaAs cap. The Be-doping level in the  $\text{Al}_{0.5}\text{Ga}_{0.5}\text{As}$  layer was  $4 \times 10^{17} \text{ cm}^{-3}$ . In order to avoid Be-diffusion, the growth temperature

was rather low of  $\sim 550$  °C. In this selectively-doped structure, we achieved a carrier density of  $2.3 \times 10^{15} \text{ m}^{-2}$  and a mobility of  $3.5 \text{ m}^2/\text{Vs}$  at 1.6 K. The point contact structures were separated by wet mesa-etching and ohmic contacts to the hole gas were made by evaporation and alloying of AuZn. Au-metal split-gates were fabricated by the electron beam lithography and the lift-off technique with a polymethyl methacrylate (PMMA) resist. The point contact orifice was designed to be  $0.4 \mu\text{m}$  in width and  $0.15 \mu\text{m}$  in length.

The two-terminal conductance was measured at temperatures from 1.6 to 4.2 K by using a lock-in amplifier with AC current of  $0.2 \text{ nA}$  at  $30\text{--}40$  Hz. Before the measurement, the sample was illuminated to reduce the resistance of the ohmic contacts.

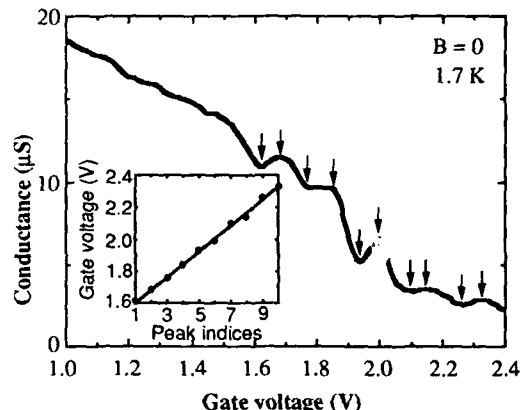


Fig. 1. Typical conductance oscillation in a p-type point contact. Inset: gate voltages at which the conductance shows peaks vs. peak indices.

Figure 1 shows a conductance observed in a p-type point contact as a function of the gate voltage,  $V_{GS}$ . For  $V_{GS}$  higher than 1.6 V, a conductance oscillation was observed reproducibly. In the inset of Fig. 1, the gate voltages that give the conductance peaks are plotted as a function of the peak indices. These points fall on a line within an experimental error, suggesting that the conductance oscillation is periodic for the gate voltage. When the sample was cycled between 1.6 K and room temperature, this oscillation period for the gate voltage did not change remarkably, although the oscillation amplitude changed. In addition, the conductance range where the oscillation was observed was always smaller than the single channel conductance per spin,  $e^2/h$ . For possible origins of such conductance oscillation, we point out the following four models which are known so far; the quantum interference effect of an electron which passes through a few different paths (Yacoby et al. 1991), the resonant tunneling (de Aguiar et al. 1991), the single carrier tunneling (van Houten et al. 1989), and the pinning of a charge density wave (CDW) (Field et al. 1990). For any of those

models, a source of conductance oscillation is potential fluctuations in a saddle-shaped potential formed by a narrow orifice of the point contact. The potential fluctuations should have at least two potential barriers and a potential dip.

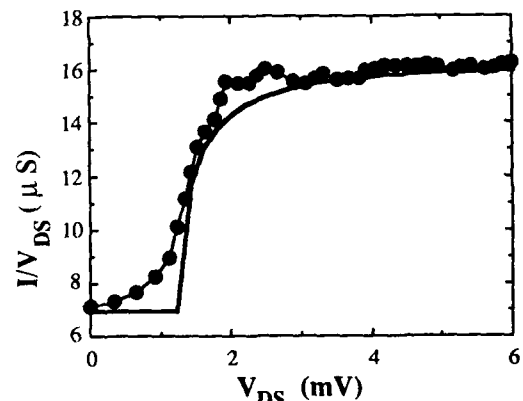


Fig. 2. Channel conductance as a function of "source to drain" DC voltage. The broad solid line shows the calculation based on the depinning charge-density wave.

Figure 2 shows a channel conductance as a function of "source-to-drain" DC voltage,  $V_{DS}$ .  $V_{GS}$  was set to be between the first conductance minimum and the second conductance maximum which were measured from a gate voltage where the channel was fully depleted. The channel conductance showed a single-threshold behavior and observed was neither oscillating

nor multiple-staircase voltage-current characteristic, which is a feature for the resonant tunneling or a single carrier tunneling (Brown et al. 1990). Furthermore, the threshold voltage of 1.2 mV is different from 0 V which is expected in a decay of the multiple paths' quantum interference, and the current near the threshold voltage was not proportional to  $(V_{DS})^3$ , as Pasquier et al. (1991) observed in an island structure separated from leads by tunneling barriers. On the other hand, when a pinning of CDW by potential fluctuations is assumed to cause the conductance oscillation, the  $V_{DS}$ -dependence is considered to be due to the depinning (Field et al. 1990, Grüner 1988). Then, by using the formula given by Grüner (1988), we can calculate the channel conductance as a function of  $V_{DS}$ , which is shown in Fig. 2 by a broad solid curve. The result is close to the observation; however, the threshold character is not so sharp as the predicted. Furthermore, the oscillation was observed up to 4.2 K, which might be higher than the expected upper limit of existence of a CDW. Therefore, at this moment any clear determination as for the most appropriate model is not possible only from the present experimental observation.

When the temperature was raised, the oscillation period did not change but the conductance minima increased more rapidly than the maxima, and as a result, the amplitude of the oscillation decreased monotonically. The oscillation was observable even at 4.2 K. This indicates that the height of barriers which cause the conductance oscillation should be in the order of the magnitude of the half width of the thermal smearing in the Fermi-Dirac distribution at 4.2 K, which is 0.7 meV. A possible source to induce such potential fluctuations is either doped impurities (Be in this case) in the AlGaAs layer, or residual impurities or defects at the vicinity of the GaAs channel, or both of them. To clarify effects of doped impurities remotely located from the channel, we calculated potential fluctuations in a one- and two-dimensional hole gases due to a random distribution of the remote-doped impurities. In the calculation, the variance of potential fluctuations in a hole gas generated by remote impurities located at 43 nm on average from the interface was summed up over  $0.2 \mu\text{m} \times 0.2 \mu\text{m}$  square in plane, and the screening effect was also taken into account in both one- and two-dimensional cases (Davies et al. 1989, Rorison et al. 1988). Figure 3 shows the mean deviation of potential fluctuations as a function of the areal hole density. (for the one dimensional case a line density is squared to be plotted on the same scale as in the two dimensional case.) The small screening length ( $\leq 1 \text{ nm}$ ) of a hole gas leads to small potential fluctuations of less than 0.7 meV for the carrier density of  $10^{14} \sim$

$1 \times 10^{15} \text{ m}^{-2}$ , and this value is not larger than the experimental potential fluctuations. This result suggests that the effect from remote impurities is relatively small and a few residual impurities, defects induced by electron-beam exposure, or interface defects at the vicinity of the channel are more important to induce potential fluctuations. This is also consistent with the observation that the conductance oscillation disappeared after a high voltage of 0.3 V was applied to the channel, while the device showed the same over-all voltage-current characteristic; residual impurities or the defects might move

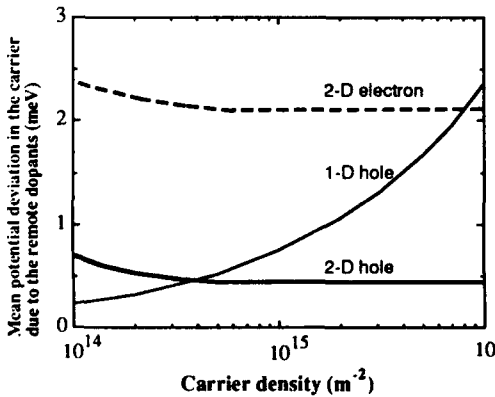


Fig. 3. Mean deviation of the potential due to random distribution of remote impurities.

Furthermore, the oscillation did not remarkably change with a thermal cycling up to 77 K and under magnetic fields up to 1.16 T (see Fig. 4). This means that the potential distribution in the

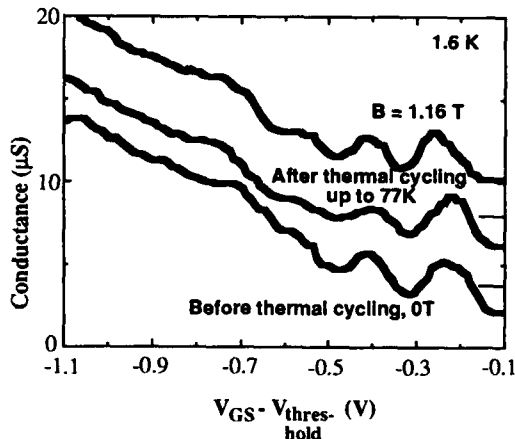


Fig. 4. Thermal cycling and magnetic field effects dip which are necessary potential shapes for on conductance oscillations. The magnetic field is a conductance oscillation to be observed. perpendicular to the two-dimensional hole gas.

In conclusion, we have observed for the first time a conductance oscillation against gate voltage in a quantum hole point contact made in an MBE grown p-type AlGaAs/GaAs hetero-structure. The channel conductance, however, showed a monotonic increase as a function of "source to drain" DC voltage with a threshold field. To explain this oscillation and the threshold behavior, we considered four different models, all of which requires potential fluctuations. We also showed that potential fluctuations induced by remote dopants are relatively small because of the short screening length of a hole gas, and pointed out the importance of residual impurities and defects at the vicinity of the channel.

We wish to express our sincere thanks to Professor Y. Iye and Professor H. Sakaki for extending us to transport measurements at low temperature and kind instruction. One of the authors (M. N.) thanks the Japan Society for the Promotion of Science and JEIDA for financial support in part. This work is partly supported by the Grand-in-Aid from the Ministry of Education, Science, and Culture, Japan and also by the Industry-University Joint Research Program "Mesoscopic Electronics".

Brown R J, Pepper M, Ahmed H, Hasko D G, Ritchie D A, Frost J E F, Peacock D C, and Jones G A C 1990 *J. Phys. Condens. Matter* **2** 2105.  
 Davies H A and Nixon J A 1989 *Phys. Rev. B* **39** 3423.  
 De Aguiar F M, Wharam D A, Heinzel T, Lorke A, and Kotthaus J P 1991 *Proc. of the 9th EP2DS-9* 794.  
 Field S B, Kastner M A, Meirav U, Scott-Thomas J H F, Antoniadis D A, Smith H I, and Wind S J 1990 *Phys. Rev. B* **42** 3523.  
 Groshev A, Ivanov T and Valtchinov V 1991 *Phys. Rev. Lett.* **66** 1082.  
 Grüner G 1988 *Rev. Mod. Phys.* **60** 1152.  
 Meirav U, Kastner M A, and Wind S J 1990 *Phys. Rev. Lett.* **65** 771.  
 Pasquier C, Glattli D C, Meirav U, Williams F I B, Jin Y and Etienne B 1991 *Proc. of the 9th EP2DS-9* 448.  
 Rorison J M, Kane M J, Herbert D C, Skolnick M S, Taylor L L, and Bass S J 1988 *Semicond. Sci. Technol.* **3** 12.  
 Van Houten H and Beenakker C W J 1989 *Phys. Rev. Lett.* **63** 1893.  
 Van Wees B J, van Houten H, Beenakker C W J, Williamson J G, Kouwenhoven L P, van der Marel D, and Foxon C T 1988 *Phys. Rev. Lett.* **60** 848.  
 Yacoby A, Sivan U, Umbach C P, and Hong J M 1991 *Phys. Rev. Lett.* **66** 1938.

channel did not vary with the thermal cycling or applying magnetic field, since the oscillation should strongly correlate with the distance between potential barriers or pinning centers (Field et al. 1990) and the pathlength difference for the quantum interference. It should be noted that a main residual impurity in an MBE-grown (100) GaAs is carbon, which is ionized to form negatively charged centers or an attractive potential for holes. In a saddle-shape potential formed by the split-gate, only one negatively charged center is sufficient to make two potential barriers and one potential

## Spectroscopy of quantum-dot atoms and antidot arrays

D. Heitmann, B. Meurer, K. Kern, P. Grambow, K. Ploog, and Y.H. Zhang  
Max-Planck-Institut für Festkörperforschung  
Heisenbergstr. 1, 7000 Stuttgart 80, Germany

**ABSTRACT:** Advances in submicron technology make it possible to realize man-made low-dimensional electronic systems with quantum confined energy states, i.e., quantum wires, quantum dots and antidots. With typical confinement energies in the meV regime far-infrared spectroscopy gives a direct access to the quantum confined energy levels in these systems. One is now approaching the limit to prepare quantum dots with well defined small numbers of electrons per dot,  $N = 1, 2, 3, \dots$ . It becomes thus possible to perform a kind of 'atomic' spectroscopy on these systems. We will show in this review that the dynamic excitations in these systems exhibit a very interesting complex interplay of atomic-like single-particle and collective many-body effects.

### 1. INTRODUCTION

Progress and success of physics in layered two-dimensional (2D) semiconductor structures with quantum confined energy states has challenged many scientists to prepare and study systems with further reduced dimensionality, specifically quantum wires, quantum dots and antidots. In these systems the original free dispersions of the electrons in the lateral directions are also quantized due to an additional lateral confinement. One ultimate limit is a quantum dot, where, induced by a confining potential in both the  $x$ - and  $y$ -directions, artificial 'atoms' with a totally discrete energy spectrum, are formed.<sup>1-8</sup> (The growth direction is labeled  $z$  in the following.) A reversed structure with respect to dots are 'antidots' where 'holes' are 'punched' into a 2D electron system (2DES).<sup>9-12</sup> The most direct information on the quantum confined energy levels in these low-dimensional systems should be obtained by investigation of optical transitions with far-infrared (FIR) spectroscopy. It turns out that the dynamic response of these systems exhibits an interesting complex interplay of atomic-like single-particle and many-body effects which will be discussed by reviewing some recent experiments on quantum dots and antidots. Within the allowed space we can only give a very brief description and a short list of references. For more information we refer to the original papers and more extended reviews (e.g. Ref.<sup>13</sup>).

### 2. QUANTUM-DOT ATOMS

Quantum-dot structures have been prepared by etching techniques<sup>1,5</sup> or field-effect confinement<sup>2-4,6-8</sup>. Field-effect confined quantum dots, which can be prepared starting from a modulation-doped  $AlGaAs/GaAs$  heterostructure, are sketched in Fig. 1a. Electrons are laterally confined by a gate voltage which is applied to a  $NiCr$ -gate with varying distance to the originally 2DES. For strong negative gate voltages the carriers are depleted in the regime with the smaller distance leaving isolated quantum dots. The gate-distance modulation is achieved by a periodically modulated photoresist layer. For our structures<sup>8</sup>, a low impedance  $\delta$ -doped layer serves as a back-contact to charge the isolated dots. This  $\delta$ -layer has a low electron concentration and impedance so that it is semi-transparent for FIR radiation.

FIR experiments were performed in superconducting magnet-cryostats, which were connected with waveguide systems to Fourier transform spectrometers or FIR lasers. The transmission  $T(B)$  of unpolarized FIR radiation through the sample was measured in magnetic fields,  $B$ , oriented normal to the surface of the sample. The temperature was  $2.2K$ . In Fig. 2a we show FIR laser transmission spectra on a field-effect confined quantum-dot array in an  $AlGaAs/GaAs$  heterostructure (Fig. 1a) with a period of  $a = 200nm$ . The active size of the array was 4mm in

diameter, so we measure about  $10^8$  dots in parallel. The spectrum exhibits one pronounced resonance. The integrated absorption strength increases significantly with increasing gate voltage  $V_g$ , the resonance position, however, does not depend strongly on  $V_g$ . In Fig. 2b we have plotted the  $B$ -dispersions of the observed resonance positions. The excitation spectrum consists of two branches, a low frequency branch with a negative  $B$ -dispersion and a high frequency branch which approaches, at large  $B$ , the cyclotron frequency  $\omega_c = eB/m^*$ .

These dispersions cannot only be observed in quantum dots with a small number of electrons<sup>3</sup>, but similarly also in finite-sized 2DES with much larger dimensions and electron numbers<sup>14-16</sup>. These latter experiments have been interpreted as depolarisation, or, equivalently, as edge magnetoplasmon modes.<sup>17-20</sup> We can explain this behavior starting from two different models: (i) transitions in an 'atom' including collective effects, and (ii) from classical plasmon type of excitations in a 2DES of finite size.

For an 'atomic' model we need information about the confining potential. Self-consistent band-structure calculations show that the external confinement potential for electrons in a field-effect confined quantum dot has a nearly parabolic shape.<sup>21</sup> In a simplified way we can see this from the model sketched in Fig. 1b. Due to the strong original 2D confinement the electron can only move in the x-y-directions. A positively charged layer of 2D density  $N_s$  and width  $w$  of donors in the  $AlGaAs/GaAs$  layer or, in a gated structure, from a gate voltage, holds the electron in an equilibrium position. Moving the electron in the x-direction produces a force approximately linear in the elongation,  $F = Kx$ , which gives rise to a parabolic confinement potential  $V(x) = \frac{1}{2}Kx^2$ . We can calculate the force constant  $K$  and thus the eigenfrequency  $\Omega_0^2 = K/m^*$  by integrating the electric fields from the charged layer at the position of the electron and find approximately  $\Omega_0^2 = N_s e^2 \pi / 2m^* \epsilon_0 w$  where we have assumed that the distance  $d$  in Fig. 1b is small and the dielectric surrounding is described by an effective dielectric function  $\epsilon$ .

Now we consider the one-electron Schrödinger equation in a magnetic field  $B$  for the potential  $V(r) = \frac{1}{2}m^* \Omega_0^2 r^2$ . The energy eigenvalues have been calculated by Fock<sup>22</sup>

$$E_{n,\ell} = (2n + |\ell| + 1) \cdot \sqrt{(\hbar\Omega_0)^2 + (\hbar\omega_c/2)^2} + \ell \cdot \hbar\omega_c/2 \quad (1)$$

where  $n = 0, 1, 2 \dots$  and  $\ell = 0, \pm 1, \pm 2 \dots$  are, respectively, the radial and azimuthal quantum numbers. From calculations of the matrix elements one finds that dipole allowed transitions have transition energies

$$\Delta E^\pm = \sqrt{\hbar^2\Omega_0^2 + (\hbar\omega_c/2)^2} \pm \hbar\omega_c/2. \quad (2)$$

This dispersion is exactly observed in our experiments as demonstrated by the fit in Fig. 2b.

However, we do not have only *one* electron in a quantum dot, but several. In this case electron-electron (ee) interaction should strongly influence the energy spectrum and the dynamic response. For a large number of electrons one usually calculates the static effective one-electron

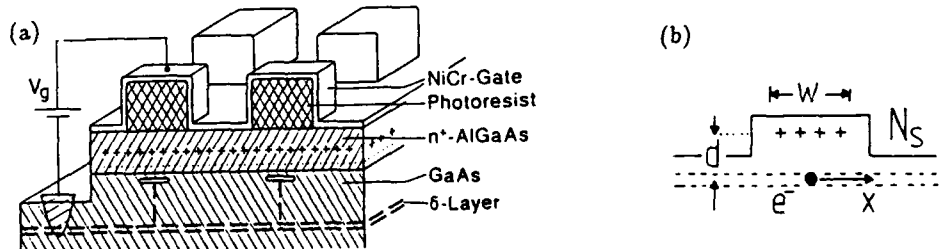


Fig. 1: (a) Sketch of field-effect confined quantum-dots in an  $AlGaAs/GaAs$  heterostructure. (b) A model to calculate the lateral confinement potential for electrons in a quantum dot.

energy spectrum within the Hartree-Fock approximation and then applies the RPA to determine the dielectric response. For a small number of electrons per dot, however, it is possible to calculate many-electron wavefunctions and energy states directly.<sup>23-26</sup> In Fig. 3 we compare the one-particle energy spectrum with the two-particle energy spectrum in a parabolic confinement.<sup>25,26</sup> The many-body energy spectrum is governed by two energies: the quantum confinement energy,  $E_q = \hbar^2/(m^*l_0^2)$ , and the Coulomb energy,  $E_c = e^2/(4\pi\epsilon\epsilon_0 l_0)$ . Here  $l_0 = \sqrt{\hbar/m^*\Omega_0}$  is the confinement length of the harmonic oscillator. With increasing  $l_0$  the Coulomb energy becomes increasingly important with respect to the confinement energy. The scale is set by the effective Bohr radius  $a^*$  which is 10nm in GaAs. In Fig. 3 with  $E_q = 3.4\text{meV}$  and correspondingly  $l_0 = 20\text{nm}$ , the Coulomb energy is  $E_c = 7\text{meV}$ .  $E_c$  reflects the energy which is required to 'squeeze' the second electron into the quantum dot. This energy is represented in Fig. 3 in the increase of the lowest energy level of the two-particle spectrum with respect to the one-particle spectrum. Due to the ee-interaction some of the degeneracies of the one-particle spectrum are now lifted giving rise to a complex excitation spectrum.

The unique and important point of a parabolic confinement is, however, that the only allowed dipole transition ( $\hbar\omega_r$  in Fig. 3) for two electrons has exactly the same energy as in the one-particle case. Moreover, this result also holds for an arbitrary number of electrons,  $N$ . It has been shown for quantum wells<sup>27,28</sup> and quantum dots<sup>24</sup> with parabolic confinement, that the Hamiltonian for  $N$  electrons, i.e., including ee-interaction, separates into a center-of-mass (CM) motion and into relative internal motions. The CM motion solves exactly the one-electron Hamiltonian and is the only allowed optical dipole excitation. Thus, the optical dipole response of a quantum dot with parabolic confinement represents a rigid collective CM excitation at the frequency of the bare external potential, i.e., for  $B = 0$ , at  $\hbar\Omega_0$ . This also means that for a parabolic confinement, dipole excitation frequencies are insensitive to ee-interactions and independent on the electron density in the dot. This result can be considered as a generalisation of Kohl's famous theorem<sup>29</sup> which says that the cyclotron frequency in a translationally invariant system is not influenced by ee-interactions. Experimentally this theorem is demonstrated by the small effect of the gate voltage and related number of electrons on the resonance position in Fig. 2a and it has also been observed by Sikorski and Merkt<sup>3</sup>. Theoretically the same conclusion has also been drawn from a classical description of an electron system in a parabolic confinement by Shikin et al<sup>17</sup>. The quantum mechanical CM motion corresponds exactly, as we will see below, to the classical dipole plasma mode of the quantum dot.

It is now the challenge for the experimentalist to realize quantum dot arrays with small numbers

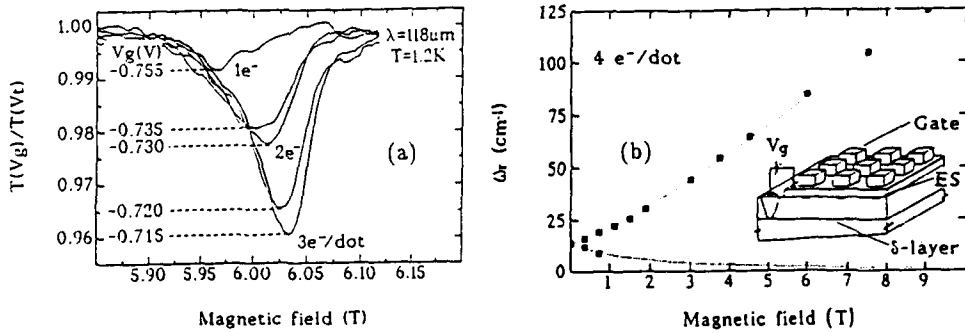


Fig. 2a: FIR transmission of a field-effect confined quantum-dot array measured at a fixed laser frequency of 10.5 meV in a sweep of the magnetic field  $B$ . From the absolute integrated absorption strength we can determine an incremental charging of the dots with  $N = 1, 2, 3$  electrons. The inset shows the dot structure schematically. In (b) we have plotted the experimental  $B$ -dispersions of the resonance frequency for a gate voltage where the dots are occupied with  $N = 4$  electrons. The full lines are fits with the theoretical dispersions (eq.(2)). (From Ref.<sup>8</sup>).

of electrons per dot to test such theoretical predictions. Indeed, recently we have prepared field-effect confined quantum dot arrays with well defined numbers of electrons in each individual dot,  $N = 1, 2, 3$  and  $4$ .<sup>8</sup> The FIR transmission experiments on a field-effect confined quantum-dot array (Ref.<sup>8</sup> and Fig. 2a) show a stepwise increase of the integrated absorption strength in its dependence on the gate voltage  $V_g$  indicating directly the incremental charging of each individual of the  $10^8$  dots in the array with successively  $N = 1, 2, 3, \dots$  electrons. The important aspect of this work was to prepare very small quantum dots with a high Coulomb charging energy. The Coulomb charging energy is the energy which is required to add one additional electron into the dot. If this energy is larger than the local fluctuations of the threshold voltage, which arises from randomly distributed ionized donors and impurities in the heterostructure, it stabilizes a well defined number of electrons in a dot. This Coulomb energy can be estimated from the charging characteristic. We find that it takes about  $\Delta V_g = 30$  mV increase in the gate voltage to increase the number of electrons per dot from  $N = 2$  to  $N = 3$ . This determines a capacitance  $C = e/\Delta V_g = 5 \cdot 10^{-18}$  F and a Coulomb energy  $E_c = e^2/2C = 15$  meV. The Coulomb energy for the transition from one to two electrons can be estimated in Fig 3 from the increase of the two-particle energy with respect to the one-particle energy. It is  $E_c = e^2/(4\pi\epsilon\epsilon_0 l_0)$  and thus about 7 meV for dots with 3 meV confinement energy. This is of the same order as estimated from the experiments. Coulomb effects are in the moment extensively studied in transport measurements on small metallic or semiconductor systems. The Coulomb islands in these experiments, contain a large number of electrons, which is not known absolutely. The experiments only indicate if this number is changed by one electron. Note that it is a unique property of our optical experiments that we can determine from the strength of the FIR absorption directly the absolute number of the electrons and, in principle, the dependence of the Coulomb energy on this number.

Since the FIR response of the quantum dots dominantly reflects the rigid CM motion and the response frequency becomes with increasing  $N$  significantly larger than the one-particle energy level separation<sup>21</sup>, we can also approach the dynamic excitations of dots from a classical plasmon type of excitation. A simple way is to assume a disk-like 2DES with 2D density  $N_s$  and radius  $R$  and start from linear edge plasmons, i.e., excitations which exist at an edge of a semi-infinite 2DES (e.g. Refs.<sup>17-20</sup>). These excitations have the dispersion  $\omega_{ep}^2 = 0.81\omega_p^2(q)$  where  $\omega_p^2(q) = N_s e^2 q / 2m^* \epsilon_0 \epsilon$  is the 2D plasmon frequency. For a disk the circumference quantises the wave-vectors in values  $q_i = i/R$  ( $i = 1, 2, \dots$ ). For  $B = 0$  we thus have

$$\omega_{0i}^2 = 0.81 N_s e^2 i / 2m^* \epsilon_0 \epsilon R. \quad (3)$$

In a magnetic field one calculates a set of double branches

$$\omega_{i\pm} = \sqrt{\omega_{0i}^2 + (\omega_c/2)^2} \pm \omega_c/2 \quad (4)$$

The prefactor 0.81 in (3) and the spacings of higher modes depend slightly on the modeling of the electron density profile. Note that the  $B$ -dispersion of the lowest modes ( $i = 1$ ) exactly agrees with the quantum mechanical result (2). In the classical model and with increasing  $B$  the  $\omega_{i+-}$  resonances correspond to cyclotron type excitations of the electrons. The  $\omega_{i--}$  modes represent

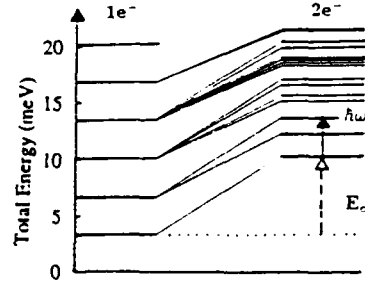


Fig. 3: The one-particle energy spectrum and the two-particle excitation spectrum ('quantum-dot-He') in a parabolic confinement.<sup>26</sup> The indicated dipole allowed transition ( $\hbar\omega_r$ ) for quantum-dot-He has exactly the same energy as for quantum-dot-H.

edge magnetoplasmon modes where the individual electrons within the collective excitation perform skipping orbits along the edge of the dot. Within this classical model we can also explain the FIR response of antidots which will be discussed in the next paragraph.

### 3. ANTIDOT ARRAYS

Antidot samples have been prepared by deep-mesa-etching starting from 2DES in modulation-doped  $\text{GaInAs} - \text{AlInAs}$  single quantum wells which have been grown lattice matched on semi-isolating InP substrates by molecular beam epitaxy.<sup>12</sup> A photoresist grid mask was prepared by a holographic double exposure and arrays of holes with typical diameters  $2r_g = 100$  to  $200\text{nm}$  were etched  $100\text{nm}$  deep, i.e., through the active layer into the buffer (Fig. 4b). The period in both lateral directions was  $a = 300\text{nm}$ . The InGaAs system has the advantage of a small lateral edge depletion ( $l_{\text{depl}} < 30\text{nm}$ ) at the etched side walls of the holes. The electronic radius  $r_e$  around a hole is thus not much larger than the geometrical radius of the etched hole  $r_g$ .

In a perpendicular magnetic field  $B$  two resonances dominate the experimental transmission spectra. The dispersions of these resonances are shown in Fig. 4a for an antidot sample with a period  $a = 300\text{nm}$ , a hole diameter  $2r_g = 200\text{nm}$  and carrier density  $N_s = 8 \cdot 10^{11}\text{cm}^{-2}$ . The two modes, a high and a low frequency branch, are labeled by  $\omega_+$  and  $\omega_-$ , respectively. We interpret these modes in the following way. At high  $B$  the dispersion of both branches resembles the excitation spectrum of quantum dots which we have discussed above. For dots the lower branch decreases with  $B$  in frequency and represents an edge magnetoplasmon mode at high  $B$ . In dots the individual electrons of this collective mode perform skipping orbits along the inner boundary of the dot. For antidots the individual electrons within the collective excitation perform skipping orbits *around* the hole. We have sketched these orbits for high  $B$ ,  $\omega_-^h$ , in Fig. 4c. With decreasing  $B$ , the resonances of the low frequency branch,  $\omega_-$ , first increase in frequency, but then, in contrast to dots, these resonances decrease in frequency at a certain magnetic field and approach  $\omega_c$ . This arises since with decreasing  $B$  the electron orbits of the  $\omega_-$ -mode become larger and eventually the electrons can perform classical cyclotron orbits  $r_c = \sqrt{2\pi N_s \hbar / e B}$  around a hole. Then the collective edge magnetoplasmon excitation gradually changes into a classical cyclotron excitation. We have estimated the critical value  $B_c \approx \sqrt{2\pi N_s \hbar / e r_g}$ , where the classical cyclotron radius  $r_c$  becomes equal to the radius of the holes  $r_g$ , and find, for the sample discussed in Fig. 4a,  $B_c \approx 1\text{T}$ . This is indeed the regime where the resonance frequency is close to  $\omega_c$  and the edge magnetoplasmon mode has changed

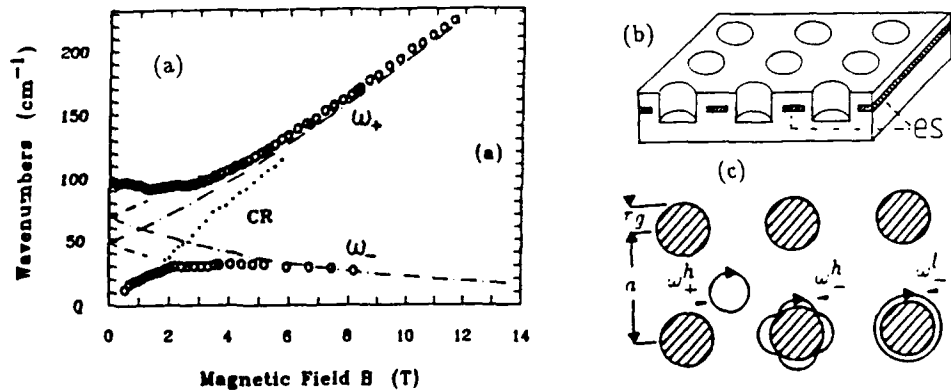


Fig. 4: (a) The experimental dispersions for an  $\text{GaInAs}/\text{AlInAs}$  antidot sample with hole diameters  $2r_g = 200\text{nm}$ . The period is  $a = 300\text{nm}$ . (b) Sketch of the antidot structure. Geometrical holes are punched into an originally 2DES. (c) shows schematically the motions of individual electrons within the collective excitation for the high-frequency mode ( $\omega_+^h$ ) at high magnetic fields and for the low-frequency mode at low ( $\omega_-^l$ ) and at high magnetic field ( $\omega_-^h$ ). The hatched areas are the geometrical holes. (From Ref.<sup>12</sup>.)

to a classical CR motion around the hole. In particular we find that for samples with smaller hole diameter and/or larger  $N_s$ , where we have a larger value of  $B_c$ , the deviations from  $\omega_c$  occur at higher  $B$ .<sup>12</sup> The high frequency  $\omega_+$ -mode increases in intensity with increasing  $B$ . It represents at higher fields, where the  $\omega_+$ -branch approaches  $\omega_c$ , a cyclotron type of excitation in the region between the holes as denoted in Fig. 4c by  $\omega_+^h$ . A unique behavior is that, at small  $B$ , this resonance shows a weak, but distinct negative  $B$ -dispersion which was observed on all our samples where we were able to evaluate the resonance position down to  $B \approx 0$ . This indicates that it represents a kind of 1D plasmon<sup>30</sup> that propagates with a wave vector  $q = 2\pi/a$  along charged stripes between the geometrical holes.

We are grateful for stimulating discussions with R.R. Gerhardts, U. Merkt and D. Pfannkuche, thank J. Behring, A. Fischer, C. Lange, R. Nötzel, M. Riek and E. Vasiliadou for expert help and acknowledge financial support from the 'Bundesministerium für Forschung und Technologie'.

#### REFERENCES

- <sup>1</sup>M.A. Reed, J.N. Randall, R.J. Aggarwal, R.J. Matyi, T.M. Moore, and A.E. Wetsel, *Phys. Rev. Lett.* **60**, 535 (1988)
- <sup>2</sup>W. Hansen, T.P. Smith III, K.Y. Lee, J.A. Brum, C.M. Knoedler, J.M. Hong, and D.P. Kern, *Phys. Rev. Lett.* **62**, 2168 (1989)
- <sup>3</sup>Ch. Sikorski and U. Merkt, *Phys. Rev. Lett.* **62**, 2164 (1989)
- <sup>4</sup>C.T. Liu, K. Nakamura, D.C. Tsui, K. Ismail, D.A. Antoniadis, and H.I. Smith, *Appl. Phys. Lett.* **55**, 168 (1989)
- <sup>5</sup>T. Demel, D. Heitmann, P. Grambow, and K. Ploog, *Phys. Rev. Lett.* **64**, 788 (1990)
- <sup>6</sup>J. Alsmeyer, E. Batke, and J.P. Kotthaus, *Phys. Rev. B* **41**, 1699 (1990)
- <sup>7</sup>A. Lörke, J.P. Kotthaus, and K. Ploog, *Phys. Rev. Lett.* **64**, 2559 (1990)
- <sup>8</sup>B. Meurer, D. Heitmann, and K. Ploog, submitted
- <sup>9</sup>K. Ensslin and P.M. Petroff, *Phys. Rev. B* **41**, 12307 (1990)
- <sup>10</sup>D. Weiss, K. von Klitzing, and K. Ploog, *Surface Sci.* **229**, 88 (1990)
- <sup>11</sup>A. Lörke, J.P. Kotthaus, and K. Ploog, *Superlattices and Microstructures* **9**, 103 (1991)
- <sup>12</sup>K. Kern, D. Heitmann, P. Grambow, Y.H. Zhang, and K. Ploog, *Phys. Rev. Lett.* **66**, 1618 (1991)
- <sup>13</sup>D. Heitmann, K. Kern, T. Demel, P. Grambow, K. Ploog, and Y.H. Zhang, *Surface Sci.* (1990), in press
- <sup>14</sup>S.J. Allen, Jr., H.L. Störmer, and J.C. Hwang, *Phys. Rev. B* **28**, 4875 (1983)
- <sup>15</sup>D.C. Glattli, E.Y. Andrei, G. Deville, J. Poitrenaud, and F.I.B. Williams, *Phys. Rev. Lett.* **54**, 1710 (1985)
- <sup>16</sup>D.B. Mast, A.J. Dahm, and A.L. Fetter, *Phys. Rev. Lett.* **54**, 1706 (1985)
- <sup>17</sup>V. Shikin, T. Demel, and D. Heitmann, *Surf. Sci.* **229**, 276 (1990)
- <sup>18</sup>A.L. Fetter, *Phys. Rev. B* **32**, 7676 (1985), *Phys. Rev. B* **33**, 5221 (1986)
- <sup>19</sup>V.B. Sandomirskii, V.A. Volkov, G.R. Aizin, and S.A. Mikhailov, *Electrochimica Acta* **34**, 3 (1989)
- <sup>20</sup>V. Shikin, S. Nazin, D. Heitmann, and T. Demel, *Phys. Rev. B* **43**, 11903 (1991)
- <sup>21</sup>A. Kumar, S.E. Laux, and F. Stern, *Phys. Rev. B* **42**, 5166 (1990)
- <sup>22</sup>V. Fock, *Z. Phys.* **47**, 446 (1928)
- <sup>23</sup>G.W. Bryant, *Phys. Rev. Lett.* **59**, 1140 (1987)
- <sup>24</sup>P. Maksym and T. Chakraborty, *Phys. Rev. Lett.* **65**, 108 (1990)
- <sup>25</sup>U. Merkt, J. Huser, and M. Wagner, *Phys. Rev. B* **43**, 7320 (1991)
- <sup>26</sup>D. Pfannkuche and R.R. Gerhardts, *Phys. Rev. B*, in press
- <sup>27</sup>L. Brey, N. Johnson, and P. Halperin, *Phys. Rev. B* **40**, 10647 (1989)
- <sup>28</sup>P. Ruden and G.H. Döhler, *Phys. Rev. B* **27**, 3547 (1983)
- <sup>29</sup>W. Kohn, *Phys. Rev.* **123**, 1242 (1961)
- <sup>30</sup>T. Demel, D. Heitmann, P. Grambow, and K. Ploog, *Phys. Rev. Lett.* **66**, 2657 (1991)

## Opto-electronics with n-i-p-i doping superlattices

G H Döhler

Institut für Technische Physik, Universität Erlangen-Nürnberg, Erwin-Rommel-Strasse 1, 8520 Erlangen, FRG

**ABSTRACT:** Semiconductor superlattices composed of alternating n- and p-doped layers, possibly with interspersed intrinsic regions ("n-i-p-i" crystals) exhibit strongly enhanced recombination lifetimes and a wide range for (dynamical) tuning of the bandgap, the conductivity, the absorption coefficient, and the refractive index. In this paper we will discuss how these properties can be used for opto-electronics and present some recent results. Special emphasis will be given to advantages which result from the application of selective n- and p-type contacts.

### 1. INTRODUCTION

There is a wide variety of possibilities for tailoring periodic "n-i-p-i" structures by appropriately choosing the doping density  $n_D$  and  $n_A$  of the n- and p-doped layers, their thickness  $d_n$  and  $d_p$ , respectively, as well as the thickness of the intrinsic layers,  $d_i$  (see Figure 1). The effective bandgap  $E_g^{nipi}$  is always smaller than the gap of the host semiconductor  $E_g^0$  and the electron hole recombination lifetimes  $\tau^{nipi}$  are always enhanced compared with those of bulk semiconductors  $\tau^{bulk}$  due to the space charge potential of the ionized impurity atoms, which induces a spatial separation of electrons and holes ("indirect band gap in real space"). Also it is always possible to tune dynamically the electronic structure and the properties of n-i-p-i crystals by optical generation of excess electrons and holes or by their injection through "selective n- and p-type contacts", which reduce the space charge potential of the fixed impurity atoms. Depending on the choice of the design parameters, however, the lifetimes  $\tau^{nipi}$  may be determined by tunneling or by thermally activated electron hole recombination and the lifetime enhancement factors may acquire any value between close to unity and  $10^{10}$ . Similarly, the range of possible effective bandgaps can even include negative values, if the product of doping density and layer thickness becomes large enough ("n-i-p-i semi-metals"), provided that a reverse bias  $U_{pn}$  is applied between "selective ohmic contacts" to all the n- and to all the p-layers. Also the magnitude of the built-in space charge fields and the range of their tunability can be determined by appropriate choice of the design parameters. Finally, the properties can be modified further by combining the periodic n- and p doping with a periodic modulation of composition ("hetero - n-i-p-i crystals"). This enormous flexibility with regard to the tailoring of semiconductor properties is particularly appealing for applications in opto electronics. In the following three sections we

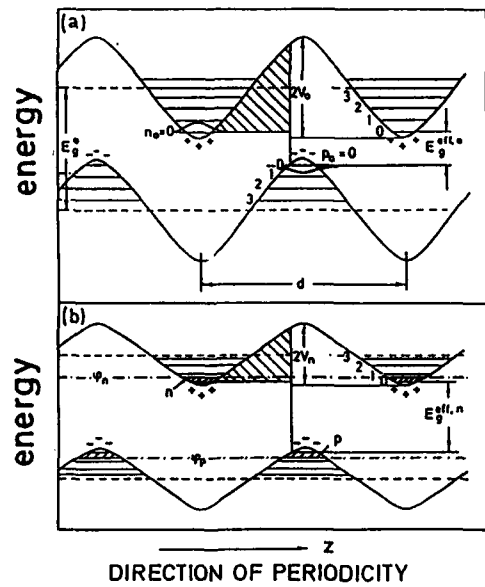


Fig. 1. Band diagram of a n-i-p-i structure. The "+" and "-" indicate the ionized donors and acceptors in the n- and p-layers, respectively. (a) ground state (b) excited state.  $\Phi_n$  and  $\Phi_p$  are the positions of the electron and hole quasi Fermi levels.

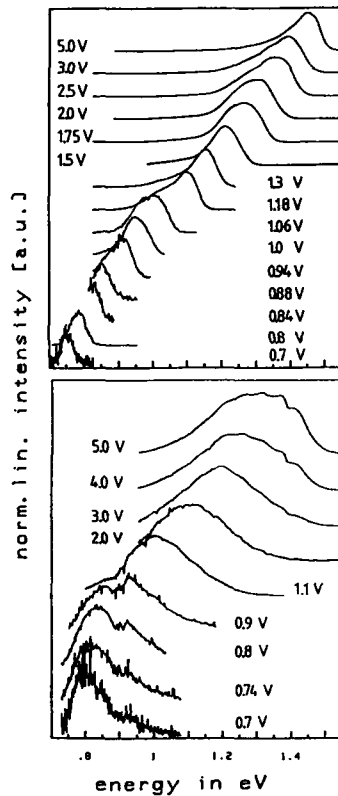


Fig. 2. Electroluminescence spectra of a n-i-p-i structure as described in the text, taken at 77K (upper part) and 300K (lower part)

will only sketch some electro optical, opto-electronic and purely optical ("opto optical") devices. For detailed discussions we refer to reviews on n-i-p-i crystals (Döhler 1986a, Döhler 1986b), on a recent review about their device applications (Döhler 1990), and to the original papers cited in the following sections.

## 2. ELECTRO-OPTICAL DEVICES

### 2.1. Tunable Light Emitters

n-i-p-i structures with high n- and p-doping level and not too thick layers are most suitable for tunable luminescence due to the (relatively) strong overlap between electron and hole subband wave functions. The electroluminescence spectra shown in Figure 2 (Renn 1991) demonstrate for a GaAs n-i-p-i structure with  $n_D = 4 \times 10^{18} \text{ cm}^{-3}$ ,  $n_A = 10^{19} \text{ cm}^{-3}$ ,  $d_n = 25 \text{ nm}$  and  $d_p = 35 \text{ nm}$ , that the position of the luminescence peak can be shifted over as much as one half of the band gap by variation of the voltage  $U_{np}$  applied between "in situ grown-in selective n- and p-contacts" (Döhler et al 1986). The shape of the spectra is in excellent agreement with theory if the disorder induced bandtailing is taken into account (Renn 1991).

Population inversion in n-i-p-i structures is possible at relatively low spontaneous recombination due to the enhanced carrier lifetimes. Recent calculations for  $\delta$  doped n-i-p-i structures yield rather broad tunable room temperature gain spectra with maxima of the order of  $100\text{cm}^{-1}$ . Tunable n-i-p-i lasers, emitting significantly below  $E_g^0$ , however, have not yet been reported.

## 2.2. n-i-p-i Modulators

The most important contributions to the excitation dependent changes of the dielectric function of a n-i-p-i structure are those due to field changes in the depleted regions (Franz Keldysh effect) and due to band filling in the central region of the doping layers (Döhler 1990). In Figure 3 the measured and calculated transmission changes through a  $2.6\mu\text{m}$  thick GaAs n-i-p-i structure with  $n_D = 1.3 \times 10^{18}\text{cm}^{-3}$ ,  $n_A = 1.7 \times 10^{18}\text{cm}^{-3}$ ,  $d_n = d_p = 60\text{nm}$  and  $d_i = 70\text{nm}$  for photon energies below the band gap are shown (Kiesel et al 1989). With a relatively small voltage sweep between  $-4.0$  and  $+0.8\text{V}$  the averaged absorption coefficient at  $\lambda = 892\text{nm}$  changes from  $400$  to  $2,300\text{cm}^{-1}$ , resulting in a 65% transmission change. The agreement between experiment and theory (with excitonic effects taken into account (Linder and Döhler 1989) is nearly perfect without using any adjustable parameter. The sample with selective contacts was grown with an improved epitaxial shadow mask technique (Wu et al 1992).

Improved performance of n-i-p-i modulators can be obtained if the intrinsic layer is replaced by a multiple quantum well (MQW) structure. For photon energies below  $E_g^0$  absorption changes between  $1,500$  and  $10,000\text{cm}^{-1}$  are expected for even smaller voltage sweeps. Promising results have already been obtained by optical modulation in samples without selective contacts (Kost et al 1988), (Ando et al 1989). Similarly, large absorption changes due to band filling in hetero n-i-p-i crystals have been reported by Larsson and Maserjian (1991).

By appropriate design of hetero n-i-p-i structures it is also possible to achieve a constructive superposition of the absorption changes due to field effects in the i regions and band filling in the central space charge regions (Döhler 1990).

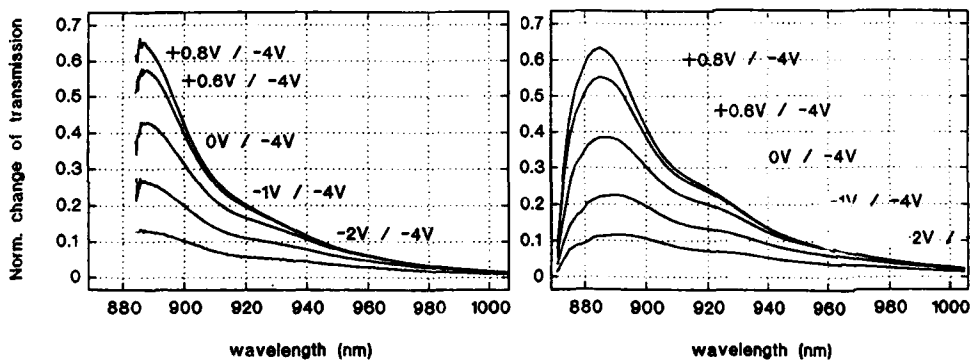


Fig. 3. Modulation of transmission through a n-i-p-i structure as described in the text. Left hand side: experiment; right hand side: theory.

## 3. OPTO ELECTRONIC DEVICES

## 3.1. Photoconductive Detectors

The extremely long recombination lifetimes in n-i-p-i crystals result in a very high photoconductivity. Contrary to bulk semiconductors, the gain factor  $g$  (i.e. the ratio of the number of charge carriers observed in the photocurrent per absorbed photon) does not saturate due to "hole sweep out". Using several "tricks" (application of a reverse bias  $U_{pn}$  in series with a suitably chosen resistor  $R^{ext}$ , fast lateral diffusion (Gulden et al 1991) of the photo-induced carriers from a relatively large "absorption area" into a small "detection area") it will be possible to achieve adjustable lifetimes  $\tau^{eff}$  and large constant gain values  $g = \tau^{eff}/\tau^{tr}$  up to high 3-dB-frequencies ( $\tau^{tr}$  = transit time between the two n-type contacts for measuring the increase of conductance) (Kiesel et al 1989, Döhler 1990).  $g = 30$  at 1 GHz should be possible for a detector with  $1\mu m$  contact separation. Figure 4 demonstrates the adjustable gain for a structure with a contact separation of about  $40\mu m$ . The range of nearly linear response saturates abruptly when internal recombination, due to lowering of the potential barrier separating electrons from holes, becomes very efficient.

## 3.2. Threshold switches with gain

The previously discussed detectors have also been used as opto-electronic threshold switch (Kiesel et al 1988). For this purpose the reverse voltage  $U_{pn}$  has to be increased beyond the point where the n-layers are totally depleted under dark conditions (assuming that the p-doping is strong enough to prevent the p-layers from being totally depleted). The n-layer conductance is practically zero up to a threshold optical power at which the voltage drop between the n- and p-contact corresponds to the depletion threshold  $U_{np}^{th}$ . With large values of the applied bias  $U_{pn}^0$  and  $R^{ext}$  the conductance saturates at an optical power  $P^{sat}$ , which may be only slightly larger than  $P^{th}$ . The gain is of differential nature: each absorbed excess photon above the threshold results in  $g$  electrons contributing to the n-layer conductance.

Finally, the switch can be made bistable. Within a certain range of photon energies above the bandgap, the absorption coefficient, and therefore also the photo current between the n- and the p-layers  $I_{pn}$ , decreases with increasing values of the internal space charge fields, i.e. with increasing reverse bias. This applies to both, n-i-p-i structures with uniform i layers due to the Franz-Keldysh oscillations (Linder et al 1990), and to MQW i layers due to the quantum-confined Stark effect (Miller et al 1984). In both cases a bistable relation between the optical power and the voltage drop  $U_{pn}$  on the n-i-p-i structure occurs for a certain range of applied voltages  $U_{pn}^0$  and resistors  $R^{ext}$ , which results in bistable switching between negligible or close to saturation n-layer conductances.

## 4. OPTO OPTICAL DEVICES

Purely optical switching due to optical non-linearities can either be achieved by small refractive index changes in a high finesse Fabry-Perot resonator, by photo current instabilities, or by threshold switching.

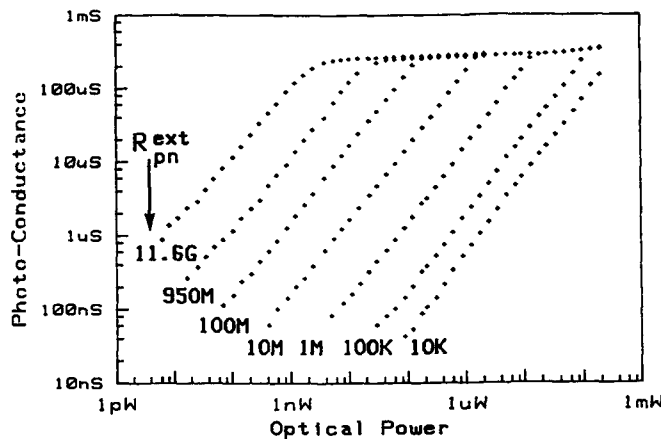


Fig. 4. Photoconductance vs. optical power for a n-i-p-i photo-conductive detector at various values of the external resistor  $R_{pn}^{ext}$

#### 4.1. Simple Optical Switches

The threshold switches and the optically bistable n-i-p-i switches, discussed in section 3.2, yield large non-linear or bistable changes of the absorption coefficient. The latter ones resemble the conventional "self-electro-optic effect devices" (SEED) (Miller et al 1984). They require lower bias but larger optical power than conventional SEEDs, and are therefore of limited interest. Band-filling induced refractive index changes, however, can be larger in reverse biased hetero - n-i-p-i - structures and may be achieved by  $\mu W/cm^2$  instead of  $kW/cm^2$  necessary for bulk or MQW structures (Schmitt-Rink et al 1989). Therefore, bistability due to detuning of high finesse Fabry-Perot resonators is expected for extremely low optical power.

#### 4.2. "Smart Pixel" Optical Switches

Simple SEEDs are far away from representing ideal optical logic gates. Although a more sophisticated version, the S-SEEDs (composed of two symmetrical SEEDs (Lentine et al 1989)) overcome a number of these drawbacks, they still suffer from the fact that the same device has to function as a detector and modulator, which leads to incompatible optimization requirements. Even more important, all the electrons required for switching the modulator have to be provided by the absorption of photons. We have recently shown (Döhler 1990) that the combination of a n-i-p-i threshold switch with gain and a n-i-p-i modulator is more appealing, as the two devices forming a "smart pixel" can be optimized separately, and the optical and electrical energy dissipation becomes significantly lower. A NOR gate is schematically shown in Figure 5. These smart pixels are suitable for monolithic integration. With a clock frequency of 100 MHz and  $10^3 \times 10^3 \text{ pixel}/\text{cm}^2$  a total energy dissipation of  $< 10W/\text{cm}^2$  seems to become feasible, which would result in up to  $10^{14}(\text{bit operations})/\text{cm}^2\text{s}$ .

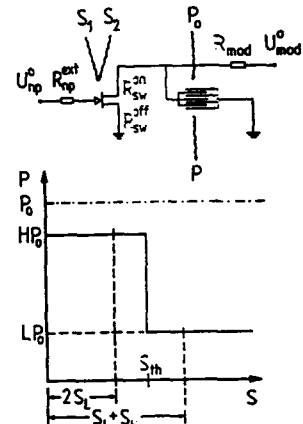


Fig. 5. Simplified equivalent circuit of a "smart pixel"-NOR-gate as described in the text (upper part) and schematic of its operation (from Döhler et al 1990)

## 5. CONCLUSIONS

The experimental and theoretical progress on n-i-p-i and hetero-n-i-p-i structures has come to the point where first prototypes of various opto electronic devices could be demonstrated. A mile stone on our way towards useful devices has been the development of the technology to provide selective contacts to n-i-p-i structures of small lateral dimensions by means of epitaxial shadow mask molecular beam epitaxy (Wu et al 1992).

## ACKNOWLEDGEMENT

The work reported in this paper is the result of a collaborative effort. I would like to acknowledge in particular the contributions of T Gabler, I Gäßner, K Gulden, P Kiesel, M Kneissl, N Linder, S Malzer, M Renn, P Riel, S Smith, J Whinnery, and X X Wu.

## REFERENCES

Ando H, Iwamura H, Oohashi H and Kanbe H 1989 IEEE J. of Quantum Electronics 25 2135  
 Burstein E 1954 Phys. Rev. 93 632  
 Döhler G H 1986a IEEE QE-22 1682  
 Döhler G H 1986b CRC Review in Solid State and Material Sciences 13 97  
 Döhler G H 1990 Superlattices and Microstructures 8 49  
 Döhler G H, Hasnain G, Miller J N 1986 Appl. Phys. Lett. 49 704  
 Döhler G H, Kiesel P, Lin H, Riel P, Ebeling K and Miller J N 1990 SPIE 1283 103  
 Eckl S, Metzner C, Schrüfer K and Döhler G H 1992 unpublished  
 Gulden K, Lin H, Kiesel P, Riel P, Döhler G H and K J Ebeling 1991 Phys. Rev. Lett. 66 373  
 Kiesel P, Riel P, Lin H, Linder N, Miller J N and Döhler G H 1989 Superlattices and Microstructures 6 363  
 Kost A, Garmire E, Danner A and Dapkus P D 1988 Appl. Phys. Lett. 52 637  
 Larsson A and Maserjian J Appl. Phys. Lett. 58 1946  
 Lentine A L, Hinton H S, Miller D A B, Henry J E, Cunningham J E and Chirovsky L M F 1989 IEEE J. Quantum Electron. 25 1928  
 Linder N and Döhler G H 1989 Superlattices and Microstructures 6 375  
 Linder N, El-Banna W, Keil U D, Schmidt K, Döhler G H, Miller J N and Ebeling K J 1990 SPIE 1286 359  
 Miller D A B, Chemla D S, Damen T C, Gossard A C, Wiegmann W, Wood T H and Burrus C H 1984 Phys. Rev. Lett. 53 2173  
 Renn M 1991 PhD thesis, Universität Erlangen-Nürnberg  
 Schmitt-Rink S, Chemla D S and Miller D A B 1989 Advances in Physics 38 89  
 Wu X X, Walker J, Smith J S and Whinnery J 1992 unpublished

## Resonant electron capture in AlGaAs/GaAs quantum well structures

A. Fujiwara, S. Fukatsu, Y. Shiraki, and R. Ito

Research Center for Advanced Science and Technology (RCAST),  
The University of Tokyo, 4-6-1 Komaba, Meguro-ku, Tokyo 153, Japan

We studied the temperature dependence of resonant electron capture in  $\text{Al}_{0.3}\text{Ga}_{0.7}\text{As}/\text{GaAs}$  quantum well structures. The capture efficiency was found to be enhanced in a resonant case where incoming electrons in the barrier band-edge are resonant with the virtual bound state of quantum wells. This resonant effect was easily smoothed out with increasing temperature. However, it was revealed that the resonant electron capture is less temperature-dependent and pronounced even at 132K for the quantum well with thin AlAs tunnel barriers inserted at the heterointerfaces.

Investigation of the electron capture in quantum wells (QW's) has been attracting particular interest from both viewpoints of fundamental physics and device applications. There have been several reports in terms of classical diffusion problem, showing a decrease of capture efficiency in QW's with well layer thickness ( $L_z$ ) smaller than the mean free path of electron due to optical phonon scattering [1][2]. However, there is little understanding of the electron capture in terms of quantum mechanics, i.e., how the barrier electron in the 3-dimensional state relaxes into the 2-dimensional state. Theoretical calculations have shown that the capture efficiency is dependent on  $L_z$ , enhanced under a resonant condition where the band-edge energy of the barrier is nearly equal to the highest QW bound state [3]. Experimentally, the capture behavior has been studied by means of time-resolved photoluminescence (PL) [4][5] and PL excitation spectroscopy [6][7]. Recently, we have reported for the first time the observation of resonant electron capture in  $\text{Al}_{0.3}\text{Ga}_{0.7}\text{As}/\text{GaAs}$  QW structures by PL and demonstrated that the resonant effect was pronounced by insertion of thin AlAs tunnel barriers at the heterointerfaces of QW [8]. In this paper, we explored the temperature dependence of resonant electron capture in  $\text{Al}_{0.3}\text{Ga}_{0.7}\text{As}$  QW structures and the difference between simple QW's and QW's with tunnel barriers.

The samples used were grown by molecular beam epitaxy (MBE) on (100) semi-insulating GaAs substrates. We used two types of QW structures. One was a simple QW structure of  $\text{Al}_{0.3}\text{Ga}_{0.7}\text{As}$  barrier layer and GaAs well. The other was a QW with thin AlAs layers inserted at the heterointerfaces. The latter structure as well as the band diagram are schematically illustrated in Fig. 1. AlAs layers of 20Å are inserted at heterointerfaces of the  $\text{Al}_{0.3}\text{Ga}_{0.7}\text{As}/\text{GaAs}$  QW structure. In both types of QW structures, the QW is sandwiched by AlAs cladding layers to prevent carriers overflowing out of the system. Insertion of the AlAs tunnel barriers enhances quantum mechanical reflectivity of electrons in the  $\text{Al}_{0.3}\text{Ga}_{0.7}\text{As}$  barrier at the heterointerface and

improves the resonant effect [8]. During MBE growth, we rotated the sample in order to gain homogeneity of both the layer thickness and the composition ratio. However, the sample rotation was intentionally stopped when the GaAs well layer was grown, providing samples with varying  $L_z$  due to beam flux inhomogeneity. This allowed us to examine the  $L_z$  dependence of the carrier capture efficiency by exploiting the PL mapping technique. PL measurements were carried out at various temperatures ( $T=20-130K$ ). The sample was excited by a cw Ar ion laser with an excitation density of  $10 \text{ W/cm}^2$ . The electron capture efficiency was evaluated by the ratio of PL integrated intensity from the QW ( $I_w$ ) and that from the barrier ( $I_b$ ). The PL mapping clarifies how the electron capture efficiency, that is,  $I_w/I_b$  depends on  $L_z$ .

Figure 2 shows the  $L_z$  dependence (50-130Å) of  $I_w/I_b$  in the QW with tunnel barriers at 77K. It is shown that the electron capture efficiency depends strongly on  $L_z$  and exhibits peaks of resonant electron capture. The left peak at  $L_z=67\text{\AA}$  and the right peak at  $L_z=107\text{\AA}$  correspond to the resonance of the second and the third quantized level of electrons in the well, respectively. We can explain the results based on a simple electron-wave model which is analogous to the optical Fabry-Perot resonator, regarding the QW interface as a mirror of electron waves [8]. Under the resonant condition, the wave function of the incoming electron in continuum states of the barrier band-edge is concentrated in the well layer, which forms a virtual bound state, and it leads to an increased capture efficiency.

Temperature dependence of the resonant electron capture in both types of QWs is

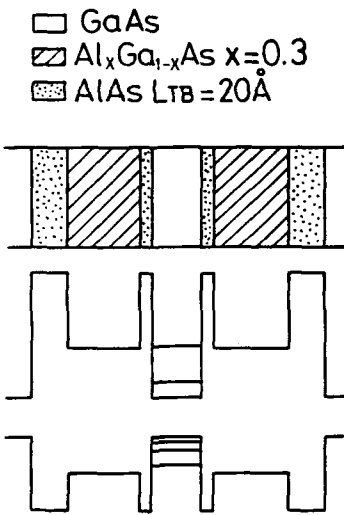


Fig. 1 The structure and the schematic band diagram of QW with tunnel barriers. AlAs tunnel barriers of  $20\text{\AA}$  were inserted symmetrically to the heterointerface. The  $\text{Al}_{0.3}\text{Ga}_{0.7}\text{As}$  barrier is  $750\text{\AA}$  thick.

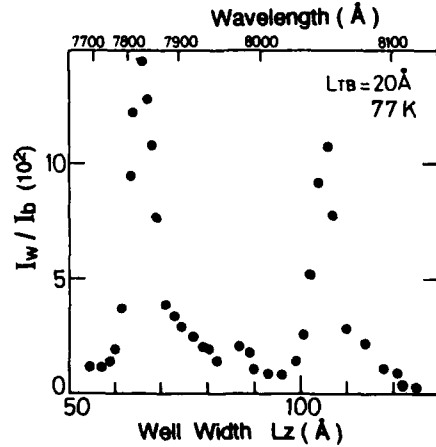


Fig. 2 Well-width dependence of  $I_w/I_b$  in the QW with AlAs tunnel barriers at 77K. Two resonant peaks are observed, which corresponds to the resonance of the second and third QW levels, respectively.

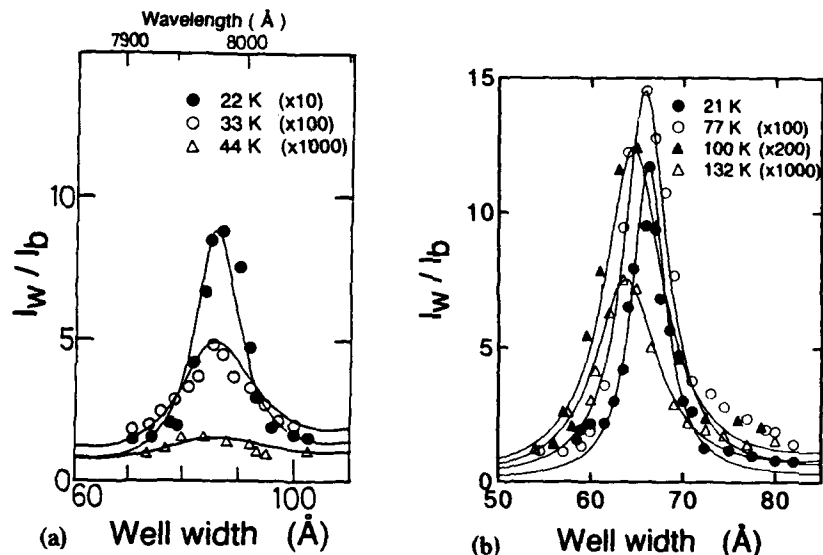


Fig.3 Temperature dependence of the resonant electron capture in the simple QW (a) and the QW with tunnel barriers (b).

depicted in Fig. 3. It is obviously seen that the temperature dependence quite differs in both types of QW structures. In the case of the simple QW, the resonant peak is rapidly smoothed out with increasing temperature, and vanishes above 44K. In contrast, the resonant effect remains pronounced even at 132 K in the case of the QW with tunnel barriers. In Fig.4 we show the temperature dependence of the resonant peak width for both cases. In our model, the full width at half maximum (FWHM) of the resonant peaks is  $\Delta L_z = (2/k_w) \sin^{-1}[(1-R)/2R]$  where R is the reflectivity of the incoming electron with an energy of  $\frac{1}{2}kT$  at the heterointerface,  $k_w$  is the wavenumber of the incoming electron in the well. In the simple QW, the experimental  $\Delta L_z$  is larger than the calculated results, e.g.,  $\Delta L_z$  (calculation) = 3.4 Å at 22K, and deviates with increasing temperature. This difference is not caused by the inhomogeneity of the structure because the well width fluctuation is estimated to be smaller than one monolayer from PL spectrum linewidth and can be neglected. The large dependence of  $\Delta L_z$  on temperature indicates that  $\Delta L_z$  is determined by the homogeneous broadening due to phonon scattering which will break the electron-wave coherency. In the QW with tunnel barriers, however, the experimental  $\Delta L_z$  is much larger than the calculated one (  $4.7 \times 10^{-3}$  Å

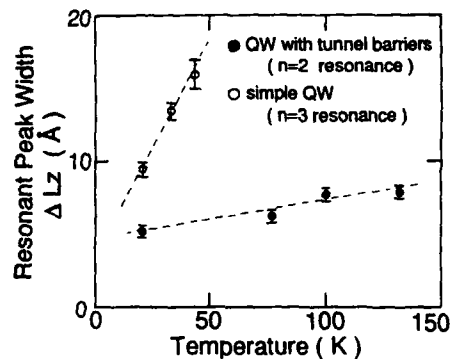


Fig.4 Temperature dependence of the resonant peak width  $\Delta L_z$  in the capture efficiency.

at 21K ) and is hardly dependent on temperature. We attribute this temperature-independent broadening to inhomogeneity of well width since the experimental  $\Delta L_z$  is very close to the well width fluctuation estimated from PL spectrum linewidth, approximately one or two monolayers. Different temperature dependence seems to suggest that the electron-phonon scattering mechanism is differently operating in the simple QW and the QW with tunnel barriers. The virtual bound states in the QW with tunnel barriers are well localized in the well compared to the simple QW, which is likely to reduce the carrier scattering rate.

In conclusion, we have investigated the temperature dependence of the resonant electron capture in  $Al_{0.3}Ga_{0.7}As/GaAs$  QW structures. Resonant peaks of the capture efficiency in the PL spectrum were clearly observed even at 132K in the QW with tunnel barriers inserted at the heterointerfaces, whereas the resonant peak in the simple QW experienced the profound temperature broadening and was obscured above 44K. The resonant peak width  $\Delta L_z$  of the simple QW seems to be dominated by the inhomogeneous broadening due to electron-phonon scattering, while the inhomogeneous broadening due to the well width fluctuation dictates that of the QW with tunnel barriers.

We are grateful to N. Ogasawara for fruitful discussion and acknowledge the technical support from S. Ohtake.

#### REFERENCES

- [1] H. Shichijo, R. M. Kolbas, N. Holonyak, Jr., R. D. Dupuis and P. D. Dapkus, *Solid State Commun.* **27** (1978) 1029.
- [2] J. Y. Tang, K. Hess, N. Holonyak, Jr., J. J. Coleman and P. D. Dapkus, *J. Appl. Phys.* **53** (1982) 6043.
- [3] J. A. Burm and G. Bastard, *Phys. Rev. B* **33** (1986) 1420.
- [4] B. Deveaud, J. Shah, T. C. Damen, and W. T. Tsang, *Appl. Phys. Lett.* **52** (1986) 1886.
- [5] D. Y. Oberli, J. Shah, J. L. Jewell, T. C. Damen and N. Chand, *Appl. Phys. Lett.* **54** (1989) 1028.
- [6] H. J. Pollard, K. Leo, K. Rother, K. Ploog, J. Feldmann, G. Peter, E. O. Gobel, K. Fujiwara, T. Nakayama, and Y. Ohta, *Phys. Rev. B* **38** (1988) 7635.
- [7] N. Ogasawara, A. Fujiwara, N. Ohgushi, S. Fukatsu, Y. Shiraki, Y. Katayama, and R. Ito, *Phys. Rev. B* **42** (1990) 9562.
- [8] A. Fujiwara, S. Fukatsu, Y. Shiraki, and R. Ito, *Surf. Sci.* (in press).

## Optical properties of in-situ grown GaAs quantum wires by MOCVD selective growth

Y. Arakawa, Y. Nagamune, S. Tsukamoto, and M. Nishioka

Research Center for Advanced Science and Technology, University of Tokyo  
4-6-1 Komaba, Meguro-ku, Tokyo 153, Japan

**ABSTRACT:** We fabricated GaAs quantum wires with the minimal lateral dimension of 20 nm by a metal organic chemical vapor deposition selective growth technique. The GaAs quantum wires were in-situ grown on a V-groove formed by two GaAs triangular prisms which are selectively grown on SiO<sub>2</sub> masked substrates. The measurement of photoluminescence and magneto-photoluminescence spectra clearly indicate existence of the quantized state in the quantum wires.

Low dimensional semiconductor structures such as quantum wires have recently received great attentions since new physical phenomena with applications to semiconductor lasers and other functional optical devices are expected[1,2]. To fabricate these quantum microstructures, various techniques such as wet chemical etching[3], reactive ion etching[4], ion beam implantation[5] and ion beam milling[6,7] have been investigated. These methods, however, suffer from free surface effects, creation of a damage field during implantation, or interface control due to the random nature of the disordering mechanism. To avoid these problems, growth techniques on masked substrates[8,9] and nonplanar substrates[10-12] have been also investigated. Recently, Kapon et al. successfully fabricated quantum wire lasers on V-grooved (100) oriented GaAs substrates[10] or submicron gratings[11] by the metal organic chemical vapor deposition(MOCVD).

In this paper, we discuss optical properties of in-situ grown GaAs quantum wires with the minimal lateral dimension of 20 nm by a MOCVD selective growth technique. An essential technique different from previously reported MOCVD growth for quantum wires on V-grooves[10,12] or submicron gratings[11] is that the V-groove is formed by using the selective growth of two GaAs triangular prisms on SiO<sub>2</sub> patterned substrates, instead of chemical etching technique. As a result, a very narrow and smooth V-groove between the triangular prisms can be formed. Measured photoluminescence (PL) spectra demonstrate the existence of the first subband state in the GaAs quantum wires. Moreover, the observed PL peak shift of the quantum wires with the increase of the applied magnetic field was much smaller than that of the bulk. In addition, it was found that the PL peak shift of the quantum wires was strongly dependent on the direction of the magnetic field. These results demonstrate the existence of the two-dimensional confinement effect in the quantum wires.

The MOCVD growth was performed in a low pressure, horizontal, rf-heated MOCVD reactor, using trimethylgallium (TMG), trimethylaluminum (TMA) and arsine (AsH<sub>3</sub>) as group III and V sources, respectively. The TMG bubbler was kept at -10 °C and the TMA bubbler was kept at 20 °C. The partial pressure of TMG, TMA and AsH<sub>3</sub> were kept at 4.4x10<sup>-6</sup> atm, 1.5x10<sup>-6</sup> atm and 4.4x10<sup>-4</sup> atm, respectively. The ratio of group V to group III was 100. The growth temperature was 700 °C. Purified H<sub>2</sub> with a 6 liter/min flow rate was used as a carrier gas. The growth pressure was 100 torr. Under these growth conditions, the GaAs growth rate for unmasked substrates is almost constant at 3.6 Å/sec.

Fabrication procedure for the quantum wires is as follows. First, a  $\text{SiO}_2$  layer with the thickness of 20nm is formed by plasma chemical vapor deposition on a semi-insulating (100) GaAs substrate. PMMA were lithographically defined on the  $\text{SiO}_2$  layer by electron beam(EB) lithography technique, followed by a wet chemical etching. After this procedure, the GaAs triangular prisms with (111)A facet sidewalls are grown on the masked substrate by MOCVD growth. Further continuation of the growth which leads to smooth (111)A facet sidewalls makes the dimension of the triangular prisms uniform. Note that this growth occurs laterally above  $\text{SiO}_2$  mask, making the space between the triangular prisms small. As a result, a sharper corner at the bottom of the V-groove between the triangular prisms is formed compared to chemical etching[10]. The space between the triangular prisms is filled up with  $\text{Al}_{0.4}\text{Ga}_{0.6}\text{As}$  layer by switching the growth layer from GaAs to  $\text{Al}_{0.4}\text{Ga}_{0.6}\text{As}$ . Thus, GaAs quantum wires which are coupled with thin quantum wells are formed between the triangular prisms without being exposed to air.

Fig. 1 shows a high-resolution backscattered electron image of vertically stacked multiple quantum wires (12nm-20nm)x(20nm-30nm) fabricated here and its illustration. As shown in this photograph, there are three quantum wires on a V-groove structure sandwiched by two GaAs triangular prisms. Each quantum wire is connected to quantum well layers. Here, the  $\text{SiO}_2$  mask was buried by the lateral growth, resulting in the excellent crystalline in the wire region. In Fig. 2, a scanning electron micrograph of the region near the quantum wires is shown. As indicated in the figure, triangular-shaped or crescent-shaped quantum wires with lateral dimension of 20nm are embedded in AlGaAs layers.

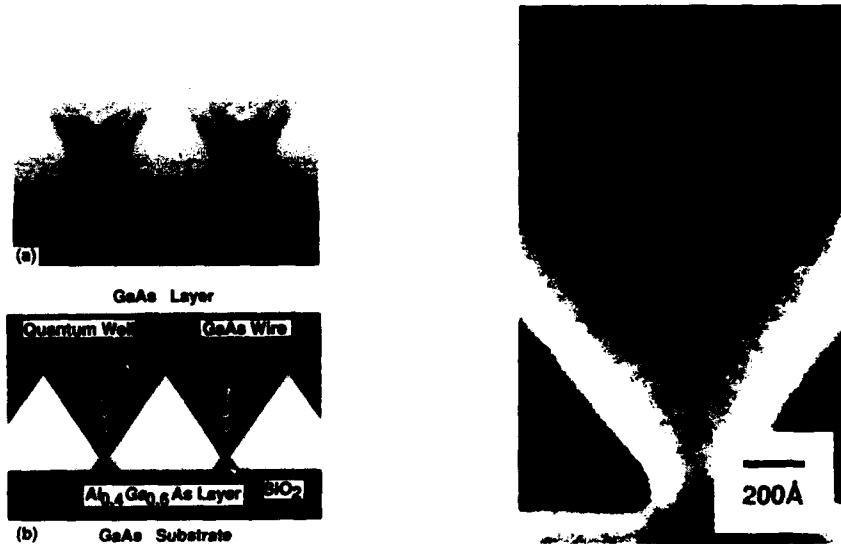


Fig. 1 (a) Schematic illustration of the cross section of the vertically stacked multiple quantum wires and (b) high resolution secondary electron image of the region near the quantum wires.

Fig.2 High resolution Secondary electron micrograph for the region near the quantum wires.

Fig. 3 shows PL spectra at 20K. The sharp luminescence peaks at 819.5nm(1.513eV) and 830.9nm(1.492eV) are coming from the bulk of the undoped GaAs triangular prism region. The weak luminescence peaks at 607nm(2.043eV) and 625nm(1.984eV) correspond to the  $\text{Al}_x\text{Ga}_{1-x}\text{As}$  layer under the GaAs triangular prisms ( $x \sim 0.40$ ) and the barriers at the (111)A sidewalls of the

GaAs triangular prisms ( $x \sim 0.36$ ), respectively. Two peaks around 710 nm (1.746 eV) and 740 nm (1.676 eV) in the broad luminescence band originate from the quantum wells regions ( $L_z = 40$  and 6 nm, respectively). The luminescence peak at 795.5 nm (1.559 eV) with a full width at half-maximum (FWHM) of 20 meV is corresponding to the quantum wire, since the energy difference (45 meV) between the PL peaks of the GaAs bulk and the quantum wires agrees well with the calculated energy difference (44 meV) assuming the PL from the first subband of a 20 nm-15 nm triangular-shaped quantum wires. Note that the quantized energy of this 20 nm-15 nm triangular-shaped quantum wires is almost the same as that of 14 nm x 14 nm rectangular-shaped quantum wires.

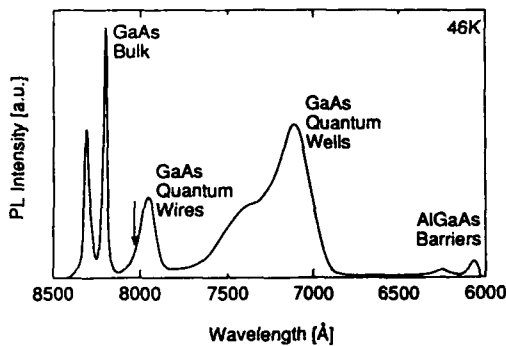


Fig. 3 Photoluminescence spectra from the quantum wires.

Next, magneto-photoluminescence spectra are measured using pulsed magnetic fields at 4.2 K. The pulse duration of the magnetic field is 10 msec and the maximum field was about 40 T. The variation of magnetic field during the measurement was within  $\pm 3\%$  at the top of the pulsed magnetic field. The spectral resolution determined by the entrance slit width of the spectrometer was about 2.4 meV around the measured wavelength range. PL spectra were detected with an optical multi-channel analyzer (OMA) system installed at the exit of the spectrometer through the optical fiber. The relationship among the direction of the quantum wires  $W$ , applied magnetic field vector  $B$  and the direction perpendicular to the substrate  $k$  is shown in Fig. 4(a). As shown in the figure, three kinds of configurations were taken for the present magneto-PL measurement, where it should be noted that  $W \perp B \parallel k$  and  $W \parallel B \perp k$  are different configurations because of the triangular-shaped quantum wires.

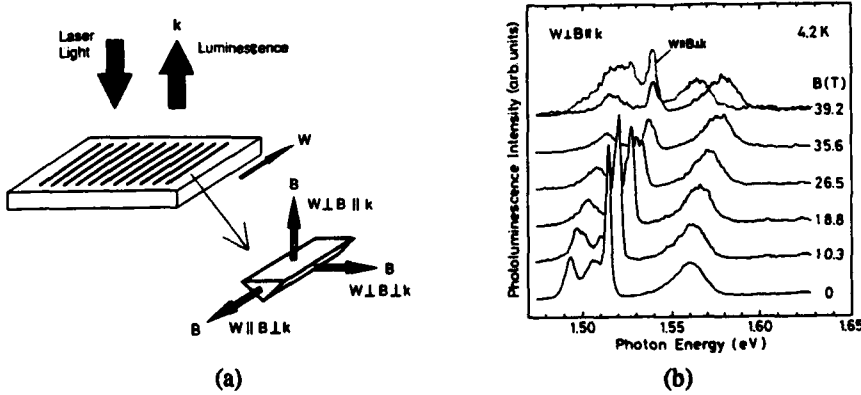


Fig. 4 (a) Relationship among the direction of the quantum wires  $W$ , that of the applied magnetic field  $B$  and that perpendicular to the substrate  $k$ , and (b) Magneto-photoluminescence spectra of the GaAs quantum wires and the bulk for  $W \perp B \parallel k$ . Each spectrum was measured at a magnetic field indicated on the right-hand side of the spectra. Spectra for  $W \parallel B \perp k$  are also shown for the highest magnetic field by dotted line.

Fig. 4(b) shows the magneto-PL spectra of the quantum wires with various magnetic fields. Each spectrum was measured at a magnetic field indicated on the right-hand side of the spectra, and at a temperature of 4.2 K with the configuration of  $W \perp B \parallel k$ . In this figure, the spectra for  $W \parallel B \perp k$  are also shown for the highest magnetic field of ~40 T by dotted line for comparison. As shown in this figure, the PL peak from the bulk shifts linearly with the increase of the magnetic fields. In addition, the shift does not depend on the configuration. On the other hand, the energy shift of the PL peak position of the quantum wires is strongly dependent on the configurations. Namely, energy shift for  $W \perp B \parallel k$  is much larger than that for  $W \parallel B \perp k$ .

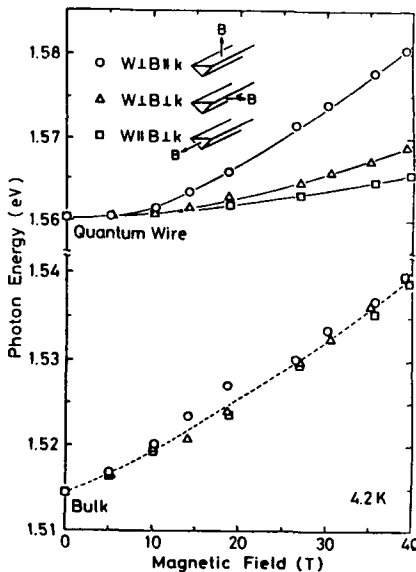


Fig. 5 PL peak positions from the quantum wires and the bulk as a function of applied magnetic field for various configurations. Circles, triangles and squares represent the data for  $W \perp B \parallel k$ ,  $W \perp B \perp k$  and  $W \parallel B \perp k$ , respectively.

The PL peak position from the quantum wires and the bulk at the three configurations are plotted as a function of applied magnetic fields in Fig. 5. As shown in this figure, the behavior of the PL peak shift  $\Delta E$  is different between the bulk and the quantum wires. The bulk PL peak shifts at various magnetic fields are almost equal independent on the configurations at all the magnetic field region. In contrast, the PL peak shift of the quantum wires is clearly depending on the configuration. In addition, the energy shifts of the quantum wires at high magnetic field region depends on the configuration of  $W \perp B \parallel k$ ,  $W \perp B \perp k$  and  $W \parallel B \perp k$ , respectively.

In order to understand these behaviors, we assume that the quantum wire potential is expressed by the following harmonic potential  $\phi(x,y)$ .

$$\phi(x,y) = (m \omega_x^2 x^2 + m \omega_y^2 y^2)/2$$

where, z-axis and x-axis are in parallel with  $W$  and  $k$ , respectively. In this case, when the magnetic field is applied perpendicularly to  $W$  or  $k$ , the energy shift  $\Delta E$  can be expressed as follows.

$$\begin{aligned} \Delta E &= \hbar (\omega^2 + \omega_x^2)^{1/2} && \text{for } W \perp B \perp k \\ \Delta E &= \hbar (\omega^2 + \omega_y^2)^{1/2} && \text{for } W \perp B \parallel k \\ \omega &= eB/m \end{aligned}$$

By fitting the curve to the measured data using above relationship, the value of  $\omega_y/\omega_x$  are 3/7, respectively. It should be noted that the  $\omega_i$  is approximately proportional to  $1/L_i^2$  ( $i = x$  or  $y$ ), where  $L_i$  is the thickness of the quantum well potentials. Since the cross sectional view in Fig. 2 shows that  $L_x$  and  $L_y$  are about 25 nm and 15 nm, the value of  $(L_x/L_y)^2$  is in agreement with the

value of  $\omega_x/\omega_y$ . On the other hand, when the magnetic field is applied in parallel with  $W$ , the energy shift  $\Delta E$  can be determined analytically only if the potential  $\phi(x,y)$  is assumed to be  $m\omega_z^2(x^2+y^2)/2$ .

$$\Delta E = \hbar (\omega^2 + \omega_z^2)^{1/2} \quad \text{for } W//B//k$$

It is found that the value of  $\omega_z$  obtained by fitting to measured data is almost equal to  $\omega_y + \omega_x$ . This fact is qualitatively reasonable, taking the relation ship of  $\omega_z \approx \omega_y + \omega_x$  into account. For more detailed discussions, Coulomb interaction should be included, which will be discussed elsewhere.

In conclusion, we fabricated quantum wires which are selectively grown on V-grooves formed by GaAs triangular prisms. PL measurement shows the PL from the quantized states in the quantum wires, which is consistent with calculated results on the basis of the high-resolution backscattered electron image. The magneto-PL spectra of the GaAs quantum wires in high magnetic fields up to 40 T are measured. The difference between the PL peak shift of the GaAs quantum wires and that of the GaAs bulk against the various configurations clearly demonstrates the existence of the two-dimensional confinement in the GaAs quantum wires.

We wish to thank Prof. T. Ikoma and Prof. H. Sakaki, University of Tokyo for their instructive discussion and encouragement, and Dr. N. Koguchi and S. Takahashi of National Research Institute for Metal for providing excellent photographs of high-resolution backscattered electron image of samples. We also would like to give our thanks for supporting to the University-Industry Joint Project on Mesoscopic Electronics. This work was also supported in part by a Grant-in-Aid for Scientific Research on Priority Area, "Electron Wave Interference Effects in Mesoscopic Structures" from the Ministry of Education, Science and Culture.

## References

- [1] Y. Arakawa, and H. Sakaki, *Appl. Phys. Lett.*, **40**, 939 (1982).
- [2] Y. Arakawa, K. Vahala, and A. Yariv, *Appl. Phys. Lett.*, **45**, 950 (1984).
- [3] B. I. Miller, A. Shahar, U. Koren, and P. J. Corvini, *Appl. Phys. Lett.*, **54**, 188 (1989).
- [4] K. Kash, A. Scherer, J. M. Worlock, H. G. Craighead, and M. C. Tamargo, *Appl. Phys. Lett.*, **49**, 1043 (1986).
- [5] J. Cibert, P. M. Petroff, G. J. Dolan, S. J. Pearson, A. C. Gossard, and J. H. English, *Appl. Phys. Lett.*, **49**, 1275 (1986).
- [6] H. Temkin, G. L. Dolan, M. B. Panish, and S. N. G. Chu, *Appl. Phys. Lett.*, **50**, 413 (1987).
- [7] D. Gershoni, H. Temkin, G. L. Dolan, J. Dunsmuir, S. N. G. Chu, and M. B. Panish, *Appl. Phys. Lett.*, **53**, 995 (1988).
- [8] E. Colas, S. Simhony, E. Kapon, R. Bhat, D. M. Hwang, and P. S. D. Lin, *Appl. Phys. Lett.*, **57**, 914 (1990).
- [9] J. A. Levens, C. S. Tsai, and K. J. Vahala, *Appl. Phys. Lett.*, **56**, 2642 (1990).
- [10] T. Fukui, S. Ando, and Y. K. Fukai, *Appl. Phys. Lett.*, **57**, 1209 (1990).
- [11] R. Bhat, E. Kapon, D. M. Hwang, M. A. Koza, and C. P. Yun, *J. Cryst. Growth*, **93**, 850 (1988).
- [12] J. M. Gaines, P. M. Petroff, H. Kroemer, R. J. Simes, R. S. Geels, and J. H. English, *J. Vac. Sci. Technol.*, **B6**, 1378 (1988).
- [13] S. Tsukamoto, Y. Nagamune, M. Nishioka, and Y. Arakawa, International Conference on Solid State Devices and Materials, Yokohama (1991) and also to be published in *J. of Appl. Phys.* Jan. Issue (1992).

## Optical properties of AlGaAs serpentine superlattice quantum wires

H. Weman, M.S. Miller, C.E. Pryor, P.M. Petroff, H. Kroemer, and J.L. Merz  
University of California, Santa Barbara, CA 93106

**ABSTRACT:** Serpentine superlattices grown on vicinal (100) GaAs substrates by MBE have been studied by photoluminescence (PL) and photoluminescence excitation (PLE). The polarization dependence of the emission has been measured with a photo-elastic modulation technique, showing a pronounced anisotropy in both PL and PLE due to the lateral confinement. It is found that about 30% of the Al intended for the barrier ends up in the well. The polarization of the PL is found to be nearly constant over large areas of the wafer indicating uniform quantum wire states.

### I. INTRODUCTION

The growth of AlAs/GaAs tilted superlattices (TSL) on GaAs (100) vicinal substrates has provided a promising way to fabricate quantum wire arrays with a lateral width of just a few nm (Gaines *et al* 1988; Fukui and Saito 1988). However, there are two problems with this approach: (1) the thermodynamic and kinetic difficulty of having the Al incorporate only at the step edge, resulting in incomplete segregation, and (2) the fact that the tilt angle is not a well-controlled parameter, which changes the electronic confinement energy. Recently we have presented a way to avoid this problem by purposely changing the tilt angle to achieve a crescent-shaped well (Miller *et al* 1991). The resulting "serpentine superlattice" (SSL) accommodates the geometric sensitivity to absolute growth rates. In this paper we present a detailed luminescence study of a SSL, and report the first observation of linear polarization effects both in PL and PLE.

### II. EXPERIMENTAL

The sample studied here contains a single array of parabolic crescents grown on a 2° misoriented substrate. The vertical barriers were intended to cover 1/2 a step and have a digital alloy composition  $x_{\text{barrier}}=1/3$ . The sample was grown while synchronously rotating the substrate with the shuttering. The lower cladding layer is  $\text{Al}_x\text{Ga}_{1-x}\text{As}$  ( $x=.3$ ) and contains 60 and 80 Å quantum wells. A control sample was grown under identical conditions but with no misorientation, replacing the SSL with an alloy of the same thickness and average composition.

For the polarized PL and PLE experiments we have employed a new technique using a photo-elastic modulator (PEM; Wassermeier *et al* 1992). We define the polarization of the light travelling in the growth direction (z axis) in the usual way,  $P_z=(I_x-I_y)/(I_x+I_y)$ , where  $I_x$  and  $I_y$  are the intensities polarized parallel and perpendicular to the wires.

## III. RESULTS

The PL spectra at 1.4 K of the SSL and control samples are shown in Figure 1. Each spectrum consists of three emission lines; the peaks at 1.565 eV and 1.593 eV are due to the 80 Å and 60 Å quantum wells (QW), and we attribute the peaks at 1.735 eV and 1.747 eV to the SSL quantum wire array and the control. Detailed polarization measurements of these samples are shown in Figure 2. The PL emission of the SSL peak is shown together with the normalized value of the linear polarization. Most of the PL emission is polarized in the x-direction, with a few percent linearly polarized in the y-direction on the high energy side of the PL emission. The maximum of the polarization, 44%, is red-shifted 7 meV from the PL peak, where the polarization is 23%. The control peak and the 60 Å and 80 Å QW peaks did not show any polarization. We have also measured the polarization of the PL emitted from the two perpendicular directions.

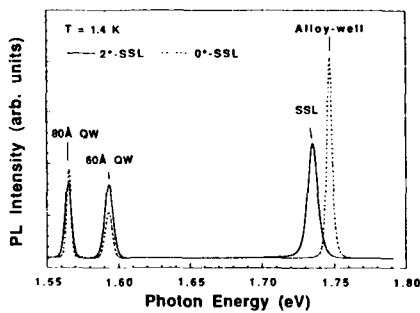


Figure 1: Photoluminescence spectrum at 1.4 K of SSL sample grown on a nominally flat (dashed line) and 2° misoriented substrate (solid line). The peaks are discussed in the text.

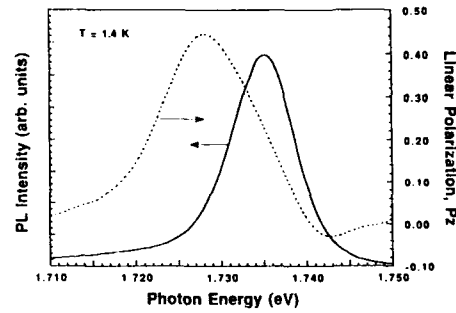


Figure 2: Photoluminescence spectrum (solid line) and linear polarization  $P_z$  (dotted line), as defined in the text, of the 2°-SSL peak.

Linearly polarized PLE was also observed for the SSL sample, Figure 3. There is a broad Stokes-shifted peak of the ground state transition (5.0 meV), with no indication of any higher subband structure. A large polarization anisotropy (solid curve) is observed around the absorption peak (dotted curve). At a few meV below the absorption peak, the absorption is stronger parallel to the wires (16%), and just above the absorption peak, the absorption is stronger perpendicular to the wires (-7%). At higher energies the absorption seems to be independent of the polarization of the exciting light. The separation between the polarization max and min is found to be about 4.6 meV. When the parallel and perpendicular excited PLE spectra are compared, the Stokes shifted peaks display a relative shift of 2.0 meV. The reference QWs and the alloy-well control peak showed no PLE anisotropy when excited normal to the vicinal (100) surface.

We have also measured decay times at 1.4 K of these emission peaks. Their decay is consistent with mono-exponential fits to the data, and gives a lifetime of 379 ps for the SSL peak, 262 ps for the control, and  $250 \pm 10$  ps for the 60 and 80 Å QWs.

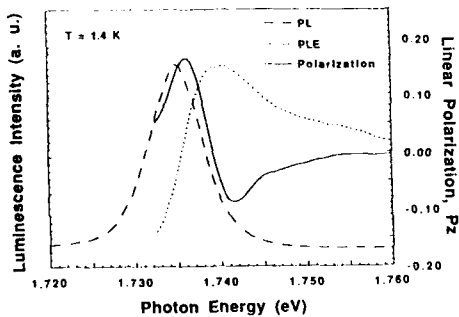


Figure 3: Photoluminescence (dashed line) and photoluminescence excitation (dotted line) spectrum at 1.4 K of the 2°-SSL peak. The solid line shows the linear polarization  $P_z$  of the PLE signal.

Finally we have measured the uniformity of the SSL peaks. The peak position varies about 1.5 meV/mm on one side of the sample, and is almost uniform on the other side. The value of the linear polarization,  $P_z$ , is nearly independent of the peak position and also varies only slightly (about  $\pm 3\%$ ) around an average of 20%, as measured at the same spatial position.

#### IV. DISCUSSION

The observation that the SSL peaks are linearly polarized along the wires (Figure 3) is in qualitative agreement with the selection rules for 1-D electron to heavy-hole (e-hh) transitions. However, this can also be caused by strain-induced effects or elongated island structures. We rule out the former because the lattice mismatch between AlAs and GaAs is less than 0.1%. Elongated island structures may also be ruled out because of the poor lateral separation of the material into GaAs wells and barriers. Therefore the polarization observed for the SSL peaks is due to the lateral confinement of the excitons. This is also supported by the fact that the alloy-well peak and the QW transitions were all isotropic in this geometry.

The expected value of the polarization for the intended SSL structure (with no lateral intermixing) depends on the geometry and potential energy of the crescent. This has been quantified by calculating the energies and wavefunctions for the SSL in the envelope approximation assuming decoupled conduction and valence band states (Pryor 1992). We know (by TEM) that there is substantial intermixing between the vertical barriers and wells, so we have calculated the optical polarization as a function of this intermixing, which will strongly modify the electronic structure, resulting in weaker lateral confinement and weakening the polarization anisotropy. The intermixing has been considered for a sharp interface where the Al is uniformly removed and uniformly redistributed into the well. The linear polarization ( $P_x$ ,  $P_y$ , and  $P_z$ ) has then been calculated in all three perpendicular directions for the e-hh and light-hole (e-lh) transitions as a function of the intermixing; the result for  $P_z$  is shown in Figure 4. The experimental result is indicated by the solid circle. The segregation inferred for this geometry (shown in the figure) and in the other two perpendicular directions (not shown) are in good agreement. We get average values of Al composition  $x_{\text{barrier}}=21\%$  and  $x_{\text{well}}=12\%$ , compared to the intended value of 33.3% and 0%. This corresponds to a conduction band potential energy difference of  $\sim 70$  meV. It should be noted that we have used the polarization values at the SSL peak position, which is not at the maximum of the polarization, as was seen in Figure 2. The polarization has been found to be red-shifted from the PL peak, and is almost a factor two larger at the low energy tail of the SSL emission in all samples we have studied. This indicates that there is a distribution of quantum wires with different segregation within the SSL peak.

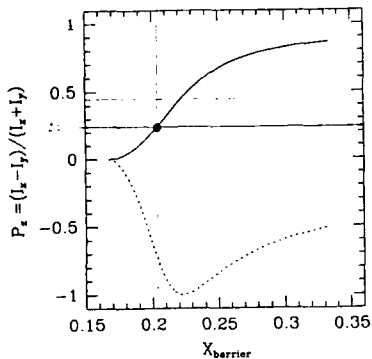


Figure 4. Calculated linear polarization ( $P_z$ ) for the electron heavy-hole transition (solid line) and electron light-hole transition (dashed line) as a function of the Al composition in the SSL barrier. The experimentally determined value of the linear polarization of the PL is indicated by the solid circle.

As was shown in Figure 3 the PLE did not show any structure that could be assigned to higher 1-D subbands, nor any hh-lh splitting. This is not surprising, because the linewidths of the SSL peak (7 meV) is greater than the expected subband splittings (5 meV). However from the polarized PLE and the calculated e-lh transition as a function of the intermixing, we have additional evidence for lateral confinement in the SSL structure. We see that for light travelling in the z-direction the hh state is resonantly excited with light parallel to the wire, and the lh state with light perpendicular to the wire, in qualitative agreement with the observed linear polarization of the PLE: the positive maximum corresponds to the e/hh state and the negative minimum to the e/lh state. We therefore take the 4.6 meV separation as an (over)estimate of the hh-lh splitting.

#### V. ACKNOWLEDGEMENTS

We want to thank M. Wassemeier for discussions on the use of the PEM for polarization measurements. This work was supported by the NSF Science and Technology Center for Quantized Electronic Structures. One of the authors (HW) is partially supported by a postdoctoral scholarship from the Swedish Natural Science Research Council (NFR).

#### REFERENCES

Fukui T and Saito H 1988, *J. Vac. Sci. Technol. B* 6, 1373.  
 Gaines J M, Petroff P M, Kroemer H, Simes R J, Geels R S and English J H 1988, *J. Vac. Sci. Technol. B* 6, 1378.  
 Miller M S, Pryor C, Weman H, Samoska L A, Kroemer H, Petroff P M and Merz J L 1991, *J. Cryst. Growth*, 111, 323.  
 Pryor C E 1992, *Phys. Rev B*, to be published.  
 Wassemeier M, Weman H, Miller M S, Petroff P M and Merz J M 1992, *J. Appl. Phys.*, to be published

## Novel linear and nonlinear optical properties of Si-Ge microstructures

M Jaros, K B Wong and R J Turton

Physics Department, The University, Newcastle upon Tyne, NE1 7RU

**ABSTRACT:** We show that Si-Ge superlattices exhibit strong optical spectra in the far infrared which lie well outside the 1-2 micrometer band normally considered in the literature. We also predict that Si-Ge superlattices exhibit optical nonlinearities which might be used to design a number of device functions required for Si-based optoelectronics.

### 1. ZONE FOLDING AND TRANSITIONS ACROSS THE SUPERLATTICE GAP

In a superlattice consisting of thin alternating layers of Si and Ge the bulk bands of Si and Ge are broken into minibands. For a suitable choice of the length of the superlattice period the Si conduction band minimum is folded upon the centre of the Brillouin zone and we obtain a direct gap material which promises useful applications in Si-based optoelectronics (see, for example, Kasper and Schaffler, 1991). This simple physical concept can be translated into numerical

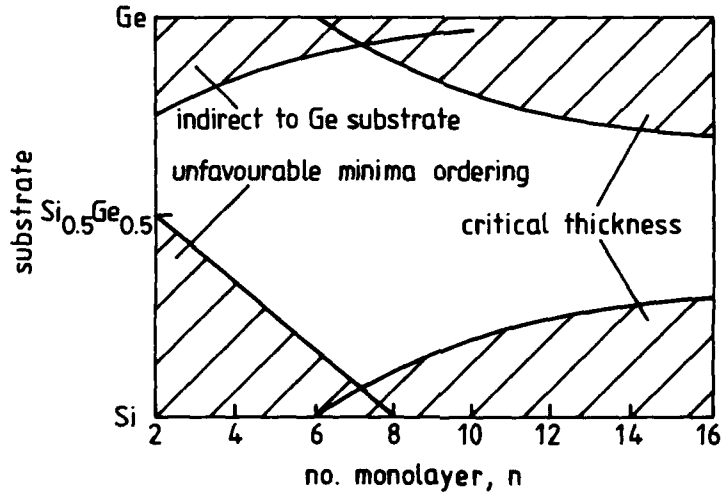


Figure 1

predictions in terms of the Kronig-Penney type (particle in a box) calculations of energy levels. The ease with which such modelling can be implemented has made the concept of zone folding popular with experimentalists, particularly after it has been shown in a variety of large scale calculations that the energies predicted from the simple model constitute a good guide.

However, detailed calculations are needed (e.g. Jaros, 1990) in order to predict the relevant optical transition probabilities as a function of structural properties. These probabilities are a sensitive function of the degree of mixing of bulk linear momentum due to the differences between the Si and Ge atomic potentials and due to the strain associated with the difference in the lattice constant of Si and Ge. This mixing which turns the forbidden transitions characteristic of Si into at least partially allowed ones in Si-Ge is of course absent in the particle in a box type calculation. Another important assessment which requires a microscopic model is concerned with the constraints imposed by the choice of substrate. The result of our pseudopotential calculations in Figure 1 shows that only in those structures that fall within the area given by the solid lines will both the conduction and valence band minimum lie in the superlattice and not in the substrate material.

The structure of particular interest is a ten monolayer superlattice (e.g. one with a period consisting of five monolayers of Si and five monolayers of Ge). The band gap of Si-Ge superlattices with this period varies from about 1 eV to 0.6 eV as shown in Figure 2.

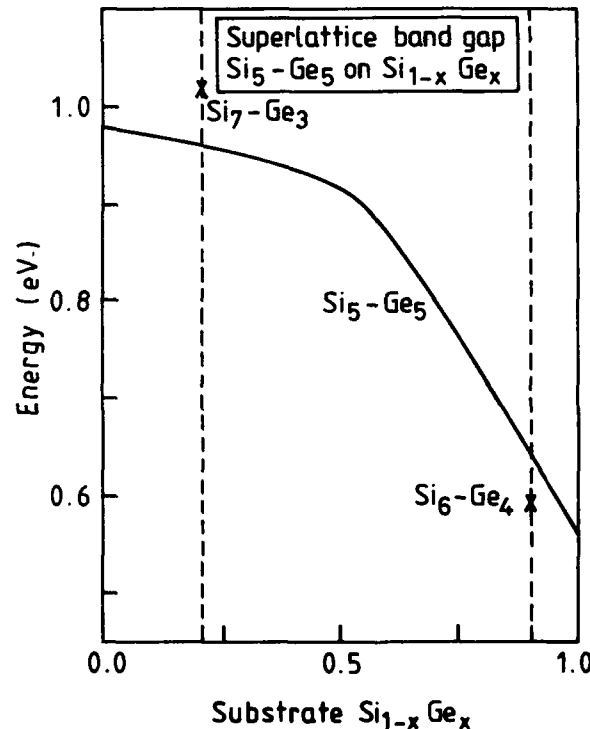


Figure 2.

## 2. FAR INFRARED TRANSITIONS

In larger period structures, e.g. with 20 or 30 monolayers periods which may also satisfy the zone folding condition, the strength of the optical transition across the gap is significantly reduced and renders such systems uninteresting for applications. In shorter period systems the conduction band minimum lies away from the zone center and this reduces the transition probability at the band edge where the relevant recombination must occur. This limits the range of wavelengths amenable for applications. However, our quantitative studies (Turton and Jaros, 1990) of the conduction minibands in 10 monolayer superlattices show that the optical transition between the lowest minibands is strong and depends weakly on the distribution of strain in the system. Furthermore, unlike the transitions across the gap, the strength of this effect decreases only slowly with the increase of the period. This is shown in Figure 3 where we plot the results of our calculations of the energy and oscillator strengths of the transitions between conduction minibands 1 and 2. In a ten monolayer structure, minibands 1 and 2 become near degenerate in energy and the transition of interest is between minibands 1 and 3. We can see that these transitions extend the range of applicable wavelengths well into the far infrared.

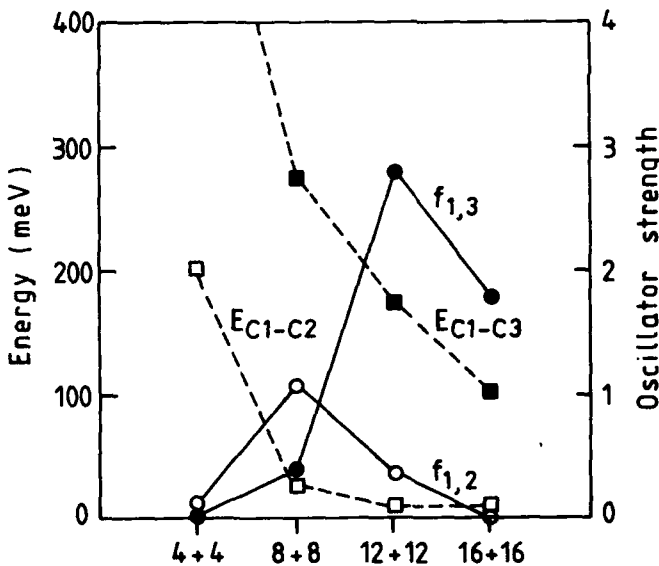


Figure 3.

## 3. NONLINEAR OPTICAL PROPERTIES

The ten monolayer structure also exhibits a strong virtual (Morrison and Jaros, 1990) optical nonlinearity. This is indicated in Figure 4. The lines with arrows connecting the conduction (C1,

C2) and valence (V1, V2) states of the ten monolayer symmetrically strained Si-Ge superlattice indicate the four photon virtual process which makes the third order susceptibility of order  $10^{-6}$ e.s.u. This is thanks to the strong optical transition probabilities associated with the transitions in question and the near equality of the energy separations C1-C2 and C1-V2 which appear in the denominator in the expression for nonlinear susceptibility. The response is excited at photon energies just below the band gap energy, with only negligible absorption. Another interesting nonlinear mechanism is associated with the band nonparabolicity (Turton *et al.*, 1988) in Si-Ge superlattices. We find that the magnitude of the conduction band nonparabolicity along the growth axis can be varied by two orders of magnitude by changes of superlattice period of order 2-3 bulk lattice constants and that it exceeds that in III-V materials. The nonparabolicity is also increased significantly in the interface plane.

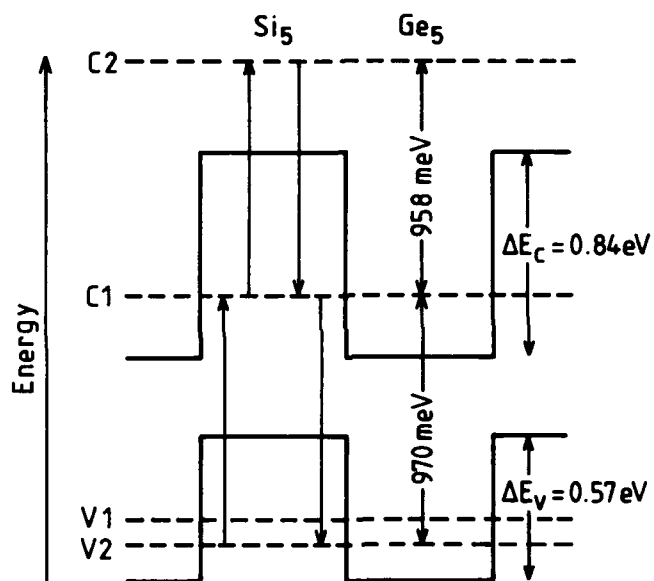


Figure 4.

#### ACKNOWLEDGEMENTS

It is a pleasure to thank the SERC (UK), ESPRIT-Basic Research European Programme, ONR (USA) and the University of Newcastle upon Tyne Research Committee for financial support.

#### REFERENCES

- M. Jaros, *Semic. and Semimet.* **32**, 175 (1990).
- E. Kasper and F. Schaffler, *Semic. and Semimet.* **33**, 223 (1991).
- I. Morrison and M. Jaros, *Phys. Rev. B* **42**, 3749 (1990).
- R.J. Turton and M. Jaros, *Mat. Sci. and Engin. B* **7**, 37 (1990).
- R.J. Turton, M. Jaros and I. Morrison, *Phys. Rev. B* **38**, 8397 (1988).

## Momentum conservation in 1D-2D tunnelling processes

J.Smoliner, W.Demmerle, E.Gornik, G.Böhm, G.Weimann

Walter Schottky Institut, TU- München, Am Coulombwall, D-8046 Garching, Germany

**ABSTRACT :**Using tunneling spectroscopy, we have investigated two independently contacted two dimensional electron gas systems, which are separated by a barrier of 195 Å. As the electron momentum parallel to the barrier is conserved for 2D-2D tunneling, resonances in the tunneling characteristics  $dI/dV$  are observed each time, a subband in one 2D channel matches a subband on the other side of the barrier. Structuring the upper 2D-channel into quantum wires, we also investigate tunneling processes between states of different dimensionality. Momentum conservation in the direction of free motion in the quantum wires leads to resonances in the tunneling characteristics each time 1D and 2D subband are aligned energetically. As the electron momentum in the direction of 1D confinement is not conserved any longer, we also observe situations, where the 2D-Fermi level matches the 1D subband energies. These two types of transitions are directly distinguished by a different temperature behavior of the corresponding peak amplitudes.

### 1. INTRODUCTION

One dimensional (1D) structures, so called quantum wires, offer a variety of new effects such as the quenching of the quantum hall effect (Roukes(1987)) mobility modulations (Ismail(1989)) or boundary scattering (Thornton(1989)), which are not observed in two dimensional (2D) systems. To understand these properties quantitatively, the 1D-subband energies can be determined by magnetic depopulation (Berggren(1986)). Alternatively, the subband spacings can be extracted from Dingle-plots (Lakrimi (1989)) the nonlinear behavior of the magneto conductance at extremely low magnetic- fields (Thornton (1986)) or tunneling spectroscopy data (Hirler (1990)). Far infrared transmission measurements were also used to study the properties of 1D-systems. On GaAs-AlGaAs quantum wires, Brinkop (1988) and Alsmeyer (1988) observed far infrared absorption lines due to intersubband resonances. The discrepancies between the far infrared data ( $\Delta E \approx 6$  meV)

and the magneto transport measurements ( $\Delta E \approx 1.5$  meV) are attributed to large depolarization effects. Similar experiments were performed on InSb (Hansen (1987)) where, due to the small effective mass, 1D-subband spacings in the order of 10 meV can be achieved easily. Since the simple oscillator model is not always sufficient to explain the experimental results, modified potentials (Berggren(1986), Rundquist(1989)) density of state effects and the influence of lifetime broadening due to scattering processes were taken into account (Berggren (1988)). For split gate geometries, self consistent calculations were performed for Si-SiO<sub>2</sub>, GaAs-AlGaAs field effect transistors (Laux (1986a) (1986b) (1988)) and on Si-grating gate structures (Warren (1986)).

In this paper, we extend our previous experiments on barrier separated 2D systems (Smoliner (1889a), (1989b), (1990)) to tunneling processes, where electrons are transferred between quantum wires and a two dimensional electron gas. By analyzing the transition rules, we are able to explain the features of the tunneling characteristics and determine quantitatively the subband energies. Subband spacings up to 4.5 meV are obtained from the experimental data and are verified by the results of a two-dimensional self consistent model.

## 2. EXPERIMENTAL :

The samples consist of an unintentionally p-doped GaAs layer grown on a semiinsulating substrate ( $p < 10^{15}$  cm<sup>-3</sup>), followed by an undoped spacer ( $d = 50$  Å), doped AlGaAs ( $d = 45$  Å,  $n = 6 \cdot 10^{18}$  cm<sup>-3</sup>, another spacer ( $d = 100$  Å) and n-doped GaAs ( $d = 800$  Å,  $n = 1.2 \cdot 10^{18}$  cm<sup>-3</sup>). An additional GaAs cap layer was highly n-doped ( $d = 150$  Å,  $n = 6.4 \cdot 10^{18}$  cm<sup>-3</sup>). Shubnikov-de Haas measurements on the unstructured samples were used to determine the electron concentrations in the inversion- and accumulation layer ( $n^{inv} = 6.1 \cdot 10^{11}$  cm<sup>-2</sup>,  $n^{acc} = 5.4 \cdot 10^{11}$  cm<sup>-2</sup>). Prior to quantum wire fabrication, ohmic contacts to both channels were aligned using a AuGe alloy. Then, a = 400 nm holographic photoresist-gratings were fabricated on the mesas. In order to deplete the accumulation layer in the uncovered regions, the wires were etched wet chemically 400 Å deep into the GaAs. After removing the photoresist, AuGe was evaporated on the total area of the tunneling contact. Contacts to the quantum wires are then induced by a shallow diffusion process, while the etched areas between the wires are still surface depleted. This is shown schematically in fig.1(a). Note, that the high doping inside the barrier screens the lower channel from depletion. Finally, the GaAs layers around the top contact were removed selectively, yielding independent contacts both to the quantum wires and to the 2D-gas. By applying a voltage  $V_b$ , the 1D-states are shifted energetically by  $eV_b$  with respect to 2D-electron gas (fig.1(b)). All transitions between these states of different dimensionality are

reflected in the tunneling current, allowing a direct determination of the 1D-quantization energies.

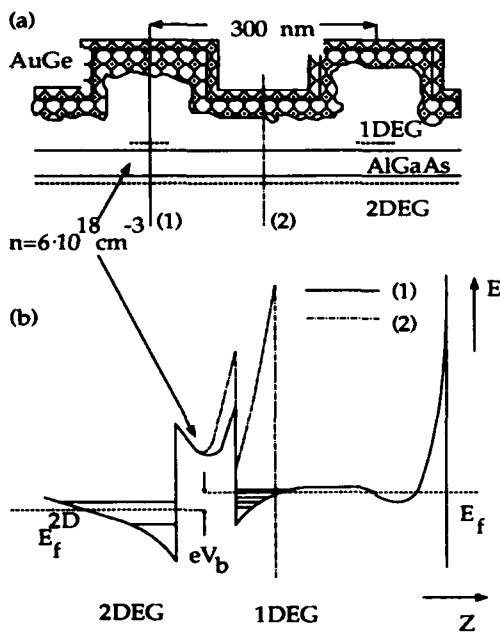


Fig.1 (a) Schematic view of the sample used. (b): Corresponding bandstructure along cut(1) (non etched areas, solid line) and cut (2) (etched areas, dashed line)

### 3. 2D-1D TUNNELING PROCESSES :

In fig.2, curve (1) shows the  $dI/dV_b$  characteristics of an unstructured sample where large peaks are observed in the considered voltage range. As demonstrated earlier, these peaks are due to resonant tunneling processes between the two barrier separated 2D-channels, which occur each time a subband in the accumulation layer matches a subband in the inversion layer lying below. The 1.7K  $dI/dV_b$  characteristics of the nanostructured sample (curve (2)), however, looks completely different. Here, rich structure is observed in the whole voltage range. At 10 K, the amplitude of the observed peaks generally decreases, certain peaks (marked by arrows) however, disappear immediately. At 35 K, there are only four broad peaks left, whose number reduces to two at 60 K. Note that these peaks are at positions, where 2D-2D resonances are observed on unstructured samples.

To analyze these  $dI/dV$  peak positions, we first consider the possible transitions from the lowest subband in the 2D-channel,  $E_0^{2D}$ , into quantum wire states. As the momentum in the direction of free motion (y-direction) can be neglected, resonant transitions from the 2D-gas into the  $n$ -th quantum wire level are possible in the entire energy range :

$$E_0^{2D} < E_n^{1D} < E_0^{2D} + \hbar^2 k_f^2 / (2m^*) \quad (1)$$

where  $k_f$  is the Fermi vector in x-direction. At positive bias, this leads to structure in  $dI/dV_b$  each time empty 1D-levels enter and leave the resonance range, which corresponds to situations where  $E_0^{2D} = E_n^{1D}$  and  $E_f^{2D} = E_n^{1D}$ . At negative bias, resonant  $dI/dV_b$  structures

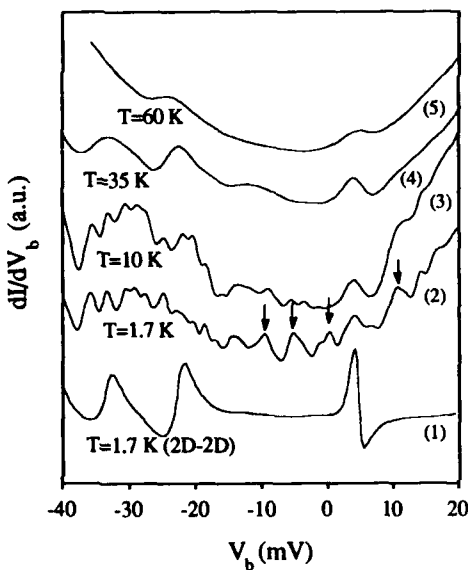


Fig.2: 1D-2D  $dI/dV$  characteristics measured at different temperatures. For comparison, a 2D-2D tunneling curve (1) is also shown.

will only occur if a filled 1D-subband matches an empty 2D-subband. In this case, the resonance condition is:

$$E_n^{2D} = E_m^{1D} \quad (2)$$

where  $n$  and  $m$  denote the subband indices. In addition to the resonant tunneling processes, non resonant processes will also cause structures in  $dI/dV_b$ . In reverse bias, electrons can tunnel from the quantum wires into the 2DEG non resonantly, if the incoming electron is energetically higher than the Fermi level in the 2D-gas,  $E_f^{2D}$ . If the energy of the incoming electron is below  $E_f^{2D}$  tunneling will not occur, since the states in the target electrode are occupied. Therefore, structure is expected in  $dI/dV_b$  each time a filled 1D subband crosses the 2D-Fermi energy :

$$E_f^{2D} = E_n^{1D} \quad (3)$$

Through these transition rules, the temperature behavior of the tunneling characteristics is qualitatively explained. Fig.3 (a) illustrates the situation at 1.7 K. According to eq. (2) and eq.(3) a large number of peaks is expected at low temperatures, which are really observed experimentally. At 10 K, the increased temperature smears out the 2D Fermi level, so that the matching between the 1D subbands and the 2D Fermi energy is no longer observed (b). Thus, the amplitude of the corresponding peaks decreases drastically. At 35 K (fig.3(c)), the increasing temperature broadens the energy levels on the 1D side, so that it is no longer possible to distinguish between single 1D states. Thus, structure in the tunneling characteristics is only produced by the lowest and the highest occupied 1D subband matching a new 2D subband edge. Above 35 K,  $kT$  is drastically larger than the 1D subband energy differences. In this temperature range, the remaining structures are due to situations, where the lowest 1D subband matches a 2D subband edge (fig.3(d)). This also explains, why these peaks are observed nearly at the same positions like the 2D-2D tunneling resonances.

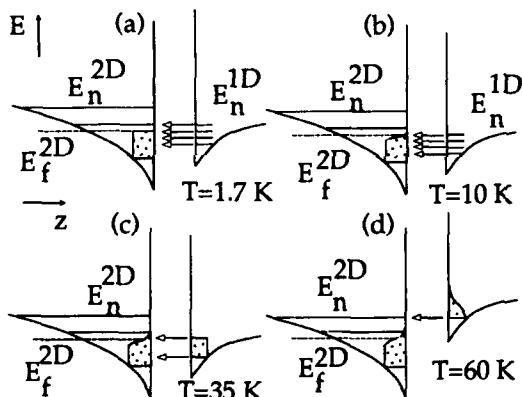


Fig.3 : Schematic view of level broadening effects due to increasing temperature.

To analyze these experimental results quantitatively, the wire potential and the corresponding 1D-subband energies were also calculated self consistently for a  $a=300$  nm sample (Smoliner (1991)). As result, we obtain a 1D-electron concentration of  $3.3 \cdot 10^6$  cm $^{-1}$  at  $V_b=0$  V and four occupied 1D subbands having energy spacings of  $\Delta E^{1D}_{01}=4.57$  meV,  $\Delta E^{1D}_{12}=4.13$  meV,  $\Delta E^{1D}_{23}=3.73$  meV,  $\Delta E^{1D}_{34}=3.41$  meV, and  $\Delta E^{1D}_{45}=3.29$  meV. The indices denote the 1D subband numbers. These extremely high quantization energies for GaAs quantum wires might be explained by the following considerations: As mentioned above, AuGe was used to establish contacts to the quantum wires. Through heating the samples for contact formation, the AuGe diffuses into the structured surface and approaches the wire from the top and the sidewalls of the etching profile. This leads to an area of high doping concentration, which closely surrounds the wire and results in a steep and narrow potential. Thus we conclude, that appropriate surface doping processes or a regrowth of

highly doped layers on the fabricated quantum wires can be used to increase the 1D-quantization energies.

#### 4. CONCLUSION

In summary, we have studied the tunneling processes between multiple quantum wires and a two dimensional electron gas. Although separated by a barrier of only 195 Å, independent contacts to the quantum wires and the 2D-gas were achieved. 1D-subband spacings up to 4.5 meV are observed and quantitatively verified by the results of a two dimensional self consistent simulation. Through temperature dependent measurements, 1D-2D subband resonances and situations where the 2D Fermi level matches a 1D subband, are directly distinguished.

**ACKNOWLEDGEMENTS :** This work was sponsored by Deutsche Forschungsgemeinschaft, SFB 348, Project A2

#### REFERENCES :

Alsmeier J Sikorsky Ch Merkt U 1988 Phys Rev B37 4314  
 Berggren K F Roos G van Houten H 1988 Phys Rev B17 10118  
 Berggren K F Newson D J 1986a Semicond Sci Technol 1 327  
 Berggren K F Thornton T J Newson D J Pepper 1986b Phys Rev Lett 57 1769  
 Brinkop F Hansen W Kotthaus J P Ploog K 1988 Phys Rev B37 6547  
 Ismail K Antoniadis D A Smith H I Appl Phys Lett 54 1130 (1989)  
 Hansen W Horst M Kotthaus J P Merkt U Sikorsky Ch Ploog K 1987 Phys Rev Lett.58  
 2586  
 Hirler F Smoliner J Gornik E Weimann G Schlapp W 1990 Appl Phys Lett 57 261  
 Lakrimi M Grassie A D C Hutchings K M Harris H H Foxon CT 1989 Semicond.  
 Sci. Technol 4 313  
 Laux S E Stern F 1986a Appl Phys Lett 49 91  
 Laux S E Warren A C 1986b Int El Device Meeting LA 567  
 Laux S E Frank D J Stern F 1988 Surface Science 196 101  
 Roukes M L Scherer A Allen S J Jr. Craighead H G Ruthen R M Beebe E D Harbison J P  
 1987 Phys Rev Lett 59 3011  
 Rundquist H J 1989 Semicond Sci Technol 4 455  
 Smoliner J Gornik E Weimann G 1989 Phys Rev B 39 12937  
 Smoliner J Demmerle W Berthold G Gornik E Weimann G Schlapp W 1989 Phys Rev Lett  
 63 2116  
 Smoliner J Berthold G Strasser G Gornik E Weimann G Schlapp W 1990 Semicond Sci  
 Technol 5 308  
 Smoliner J Berthold G Reinacher N 1991 Semicond Sci Technol 6 642  
 Thornton T J Roukes M L Scherer A van de Gaag B P 1989 Phys Rev Lett 63 2128  
 Thornton T J Pepper M Ahmed H Andrews D Davies G J 1986 Phys Rev Lett 56 1198  
 Warren A C Antoniadis D A Smith H I 1986 IEEE El Dev Lett EDL-7 7 413

## Gated resonant tunnelling diodes

**P. H. Beton, M. W. Dellow, P. C. Main, L. Eaves, T. J. Foster, C. J. G. M. Langerak  
M. Henini and A. F. Jezierski**

Department of Physics, University of Nottingham Nottingham NG7 2RD, United Kingdom.

**S. P. Beaumont and C. D. W. Wilkinson**

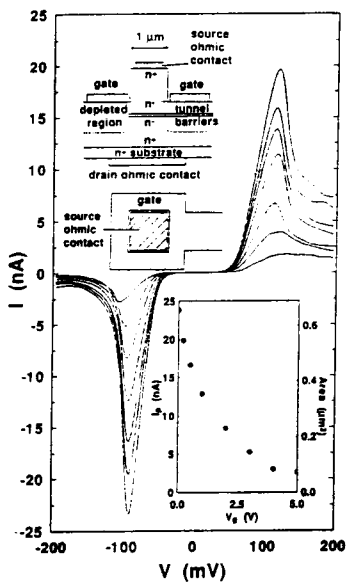
Department of Electronics and Electrical Engineering, University of Glasgow, Glasgow G12 8QQ, United Kingdom.

**ABSTRACT:** The fabrication and operation of a gated GaAs/(AlGa)As resonant tunnelling diode is described. By biasing the gate the cross-sectional area, and hence the I(V) characteristic may be varied. At low temperatures, the I(V) characteristics exhibit a series of sharp peaks below the expected threshold for resonant tunnelling. We argue that this is due to inhomogeneities in the device, which give rise to localised preferential current paths, and that the inhomogeneities are due to donor impurities in the quantum well. At large negative gate biases an asymmetry in I(V) develops. This is discussed in terms of a lateral variation of the voltage drop across the tunnel barriers.

The strongly non-linear I(V) characteristics of double-barrier resonant tunneling diodes (RTDs) are a direct manifestation of the quantum confinement of electrons in a potential well formed between two barriers (Chang et al, 1974). This leads to quantisation of motion perpendicular to the barriers. By fabricating RTDs with sufficiently small lateral dimensions ( $< 1 \mu\text{m}$ ), it may be possible to form laterally confined *zero dimensional states* for which motion parallel, as well as perpendicular, to the barriers is quantised. New features appearing in the I(V) of such devices have been attributed to both lateral confinement (Reed et al, 1988; Tewordt et al, 1990; Su et al, 1991a) and Coulomb blockade (Groshev et al, 1990; Su et al, 1991b). However, it is difficult to show experimentally that these features are directly related to the lateral dimension of the device, since two-terminal devices with fixed lateral dimensions have been used. We have recently fabricated (Dellow et al, 1991a) a three terminal RTD in which the effective lateral dimension may be varied using a gate electrode. In this paper we describe the basic features of this type of device and give an account of the variation of I(V) with gate voltage and temperature.

Our device, shown schematically in the inset of Figure 1, is similar to one described by Kinard et al, (1990). It is fabricated from a semiconductor layer grown by molecular beam epitaxy (MBE) with  $\text{Al}_{0.4}\text{Ga}_{0.6}\text{As}$  barriers, of thickness  $b=5.7\text{nm}$ , separated by a GaAs quantum well of thickness  $w=12\text{nm}$ , in which the lowest quasi-bound state energy  $E_1$  is calculated to be 24meV. The barriers are separated from the doped n-type GaAs contact regions by an undoped GaAs spacer layer 3.4nm thick and the doping varies from a low value,  $2 \times 10^{16}\text{cm}^{-3}$ , close to the barriers, to a high value,  $2 \times 10^{18}\text{cm}^{-3}$ , over a thickness of order  $1 \mu\text{m}$ . By increasing the (negative) gate voltage,  $V_g$ , the extent of the depletion region may be increased, thereby reducing the effective conducting area of the device.

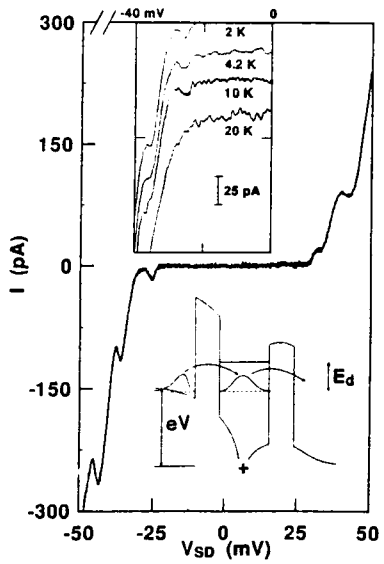
Figure 1 shows the low temperature ( $T=4.2\text{K}$ ) I(V) curves, for various  $V_g$ , measured on a typical device (Device 1). The gate voltage is applied with respect to the earthed substrate. The current  $I$  is measured from the voltage across a series resistor. In the figure,  $V_{SD}$  refers to the voltage drop

**Figure 1**

The source-drain  $I(V)$  characteristic measured at 4.2K for various gate voltages  $-V_g=0V, 0.2V, 0.5V, 1.0V, 3.0V, 5.0V$  in order of decreasing peak current. Forward bias corresponds to top contact biased positive for a typical device (Device 1). A schematic diagram of the device is shown in the top inset. The variation of peak current and cross sectional area with gate voltage is shown in the lower inset.

between the top contact and the substrate. Peaks are observed in each polarity due to resonant tunneling of electrons through the quasi-bound well state. The current, and therefore the effective cross sectional area,  $A$ , of the device, may be varied by applying a voltage to the gate. By comparing the values of peak current in reverse bias for samples with widths  $1\ \mu\text{m}$ ,  $1.5\ \mu\text{m}$  and  $2\ \mu\text{m}$ , we can calculate the reverse bias peak current density,  $j$ . We find  $j = 3.6 \times 10^4\ \text{A/m}^2$ . To a good approximation  $I(V)$  in reverse bias scales with the peak current in reverse bias,  $I_p$ , and so we may deduce a value for  $A$  from the relation  $A = I_p/j$ . The variation of  $A$  with  $V_g$  is shown in Figure 1 (inset).

We now focus on the  $I(V)$  close to the threshold for conduction. These are plotted for  $V_g=0$  in Figure 2 (for Device 2,  $1\ \mu\text{m}^2$  mesa, similar to Device 1) in which a series of peaks are clearly seen. A peak to valley ratio (PVR)  $\sim 3$  is observed for the first peak in reverse bias. We have observed similar, although not identical, structure in several devices. Figure 2 (inset) plots  $I(V)$  at temperatures from 2K to 20K at  $V_g=0$ . The structure clearly persists up to  $\sim 10\text{K}$ . The peaks in reverse bias occur at  $-26, -36$  and  $-44\text{mV}$ , and those in forward bias at voltages  $31, 40$  and  $50\text{mV}$ . The voltage threshold for resonant tunneling is  $V_{th} \sim 50\text{mV}$  (calculated from the well width and doping profile (Leadbeater et al, 1989)), so the structure shown in Figure 2 occurs at subthreshold values of voltage.

**Figure 2**

$I(V)$  close to threshold at zero gate voltage measured at 39mK for Device 2. The lower inset shows the conduction band profile close to an ionised donor for an applied voltage  $V$ . The upper inset shows  $I(V)$  in reverse bias close to threshold at zero gate voltage for temperatures  $T=2\text{K}, 4.2\text{K}, 10\text{K}, 20\text{K}$  from top to bottom respectively.

In Figure 3 we plot  $I(V)$  measured at  $T=39\text{mK}$  for various gate voltages in reverse bias. For  $1.7\text{V} > V_g > 0\text{V}$  the amplitude and position in voltage of the first maximum in reverse bias is very weakly affected. In Figure 3 (inset) the voltage positions of the peaks in reverse bias are plotted against gate voltage. The peaks at  $V_{SD} = -36\text{ mV}$  and  $V_{SD} = -43\text{ mV}$  are also weakly dependent on  $V_g$ , although the peak at  $V_{SD} = -36\text{ mV}$  splits into two peaks, then moves to a lower voltage. For  $V_g > 1.7\text{V}$  the subthreshold structure is more strongly affected by gate voltage. In particular, there is no longer any structure at  $V_{SD} = -26\text{mV}$  for  $V_g > 2.1\text{V}$ .

As we have discussed previously (Dellow et al, 1991b) this body of experimental indicates that the additional sub-threshold peaks in  $I(V)$  cannot be explained by a model based on either lateral quantisation or Coulomb blockade, resulting from the electrostatic confining potential of the gate. Our explanation of these effects is that current flows through a locally favourable path associated with an inhomogeneity in the active region of the device. This also consistent with the relative insensitivity of the peak position on magnetic field up to  $5\text{T}$ . We propose that the microscopic origin of the inhomogeneity is a donor impurity unintentionally situated in the quantum well of the RTD. A local minimum in the potential is formed due to this donor with associated bound states in the well. The binding energy,  $E_d$ , of the lowest energy bound state depends on the position of the donor in the quantum well. For a well width  $w=12\text{nm}$   $E_d$  has been calculated (Greene and Bajaj, 1983) to be  $12\text{meV}$  for a donor at the centre of the well and  $8\text{meV}$  for a donor at the well/barrier interface. Current flows when sufficient voltage is applied for an electron close to the emitter to tunnel through the donor-bound well states. Taking  $E_d \sim 10\text{meV}$ , the corresponding applied voltage for current to flow is  $\sim 2(E_1 - E_d)/e \sim 30\text{mV}$ , in good agreement with our data. In effect, we have proposed that lateral quantum confinement does occur. However, it does not arise from the depletion potential provided by the gate but rather from the presence of one or a small number of randomly placed ionised donors which form bound states through which electrons may resonantly tunnel. A likely mechanism for these unintentionally placed impurities is Si segregation on the growing front. On the basis of the data presented by Harris et al (1991) we would expect Si segregation to give rise to  $\sim 1\text{-}2$  donors in the quantum well of a device with area  $0.1\mu\text{m}^2$ .

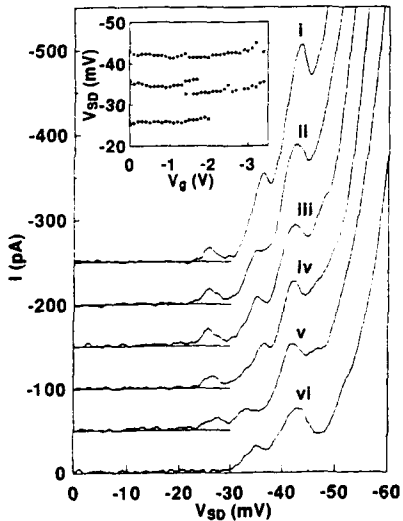


**Figure 3**  
The gate voltage dependence of the reverse bias  $I(V)$  for various gate voltages -  $V_g$  = (i) 0V, (ii) 0.6 V, (iii) 1.1 V, (iv) 1.5 V, (v) 1.9 V, (vi) 2.5 V (Device 2).

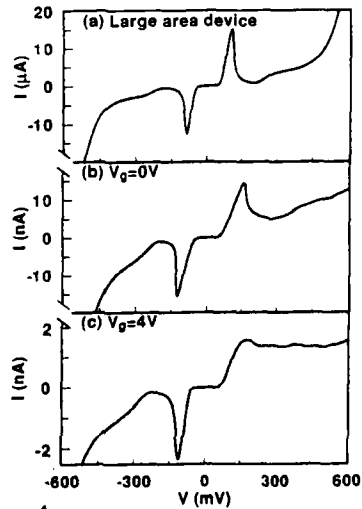


**Figure 4**  
 $I(V)$  characteristics measured at  $T=4.2\text{K}$  of (a) a large diameter device; (b) a gated device (Device 3) at zero gate voltage; (c) a gated device (Device 3) with a voltage  $V_g = 4\text{V}$  on the gate.

Figure 4a shows  $I(V)$  for a large diameter device fabricated from the same wafer as the gated device in which there is a peak in each bias direction due to resonant tunneling of electrons through the well (for a general discussion of resonant tunneling in conventional large area devices, see Leadbeater et. al, 1989). As expected for a symmetric RTD,  $I(V)$  has a high degree of symmetry. Figure 4b shows  $I(V)$  of a gated device (Device 3) with  $V_g=0V$ , for which  $A=0.45 \mu\text{m}^2$ , and Figure 4c shows  $I(V)$  for the same gated device with  $V_g=4V$ , for which we deduce  $A=0.06\mu\text{m}^2$ . The three sets of data in Fig. 4 are plotted on different scales in order to emphasise the reduction of the degree of symmetry as the device dimension,  $d$ , ( $\sim A^{1/2}$ ) is reduced. Comparing Figs. 4a, 4b and 4c it is clear that in reverse bias all three curves are similar, if they are scaled in proportion with their peak current, with a PVR  $\sim 20$ . In contrast if we compare the forward bias curves in Figs 4a and 4b we see a reduction in the PVR in the small device as compared with the large device. When  $V_g$  is increased to 4V the PVR is further reduced to  $\sim 1$  (see figure 4c). A further difference in the forward bias  $I(V)$  shown in Figs 4a-c is the appearance of extra structure as  $A$  is decreased. The structure is absent for the large diameter device, but develops into a series of clear maxima and minima as  $A$  is progressively decreased. The forward bias data is similar to that observed for sub-micron two terminal devices (Reed et al, 1988; Su et al, 1991, Tarucha et al, 1990). Note also that the ratio between peak currents in forward and reverse bias is a factor of 2 lower in Figure 4c compared with Figure 4a.

We propose that the origin of the asymmetry and low peak to valley ratio in the gated device is related to the shape of the equipotentials close to the tunnel barriers, which in forward bias gives rise to a voltage drop across the barriers which is not uniform over the device. Figure 5a-c shows a schematic diagram of the potential distribution close to the barriers in zero, forward and reverse bias respectively.

In a large area device, when a source drain voltage is applied, an accumulation layer is formed close to the cathode barrier and a depletion region formed by the anode barrier. The resulting electric field is perpendicular to the barriers and the consequent voltage drop across the barriers is uniform across the device. In contrast, close to the edge of the conducting region (i.e. the accumulation layer) of the gated samples in forward bias, the electric field is not perpendicular to the barriers and the potential drop across the barriers is therefore not uniform across the device. To understand this we consider the maximum thickness  $t_e(\rho)$  as shown in Figure 5a, which may be further depleted at a distance  $\rho$  from the centre of the device, when a source drain voltage  $V$  is applied. To a first approximation this is equal to the thickness of the region following the anode barrier which, for  $V=0$ , remains undepleted under the application of a gate voltage. For a large area device, the depth of the depletion region,  $t$ , is related to the voltage drop across the barriers,  $V_b$ , by the equation  $V_b = n(b+t/2)/\epsilon_f\epsilon_0$ , where  $n=2\times 10^{16}\text{cm}^{-3}$  is the doping in the GaAs close to the barriers, and  $b \sim 30\text{nm}$ , is the total thickness of the well, barriers and spacer layers. In forward bias there is therefore an "edge region" of width  $w$  for which  $t > t_e$ , in which the electric field is not perpendicular to the plane of the barriers. The lateral variation of the voltage drop across the device means that the edge of the device goes on and off resonance at a higher voltage than the centre of the device, as shown schematically in the two band diagrams directly below Figure 5b. This results in a smearing of the resonance over a range of source drain bias with a consequent reduction of the PVR.

In reverse bias (Fig. 5c) no such complications arise, since there is no practical limit to the thickness of the depletion layer which may be formed directly below the electron accumulation layer. The voltage across the barriers at the edge of the device is therefore the same as it is at the centre of the device. Accordingly the reverse bias  $I(V)$ , if scaled by the peak current, closely resembles that of a large area device.

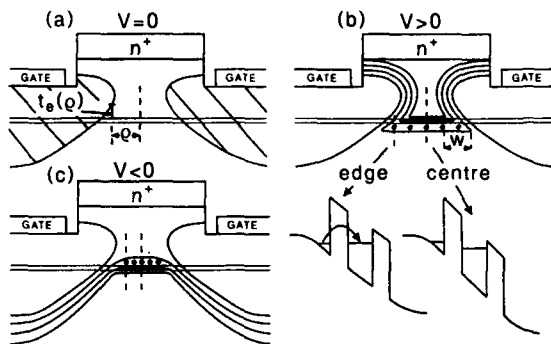


Figure 5

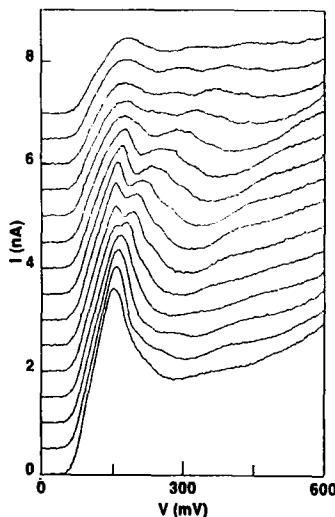
Schematic diagram of the equipotentials and depleted regions in (a) zero, (b) forward, and (c) reverse bias. The region depleted by the gate is shown hatched in (a). The electrons in the emitter accumulation layer are shown as closed circles. The band diagrams below Figure 5b show the situation with the device on resonance at the edge but off resonance at the centre.

We now estimate the voltage over which the resonance is smeared and the relative areas of the *edge region*, where the voltage across the barriers varies, and the *centre*, where this voltage is constant as it would be in a large area device. We estimate that the effective width of the edge region,  $w$ , is equal to  $t$  the depth of the depletion region,  $w \sim t$ . Note that this relation would be exact if the equipotentials crossed the tunnel barriers at an angle  $45^\circ$  and is correct to within a factor 2 over a large range of angles. The ratio,  $r$ , of the area of the edge and the central area which remains unaffected by the edge is  $r \sim [d^2/(d-2w)^2 - 1]$ . For  $V=0.15V$ , where we would expect to see a minimum in current in a large area device,  $w \sim t \sim 70nm$ . For  $V_g=0$ ,  $d \sim 0.65\mu m$  and  $r \sim 0.6$ , and when  $V_g=4V$ ,  $d=0.24\mu m$  and  $r$  is large ( $\sim 5$ ). The voltage shift of the peak at the edge of the device will be a complicated function of gate voltage, lateral position and source drain voltage. In particular it is expected to vary over the edge region from 0, close to the centre, up to  $V_b$  at the extreme edge of the device. On the basis of this simple model it is clear that edge effects will dominate  $I(V)$  in forward bias for  $V_g=4V$  reducing the PVR drastically. Edge effects are also significant even for  $V_g=0V$  leading to a reduction in PVR as compared with large area devices.

Our simple model represents a first order approximation since the application of a source drain voltage will interplay with the gate voltage so that the equipotentials shown in Fig. 5 become slightly distorted. This combination will increase the convergence of the field lines in forward bias, further exaggerating the asymmetry, whereas in reverse bias it will decrease the convergence of the equipotentials. Our model should be valid if the point of maximum depletion remains on the source side of the barriers, so that in forward bias electrons always tunnel from a region where the equipotentials diverge, to a region where they converge, and vice versa for reverse bias.

Figure 6 shows the development of the structure in the forward bias  $I(V)$  as the gate voltage is increased. We stress that over the same gate voltage range no such structure is observed in the reverse bias  $I(V)$ . Several peaks, each of which moves to higher source drain voltage as the gate voltage is increased, may be clearly seen in Fig. 6. Although these data are similar to that observed by Reed et al, 1988, Su et al, 1991 and Tarucha et al, 1990, it is clear that the peaks are due neither to Coulomb blockade, nor to lateral quantisation since: (i) they appear in only one bias direction; (ii) they are observed at a temperature  $T=4K$ , whereas such effects would be quenched for  $T>1K$  for  $d=0.5\mu m$ ; (iii) they persist up to a magnetic field of 12 T. A possible origin of the peaks is the formation of a hot electron bottleneck in the region between the barriers and the top contact which leads to a build-up of space charge. We will discuss this model together with the magnetic field data in more detail in a future publication.

The possibility of resonant tunnelling into a "zero-dimensional quantum box" has attracted great interest since the first work on this subject by Reed et al, 1988. Coulomb blockade effects in small area devices are also of great interest (Groshev et al, 1990). We believe that these effects can only

**Figure 6**

$I(V)$  characteristics of a gated resonant tunnel device (Device 3) for gate voltages from  $V_g = 2.6V$  (bottom) to  $V_g = 4V$  (top) in steps of  $0.1V$ .

be unambiguously identified in devices in which the cross sectional area can be controllably varied by a third terminal. We have described how such a device can be fabricated and have discussed its properties. Although we observe additional structure in  $I(V)$  which is similar to that previously reported, we can eliminate the possibility that it is due to either Coulomb blockade or lateral quantisation caused by the small area of the gate confinement potential.

P.H.B thanks the Royal Society for financial support. This work was funded by the Science and Engineering Research Council, U.K.

Bastard G, 1981, *Phys. Rev.* **B24**, 4714.  
 Chang L L, Esaki L and Tsu R, 1974, *Appl. Phys. Lett.* **24**, 593.  
 Dellow M W, Beton P H, Henini M, Main P C, Eaves L, Beaumont S P and Wilkinson C D W, 1991a, *Electron. Lett.* **27**, 134.  
 Dellow M W, Langerak C J G M, Beton P H, Foster T J, Main P C, Eaves L, Henini M, Beaumont S P and Wilkinson C D W, 1991b to be published in *Proceedings of NANOMES Conference*, Santa Fe.  
 Greene R L and Bajaj K K, 1983, *Solid State Commun.* **45**, 825.  
 Groshev A, 1990, *Phys. Rev.* **B42**, 5895.  
 Harris J J, Clegg J B, Beall R B, Castagne J, Woodbridge K, and Roberts C, 1991, *J. Cryst. Growth* **11** 1239.  
 Kinard W B, Weichold M H, Spencer G F and Kirk W P, 1990, *J. Vac. Sci. Technol.* **B8**, 393.  
 Leadbeater M L, Alves E S, Sheard F W, Eaves L, Hughes O H and Toombs G A, 1989, *J. Phys.: Condens. Matter* **1**, 10605.  
 Reed M A, Randall J N, Aggarwal R J, Matyi R J, Moore T M and Wetsel A E, 1988, *Phys. Rev. Lett.* **60**, 535.  
 Stanaway M B, Grimes R T, Halliday D P, Chamberlain J M, Henini M, Hughes O H, Davies M and Hill G, 1989, *Proc. Int. Conf. Shallow Impurities in Semiconductors*, published in *Inst. Phys. Conf. Ser.* **95**, 295.  
 Su B, Goldman V J, Santos M and Cunningham J E, 1991a, *Appl. Phys. Lett.* **58**, 747.  
 Su B, Goldman V J and Cunningham J E, 1991b, preprint.  
 Tarucha S, Hirayama Y, Saku T and Kimura T, 1990, *Phys. Rev. B* **41**, 5459.  
 Tewordt M, Law V J, Kelly M J, Newbury R, Pepper M, Peacock D C, Frost D E F, Ritchie D and Jones G A C, 1990, *J. Phys.: Condens. Matter* **2**, 8969.

## Tunnelling spectroscopy of a leaky electron waveguide

J. A. del Alamo and C. C. Eugster

Massachusetts Institute of Technology, Cambridge, MA 02139

**ABSTRACT:** Using an AlGaAs/GaAs modulation-doped heterostructure, we have fabricated a novel split-gate electron waveguide with a thin gate as one of its confining electrodes. This scheme implements a "leaky" waveguide out of which electrons can tunnel through the thin side-wall. The resulting tunneling current shows strong oscillations as the electron concentration in the waveguide is modulated. This result is attributed to a direct observation of the one-dimensional density of states of the electron waveguide.

### 1. INTRODUCTION

Electron waveguiding in high-mobility one-dimensional (1D) semiconductor heterostructures was unmistakably and dramatically identified when quantized steps of magnitude  $2e^2/h$  were observed in the conductance of a split-gate waveguide as its width was modulated (van Wees et al 1988, Wharam et al 1988, Timp et al 1989). In analogy with microwave and optical guided structures, this remarkable finding suggests the possibility of novel electron waveguide devices with unusual and perhaps useful characteristics. Towards this goal, in this experiment we have carried out tunneling spectroscopy of a "leaky" electron waveguide. This has allowed us to directly image the one-dimensional density of states (1D-DOS) of an electron waveguide (Eugster and del Alamo 1991).

### 2. DEVICE FABRICATION

The starting material consists of an AlGaAs/GaAs modulation-doped heterostructure with the active interface located at a depth of 545 Å from the surface. The mobility and carrier concentration at 4 K were, respectively,  $170,000 \text{ cm}^2/\text{V sec}$  and  $7 \times 10^{11} \text{ cm}^{-2}$ . A simple four-mask fabrication process utilizing conventional optical lithography was followed to define mesa, ohmic contacts, and two levels of metal interconnects. Subsequently, the samples were taken to Cornell University's National Nanofabrication Facility (NNF) where electron-beam lithography and liftoff of the active portion of the device were carried out. Micrographs of the central region of a typical device are shown in Fig. 1.

The split-gate pattern shown in Fig. 1 implements a dual electron waveguide device (Eugster et al 1992) with the ultimate goal of demonstrating a quantum field-effect directional coupler (del Alamo and Eugster 1990). The two side gates independently control the electron concentration in each waveguide, while the narrow middle gate modulates the degree of coupling between them. In order to obtain a very narrow middle gate, we drew it with a single e-beam ~~sets~~ and only the periphery of the side gates was defined (Eugster et al 1990). This allowed us to achieve a dimension of 300 Å for the critical middle gate width. Several devices with gate separations of 0.2 and 0.25  $\mu\text{m}$  and intrinsic lengths of 0.1 and 0.5  $\mu\text{m}$  were implemented. Fig.

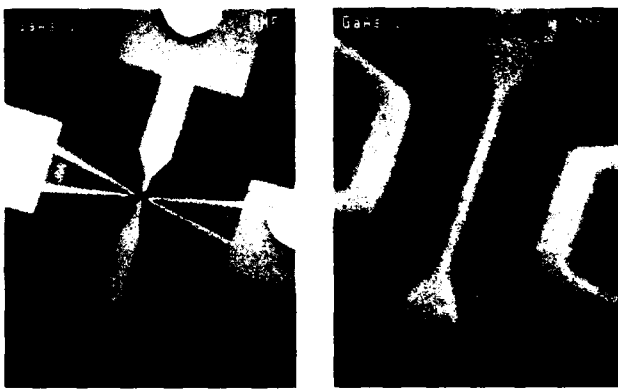


Fig. 1. Micrograph of the e-beam drawn gates of a typical device. The right picture is an enlargement of the intrinsic portion. The middle gate is 300 Å wide.

1 shows a  $0.5 \mu\text{m}$  long device with a  $0.2 \mu\text{m}$  gate separation. As seen in the figure, the middle gate was widened outside the intrinsic region to provide good isolation through short-channel effects. Four ohmic contacts (not shown) provide access to both ends of each waveguide.

### 3. DEVICE CHARACTERIZATION

In this experiment, the gates of the dual-waveguide device were biased so as to implement a leaky electron waveguide (Fig. 2). One of the gates (the "bottom" one in Fig. 2) was biased at 0 V. This results in a 2DEG underneath it. The middle-gate bias was selected so as to permit tunneling to take place through the intrinsic portion of the waveguide while providing complete isolation elsewhere. The other side gate (the "top" gate in Fig. 2) was swept to modulate the electron concentration in the waveguide. Standard lock-in techniques were used. Typically  $100 \mu\text{V}$  AC was applied across the waveguide. The side 2DEG was grounded. The currents through the waveguide and tunneling out of the waveguide into the 2DEG were monitored independently by means of two lock-in amplifiers. Temperatures down to 1.6 K were utilized.

Fig. 3 shows typical I-V characteristics for a  $0.1 \mu\text{m}$  long device with a gate separation of  $0.2 \mu\text{m}$ . The waveguide current  $I_{S1}$  shows the now familiar staircase structure with a corresponding conductance approaching  $2e^2/h$  which is characteristic of the electron waveguide regime (van Wees et al 1988, Wharam et al 1988, Timp et al 1989). The tunneling current  $I_{S2}$  displays dramatic peaks and valleys roughly lined up with the steps in  $I_{S1}$ . For  $V_{GT} > -0.6 \text{ V}$  when the waveguide has opened up into a 2DEG,  $I_{S2}$  has no features. For  $V_{GT} < -2.2 \text{ V}$  when the waveguide is turned off,  $I_{S2}$  also is turned off.

We have observed this strong structure in the tunneling current in many devices on the same wafer with a length of  $0.1$  and  $0.5 \mu\text{m}$ . The data of Fig. 4, for example, was obtained on a different device. The structure is also quite robust to temperature cycling up to room temperature, as Fig. 4 also shows. Temperature cycling results in a small shift in the threshold voltages which requires a slight adjustment of the middle gate voltage. When that is done, the structure is recovered. For devices with a wider gate separation, more plateaus in  $I_{S1}$  and correspondingly more oscillations in  $I_{S2}$  are observed - about 8 for a  $0.25 \mu\text{m}$  gate separation device.

More recently, we have processed a second wafer with a 2DEG mobility of  $1.2 \times 10^6 \text{ cm}^2/\text{V sec}$

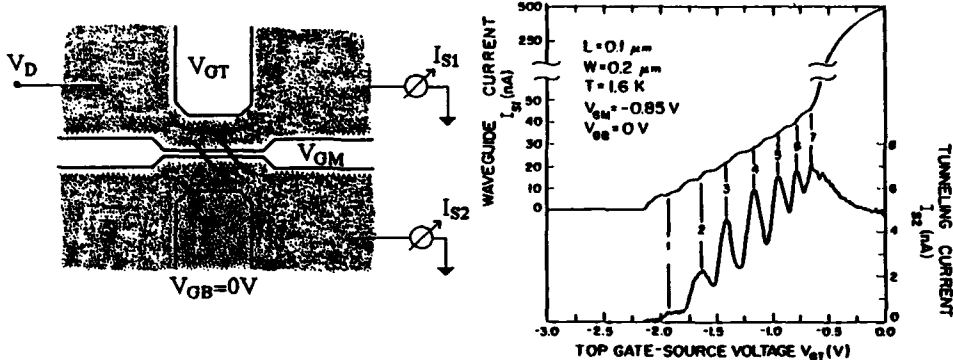


Fig. 2. Biasing scheme for the implementation of the leaky electron waveguide. The shaded regions represent the electron gas at the heterointerface.

and a carrier concentration of  $4.2 \times 10^{11} \text{ cm}^{-2}$  at 4 K where the 2DEG is located at a depth of 890 Å from the surface (Eugster et al 1992). E-beam lithography and the rest of device fabrication was carried out at a later time from the previous wafer. Much of the same structure in the tunneling current has been obtained. The improved quality of this sample allowed us to observe the structure in the tunneling current with either waveguide acting as source in the same dual-waveguide device. Additionally, the oscillations in  $I_{S2}$  are now visible in devices with lengths of 1  $\mu\text{m}$  (the quantized conductance steps are not observed in these longer devices).

The oscillations of the tunneling current are seen to wash out with a voltage across the waveguide between 2 and 3 mV and a temperature of about 10 K. They are also suppressed as the middle-gate voltage is made more negative (Eugster and del Alamo 1991).

#### 4. DISCUSSION

An understanding of the origin of the sharp structure in the tunneling current can be gained by examining Fig. 5. The application of a voltage across the waveguide splits the Fermi level between both ends by an amount equal to the electron charge times the voltage across the intrinsic device. If the waveguide is short enough, electron transport will take place ballistically giving rise to the well known staircase structure in the waveguide current.

In a leaky waveguide, some of the electrons will actually tunnel out of it. In the limit of negligible temperature and voltage broadening, the tunneling current is proportional to the product of  $T$ , the tunneling probability,  $k_{\perp}$ , the perpendicular momentum against the barrier, and  $g_{1D}$ , the 1D-DOS in the waveguide. Since  $k_{\perp}$  and  $T$  are constant for a given 1D subband, the tunneling current preserves the shape of  $g_{1D}$ . This experiment constitutes in fact true tunneling spectroscopy of the DOS of the electron waveguide.

Finite voltage and temperature result in broadening of the structure in  $I_{S1}$  and  $I_{S2}$  when the corresponding window of electrons approaches the electron subband separation in the waveguide. Our observations then allow us to conclude that the subband separation is on the order of 2 to 3 meV, in agreement with calculations for similar split-gate structures (Snider et al 1990).

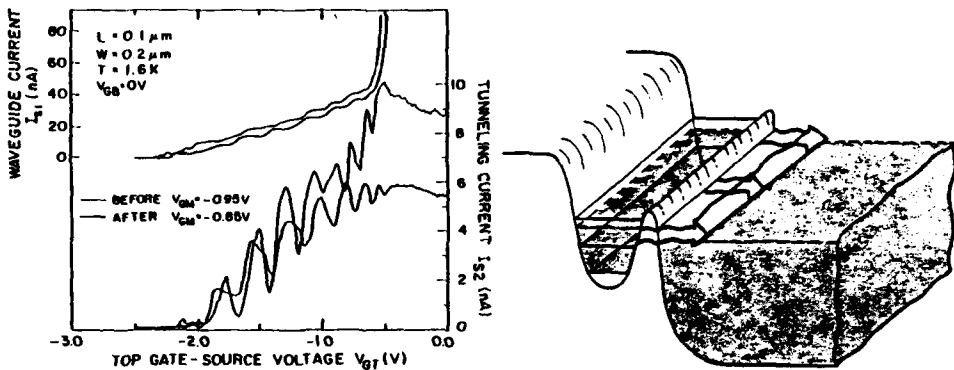


Fig. 4. I-V characteristics before and after temperature cycling of a device up to 300 K.

Fig. 5. Illustration of energy diagram of leaky electron waveguide. The arrow indicates electron tunneling.

The fact that the tunneling structure is more robust with length than the quantization of the waveguide current suggests that tunneling might not be uniformly occurring through the entire length of the intrinsic device. The unavoidable randomness of the potential distribution underneath the middle gate can easily result in relatively narrow spots where most of the tunneling actually takes place. A detailed length study is required to verify this hypothesis.

## 5. CONCLUSIONS

In summary, we have fabricated a leaky electron waveguide with a thin confining side-wall. The tunneling current leaking out of the waveguide constitutes direct spectroscopy of its one-dimensional density of states.

## ACKNOWLEDGMENTS

We would like to acknowledge M. J. Rooks of NNF, Cornell University, for electron-beam lithography, C. G. Fonstad, K. Ismail, and M. R. Melloch for epitaxial sample growth, and B. J. Wuensch for encouragement and support. This work has been funded by NSF contracts 87-19217-DMR and DMR-9022933. C. C. E. acknowledges an IBM Graduate Fellowship award.

## REFERENCES

- del Alamo J A and Eugster C C 1990 *Appl. Phys. Lett.* **56** 78
- Eugster C C, del Alamo J A, and Rooks, M. J. 1990 *Jpn. J. Appl. Phys.* **29** L2257
- Eugster C C and del Alamo J A 1991 *Phys. Rev. Lett.* **67** 3586
- Eugster C C, del Alamo J A, Rooks M J, and Melloch M R 1992 *Appl. Phys. Lett.*
- Snider G L, Tan I-H, and Hu E L 1990 *J. Appl. Phys.* **68** 5922
- Timp G, Behringer R., Sampere S, Cunningham J E, and Howard R E 1989 *Nanostructure Physics and Fabrication* eds M A Reed and W P Kirk (New York: Academic) pp 331-345
- van Wees B J, van Houten H, Beenakker C W J, Williamson J G, Kouwenhoven L P, van der Marel D, and Foxon C T 1988 *Phys. Rev. Lett.* **60** 848
- Wharam D A, Thornton T J, Newbury R, Pepper M, Ahmed H, Frost J E F, Hasko D G, Peacock D C, Ritchie D A, and Jones G A C 1988 *J. Phys. C* **21** L209

## Single electron pump and turnstile in semiconductor nanostructures

Leo P. Kouwenhoven, Alan T. Johnson, Nijs C. van der Vaart, and Kees J.P.M. Harmans

Faculty of Applied Physics, Delft University of Technology  
P.O.Box 5046, 2600GA Delft, The Netherlands

**ABSTRACT:** We have observed a quantized current in a lateral quantum dot defined by metal gates in the two dimensional electron gas (2DEG) of a GaAs/AlGaAs heterostructure. By modulating the tunnel barriers in the 2DEG with two phase shifted RF signals, and employing the Coulomb blockade of electron tunneling, we produced quantized current plateaus in the current-voltage characteristics at integer multiples of  $ef$ , where  $f$  is the RF frequency. This demonstrates that an integer number of electrons pass through the quantum dot each RF cycle.

### 1. INTRODUCTION

The ability to control electronic current on a single-electron level has become feasible by employing the Coulomb blockade in submicron devices. This single-electron control is not only interesting from a fundamental point of view, but also for obtaining a current standard and possibly for various device applications (for two reviews see: Averin, and Likharev 1990; and Grabert, Martines, and Devoret 1991). RF studies in conjunction with Coulomb effects have been performed by Geerligs et al. (1990), who applied a RF signal to the central island of a sample of 4 metal tunnel junctions in series. They observed a plateau at a current  $I = ef$ , with  $f$  the frequency of the RF signal, demonstrating that exactly one electron per RF cycle passed through their so-called *turnstile* device. Here we present the realization of a turnstile operation in a semiconductor quantum dot defined by metal gates in a two dimensional electron gas (2DEG). In contrast to the metal systems, our quantum dot turnstile relies on the ability to induce *oscillating tunnel barriers* between the quantum dot and the wide 2DEG regions by applying RF signals to the gates (see also Kouwenhoven et al. 1991a)

© 1992 IOP Publishing Ltd

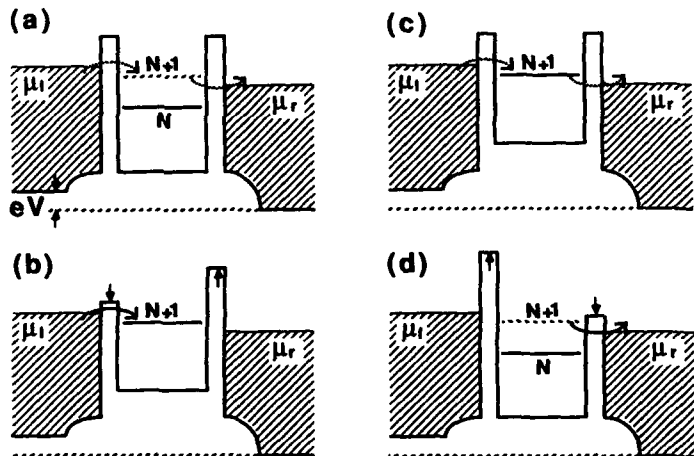


Fig. 1. Potential landscape through the quantum dot.  $\mu_l$  and  $\mu_r$  are the electrochemical potentials of the left and right reservoirs, and  $V = (\mu_l - \mu_r)/e$  is the bias voltage. The level  $N$  indicates  $\mu_d(N)$  when  $N$  electrons are confined in the quantum dot, while the level  $(N+1)$  indicates  $\mu_d(N+1)$ . (a) to (d) are 4 stages of a RF cycle where the probability for electron tunneling is large when the barrier is low (solid arrows), and small when the barrier is high (dashed arrows).

## 2. COULOMB ISLAND DEVICE

The inset of Figure 3 is a SEM photograph of the gate geometry, which is fabricated on top of a GaAs/AlGaAs heterostructure containing a 2DEG about 100 nm below the surface. The ungated 2DEG has a mobility of  $2.3 \cdot 10^6 \text{ cm}^2/\text{Vs}$  and an electron density of  $1.9 \cdot 10^{15} \text{ m}^{-2}$  at 4.2 K. We denote gate F as the finger gate, gates 1 to 4 as quantum point contact (QPC) gates, and gate C as the center gate. We do not use QPC gates 3 and 4; these gates are grounded and have no effect on the 2DEG. Applying -400 mV to gates F, C, 1, and 2 depletes the electron gas underneath them and forms a quantum dot with a diameter of about 0.8  $\mu\text{m}$  in the 2DEG. The narrow channels between gates 1-C, and 2-C are pinched-off at this gate voltage. Electron transport occurs only through the constrictions induced by gates 1-F, and 2-F, which couple the dot to the two wide 2DEG regions.

Charging effects become important when the gate voltages are such that the constrictions form tunnel barriers with conductances  $G_1, G_2 \ll 2e^2/h$ . On varying the voltage on the center gate, the conductance  $G$  of the dot is expected to oscillate between zero (Coulomb blockade) and non-zero (no Coulomb blockade). These *Coulomb oscillations* have recently been observed in quantum dots (Meirav et al. 1989; McEuen et al. 1991; charging effects on this structure without RF signals are reported by Kouwenhoven et al. 1991b) and are shown in the upper inset of Figure 2 for our sample. All measurements are performed at 10 mK and zero magnetic field. The period of the oscillations is 4.6 mV; each period corresponding to a change of one electron in the dot. For unequal tunnel barriers, a

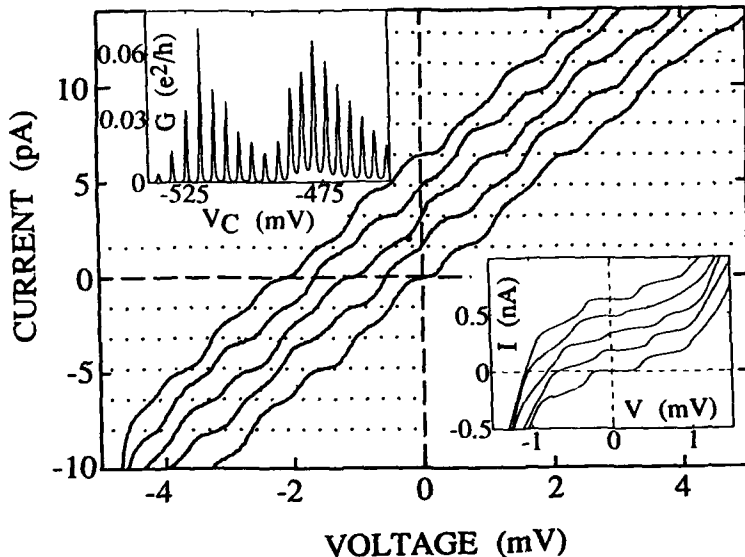


Fig. 2. Main figure: I-V characteristics when two phase shifted RF signals are applied with a frequency  $f = 10$  MHz, showing current plateaus at integer multiples of  $eV$  (dotted lines). The curves correspond to different center gate voltages and are offset for clarity by an integer times  $eV$ . Upper inset: Coulomb conductance oscillations versus center gate voltage. Lower inset: Coulomb staircase in the I-V characteristics (the curves correspond to different center gate voltages and are offset for clarity).

stepwise increase of the current  $I$  upon increasing the bias voltage  $V$  is expected (Averin, and Likharev 1990). This *Coulomb staircase* is shown in the lower inset of Figure 2. The 5 different curves correspond to different center gate voltages: the lowest curve is at a Coulomb oscillation minimum, the curve in the middle at a conductance peak, and the uppermost curve at the next minimum. The width  $\Delta V = 0.67$  mV of the current plateaus is a direct measure of the charging energy:  $e\Delta V = e^2/C$ , from which we deduce the total capacitance  $C = 2.4 \cdot 10^{-16}$  F.

### 3. QUANTUM DOT TURNSTILE

We now demonstrate that with oscillating tunnel barriers, the Coulomb oscillations and staircase are determined by the frequency of the applied RF signals. Figure 1 represents 4 stages of a RF cycle, where the tunnel barriers oscillate with a phase difference of  $\pi$  (Odintsov 1991). In (a) the dashed arrows indicate possible tunneling via the  $\mu_d(N+1)$  charge state.  $\mu_d(N)$  is the electrochemical potential when  $N$  electrons are confined in the dot. Addition of an extra electron to the dot increases the

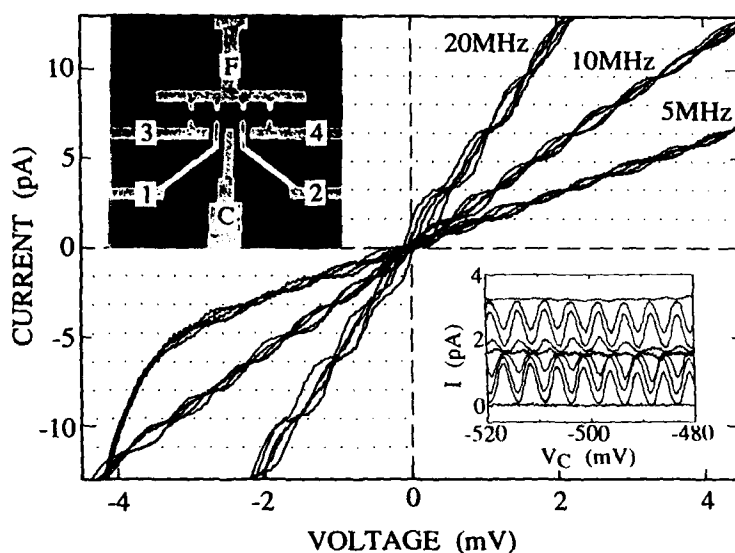


Fig. 3. Main figure: I-V curves for RF frequency  $f = 5, 10$ , and  $20$  MHz, demonstrating scaling with frequency. Dotted lines indicate multiples of  $e\cdot f$  for  $f=10$  MHz. Upper inset: Gate geometry. Lower inset: Current versus center gate voltage for  $f=10$  MHz and different fixed bias voltages. The current oscillations have a frequency determined amplitude in the interval between  $n\cdot e\cdot f$  and  $(n+1)\cdot e\cdot f$ .

electrochemical potential by  $\mu_d(N+1) - \mu_d(N) = e^2/C$ . When the left barrier is reduced, the probability for the  $(N+1)$  electron to tunnel into the dot is strongly enhanced, as illustrated by the solid arrow in (b). Simultaneously, the increase of the right barrier makes the probability to tunnel out of the dot virtually zero. Tunneling into the dot of a second electron is prevented by the Coulomb blockade. At half the cycle time, shown in (c), the barriers are in their equilibrium position again, but compared with (a), one extra electron is confined in the dot. The  $(N+1)$  electron tunnels out when the right barrier is reduced, and simultaneously, the left barrier is increased, which is illustrated in (d). Completing the cycle, yields the initial situation shown in (a), and exactly one electron has passed through the quantum dot. Repeating this process with a frequency  $f$  results in a current  $I = e\cdot f$ . Increasing the bias voltage, thereby increasing the number  $n$  of charge states contained in the energy interval between  $\mu_l$  and  $\mu_r$ , produces a quantized current  $I = n\cdot e\cdot f$ , corresponding to frequency determined current steps in the Coulomb staircase. The steps in the staircase come at voltage intervals of  $e/C$ , from which we expect an average conductance  $\langle G \rangle = e\cdot f/(e/C) = fC$ . An estimate of the accuracy of this quantized current for our experimental values (Kouwenhoven et al. 1991a) gives about 1%, somewhat better than observed in the data below.

In Figure 2 we show measured I-V characteristics with 10 MHz RF signals with a phase difference of

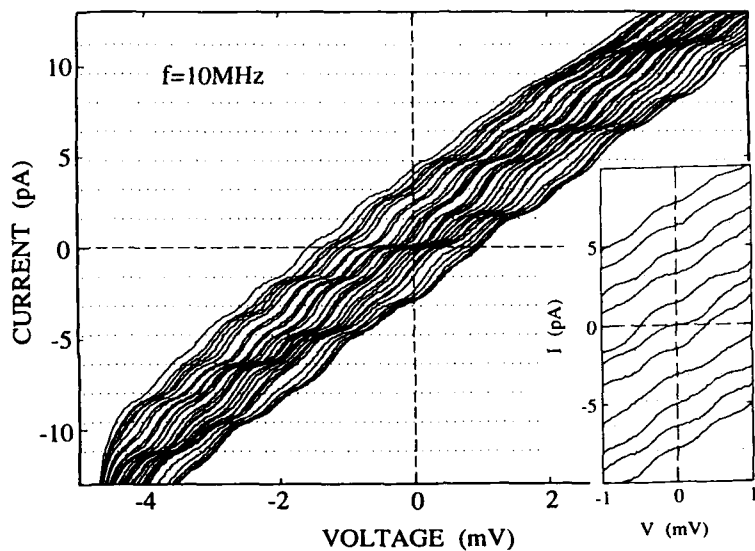


Fig. 4. I-V characteristics with fixed RF amplitude on QPC<sub>2</sub> and different RF amplitudes on QPC<sub>1</sub>, showing all the current plateaus from -7·ef to 7·ef. Inset: I-V characteristics with current plateaus from -5·ef to 5·ef at zero bias voltage, demonstrating discrete electron pumping.

$\pi$  applied to QPC gates 1 and 2. The quantized current values  $n \cdot ef$  are indicated by dotted lines [ $e(10\text{MHz}) = 1.6 \text{ pA}$ ]. The curves correspond to different center gate voltages, and are offset from each other by  $ef$ . Figure 2 shows that on applying RF, the I-V curves have current plateaus at integer multiples of  $ef$ , demonstrating that a discrete number of electrons pass through the quantum dot each RF cycle. Some of the plateaus are missing or weakly developed. This plateau averaging occurs for roughly equal tunnel barriers: the bias voltage drops across both barriers instead of dropping mainly over one barrier, as required for a well-developed staircase (Averin, and Likharev 1990).

The current plateaus are illustrated in Figure 3, where for  $f = 10 \text{ MHz}$  the same curves are shown as in Figure 2, but now without offsets. The dotted lines indicate the quantized current values  $n \cdot ef$  for  $f = 10 \text{ MHz}$ . As expected from the model, the curves have crossings that occur at current multiples of  $ef$  and voltage multiples of  $e/C$ , for  $n$  between -7 and 7. To demonstrate scaling with frequency, also I-V curves are shown for  $f = 5$  and  $20 \text{ MHz}$ , which have respectively, twice and half as many crossings as the curves for  $10 \text{ MHz}$ . Moreover, the average conductance  $\langle G \rangle = fC$  scales with frequency, and is in agreement with the value for  $C$  obtained from the Coulomb staircase shown in the lower inset of Figure 2. An alternative way of measuring the same curves is shown in the lower inset of Figure 3, where the current is shown versus center gate voltage for different bias voltages and  $f = 10 \text{ MHz}$ . The current is independent of center gate voltage and equal to  $n \cdot ef$  when the bias voltage corresponds to a crossing in the I-V curves. In between, the current oscillates with a period equal to that of the Coulomb oscillations

shown in the upper inset of Figure 2. However, the amplitude is now determined by the frequency and lies in the interval between  $n \cdot e\hbar$  and  $(n+1) \cdot e\hbar$ .

To examine the dependence of the current plateaus on RF amplitude, we measured I-V curves for  $f = 10$  MHz and fixed RF amplitude on QPC<sub>2</sub>. The RF amplitude on QPC<sub>1</sub> is increased in constant steps from the uppermost curve in Figure 4 to the lowest curve. Figure 4 shows that for the same center gate voltage, all the plateaus from  $n = -7$  to 7 are made visible by changing the RF amplitude on one QPC gate. A striking feature is that at zero voltage a non-zero current is observed, which can be either positive or negative. This is due to the influence of the RF signal on the conduction band bottom of the dot. For equal RF amplitudes on the two QPCs and phase difference  $\pi$ , this influence is compensated, so the band bottom does not move, and consequently  $I(V = 0) = 0$ . However, for unequal RF amplitudes, charge states can be pumped to higher energy and give rise to a non-zero current at zero bias voltage. From these measurements, we have been able to deduce the effect on the quantized current plateaus of the center gate voltage, the RF amplitudes, and the phase difference. To demonstrate the tunability of the quantum dot turnstile, we have measured the pumping in more detail, which is shown in the inset of Figure 4. Tuning the different parameters, *we found quantized current plateaus from  $n = -5$  to 5 around zero voltage, showing that a discrete number of electrons are pumped per RF cycle.*

In summary we have realized a quantum dot turnstile using oscillating tunnel barriers. The observation of quantized current plateaus at multiples of  $e\hbar$  demonstrates the ability to control current on a single-electron level. The accuracy of the current plateaus is a few percent, but it can be argued that this can be largely improved which is presently investigated.

We wish to thank L.J. Geerligs, K.K. Likharev, J.E. Mooij, and B.J. van Wees for stimulating discussions, A. van der Enden and D.J. Maas for their contributions to the device fabrication, and the Delft Institute for MicroElectronics and SubmicronTechnology for the use of their facilities. Financial support from FOM and ESPRIT (project 3133, NANSDEV) is gratefully acknowledged.

#### REFERENCES

Averin D.V. and Likharev K.K. 1990 in *Quantum Effects in Small Disordered Systems*, edited by B. Al'tshuler, P. Lee, and R. Webb (Elsevier, Amsterdam)  
Geerligs L.J., Anderegg V.F., Holweg P.A.M., Mooij J.E., Pothier H., Esteve D., Urbina C. and Devoret M.H. 1990 *Phys. Rev. Lett.* 64 2691  
Grabert H., Martinis J.M. and Devoret M.H. 1991 editors of *Single Charge Tunneling* (Plenum, New York)  
Kouwenhoven L.P., Johnson A.T., van der Vaart N.C., Harmans C.J.P.M. and Foxon C.T. 1991a *Phys. Rev. Lett.* 67 1626  
Kouwenhoven L.P., van der Vaart N.C., Johnson A.T., Harmans C.J.P.M., Williamson J.G., Staring A.A.M. and C.T. Foxon 1991b *Festkörperprobleme/Advances in Solid State Physics* 31 329  
McEuen P.L., Foxman E.B., Meirav U., Kastner M.A., Meir Y., Wingreen N.S. and Wind S.J. 1991 *Phys. Rev. Lett.* 66 1926  
Meirav U., Kastner M.A. and Wind S.J. 1989 *Phys. Rev. B* 40 5871  
Odintsov A.A. 1991 *Appl. Phys. Lett.* 58 2695

## Coulomb blockade in the few-electron limit

C J B Ford, M Field, P J Simpson, M Pepper, D Popovic<sup>†</sup>, D Kern<sup>†</sup>,  
J E F Frost, D A Ritchie and G A C Jones

Cavendish Laboratory, Madingley Road, Cambridge, CB3 0HE, UK

<sup>†</sup>IBM T J Watson Research Center, PO Box 218, Yorktown Heights, NY 10598, USA

**ABSTRACT:** We have studied Coulomb blockade effects in semiconductor quantum dots connected to leads via adjustable tunnel barriers. The single-particle energy level spacing becomes non-negligible compared with the Coulomb charging energy. The oscillations become irregularly spaced as the dot is made very small.

### 1. INTRODUCTION

In the past few years, technological advances in lithography and crystal growth have made it possible to create structures smaller than the elastic and inelastic mean free paths (at low enough temperatures). At the same time, the carrier concentration can be low enough that the Fermi wavelength is not much smaller than the structure, in all directions; the number of electrons in the region is then also small, less than a few hundred, for example, with very low capacitive coupling to the rest of the sample. We thus have a "quantum dot" in which the quantum-mechanical states are discrete, but in which the states are perturbed significantly by adding even one extra electron to the dot, due to the Coulomb interaction.

We have fabricated such structures using a high-mobility GaAs-AlGaAs heterostructure where the electrons form a two-dimensional electron gas (2DEG) sandwiched between a layer of GaAs and one of  $Al_xGa_{1-x}As$  (2DEG mobility  $\sim 100\text{ m}^2/\text{Vs}$ , sheet carrier concentration  $\sim 1.5 \times 10^{15}\text{ m}^{-2}$ ). A titanium/gold Schottky gate deposited on the surface depletes out the 2DEG beneath it, when negatively biased. In gaps left between such gates, the electrons are not removed, so narrow wires or pools of electrons can be formed. The depletion regions spread sideways too, depending on the gate voltage  $V_g$ , squeezing the wires. This split-gate technique has been used extensively to investigate transport in one-dimensional wires and rings (Thornton *et al* 1986, Ford *et al* 1989). Short split-gates form constrictions where the conductance is  $2ie^2/h$ , where  $i$  is the number of spin-degenerate 1D subbands (modes) formed in the constriction (Wharam *et al* 1988, van Wees *et al* 1988). When close to pinch-off, these constrictions form barriers through which the electrons have to tunnel. A pair of such tunnel barriers can be used to isolate a pool of electrons (Meirav *et al* 1989, Ford *et al* 1991, Kouwenhoven *et al* 1991). Such systems show conductance oscillations as a function of the size of the region. These are attributed to the Coulomb Blockade of electron tunnelling, due to the charging energy  $e^2/C$  associated with adding an electron to the dot (see Averin and Likharev 1991). ( $C$  is the capacitance between the dot and the rest of the sample, and may be as low as  $10^{-16}\text{ F}$ .) When the applied source-drain bias is less than the charging energy, an electron cannot tunnel into the dot as it is made larger, so conduction is suppressed until the energy of the lowest unoccupied state in the dot is  $e^2/C$  below the Fermi energy in the leads. The dot then becomes neutral again, and the process repeats, giving an oscillation in conductance every time the number of electrons in the dot changes by one. The single-

particle, quantum-mechanical states in the dot are usually much more closely spaced in energy than  $e^2/C$ , in these samples, so they are relatively unimportant. Ignoring effects of the number  $n$  of electrons in the dot on the charging energy (not necessarily a good assumption, according to Johnson and Payne 1991), the charging energy is just added to the single-particle energy level  $E_n$ , giving the change in Fermi energy  $E_F$  in the leads between oscillations as  $\Delta E_F = E_{n+1} - E_n + e^2/C$  (Meir *et al* 1991). If  $E_F$  is constant, but a gate near the dot is used to change the size of the dot, effectively moving the single-particle levels past  $E_F$ , then for reasonably large  $n$ ,  $\Delta V_g \approx \alpha(E_{n+1} - E_n + e^2/C)$  for some constant  $\alpha$ .

We have tried to move into the régime where  $E_{n+1} - E_n$  is not much smaller than  $e^2/C$ , by squeezing the dot as much as possible. We have studied two types of device, two and four-probe dots, (shown inset in Figures 1 and 2). They consist of a set of narrow gates, allowing approximately independent control of each constriction and of the size of the dot. Some gates have such small gaps between them that electrons there are depleted immediately the gates are defined, but the gates are separate so they can be biased independently. The constriction widths are 0.4  $\mu\text{m}$ , and the dot in the four-probe device starts as a 0.4  $\mu\text{m} \times 0.4 \mu\text{m}$  dot when the gates are first defined. The distance between constrictions in the two-probe device is about 0.5  $\mu\text{m}$ .

## 2. RESULTS AND DISCUSSION

The conductance of a four-probe device is shown in Figure 1, as a function of the gate shown in outline in the inset. The other gates (shown in black) are set to fairly negative voltages, pinching off the upper and right-hand constrictions, and forming tunnel barriers in the other two. The various curves are for different perpendicular magnetic fields  $B$  from 0 to 8 T. All measurements were carried out using a constant low-frequency ac voltage of 10  $\mu\text{V}$ , at temperatures below 100 mK. The oscillations have a period of 7 mV, independent of  $B$ . Although the field increases the confinement in the constrictions, raising the tunnel barriers so that they pinch off sooner, the capacitance between the dot and the rest of the sample (gates and leads) is largely unchanged.

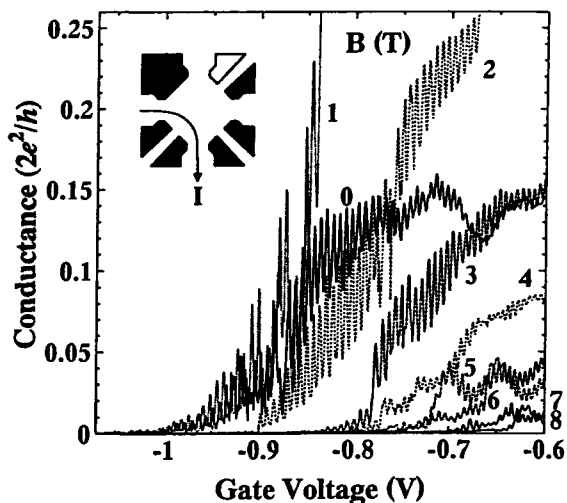


Figure 1. The conductance of a four-probe dot as a function of the voltage on gate shown in outline in the inset, for various magnetic fields, as indicated, for a particular set of voltages on the other gates.  $T < 100 \text{ mK}$ .

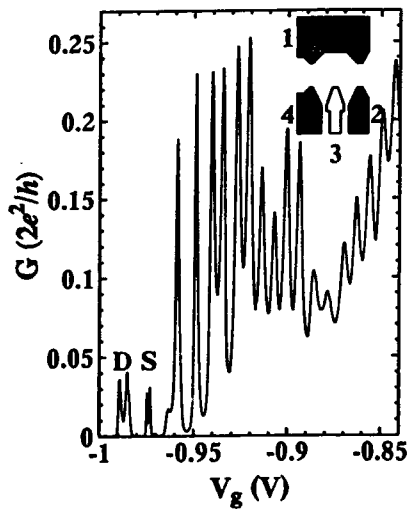


Figure 2. The conductance as a function of the plunger gate's voltage for the two-probe dot, close to pinch-off.  $B = 0$ .

If these oscillations were due to resonant tunnelling through a ladder of single-particle states, these states would easily have become spin-split by 8 T and would have changed their spacing as the magnetic confinement took over from the electrostatic confinement. The periodicity fits in with the capacitance estimated for such a gate, if the number of electrons in the dot changes by one in each period, and it scales with the number of gates (Ford 1991), although individual gates may suffer from imperfect lithography giving more or less coupling to the dot. Thus we can attribute the oscillations to Coulomb Blockade (CB) as described in the introduction.

Figure 2 shows CB oscillations for a two-probe device, where we have again two tunnel barriers and another gate (the "plunger", shown in outline in the inset) which can change the area of the dot. The periodicity is much the same as in Figure 1, but we have tried to squeeze the dot as much as possible in order to increase the single-particle energy level spacing. The oscillations become much less regular near pinch-off, with some peaks moving apart or together (such as the double peak labelled "D"). Alternatively, some peaks seem to split (eg the peak labelled "S"), although they are still so narrow that it seems unlikely that they are two peaks. Instead, we suggest that the dot may break up into two parts, effectively two dots in series, each exhibiting Coulomb Blockade. Then a zero of conductance in either dot gives a zero for the pair, causing some peaks to appear split when a zero of one lies near the middle of a peak of the other. A similar effect has been reported by Staring *et al* (1991). Figure 3 shows how the split peaks vary as one of the tunnel barriers is adjusted: the dominant peak moves from the left side of the split to the right (or the dip moves across the wide peak). Figure 4 shows how the irregular oscillations vary with  $B$ . Each curve is at a particular field  $B$ , in intervals of 0.1 T from 0 at the top to 2.9 T at the bottom. The inset

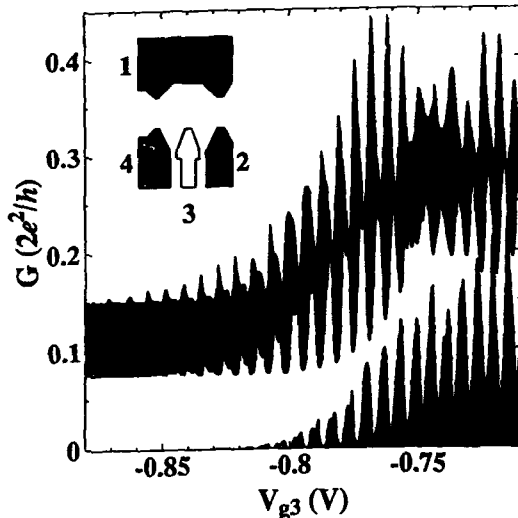


Figure 3. The conductance of the two-probe dot as a function of plunger voltage for  $V_2 = -0.85$  V and  $V_4 = -0.73$ ,  $-0.74$  and  $-0.75$  V respectively (from top to bottom), showing how the split peaks vary. The area under some of the curves is shown shaded just to make them easier to distinguish. The threshold shifts because of the change in height of the tunnel barrier on the left.  $B = 0$ .

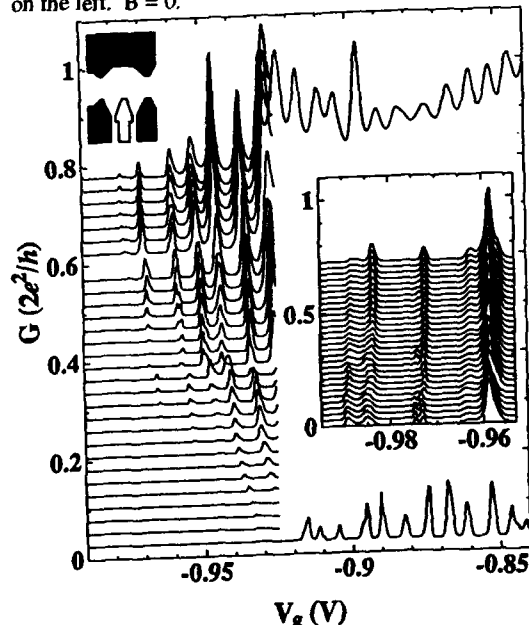


Figure 4. The conductance of the two-probe dot measured at various values of  $B$ , ranging from 0 to 2.9 T (top to bottom) in steps of 0.1 T, and in the inset from 0 to 0.6 T (bottom to top) in 0.02 T steps.

graph shows in more detail the region from  $B = 0$  (at the bottom) to  $0.6$  T (at the top) in steps of  $0.02$  T. It is apparent that the structure of each peak changes with  $B$ , but there are as yet few clear trends which can be associated with the increasing dominance of magnetic confinement or with spin splitting. We estimate  $e^2/C \sim 0.3$  meV and the energy level spacing  $\sim 0.05$  meV.

We have also tried to make a four-probe dot small by continually squeezing with one gate and occasionally relaxing the tunnel barriers to maintain conduction (Figure 5). The inset graphs show enlargements of certain areas, indicating how the period increases as the dot is made smaller, probably because the capacitance between the gate and the dot decreases (the dot is receding from the gate). In one region, the peaks become split, but then they recover, with a longer period. It would seem that the dot becomes two regions in series and then one of those regions depletes out completely, leaving only a much smaller dot. Gate hysteresis makes it difficult to optimise the size of the dot further.

### 3. CONCLUSIONS

In conclusion, we have measured multi-gate devices in which a few (between 0 and 150) electrons can be confined by tunnel barriers. Coulomb Blockade oscillations are seen, and these become irregularly spaced when the dot is small, indicating that single-particle level separations are no longer negligible compared with the charging energy. A dot may sometimes split into two smaller regions, giving rise to some of the irregular structure.

We would like to acknowledge financial assistance from the SERC.

### REFERENCES

Averin D V and Likharev K K 1991 in *Mesoscopic Phenomena in Solids*, eds Altshuler B L, Lee P A and Webb R A (Elsevier, Amsterdam)  
 Ford C J B *et al* 1989 *Appl. Phys. Lett.* **54** 21  
 Ford C J B 1991 *Physica Scripta* **T39** 288  
 Johnson N and Payne M 1991 *Phys. Rev. Lett.*  
 Kouwenhoven L P *et al* 1991 *Phys. Rev. Lett.* **67** 1626  
 Meir Y *et al* 1991 *Phys. Rev. Lett.* **66** 3048  
 Meirav U *et al* 1989 *Phys. Rev. B* **40** 5871  
 Staring A A M *et al* 1991 *unpublished*  
 Thornton T J *et al* 1986, *Phys. Rev. Lett.* **56** 1198  
 van Wees B J *et al* 1988 *Phys. Rev. Lett.* **60** 848  
 Wharam D A *et al* 1988 *J. Phys. C* **21** L209

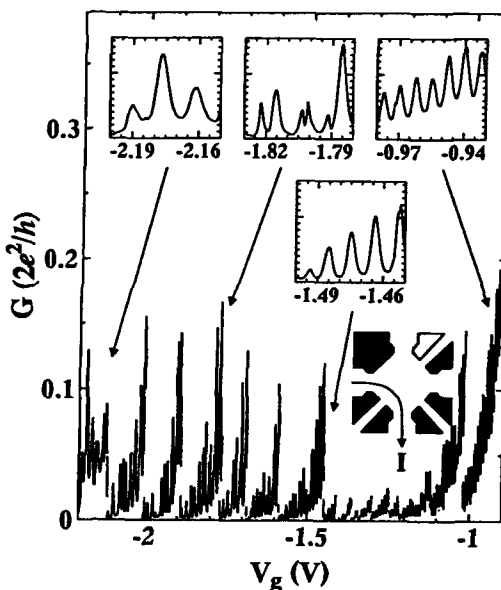


Figure 5. The conductance of a four-probe dot as a function of the voltage  $V_g$  on the unshaded gate, for various tunnel barrier heights. As  $V_g$  is made more negative, the tunnel barriers pinch off due to stray fields. To restore some conduction, the two tunnel barriers were backed off (made more positive) by 5mV each time, adding 2-4 more electrons to the dot, before  $V_g$  was swept further. The insets show some of the oscillations in more detail.

## Circuit-level applications of quantum effect device (RHET)

A. Shabatomi and N. Yokoyama

FUJITSU LIMITED

10-1 Morinosato-Wakamiya, Atsugi, 243-01, Japan

**ABSTRACT:** This paper focuses on the high-speed properties of resonant-tunneling hot electron transistor and the circuit applications. Experimental work on the cut off frequency up to 121GHz is summarized, and full adder circuit and frequency divider are fabricated.

### 1. INTRODUCTION

Functional devices will open the door for revolutionary computing architectures based on functional logic circuits. In order to make such functional device, the application of resonant-tunneling barrier structure proposed by Tue and Esaki<sup>1)</sup> to transistor is one of the candidate. Because the resonant-tunneling barrier structure has the intriguing characteristics of high speed charge transport and a pronounced negative differential resistance. Now, many kinds of three terminal functional transistor using resonant-tunneling barrier structure have been demonstrated such as; Resonant-tunneling hot electron transistor (RHET)<sup>2)</sup> by Yokoyama, in which the resonant-tunneling barrier was applied between emitter and base layer as the hot electron injector in the hot electron transistor<sup>3)</sup>, Resonant-tunneling bipolar transistor (RTBT) by Capasso<sup>4)</sup>, and (BiQuaRTT)<sup>5)</sup> by Seabough, in which the resonant-tunneling barrier was applied instead of base layer of hetero-junction bipolar transistor, (RBT)<sup>6)</sup> by Futatsugi, in which the resonant-tunneling barrier was applied between emitter and base layer of hetero-junction bipolar transistor as the hot electron injector. All of these devices have a similar operating principle, characteristics, and functions.

This paper describes the high speed performance and demonstrates the circuit-level applications of RHET covering the potential of this functional device, RHET.

### 2. FABRICATION OF RHET

First we started to fabricate RHET with GaAs/AlGaAs materials grown by MBE. By optimizing the resonant-tunneling barrier structure, and the collector barrier height, we were able to increase the peak to valley ratio to 2.6 and the

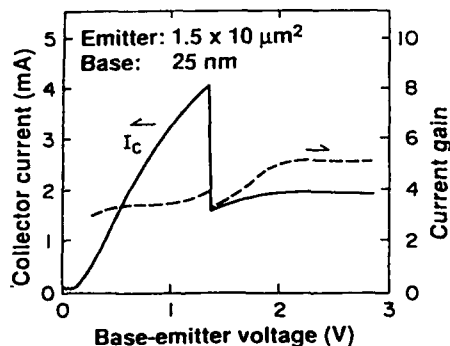


Fig. 1 I-V characteristics of RHET.

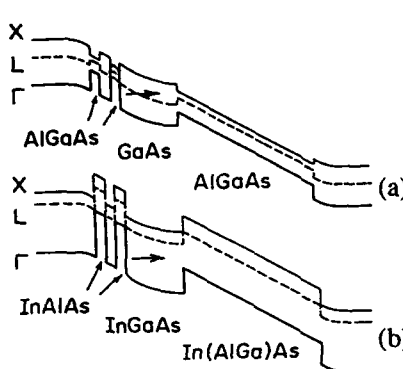


Fig. 2. Band diagrams of (a) GaAs RHET  
(b) InGaAs RHET

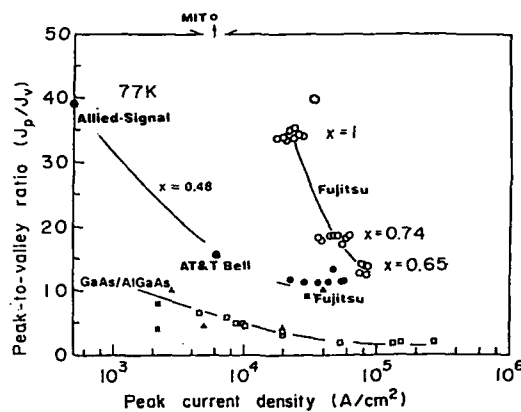


Fig.3. p/v ratio vs peak current density  
InGaAs/InAlAs RTB

current gain to about 5 shown in Fig.1. But this peak to valley ratio and the current density are not sufficient for the fabrication of the integrated circuits. In order to get a sufficient values of peak to valley ratio and current density, we changed the materials from GaAs-based RHET material to InGaAs-based material. Fig.2 shows the band diagrams of GaAs-RHET and InGaAs-RHET. The InGaAs-base RHET has a wider separation energy, 0.55 eV between  $\Gamma$  and L points. It also has a wider separation energy at this heterointerface with the collector barrier. Because of its wider energy window, where hot electron transport is near-ballistic and electrons can reach the collector, this RHET has higher current gain than the GaAs based RHET, which was simulated by the numerical Monte Carlo calculations. Another important factor is that the effects of indirect valleys in tunneling transport in the barrier are reduced in this material system due to their higher energies, decreasing the valley current. The InAlAs barrier also has a lighter effective mass, 60 percent that of AlGaAs barriers. This decreased effective mass increases tunneling-current density, thus increasing the peak-to-valley current ratio. The experimental results<sup>7)</sup> are shown in Fig.3. These plots show the performance of GaAs-based resonant tunneling barriers, InGaAs/InAlAs resonant tunneling barriers lattice matched with InP, and pseudomorphic InGaAs/InAlAs barriers. It is clear that InGaAs-Based materials, Particularly pseudomorphic materials, show a higher peak-to valley ratio with increased collector current peak density.

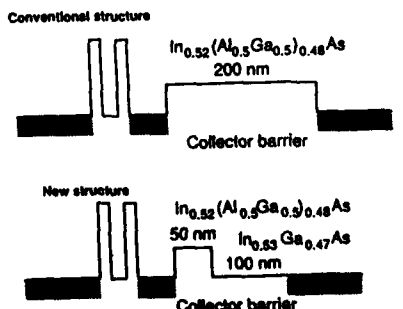


Fig.4. Band diagram of RHET.

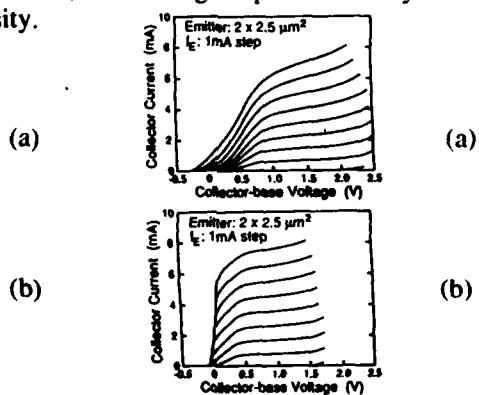


Fig.5. I-V characteristics of RHET

## 2. HIGH SPEED PERFORMANCE OF RHET

Monte Carlo simulation of RHET<sup>8</sup> was carried out to improve the RF performances. Our simulation suggested that electrons injected into the collector barrier begin to lose kinetic energy by intervalley scattering after traveling about 50 nm, and accumulate in the collector barrier. It also suggested that electrons turn back to the base due to the potential raised by the accumulated electrons at a weak or negative collector-base bias. We fabricate the two kinds of collector barrier structure RHET, one is 200 nm  $In_{0.52}(Al_{0.5}Ga_{0.5})_{0.48}As$  and the other one is 50 nm i- $In_{0.52}(Al_{0.5}Ga_{0.5})_{0.48}As$  and 100 nm i-InGaAs to lower the collector capacitance and raise the breakdown voltage. The resonant-tunneling barrier of this RHET consists of 3.52 nm  $In_{0.53}Ga_{0.47}As$  sandwiched between 2.86 nm  $In_{0.35}Al_{0.65}As$  barriers. The base width is 30 nm and the carrier concentration is  $1 \times 10^{18} \text{ cm}^{-3}$ , shown in Fig.4. RHET's respectively, were fabricated using self-alignment technology to decrease extrinsic resistance. DC measurement was carried out with a cryo-wafer probe. Each common-base current gain reaches 0.9 at a collector-base voltage of 0.75 V for an emitter current of 5 mA shown in Fig.5. respectively. The peak current density is  $2.2 \times 10^5 \text{ A/cm}^2$ . The peak-to-valley ratio is 15. This result shows that performance with a new collector barrier (b) is superior than that of (a). These static characteristics are suitable for the RHET digital circuit applications. Microwave measurement was also carried out using a cryostat microwave wafer probe. The cut-off frequency,  $f_T$ , peaks at 121 GHz<sup>9</sup> at a collector-emitter voltage of 1.4 V and an emitter current density of  $6.5 \times 10^4 \text{ A/cm}^2$  measured at 77K. The low-frequency current gain reaches 36.3 dB, which corresponds to an  $h_{fe}$  of 65 shown in Fig.6. The cut-off frequency is comparable to that of HEMT with a gate length of a quarter of a micron or less. This makes the RHET an ultra high-speed device.

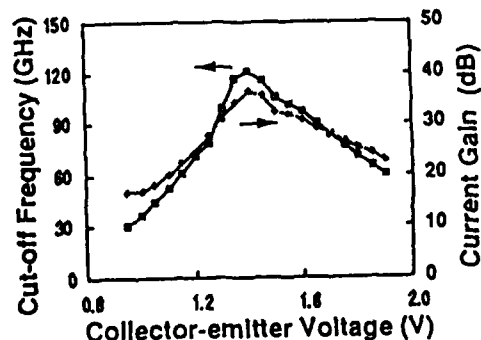


Fig. 6. Microwave characteristics

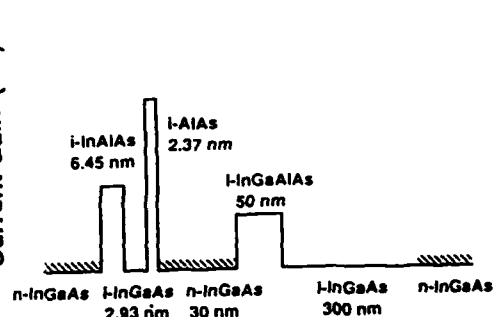


Fig. 7. RHET band diagram for IC

## 3. LOGIC APPLICATIONS OF RHET

We have already constructed a elementary logic gate family<sup>10</sup> of a NOR gate, an exclusive-NOR(E-NOR) gates, and a latch. In principle, any logic function can be obtained using NOR gates and latches, but logic family becomes more powerful and

efficient when it includes a number of logic circuits taking the best advantage of HET futures.

The RHET used an asymmetric resonant-tunneling barrier shown in Fig.7. The high AlAs barrier height and relatively narrow well width increase the logic margin. The circuits are fabricated using self-aligned RHET and thin-film resistors of WSiN. The RHETs have a dc current gain of 10, a peak-to-valley ratio of 15, and a collector-base breakdown voltage of 2.5 V.

A full adder is a basic component of arithmetic logic circuits. The sum signal logic is a 3-input exclusive-OR and that of the carry output is a 3 input majority logic. Both circuits can be made simply using RHET feature. The full adder is basically constructed with 7 RHETs and 13 resistors as shown in Fig. 8. It contains 3 inverters for each input A, B, and Carry ( $C_i$ ) to confirm the ability to be driven by previous circuits. It also contains 2 inverters for Sum (S) and Carry ( $C_o$ ) to confirm the ability to drive the next stage. We tested the operation of a full adder at 77K. We confirmed that the full adder operated correctly<sup>11)</sup>. Note that the number of transistors is reduced to about one fourth and the supply voltage is about one half that of ECL logic circuits.

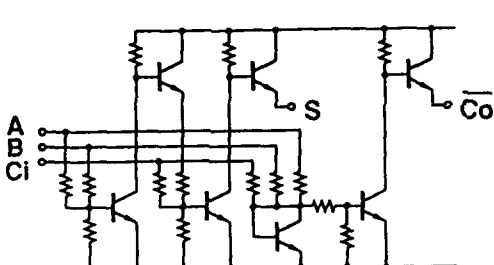


Fig. 8. RHET full adder circuit

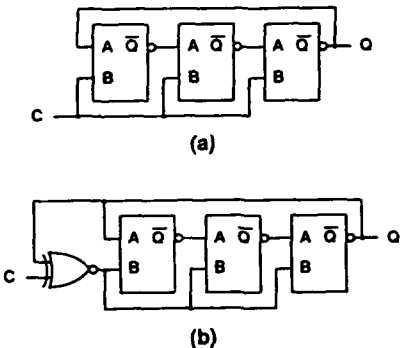


Fig. 9. Frequency divider block diagram (a) 1/3, (b) 1/2

We also succeeded to fabricate the frequency dividers using RHETs. Frequency divider is usually made using flip-flops, which can be made using two latches. However, we succeeded to make this by state-holding circuits instead of D-flip-flops. The state-holding circuits holds data using hysterics similar to the majority logic gate of RHETs. A chain of state-holding circuits functions similarly to a shift register. Data in the chain is passed to the next stage at each edge of the clock. The frequency divider is constructed by adding a feedback loop to the quasi-shift register shown in Fig.9.(a) The loop of the 3-stage state-holding circuits is used to obtain a 1/3 frequency divider. To obtain a 1/2 frequency divider, the E-NOR gate was inserted in the clock line, shown in Fig.9(b). We confirmed that the 1/3 and 1/2 frequency divider are operated correctly at 77K.

#### 4. SUMMARY

We demonstrated the high speed operating performance of RHET. And also, we demonstrated the full adder circuits and frequency dividers using RHETs and confirmed the stable operation at 77K. with a fewer transistors than bipolar circuits and lower power consumptions.

This results indicate the great potential of functional device of RHETs in fabricating the future high-speed, low power logic LSI.

#### ACKNOWLEDGEMENT

This work was performed under the management of R&D Association for Future Electron Devices, as a part of R&D of Basic Technology for Future Industries supported by NEDO.

#### REFERENCE

- 1) R. Tue and L. Esaki: *Appl. Phys. Lett.* 22 (1973)pp562
- 2) N. Yokoyama, K. Imamura, S. Muto, S. Hiyamizu, and H. Nishi: *Jpn. J. Appl. Phys.* 24 (1985)L853
- 3) M. Heiblum: *Solid-State Electron.* 24, (1981)pp343
- 4) F. Capasso and R.A. Kiehl: *J. Appl. Phys.* 58 (1985)pp1366
- 5) A.C. Seabough, W.R. Flensley, J.N. Randall, M.A. Reed, D.L. Farrington and R.J. Matyi: *IEEE Trans. on ED* 36. 10, Oct. (1989)pp2329
- 6) T. Futatsugi, Y. Yamaguchi, K. Ishii, K. Imamura, S. Muto, N. Yokoyama, and A. Shabatomi : *IEDM Tech. Digest*, (1986)pp286
- 7) S. Muto, N. Yokoyama, T. Inata, S. Sasa, K. Imamura, H. Ohnishi, T. Mori, T. Fujii, and N. Nishi : *JSAP-MRS Int. Conf. on Electron. Mats.* (1989)pp179
- 8) H. Ohnishi, N. Yokoyama, and A. Shabatomi : *IEEE Trans. on ED* 36, (1989)pp2335
- 9) T. Mori, T. Adachihara, M. Takasu, , H. Ohnishi, K. Imamura, S. Muto, and N. Yokoyama: *Electron. Lett.* 15th Aug. 27, 19, (1991)pp1523
- 10) T. Takatsu , K. Imamura, H. Ohnishi, T. Mori, T. Adachihara, S. Muto and N. Yokoyama : *SRC, Santa-Barbara*, June, (1990)
- 11) T. Takatsu, K. Imamura, H. Ohnishi, T. Mori, T. Adachihara, S. Muto, and N. Yokoyama : *13th GaAs TC Symp. Tec. Dig. Oc.* (1991)pp95

**Buried-quantum well resonant tunnelling transistor in the  
 $\text{Al}_x\text{Ga}_{1-x}/\text{In}_y\text{Ga}_{1-y}\text{As}$  material system**

D. Lippens, P. Mounaix, H. Leroux, O. Vanbésien, V. Sadaune and E. Barbier\*

Centre Hyperfréquences et Semiconducteurs - U.A. CNRS N° 287  
Université des Sciences et Techniques de Lille Flandres Artois  
59655 Villeneuve d'Ascq Cédex - France

\* Laboratoire Central de Recherche de Thomson-CSF  
Domaine de Corbeville, B.P. 10 - 91404 Orsay Cédex - France.

**ABSTRACT :** Resonant Tunneling devices in a three-terminal configuration have been fabricated in the  $\text{Al}_x\text{Ga}_{1-x}\text{As}/\text{In}_y\text{Ga}_{1-y}\text{As}$  material system. The devices contain a bound state, filled up with a  $\delta$  doping, to ensure the transistor action while current flow is due to resonant tunneling via the second level. The common emitter characteristics show that a bias on the base modulates significantly the collector current however with a lack of isolation between the base and emitter contacts. This is analyzed in terms of intersubband scatterings between the tunneling and ground states.

## 1. INTRODUCTION

Resonant Tunneling Devices in a three-terminal configuration are potentially useful for high speed applications because they should be able to respond very quickly and sensitively to the base control. Several resonant tunneling transistor structures have been proposed and implemented which can be divided into two classes. In one class, the device is obtained from the series connection of a resonant tunneling structure and a high speed transistor. This can be a field effect transistor (Bonnefond 1985), a bipolar transistor (Capasso 1989) or a hot electron transistor (Yokoyama, 1985). In the second class, the tunneling current is directly controlled by modulating the potential inside the well. Also with this option, several bipolar (Reed, 1988) and unipolar (Haddad, 1989) versions have been realized. The voltage on the base modulates the amount of charge in a truly confined state as suggested by Haddad et al (1989) and Schulman and Waldner (1987) for unipolar structures. Another option is to use resonant tunneling structures with large asymmetry in the thickness of the two barriers so that applying a voltage across the thicker barrier electrostatically modulates the emitter collector current (Bonnefond 1988) (Beltram 1988).

In the present work, we fabricate a unipolar resonant tunneling transistor in the context of  $\text{Al}_x\text{Ga}_{1-x}\text{As}/\text{In}_y\text{Ga}_{1-y}\text{As}$  technology. For the device fabrication outlined in section 2, we developed specific processes which allow us to deposit the ohmic contact directly on the emitter barrier. The electrical measurements are reported in section 3. Varying the emitter base voltage produced very significant changes in the tunneling current with measured transconductance as high as 80 mS. However, we observed a lack of isolation between the base and the contact layers. To analyse these results, we reported in section 4 numerical calculations of output characteristics and intersubband scattering rates between the tunneling and ground states.

### 1. EPITAXY AND DEVICE FABRICATION

The epitaxial material was grown by molecular beam epitaxy in a varian GEN-II system. We start from a semi-insulating [100], 2-in, substrate. The first layer grown was a highly doped layer ( $N_D = 2 \times 10^{18} \text{ cm}^{-3}$ ) of GaAs of 1  $\mu\text{m}$  followed by a 2 000  $\text{\AA}$  thick undoped GaAs layer. A double barrier heterostructure was then deposited. It consists of two 17  $\text{\AA}$  - thick AlAs used for the tunnel barriers separated by a 10  $\text{\AA}$  GaAs/60  $\text{\AA}$  -  $\text{In}_{0.22}\text{Ga}_{0.78}\text{As}/10 \text{\AA}$  GaAs strained-layer quantum well, planar doped at  $4 \times 10^{12} \text{ cm}^{-2}$ . We thus create a bound ground state to ensure the transistor action while current flow is due to resonant tunneling via the second level. On top, a 50  $\text{\AA}$ -thick undoped GaAs layer followed by a lightly doped ( $N_D = 2 \times 10^{16} \text{ cm}^{-3}$ ) GaAs of 450  $\text{\AA}$  and a 3 000  $\text{\AA}$  thick GaAs ( $N_D = 2 \times 10^{18} \text{ cm}^{-3}$ ) were successively grown to prevent dopant diffusion, to optimize the 2D injection of electron (Mounaix 1990) and to make the emitter contact.

For the device fabrication, we used an integrated technology we developed recently (Lippens 1991). The main advantage of this technology is the feasibility of low parasitics-small area devices. With respect to previous attempts (Haddad 1990) for making the base contact with the emitter not completely etched, we tried to implement the base ohmic contact directly on the emitter barrier. In this aim, a selective wet etching with citric acid/hydrogen peroxide solutions was used, the AlAs barrier acting as an etch stop layer. For the shallow base contact, AuGeNi was fastly alloyed with Rapid Thermal Annealing

Figure 1 is a scanning electron micrograph of a typical device. The emitter area ranging from  $25 \times 25 \mu\text{m}^2$  down to  $5 \times 5 \mu\text{m}^2$  were directly written by electron beam lithography. The top layer is contacted with two strips to wafer-probing footprints. The separation between the emitter mesa and the base ohmic contact with a U shape visible on the left-hand side was made as short as possible, thus reducing depletion effects. Also apparent in this figure is the collector on the right hand side implementing in a deep recess.

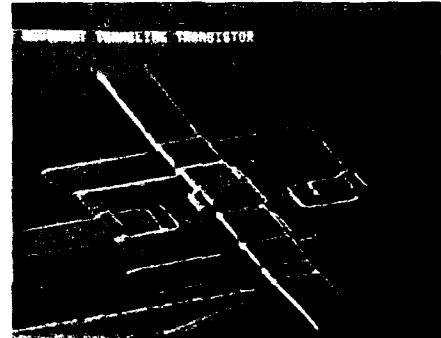


Fig. 1: Scanning Electron Micro-photograph of device.

### 3. DC CHARACTERISTICS

DC current voltage characteristics of the device in two-and-three terminal configurations have been measured at 300 K and 77 K. With the base terminal open, the collector currents exhibit anomalies in the tunneling conduction or weak negative differential resistance features with a slight improvement at low temperatures. In comparison with undoped pseudomorphic resonant tunneling diodes which contrarily exhibit strong negative differential effects, (Lippens 1991) this suggests that the planar doping degrades greatly the coherence of transport and hence the strength for NDR feature. When a bias is applied between the emitter and base terminals a modulation of the tunneling current flow via the second level is obtained. Typical common emitter characteristics obtained in that case are displayed in Figure 2.

The output collector characteristics do not saturate. This can be attributed to the fact that the charge in the well does not completely screen the electric field in that region. Another problem with the realized device is the large base leakage current. In order to make sure that the electrons are not collected by the base after experiencing the double barrier as a whole, we fabricated a structure similar to the one in Figure 1 but this time the base contact was not alloyed. The I-V characteristics remain practically the same. This tends to indicate that the observed leakage current is not a result of a poor control of the diffusion depth.

#### 4. DISCUSSION

The theoretical model used in the analysis of tunneling current is a self consistent version of simulation procedures developed in our laboratory (Vanbesien 1991). We solve self-consistently the Poisson's and Schrödinger's equations to determine the charge trapped on the ground state and the band bending of potential. The amount of charge is established by the Fermi level of the base contact  $E_{FB}$  as a function of the base emitter voltage drop  $V_{be}$  (Schulman 1987). Increasing  $V_{be}$  pulls down the position of  $E_{FB}$  relatively to the ground state. Subsequently, the sheet density in the well is reduced and the potential is less affected.

In contrast at low bias  $V_{be}$ , increase in the sheet density leads to a shift in the collector voltage at a larger value in a manner similar to that observed in intrinsic bistability effects. Figure 3 displays the collector current versus  $V_{EC}$  for a structure comparable to that fabricated. For sake of simplicity, the GaAs transitions and the cladding layers were not included in the simulation. Shifts in the peak voltage are effectively observed in agreement with the previous discussion. It remains to explain why the base leakage current is so high. Let us note that in the simulation reported above the scatterings and notably the intersubband transitions (Eaves 1988) during the tunneling process, were ignored. To address this issue, we calculated the phonon scattering rates of a 70-Å

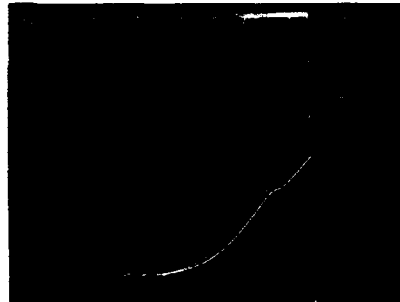


Fig. 2 : Experimental output collector characteristics of the resonant tunneling transistors for various  $V_{be}$  at 300 K.

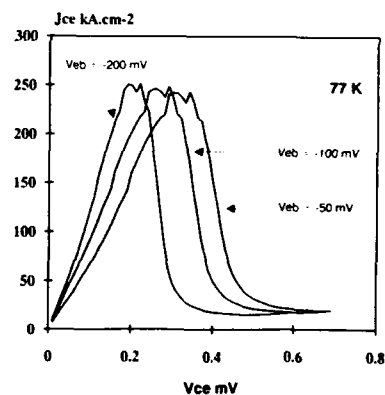


Fig. 3 : DC solution for the resonant tunneling transistor with  $V_{be}$  as parameter.

thick GaInAs well bounded on each side by two AlAs layers following the general procedure of overlap integrals (Vinter 1991).

The variations versus energy of various interaction rates calculated for the first and second subbands at 300 K are given in figure 4. The energies are measured from the bottom of the well. It can be seen that intersubband transitions occur in average in 1 ps. It is clear that this time is quite comparable to the life time of carriers in the well during the resonant tunneling charge transfer. This suggests that an appreciable density of tunneling electrons relaxes and hence is trapped in the buried well increasing the base leakage current.

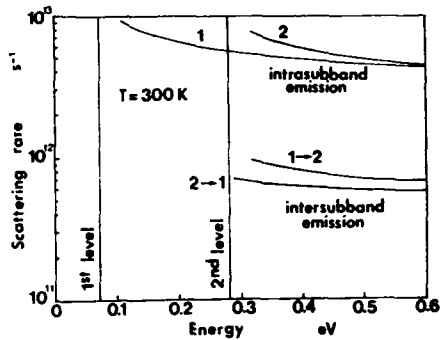


Fig. 4: Phonon scattering rates for the first and second subbands.

## 5. CONCLUSION

In summary, we have fabricated a unipolar,  $\delta$  doped resonant tunneling transistor with a bound ground-state in the  $\text{Al}_x\text{Ga}_{1-x}\text{As}/\text{In}_y\text{Ga}_{1-y}\text{As}$  material system. Technological processes have been developed for directly implementing the base contact on the double barrier heterostructure. Modulation of the collector currents have been demonstrated but with a large leakage base current. We found that the inelastic scatterings can account for the observed base current. More careful design of a structure with ultra-thin barrier in order to decrease the lifetime in the well should improve this aspect.

## ACKNOWLEDGMENTS

The authors would like to thank A. Fattorini, M. François, B. Grimbert and A. Leroy for technical assistance during the process.

## REFERENCES

- Beltram. F., Capasso F., Luryi S., Chu S.N.G., Cho A.Y. and Sivco D. 1988 *Appl. Phys. Lett.* 53, 219.
- Bonnefond A.R., McGill T.C., and Burnham R.D. 1985 *IEEE Electron Dev. Lett.* 12, 636.
- Bonnefond A.R., Chow D.H. and McGill T.C., 1985 *Appl. Phys. Lett.* 47, 888
- Capasso F. et al. 1989 *IEEE Trans. on Electron Dev.* 36, 2065.
- Eaves L. et al. 1988. *Appl. Phys. Lett.* 53, 212.
- Haddad G.I., Reddy U.K., Sun J.P. and Mains R.K. 1990. *Superlattices and Microstructures* 7, 369.
- Lippens D., Mounaix P. and Barbier E. 1991, *IEEE Electron Dev. Lett.* 12, 114.
- Mounaix P., Vanbesien O. and Lippens D. 1990, *Appl. Phys. Lett.* 57, 1517.
- Reed M.A., Frensel W.R., Matyi R.J., Randall J.N. and Seabaugh A.C. 1989, *Appl. Phys. Lett.* 54, 1034.
- Schulman J.N. and Waldner M., 1988, *J. Appl. Phys.* 63, 2859.
- Vanbesien O., Bouregba R., Mounaix P. and Lippens D. 1991, *Resonant tunneling in semiconductors : physics and applications* (Plenum publishing Corporation).
- Vinter B. and Chevoir F. 1991 *Resonant tunneling in semiconductors : physics and applications* (Plenum publishing Corporation).
- Yokoyama N., Imamura K., Muto S., Hiyamizu S. and Nishi H., 1985, *Jap. J. Appl. Phys.* 24, L. 853.

## Voltage tuned interference in an AB ring

S. Katsumoto, \*N. Sano and S. Kobayashi

Department of Physics, Faculty of Science, University of Tokyo  
7-3-1 Hongo, Bunkyo-ku, Tokyo 113, Japan

\*Department of Physics, Faculty of Science, Kwansei-Gakuin University  
Uegahara, Nishinomiya 662, Japan

**ABSTRACT:** We propose a simple method to tune the quantum interference of electrons by gate voltage in a ring-shaped 2-dimensional system at GaAs-AlGaAs interface. We also present an experimental evidence of the effect.

External magnetic field is most frequently used as an external parameter to shift the phase of the electrons in the experiments on the quantum interference effects in solids (Aronov 1987, Webb 1985). Another possible parameter is the electrostatic potential. Washburn et al. (1986) observed the shift of the Aharonov-Bohm (AB) oscillation pattern by applying the external electric field (Aharonov 1959). However the origin of the shift is not clear because the screening length is short in the metallic rings. De Vegvar et al. (1989) succeeded in turning on and off the AB effect using a short metallic gate on one of the branches of a 2-dimensional electron gas (2DEG) AB ring.

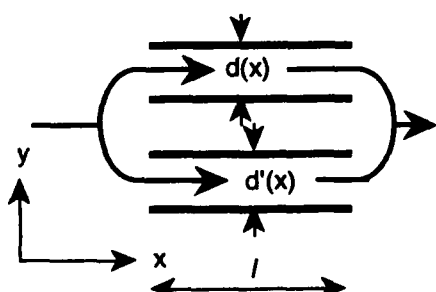


Fig.1 Two parallel quantum point contacts.

The re-population of the electrons between subbands prevented them from observing clear resistance oscillation against the gate voltage.

In this article, we propose a novel method to tune the quantum interference in a simple device by applying external voltage (Sivan 1990) and present an experimental evidence of the effect.

We use a quantum point contact (QPC) to tune the phase of electrons (Van Wees 1988). We treat the QPC in adiabatic limit and solve the Schrodinger equation separately for x- and y-axes for the configuration shown in Fig.1 (Yacoby 1990). The transverse (y) solution gives the energies

$$E_{yn}(x) = \frac{\hbar^2}{2m} \left( \frac{n\pi}{d(x)} \right)^2 \quad (1)$$

for the contact width  $d(x)$ . This serves as the "effective potential" (EP) for the motion along the  $x$ -axis. As the contact width narrows, the EP grows up and the kinetic energy for the  $x$ -direction decreases while the total kinetic energy does not change. This results in the increase of the  $x$ -component of the phase velocity  $v_{ph-x} = \omega/k_x$ .

Next we consider two parallel QPCs as illustrated in Fig.1. An electron which goes through these contacts interferes with itself at the exit. If we can change the contact width independently for the two QPCs, the interference is easily tuned. To be more realistic, we apply a single gate voltage ( $V_G$ ) to them, instead of the different gate voltages. We make a difference in the widths of QPCs. Because  $E_y$  depends on  $V_G$  non-linearly, the phase difference between the two branches:

$$\frac{1}{\hbar} \sqrt{\frac{m}{2E_F}} \int_0^l (E(x) - E'(x)) dx \quad (2)$$

can be varied by varying  $V_G$ . Here  $E(x)$  and  $E'(x)$  are the transverse kinetic energies for each QPC and  $l$  is the length of the QPCs.

In order to observe this phase tuning effect, we prepared the following structures. A 2DEG at AlGaAs-GaAs interface was prepared by molecular beam epitaxy. The Hall mobility was  $9 \times 10^4 \text{ cm}^2/\text{Vs}$  and the concentration was  $2 \times 10^{11} \text{ cm}^{-2}$  in the dark. They increased to  $1.2 \times 10^5 \text{ cm}^2/\text{Vs}$  and to  $5 \times 10^{11} \text{ cm}^{-2}$  respectively by photo-exposure. Figure 2 shows the two types of the gate configuration used in the experiment. Using electron beam lithography, we removed the PMMA film with thickness of about 2000 Å coated over the surface of the sample leaving the hatched regions in Fig.2. 4000 Å thick Au film was deposited over it to make the Schottkey gates and also to make bridges which terminate the center gates (Ford 1988). The specimen was cooled down to 0.5K in liquid  $^3\text{He}$ . The resistance was measured by a simple 4-terminal AC bridge at the frequency of 400Hz.

In the following we describe the results obtained in the sample with type (a) configuration. Similar results were obtained in type (b) samples.

The dependence of the resistance on  $V_G$  is shown in Fig.3. When the conductance  $g$  was lower than  $6g_0$  ( $g_0 \equiv 2e^2/h$ ), a wavy structure in the  $V_G$  dependence appeared instead of well defined quantized plateaux. The structure was rigid against the

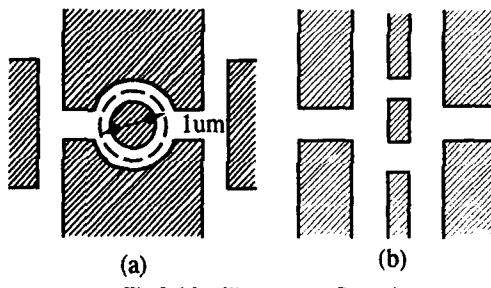


Fig.2 Metallic gates configurations

perpendicular magnetic field, suggesting that it is due to the reflection at the entrance of the QPCs or to the impurity scattering.

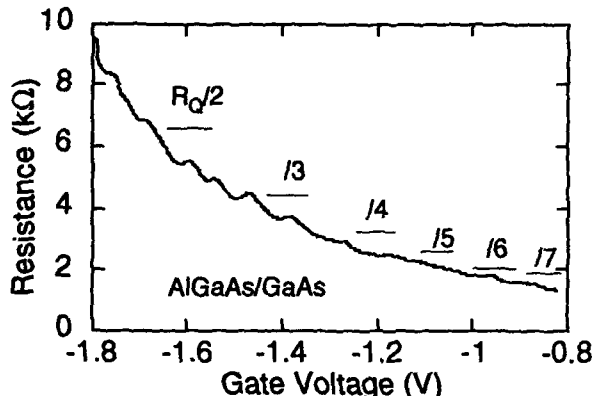


Fig3. Gate voltage dependence of the resistance.

most pronounced when the mode number  $n=1$  for one of the QPCs, because  $E_y$  depends on  $n$  as shown in (1) and large  $n$  would result in the cancellation of the tuning effect. Therefore we examined the voltage effect where  $3g_Q < g < 7g_Q$ . The magnetic field AB effect also gives us the amplitude of the interference effect in the present experimental conditions.

We found conductance oscillations against  $V_G$  when  $g > 3g_Q$ . The amplitude was level with that of the magnetic field AB effect. However weak perpendicular magnetic

The AB oscillation in the magnetoresistance appeared when  $g > 3g_Q$ , a part of which is shown in Fig.4. The inset shows the Fourier spectrum which has a peak at  $h/e$ . This means that only one of the QPCs is open when  $g < 3g_Q$  because of the imbalance between them. On the other hand, the interference tuning by  $V_G$  should be

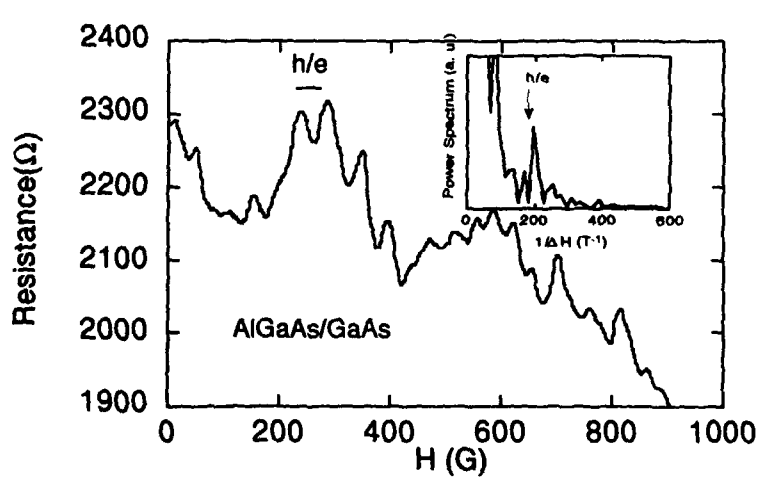


Fig4. Magnetic field AB effect.

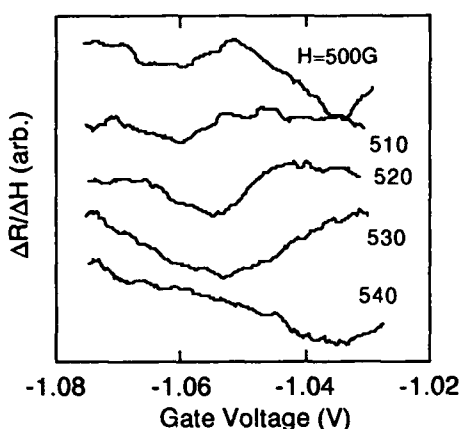


Fig.5 Differential magnetoresistance as a function of the gate voltage. The parameter is magnetic field.

differential magnetoresistance by using slow (8Hz) field modulation. Reproducible results are shown in Fig.5. The oscillation pattern versus  $V_G$  was shifted with the increase of the magnetic field. The increase needed for one period shift was 40 Gauss which is close to the period in the magnetic field AB effect. From the above result, we conclude that we have observed the interference tuned by the voltage.

#### References

Aharonov Y and Bohm D 1959 Phys. Rev. 115 485  
 Aronov A G and Sharvin Y V 1987 Rev. Mod. Phys. 59 755  
 Beenakker C W J and Van Houten H 1991 Solid State Physics 44 1  
 De Vegvar P G, Timp G, Mankiewich P M, Behringer R and Cunningham J 1989 Phys. Rev. B40 3491  
 Ford C J B, Thornton T J, Newbury R, Pepper M, Ahmed H, Foxon C T, Harris J J and Roberts C 1988 J. Phys. C21 L325  
 Sivan U, Heiblum M, Umbach C P and Shtrikman H 1990 Phys. Rev. B41 7939  
 Van Wees B J, Van Houten H, Beenakker C W J, Williamson J G, Kouwenhoven L P, Van der Martel D and Foxon C T 1988 Phys. Rev. Lett. 60 848  
 Washburn S and Webb R A 1986 Adv. Phys. 35 375  
 Webb R A, Washburn S, Umbach C P and Laibowitz R B 1985 Phys. Rev. Lett. 54 2696  
 Yacoby A and Imry Y 1990 Phys. Rev. B41 5341

fields caused structural changes in the oscillations instead of simple phase shifts which are expected in the ideal case. The structural changes are probably due to the superposition of the interference and the reflection effects among which the latter is insensitive to the magnetic field.

In order to eliminate the undesirable reflection or other effects which cause the conductance oscillation but are insensitive to the magnetic field, we measured the dif-

## Technical developments towards quantum-effect microwave electronics

H.L. Hartnagel

Technische Hochschule Darmstadt, Institut für Hochfrequenz-  
technik, Merckstr. 25, 6100 Darmstadt, FRG  
Tel.: +49-6151-16-2162, Fax: +49-6151-16-4367

Electrolytic structurization techniques (Grüb (1991a) give the promise of damage-minimized surface and interface structures, where for quantum-effect microwave-devices the surface to volume ratio becomes very important. A particular application represents a distributed, extremely broad-band electronic-signal processing. Here, the frequency limit is significantly improved by the small relevant input capacitance of quantum wire devices. This occurs in addition to the improved transport properties of charge carriers. Therefore a systematic assessment of these broad-band frequency limitations should be capable to bring the performance well into the range of 300 GHz.

An interest exists in extending the frequency capabilities of broad-band signal processing towards the Terahertz range. There are indications that this is possible with nanometric structures of hetero-junction charge-transport confinement, as long as the normal deficiencies of standard-technology surfaces are avoided such as vacancies, oxide clustering and many of the other surface-lattice faults, where electronic scattering limits the speed of charge transfer. Such a new surface-quality technology is either possible by using selective epitaxy for the definition of the component structures or by a soft material removal. The former approach has generally problems with more sophisticated structures since it involves relatively high-temperature effects. The other technique relies on wet processes. Some of these details are described here. Also, some of the concepts of achieving the goal of broadband signal processing are then described.

A common approach for this structurization has been to use such processes as electron beam lithography and reactive ion etching. However, some destruction of the semiconductor surface is found due to reactive ion etching and electron-beam bombardement (Pang, 1986). Therefore, the electrolytic processes presented here, making use of wet chemical etching and direct writing of metallisations, appear to be more promising. Electrolytic solutions offer both the possibilities of material removal and metal deposition, as recently shown (Keen 1991, Grüb 1991a). Direct writing processes have already been intensively studied in connection with the various possibilities of scanning tunnelling microscopes and their varieties. Here, such techniques are applied in particular by using local cathodic deposition and anodic etching employing also nanometric probe control by piezo electric actuators similar to the STM. Using suitable illumination, the techniques are applicable to various heterostructures and semi-insulating substrates. For the etching process e-beam lithography has to be applied to define test structures in resist layers. The backside of the samples is covered by an ohmic contact. Soft-etching is achieved by using electrolytic solutions containing sulphuric and phosphoric acids (Grüb, 1991b). By the application of about 150 voltage pulses with 25V amplitude and 300ns pulselwidth, 600nm of GaAs are removed. The conventional method for fabricating structures is dry etching, but its drawback is the damage that occurs at the crystal surface, resulting in additional noise as experimental results demonstrate. The soft process described here, based on wet chemical etching, does not show such a noisy behaviour. The deposition of metal lines and dots in the submicron range on GaAs is achieved by a direct writing process in an electrolyte with a process whose basic details were recently described (Richter, 1990). A tungsten wire is almost entirely covered with glass and its tip is electrochemically etched in an NaOH solution (as typical for scanning tunnelling microscopy). Tip radii of nanometric size can easily be obtained. Deposition of dots and lines with nanometric diameters and

widths are achieved by the application of voltage pulses between 0.5V and 20V with 0.5μs to 1ms length. The structure size is mainly influenced by the radius of the tip and the amount of transported charge depending on the pulses. The linewidth is additionally influenced by the tip movement between the pulses. Many types of metals can be deposited (Stremsdörfer, 1990).

In order to reach the 300GHz operating range of broad-band applications it is necessary to avoid the frequency dispersion of capacitive components of the equivalent circuit. This is possible by the idea of the distributed circuit, where the device capacitances are then part of the transmission line up to the frequencies where the transmission-line distances between the active devices produce resonances. Using coplanar transmission lines, also fabricated by the above techniques, the separation needs to be then less than 100μm. Correspondingly, every 50μ could be either a sub-μ wide HEMT-type structure for broad-band amplification or a Schottky-diode tower for broad-band mixing, together with suitable beam-lead bridging to the transmission line. The structures envisaged are then as outlines by figures 1.

#### References

1. A. Grüb, R. Richter, H.L. Hartnagel, 1991a: 'Electrolytic processes for etching and metal deposition towards nanometre quantum structures', Electronics Letters, vol. 27, (4), p. 306
2. A. Grüb, K. Fricke, H.L. Hartnagel, 1991b: 'Highly controllable etching of epitaxial GaAs layers by the pulse etching method', J. Electrochem. Soc., vol. 138, (3), pp. 856-857
3. N.J. Keen A. Grüb, H.L. Hartnagel, J. Freyer, H. Grote, R. Zimmermann, 1991: 'New Submillimeter-Wave Schottky-Barrier Mixer Diodes: First Results', Paper presented at 16th Int. Conference on Infrared & Millimeter Waves, Lausanne, Switzerland
4. Pang, S.W., 1986: 'Surface damage on GaAs induced by reactive ion etching and sputtering etching', J. Electrochem. Soc., 133, (4), pp. 784-787

5. Richter, R., Hartnagel, H.L., 1990: 'Direct writing of submicron Au-lines on GaAs in an electrolyte', *Int. J. Electronics*, 69, (5), pp. 631-634
6. Stremsdörfer, G., Martin, J.R., Clechet, P., Nguyen-Du, 1990: 'Use of Au-InPd and Pd-In electroless deposits for ohmic contacts on n-GaAs', *J. Electrochem. Soc.*, 137, (1), pp. 256-259

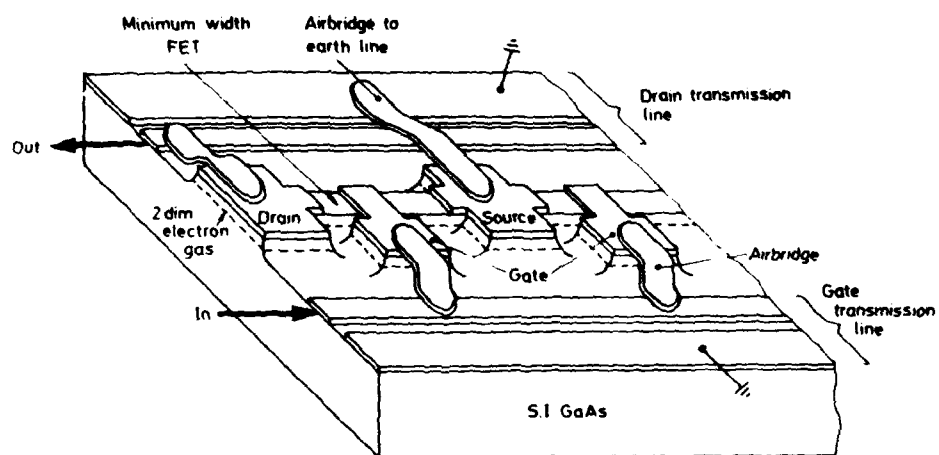


Fig. 1: A distributed FET structure with minimal transistor width and two one-sided coplanar transmission lines

## **Optically driven quantum networks: an approach to programmable matter?**

G Mahler and H Körner

Institut für Theoretische Physik, Universität Stuttgart, Pfaffenwaldring 57, 7000 Stuttgart 80,  
Germany

**ABSTRACT:** Arrays of quasi-molecular subunits, which couple via dipole-dipole interaction, may exhibit novel types of optical properties. These properties could be exploited for optical information processing.

### **1. INTRODUCTION**

Networks abound whenever complex systems are the target, whether in nature or in man-made technical devices. Generically, networks are characterized by a strongly constrained dynamical behavior in some (usually) high-dimensional phase space; the constraints derive from a network structure specified in real space. For example, the "traffic nets" define the allowed routes for transfer ("street map"), traffic rules, traffic capacity, in short what are allowed processes. The resulting behavior thus constitutes an abstract network of states and interconnecting processes. Direct modelling on this level has become quite popular: Cellular automata, (mathematical) neural nets, parallel algorithms etc merely define rules without, what is then called, implementation. On the other hand, the physical description of real networks amounts to find the connection between chemical-physical structure, the influence of environment, and the resulting network dynamics on a specific level of description.

The behavior of physical networks is usually characterized in terms of certain macroscopic or mesoscopic observables ("signals" as a function of time). This observational level, however, is not necessarily identical with the relevant level for the underlying network dynamics. The resulting "reconstruction problem" becomes demanding when networks based on synthetic nanostructures are concerned. The possibility of a network analysis then strongly rests upon structural pre-knowledge based, *inter alia*, on structural control during manufacturing, and on quantum-dynamical modelling. Only well-defined networks may eventually serve as control systems ("nano-devices"). It is the purpose of this contribution to address (theoretically) the expected properties of optically driven quantum networks.

### **2. THE OPEN UNIT CELL**

Among the best-known examples of a real nano-scale network are the ideal crystals. However, due to their strong inter-cell interaction the respective network dynamics would have to refer to (quasi-) momentum space, in which (delocalized) processes are constrained only by selection rules which respect to the coupling between different groups of degrees of freedom (electron, phonon etc), and with respect to external fields (photons). This is the realm of conventional solid state physics.

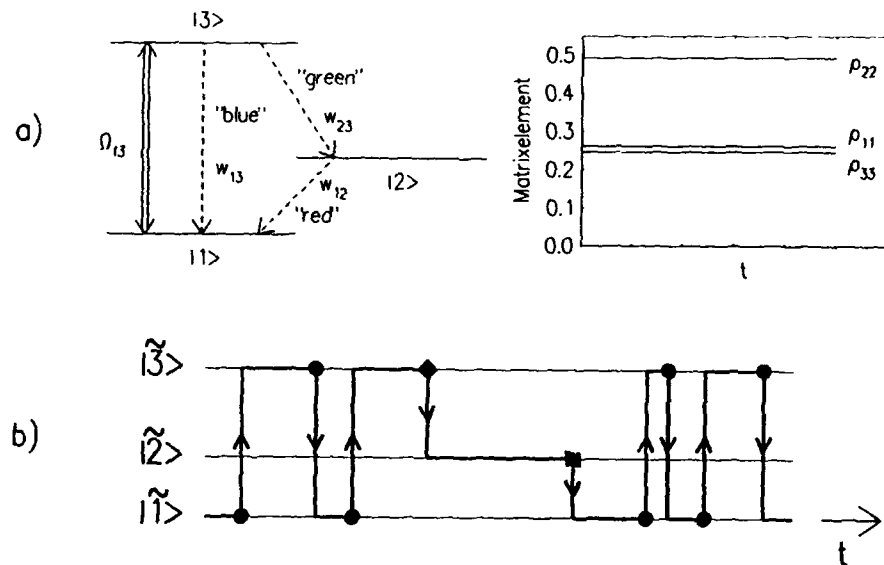


Figure 1. Driven three-level system. Field intensity  $\Omega_{13} = 2\omega_{13}$ , frequency  $\omega = \omega_{13}$ , spontaneous emission rates  $w_{23} = 2w_{12} = 10^{-2}\omega_{13}$ . a) Stationary solution for the density matrix, b) Stochastic process  $\hat{\mu}(t) \rightarrow \hat{\mu}'(t)$  with rate  $\hat{R}_{\mu'\mu}$ . The events in the material system are correlated with spontaneous photon emission:  $\bullet$  = "blue",  $\blacklozenge$  = "green",  $\blacksquare$  = "red".

In the opposite limit the local coupling of the unit cell to external driving forces and to the bath is large compared to inter-cell coupling. In this case network dynamics reflects the real local network structure, and, in that, can directly be manipulated by nanoscale artificial structuring.

Examples of experimentally studied individual quantum objects are the optically driven atom in a Paul trap (Sauter 1986) and the driven defect in an organic matrix (Ambrose 1991). In both cases the pertinent electronic model is a localized 3-level-structure (discrete, non-degenerate states  $|\mu\rangle$ , see Figure 1a) with a rapid decay channel ("blue") and a slow 2-step channel ("green" / "red"). Contrary to the ensemble description given by the stationary solution of the respective master equation for the density matrix, the behavior of the individual object is described by a stochastic process ("quantum jumps", see Figure 1b). As has been shown by Teich (1992), this process can systematically be derived from the master equation for the system's reduced density matrix, if this equation is transformed into the instantaneous diagonal representation  $|\bar{\mu}\rangle$ .

### 3. CELL COUPLING

Simple atoms or small molecules are not suitable as building blocks for the type of networks under consideration: Chemical binding, necessary as a "glue" to put things together, would have too strong an influence on the local properties and transition rules.

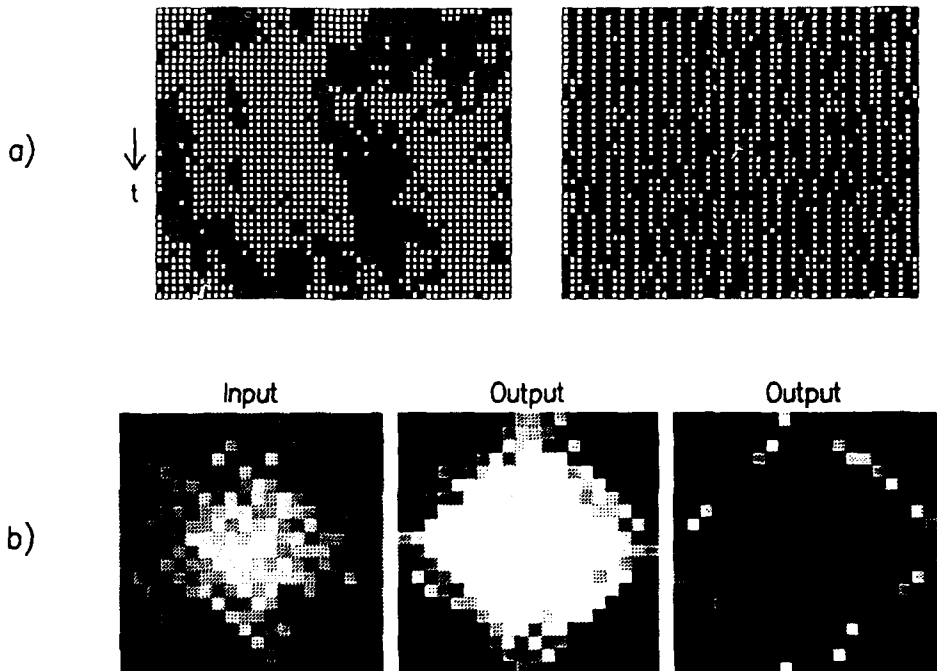


Figure 2. a) Quantum dot chain under stationary two-laser excitation: Trace of stochastic simulation. Ferro-coupling (left) and antiferro-coupling (right).  $\square = |1\rangle$ ,  $\blacksquare = |2\rangle$ . b) Simulated "pump and probe"-experiment on a Quantum dot array: Inhomogeneous pump-intensity as "input" and probe-absorption pattern as "output" for two different "program" parameters: Threshold decision and edge detection.

One working scenario, however, is, again, the single defect in matrix: It has been demonstrated that jumps of the resonance frequency mirror the stochastic quantum behavior going on in some degrees of freedom of the intermediate neighborhood (Ambrose 1991). This - here unintentional - parametric coupling might be exploited by two externally driven charge-transfer quantum dots (Mahler 1991), realized by means of semiconductor material: In this case the three-level system of Figure 1a is supposed to consist of two rapid transitions ("blue" and "green") and an extremely slow transition ("red"): With states  $|1\rangle$  and  $|2\rangle$  localized in different spatial regions of the dot, the optically induced transfer via transient  $|3\rangle$  induces a charge transfer and thus a flip of electric dipole moment. The parametric interaction is then due to the respective dipole-dipole interaction between the bistable dots.

#### 4. NETWORK BEHAVIOR

We first consider one-dimensional and two-dimensional arrays of (identical) quantum dots. Those parametrical interactions may then result in collective phenomena, which, in turn, imply unusual optical properties in real- and frequency space: With two (incoherent) but

homogeneous driving fields ("blue and "green") the behavior of a one-dimensional array of  $N$  quantum dots can be mapped onto the Ising model (Mahler 1991), where the interaction is of ferro-type, if the two lasers are below resonance, and of antiferro-type, if both lasers are above resonance (see Figure 2a). In a more general scenario (Körner 1992) inhomogeneous laser fields can even be used to implement some simple tasks of optical information processing (see Figure 2b): In the example shown the "input" is specified as the two-dimensional normalized spatial intensity pattern, the absorption pattern as "output", and parameters of observation (detuning, spectral observation etc) as "program".

These networks can further be generalized if physically different quantum dots of type *A*, *B*, say, are taken into account. One-dimensional strings of *ABAB*... can then selectively be addressed by appropriate laser fields controlling the *A*- and *B*- transitions, respectively. In this way, a quasi-molecular (stochastic) cellular automaton can be realized (Teich 1988).

## 5. CONCLUSIONS

Arrays of charge-transfer quantum dots should response to a non-equilibrium environment (laser fields) in a way that is conveniently described in terms of stochastic network dynamics. The repertoire of possible adaptive behavior appears to be large enough to be applicable in some tasks of highly parallel information processing. This information processing can either be realized in terms of an abstract machine ("cellular automaton") or by directly selecting the appropriate environment and observation level ("programmable matter").

This work has been supported by the Deutsche Forschungsgemeinschaft (Sfb 329).

## REFERENCES

Ambrose W P and Moerner W E 1991 *Nature* 349 225  
Körner H, Teich W G and Mahler G 1992 to be published  
Mahler G and Körner H 1991 in: *Advances in Solid State Physics* 31 ed. by Rössler U  
(Braunschweig: Vieweg) pp 357-67  
Sauter Th, Blatt R, Neuhauser W and Toschek P E 1986 *Opt. Commun.* 60 287  
Teich W G, Obermayer K, and Mahler G 1988 *Phys. Rev. B* 37 8111  
Teich W G and Mahler G 1992 *Phys. Rev. A* in press

## Author Index

Abu-Mostafa Y S, 7  
 Ahmed H, 83, 133, 163  
 Akazawa M, 115  
 Alves E S, 149  
 Ando T, 37  
 Aoyagi Y, 167  
 Arakawa Y, 199  
 Arimoto H, 33  
 Asai S, 1  
 Bagwell, 45  
 Barbier E, 245  
 Beaumont S P, 219  
 Behringer R E, 79  
 Berggren K-F, 25  
 Berggren K K, 79  
 Berthold O, 137  
 Besev C, 25  
 Beton P H, 149, 219  
 Bird J P, 167  
 Blaikie R J, 163  
 Böhm G, 137, 213  
 Bowers J, 99  
 Büttiker M, 19  
 Caro J, 141  
 Cleaver J R A, 133, 163  
 de Graaf C, 141  
 de Jongh L J, 171  
 del Alamo J A, 225  
 Dellow M W, 149, 219  
 Demmerle W, 213  
 Döhler G H, 189  
 Eaves L, 149, 219  
 Endoh A, 33  
 Eugster C C, 225  
 Feng Y, 111  
 Field M, 235  
 Forchel A, 103  
 Ford C J B, 235  
 Foster T J, 219  
 Frost J E F, 235  
 Fujikura J, 115  
 Fujiwara A, 189  
 Fukatsu S, 107, 195  
 Furuya K, 119  
 Gao J R, 141  
 Georgsson K, 95  
 Gornik E, 213  
 Goto H, 65  
 Grambow P, 183  
 Greus Ch, 103  
 Gustafsson A, 95  
 Hamaguchi C, 55  
 Harmans K J P M, 229  
 Harris J J, 111  
 Hartnagel H L, 253  
 Hasegawa H, 115  
 Haupt R, 51  
 Hausler W, 59  
 Heitmann D, 183  
 Henini M, 219  
 Heyers K, 141  
 Hirakawa K, 157, 179  
 Hirayama Y, 127  
 Horikoshi Y, 127  
 Hornsey R I, 133  
 Hu E L, 99, 175  
 Ikoma T, 157, 179  
 Ishibashi K, 167  
 Ishikawa E, 107  
 Ismail K, 153  
 Ito R, 107, 195  
 Jaros M, 209  
 Jezeierski A F, 219  
 Ji Z-L, 25  
 Johnson A T, 229  
 Jones G A C, 235  
 Katsumoto S, 65, 249  
 Kawabe M, 167  
 Kawamura K, 41  
 Kern D P, 73, 235  
 Kern K, 183  
 Kitatani T, 167  
 Kobayashi S, 65, 249  
 Körner H, 257  
 Kouwenhoven L P, 229  
 Kramer B, 59  
 Kroemer H, 205  
 Kumar A, 45

Lake R, 45  
 Langerak C J G M, 219  
 Lee K Y, 153  
 Leroux H, 245  
 Li Y J, 85  
 Lippens D, 245  
 Lishan D, 99  
 Mahler G, 257  
 Main P C, 149, 219  
 Maximov I, 95  
 Merz J L, 99, 205  
 Meurer B, 183  
 Miller M S, 85, 175, 205  
 Mirin R, 99  
 Miyamoto Y, 119  
 Miyao M, 123  
 Momma K, 107  
 Momose H, 55  
 Montelius L, 95  
 Mori N, 55  
 Mounaix P, 245  
 Muller C J, 171  
 Muto S, 33  
 Nagamune Y, 199  
 Nakagawa K, 123  
 Nakamura K, 145  
 Nakazato K, 133, 163  
 Namba S, 167  
 Nihey F, 145  
 Nilsson S, 95  
 Nishioka M, 199  
 Noguchi M, 179  
 Ochiai Y, 167  
 Odagiri T, 157  
 Ogasawara N, 107  
 Onabe K, 107  
 Onishi T, 167  
 Orth A, 103  
 Pepper M, 235  
 Petroff P M, 85, 205  
 Phillips J R, 127  
 Pieger K, 103  
 Pistol M-E, 95  
 Ploog K, 183  
 Popovic D, 235  
 Prentiss M, 79  
 Pryor C E, 205  
 Radelaar S, 141  
 Ritchie D A, 235  
 Roßkopf V, 137  
 Rooks M J, 175  
 Sadaune V, 245  
 Sakaki H, 129  
 Saku T, 127  
 Samuelson L, 95  
 Sano N, 249  
 Sasa S, 33  
 Sawano H, 41  
 Seifert W, 95  
 Semu A, 95  
 Shibatomi A, 239  
 Shimizu A, 29  
 Shiraki Y, 107, 195  
 Simpson P J, 235  
 Smoliner J, 137, 213  
 Snider G L, 175  
 Straka J, 103  
 Tan I-H, 99  
 Tarucha S, 127  
 Thomas H, 19  
 Thornton T J, 111, 133, 163  
 Timp G, 79  
 Tomozawa H, 115  
 Tsubaki K, 127  
 Tsukamoto S, 199  
 Turton R J, 209  
 Ueda M, 29  
 Ueta T, 41, 69  
 Vanbésien O, 245  
 van der Vaart N C, 229  
 van Ruitenbeek J M, 171  
 Washburn S, 153  
 Wassermeier M, 85  
 Weimann G, 137, 213  
 Weman H, 205  
 Wendler L, 51  
 Wilkinson C D W, 13, 219  
 Williams D, 111  
 Wong K B, 209  
 Xu Z, 85  
 Yamazaki D, 119  
 Yasuda T, 99  
 Yokoyama N, 239  
 Zhang Y H, 183

## Keyword Index

- 1/f noise, 127
- 2DEG, 137, 141, 213
- III-V material, 245
- AC conductance, 19
- Aharonov-Bohm effects, 153, 249
- AlGaAs/GaAs heterostructure, 157
- Anderson localization, 37
- Anti-dots, 145, 183
- Atom optics, 79
- Atom, 1
- Atomic layer doping, 123
- Ballistic conductance, 153
- Ballistic constriction, 175
- Ballistic electron transport, 133
- Ballistic transport, 69, 127, 145, 175
- Behaviour of social insects, 13
- Billiard-ball model, 163
- Boundary element method, 69
- Boundary scattering, 163
- Buttiker formula, 127
- Cathodoluminescence, 95
- Cellular automata, 257
- Charge carriers, 189
- Collective excitations, 51
- Compound semiconductor, 115
- Conductance oscillations, 59
- Conductance steps, 153
- Coulomb blockade, 183, 235
- Coulomb interaction, 59
- Cultured cells, 13
- Current fluctuations, 19
- Cyclotron orbits, 153
- Delta doping, 111
- Diffraction, 33
- Diffuse scattering, 163
- Diode, 219
- Dissipation, 29
- Distributed amplifier, 253
- Double heterostructure, 123
- Edge states, 37
- Electron-beam lithography, 95, 107
- Electron focusing, 133, 153
- Electron-phonon interaction, 51, 55
- Electron scattering mechanism, 157
- Electron waveguide, 45, 225
- Electron-wave packets, 33
- Etching, 95
- Etching methods, 153
- Exact Green's function in magnetic field, 69
- Fabrication, 107, 245
- Fermi level pinning, 115
- Focused ion beam, 157
- GaAs, 219
- GaAs-AlGaAs, 85
- GaAs/AlGaAs heterojunction, 167
- GaAs/AlGaAs heterostructure, 229
- Gate, 219
- Hall resistance anomalies, 41
- HEMT, 253
- Heterostructures, 1, 183
- High mobility, 127
- High speed operation, 239
- High-mobility hole gas, 179
- InGaAs, 115
- InGaAs quantum wires, 103
- Interface control, 115
- Interference, 33, 249
- Ion implantation, 95, 163
- Laminar flow, 25
- Landau levels, 37
- Landauer formula, 45
- Lateral quantization, 103
- Lateral surface superlattice, 141
- Learning theory, 7
- Level discreteness, 65
- Light pressure forces, 79
- Logic application, 239
- Low dimensional, 137
- Low dimensional system in GaAs heterostructures, 133
- LSI, 1
- Luminescence, 205
- MOSFET, 141
- Magneto-phonon resonances, 55
- Magneto-photoluminescence, 199
- Magneto-resistance, 133, 145, 149

Magneto-transport, 111, 137  
 Materials, 1  
 Mesoscopic physics, 45  
 Mesoscopic systems, 29, 41  
 Metallic particles, 65  
 Microelectrodes, 13  
 MOCVD, 199  
 Modelling, 245  
 Modulation doping, 85  
 Molecular beam epitaxy, 205

Nanofabrication, 73  
 Nanolithography, 73, 79  
 Nanometric electronics, 253  
 Nanostructures, 19, 213  
 Neural networks, 7, 13  
 NMR, 65  
 Nonequilibrium electron, 127  
 Nonlinear optical properties of semiconductors, 209

One-dimensional conductors, 29  
 One-dimensional density of states, 225  
 Optical information processing, 257  
 Optical logic devices, 189  
 Optical properties of superlattices, 189  
 Optical properties, 205  
 Oscillating barriers, 45  
 Oscillating tunnel barriers, 229

Periodic conductance oscillation, 179  
 Periodic potential modulation, 145  
 Permeable base transistor, 123  
 Phase coherence length, 157  
 Phase-coherent conductor, 19  
 Pheromone, 13  
 Photoconduction, 189  
 Photoluminescence, 189, 199  
 Plasmons, 51, 183  
 Point contact, 249  
 Polarization, 205  
 Potential fluctuation, 179

Quantized current, 229  
 Quantum dots, 137, 183, 235, 257  
 Quantum effect device, 175  
 Quantum effects, 73  
 Quantum Hall effect, 37  
 Quantum interference, 141  
 Quantum jumps, 257  
 Quantum noise, 29  
 Quantum point contacts, 45, 179, 229  
 Quantum stochastics, 257  
 Quantum structures, 103  
 Quantum transistor, 245

Quantum transport, 25, 41  
 Quantum wells, 95, 195  
 Quantum well wire, 51, 107  
 Quantum wires, 37, 55, 111, 115, 163, 167, 199, 205, 213, 225

Resonant tunnelling, 25, 239, 245  
 Resonant tunnelling diodes, 85

Scattering matrix, 19  
 Semiclassical, 149  
 Semiconductor heterostructures, 55, 127  
 Semiconductor microstructures, 51  
 Semiconductor nanostructure, 25  
 Semiconductor x-ray mask, 119  
 Shot noise, 29  
 Silicon, 1  
 Silicon-germanium heterostructures, 123, 209  
 Si molecular beam epitaxy, 123  
 Simulation, 33  
 Single-electron effects, 235  
 Spin lifetime, 65  
 Spin susceptibility, 65  
 Split-gate, 225  
 Stessor structures, 85  
 Strain-induced quantum wires/dots, 99  
 Subband effects, 167  
 Submicron lithography, 79  
 Superlattice, 119

Threshold functions, 7  
 Time delay, 33  
 Translational symmetry breaking, 69  
 Transport, 149  
 Transport properties, 55  
 Traversal time, 19  
 Tunnelling, 171, 213, 219  
 Tunnelling spectroscopy, 225  
 Turnstile, 229  
 Two-dimensional electron gas, 127

Ultrafine grating, 119  
 Universal conductance fluctuations, 167

Vortex flow, 25

Weak link, 171  
 Weak localization, 141  
 Wigner crystal, 59  
 Wire, 95

X-ray absorber, 119  
 X-ray lithography, 119

Zone folding, 209

The Institute of Physics Conference Series regularly features papers presented at important conferences and symposia highlighting new developments in physics and related fields. Recent titles include:

- 116 X-ray Lasers 1990, proceedings of the 2nd International Colloquium held in York, 1990 (published June 1991)
- 117 Microscopy of Semiconducting Materials 1991, invited and contributed papers from the International Conference held in Oxford, 1991 (published November 1991)
- 118 Electrostatics 1991, proceedings of the Eighth International Conference held in Oxford, 1991 (published September 1991)
- 119 Electron Microscopy and Analysis 1991, proceedings of the Conference held in Bristol, 1991 (published January 1992)
- 120 Gallium Arsenide and Related Compounds 1991, proceedings of the Eighteenth International Symposium held in Seattle, 1991 (published February 1992)
- 121 Photoelectronic Image Devices 1991, proceedings of the Tenth Symposium held in London, 1991 (published January 1992)
- 122 Correlations and Polarization in Electronic and Atomic Collisions and (e,2e) Reactions, proceedings of the Sixth International Symposium held in Adelaide, 1991 (published February 1992)
- 123 Optics of Excitons in Confined Systems, invited and contributed papers from the Conference held in Giardini Naxos, Italy, 1991 (published March 1992)
- 124 Physics at SuperLEAR, proceedings of the Workshop held in Zurich, 1991 (published April 1992)